NTNU – Trondheim
Norwegian University of
Science and Technology

On Locking-free Methods for Isogeometric Large Deformation Analysis of Geometrically Exact 3D Timoshenko Beams

Tore Andreas Helgedagsrud

Civil and Environmental Engineering
Submission date: June 2015
Supervisor: Kjell Magne Mathisen, KT

Norwegian University of Science and Technology
Department of Structural Engineering

Preface

This master thesis is prepared in the 10th semester at Department of Structural Engineering at the Norwegian University of Science and Technology (NTNU) in the spring of 2015.
The subject of the thesis is a continuation of my project work in the 9th semester, where isogeometric analysis of a rotation-free Euler-Bernoulli beam was performed.

I would like to acknowledge my advisor, prof. Kjell Magne Mathisen, for superior guidance, feedback and motivation throughout the whole work. I am also grateful to be given the opportunity to be coauthor on my first scientific article submitted for reviews in May 2015 [20], and present the work on the VIII National Conference on Computational Mechanics 2015 and the III International Conference on Isogeometric Analysis 2015.

Trondheim
June 3, 2015

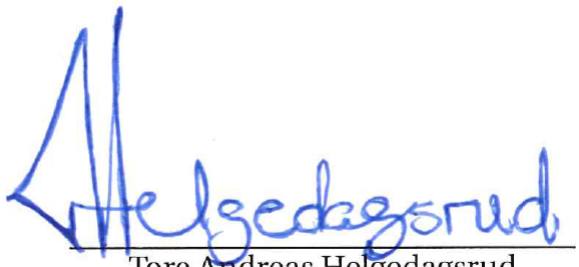

Tore Andreas Helgedagsrud

Abstract

In this thesis the geometrically exact 3D shear-flexible beam model is discretized with the Lagrangian and the NURBS basis functions, and has been used as a basis to develop a family of locking-free NURBS-based elements. This beam model has no restrictions with respect to the size of displacements, rotations and deformations, and is thus well accommodated for large deformation analyses.

In the C^0-continuous Lagrange element, numerical locking is overcome by reduced integration. However, for the higher continuous NURBS elements, there exists at the present time no element-by-element Gaussian quadrature rule which effectively alleviates locking. Instead, by a patch-wise approach a selective reduced integration rule has been proposed, and the resulting elements are free for transverse shear and membrane locking.

The performance is evaluated on a range of numerical tests and compared to the conventional reduced integration rule. For comparison, also the standard Lagrange interpolated elements have been tested in parallel.

Contents

Chapter 1

Introduction

The finite element method has been widely used in computational mechanics, engineering and sciences for several decades, but unfortunately, the traditional Lagrangian approximation functions are unable to represent many common geometries in an exact manner. With the introduction of isogeometric analysis (IGA), Lagrangian polynomials are replaced with *non-uniform rational B-splines* (NURBS), which may represent geometries exactly by the same approximation functions used to discretize the solution space. Due to their ability to describe exact geometries even for coarse discretizations, NURBS constitute today the most commonly used technology in computer-aided design (CAD).

Hughes *et al.* [22] introduced in 2005 the concept of using NURBS as interpolation functions in numerical analyses. They called the framework isogeometric analysis, and their motivation was to describe and simplify mesh refinement by eliminating the need for communication with the CAD geometry once the initial mesh was defined. Since its conception, IGA has penetrated many areas of computational mechanics, and in many cases shown improved performance over the traditional finite element method. In the area of structural and solid mechanics IGA has been successfully employed in computation of cable structures [34], 2D and 3D solids, including large deformations, incompressibility, near-incompressibility and plasticity [18, 28], contact problems [29, 30], fracture [8] and fluid-structure interaction [42].

Implementation of NURBS-based discretizations does however bring some challenges, and has been subject to a lot of research in recent years. One of them is shear-flexible beams, which suffer from the same locking phenomena as the Lagrangian-based finite element analysis (FEA), as pointed out by e.g. Echter and Bishoff [16] and Bouclier *et al.* [9]. This imply transverse shear locking in straight beams, and transverse shear and membrane locking in initially curved beams [41]. An element subjected to locking becomes unable to reproduce bending properly in the Kirchoff limit, i.e. when the thickness become very small compared to the length of the beam (or the curvature radius for curved beams). Several remedies to alleviate the occurrence of locking in IGA has been successfully applied: 1) Reduced and selective reduced integration [1, 2, 10], 2) NURBS-based discrete shear gap (NURBS DSG) methods [16, 17], 3) $\overline{B}$ and $\overline{F}$ projection techniques [9, 10, 11, 18], 4) assumed natural strain methods [12], 5) hybrid-mixed methods [17], and 6) collocation methods [4, 6]. However, apart from the $\overline{B}$ and $\overline{F}$ projection methods proposed by Elguedj *et al.* [18] and Bouclier *et al.* [9], these works were limited to linear elastic analyses.

In this context, the objective with this thesis is to develop a family of NURBS-based geometrically exact 3D shear-flexible beam elements which are free of numerical locking for analyses of geometrically non-linear finite deformation curved beam systems. In order to do that, the beam model proposed in [38, 39, 40], extended to an arbitrary order discretization of geometry, displacement and rotation fields with Lagrangian and NURBS are implemented in MATLAB®, and verified through a range of numerical tests. For non-linear analyses the FENRIS® solver is used. To alleviate locking, a lower order, patch-wise Gaussian quadrature rule for selective reduced integration of the stiffness matrix has been implemented and carefully tested on the verified code.

This thesis is outlined as follows. Chapter 2 gives an introduction to B-splines and NURBS and how these are used to describe geometric objects. The basic strategies for enrichment of the approximation space is also presented. In Chapter 3, a linear, straight beam formulation of the shear-flexible beam element is derived and verified through a few numerical examples for Lagrange and NURBS discretizations. Transverse shear locking is also highlighted in this

chapter. In Chapter 4, the geometrically exact 3D beam model is firstly presented at a continuous level, and then given on discrete form with both the Lagrangian and the NURBS basis. A presentation of the membrane locking phenomenon is also given here. The geometrically exact beam model is verified through a range of numerical examples in Chapter 5, where the impact of exact and conventional reduced integration on the convergence and thickness dependency has been emphasized. In Chapter 6 a study of the constraint ratio results in two new quadrature rules, which are carefully tested and compared on a selection of numerical examples. In Chapter 7 the performance of selective reduced integration has been studied in the non-linear regime, and finally, in Chapter 8 conclusions are drawn.

Chapter 2

NURBS-based geometries

NURBS curves and surfaces are, because of their ability to describe geometries in an exact manner, standard in computer-aided design (CAD) and computer-aided modeling (CAM) today. However, it is not until recently that NURBS has entered area of computational mechanics, engineering and sciences, which since its development in the late 50s and early 60s have been the property of Lagrangian polynomials [7].

In the area of solid and structural mechanics the NURBS-based isogeometric analysis has in many cases shown improved performance over the traditional FEA, due to the increased accuracy of the approximated geometry and the higher inter-element continuity. IGA does also bring the branches of CAD and FEA closer.

This chapter presents the basic definitions and properties of the NURBS basis, and how this is used for geometry modeling. In Section 2.1, the history of NURBS is briefly presented. In Section 2.2 the parameter space is defined, and derivation of the basis functions are shown in Section 2.3. Finally, in Section 2.4 it is described how the basis functions are used in geometry modeling, and how the approximation space may be enriched without changing the geometry or the parameterization.

For further details on geometry modeling with NURBS, the reader is referred to [19, 32].

2.1 History

NURBS have their origin in Bézier curves. These were originally developed by Bézier in the 60s [15] to give a parametric description of curves and surfaces. Unlike interpolation polynomials, the geometry could now be changed without changing the properties of the basis functions.
The main drawback with Bézier curves are their global support, which was resolved by Riesenfield in the early 70s with introduction of the B-splines [36]. B-splines with their compact support enable local shape modifications. Another benefit with B-splines is that the degree of continuity between the curve segments can be controlled.
Rational B-splines were introduced in 1975 by Versprille [45]. These were denoted NURBS, and allowed an exact formulation of circles and cones. Today NURBS are standard in CAD and CAM.

The concept of using NURBS in numerical analyses, instead of Lagrangian polynomials, was proposed by Hughes *et al.* in 2005 [22], and have since then been of large interest as an alternative to FEA.

2.2 Parameter space

As in FEA, NURBS-geometries are utilizing isoparameterization. With this concept, an object has a parametric formulation in a *parameter space*, which is connected to the physical space by a transformation (mapping).
A parametric representation is independent of the axes and uses the same set of shape functions, which offers a straightforward definition of free-form shapes and easily computed derivatives. In addition, there exist a lot of stable and efficient algorithms for parametric formulations, which is why they are preferred in IGA.

Knot vectors

For NURBS-geometries, the parameter space is local to *patches* (rather than elements in FEA). A patch is related to a *knot vector,* Ξ. For each dimension this is a non-decreasing sequence of

numbers, written:

$$\Xi = [\xi_1, \xi_2, ..., \xi_{n+p+1}] \tag{2.1}$$

which directly determines the properties of the basis functions, and thus the NURBS-geometry, which is constructed from a linear combination of the basis functions and their associated *control points*. The length of the knot vector, $n+p+1$, matches the polynomial degree, p, and the number, n, of the basis functions. A nonzero knot span, $\xi_{i+1} - \xi_i$, partition the patch into elements.

A knot vector is referred to as *open* if the first and last value appear $p+1$ times, and have the essential property of being interpolatory at the endpoints. Therefore open knot vectors are standard in IGA. Further, a knot vector can be *uniform* or *non-uniform*. In uniform knot vectors the knot spans are equal, and each interior knot may only appear once. Non-uniform knot vectors are not restricted to equal knot spans and may have repeated knot values, which allows much richer behavior, such as corners, sharper curves, local refinement, etc.

As an example, two knot vectors for computing quadratic basis functions are shown below:

$$\begin{aligned} \Xi_1 &= [0,0,0,\tfrac{1}{3},\tfrac{2}{3},1,1,1] \\ \Xi_2 &= [0,0,0,\tfrac{1}{6},\tfrac{2}{3},\tfrac{2}{3},1,1,1] \end{aligned} \tag{2.2}$$

Because the first and the last knot values appear $p+1$ times, they are both open. In Ξ_1, the knot spans are equidistant and the interior knots $\xi_4 = \frac{1}{3}$ and $\xi_5 = \frac{2}{3}$ appear only once. Therefore, this is a uniform knot vector. By the same argument, Ξ_2 is obviously nonuniform.

2.3 Basis functions

NURBS are built from the non-rational B-splines, and are constructed from linear combinations of a set of basis functions, uniquely defined by the knot vector, which represents the parameter space. This is for curves one-dimensional and thus function of the parameter ξ only.

The basis functions may be thought of as shape functions in FEA, and are recursively computed

from piecewise constants in each knot spans, expressed as:

$$\mathbf{N}_0 = N_{i,0}(\xi) = \begin{cases} 1 & \text{for } \xi_i \leq \xi < \xi_{i+1} \\ 0 & \text{otherwise} \end{cases} \tag{2.3}$$

For $p \geq 1$ the functions are expressed in terms of the lower order ones:

$$\mathbf{N}_p = N_{i,p}(\xi) = \frac{\xi - \xi_i}{\xi_{i+p} - \xi_i} N_{i,p-1}(\xi) + \frac{\xi_{i+p+1} - \xi}{\xi_{i+p+1} - \xi_i + 1} N_{i+1,p-1}(\xi) \tag{2.4}$$

To avoid singularity in Equation 2.4, $\frac{0}{0}$ is defined to be zero.

Figure 2.1 illustrates the recursive structure of the basis functions, and from which lower order functions they are constructed.

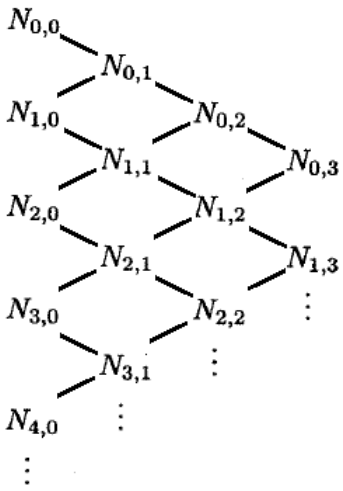

Figure 2.1: Recursive computation of basis functions, taken from [32].

The B-splines basis functions satisfy the following important properties:

- They are nonnegative over the entire domain, Ξ: $N_{i,p} \geq 0$, $\forall \xi \in [\xi_i, \xi_{n+p+1}]$.
- Partition of unity, $\sum_{i=1}^{n} N_{i,p} = 1$, $\forall \xi \in [\xi_i, \xi_{n+p+1}]$.
- Infinitely continuously differentiable between the knots, C^{p-m_i}-continuous at interior knots (where m_i is the knot multiplicity).
- Each basis function has support over the half-open interval, $[\xi_i, \xi_{i+p+1}\rangle$.

- Non-interpolatory: $N_{i,p}(\xi_j) \neq 1$, except for the end knots or knots with multiplicity $m_i = p-1$.
- For $p = 0$ and $p = 1$, B-spline and Lagrangian basis functions coincide.

To illustrate the development of these basis functions, they will be recursively computed from $0th$ to $2nd$ order for the knot vectors in Equation 2.2.

Basis functions for $\Xi_1 = [0,0,0,\frac{1}{3},\frac{2}{3},1,1,1]$

According to Equation 2.3, the constant functions are computed:

$$N_{1,0} = N_{2,0} = 0 : -\infty < \xi < \infty$$

$$N_{3,0} = \begin{cases} 1 & : 0 \leq \xi < \dfrac{1}{3} \\ 0 & : \text{otherwise} \end{cases}$$

$$N_{4,0} = \begin{cases} 1 & : \dfrac{1}{3} \leq \xi < \dfrac{2}{3} \\ 0 & : \text{otherwise} \end{cases}$$

$$N_{5,0} = \begin{cases} 1 & : \dfrac{2}{3} \leq \xi < 1 \\ 0 & : \text{otherwise} \end{cases}$$

$$N_{6,0} = N_{7,0} = 0 : -\infty < \xi < \infty$$

and plotted in Figure 2.2.

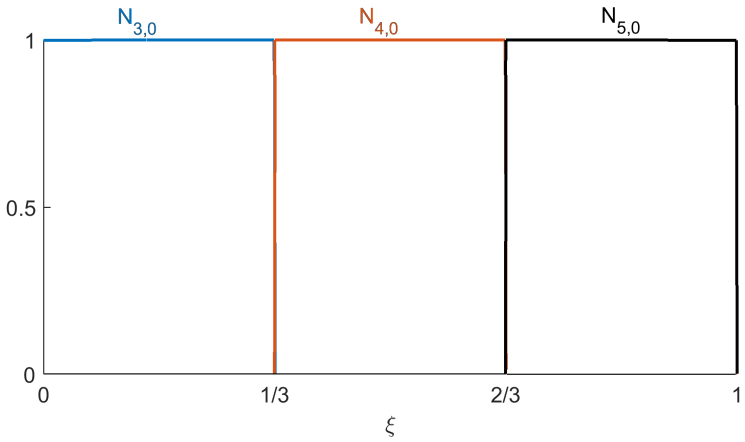

Figure 2.2: Constant basis functions for Ξ_1.

With the constant functions at hand, the linear and quadratic basis functions ($N_{i,1}$ and $N_{i,2}$) are computed from Equation 2.4:

$$N_{1,1} = 0 : -\infty < \xi < \infty$$

$$N_{2,1} = \begin{cases} 1-3\xi & : 0 \le \xi < \frac{1}{3} \\ 0 & : \text{otherwise} \end{cases}$$

$$N_{3,1} = \begin{cases} 3\xi & : 0 \le \xi < \frac{1}{3} \\ 2-3\xi & : \frac{1}{3} \le \xi < \frac{2}{3} \\ 0 & : \text{otherwise} \end{cases}$$

$$N_{4,1} = \begin{cases} -1+3\xi & : \frac{1}{3} \le \xi < \frac{2}{3} \\ 3-3\xi & : \frac{2}{3} \le \xi < 1 \\ 0 & : \text{otherwise} \end{cases}$$

$$N_{5,1} = \begin{cases} -2+3\xi & : \frac{2}{3} \le \xi < 1 \\ 0 & : \text{otherwise} \end{cases}$$

$$N_{6,1} = 0 : -\infty < \xi < \infty$$

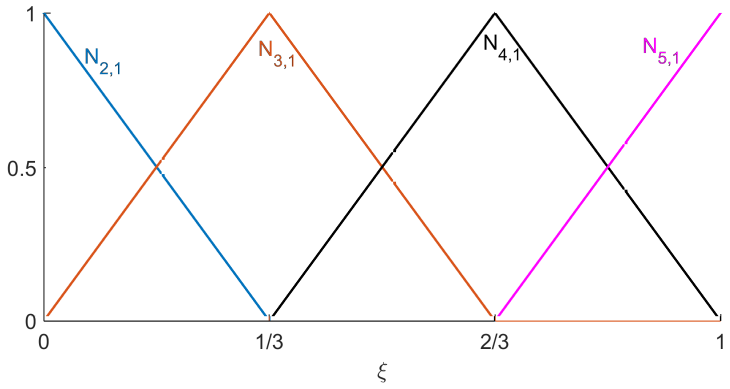

Figure 2.3: Linear basis functions for Ξ_1.

$$N_{1,2} = \begin{cases} (-1+3\xi)^2 & : 0 \le \xi < \frac{1}{3} \\ 0 & : \text{otherwise} \end{cases}$$

$$N_{2,2} = \begin{cases} 6\xi - \frac{27}{2}\xi^2 & : 0 \le \xi < \frac{1}{3} \\ \frac{1}{2}\left(-2+3\xi\right)^2 & : \frac{1}{3} \le \xi < \frac{2}{3} \\ 0 & : \text{otherwise} \end{cases}$$

$$N_{3,2} = \begin{cases} \frac{9}{2}\xi^2 & : 0 \le \xi < \frac{1}{3} \\ -\frac{3}{2} + 9\xi - 9\xi^2 & : \frac{1}{3} \le \xi < \frac{2}{3} \\ \frac{9}{2}\left(-1+\xi\right)^2 & : \frac{2}{3} \le \xi < 1 \\ 0 & : \text{otherwise} \end{cases}$$

$$N_{4,2} = \begin{cases} \frac{1}{2}\left(-1+3\xi\right)^2 & : \frac{1}{3} \le \xi < \frac{2}{3} \\ -\frac{15}{2} + 21\xi - \frac{27}{2}\xi^2 & : \frac{2}{3} \le \xi < 1 \\ 0 & : \text{otherwise} \end{cases}$$

$$N_{5,2} = \begin{cases} (-2+3\xi)^2 & : \frac{2}{3} \le \xi < 1 \\ 0 & : \text{otherwise} \end{cases}$$

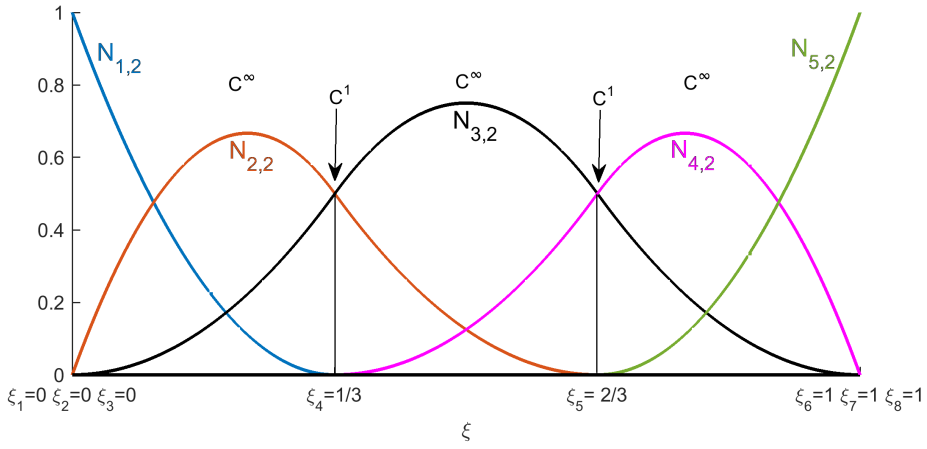

Figure 2.4: Quadratic basis functions for Ξ_1.

It is confirmed that the $0th$ and $1st$ degree basis functions coincide with the Lagrangian basis. For higher orders, the B-spline basis are more homogeneous and do not show the oscillatory properties as the Lagrangian basis.

Other properties of the basis functions can be seen in Figure 2.4. While the polynomials are completely differentiable in the knot spans (C^∞-continuous), the continuity at the interior knots are $C^{p-m_i} = C^1$. Further, each basis function has support over the interval $[\xi_i, \xi_{i+p+1}\rangle$. E.g. $N_{2,2}$ is nonzero on the interval $[\xi_2, \xi_5\rangle = [0, \frac{2}{3}\rangle$.

Basis functions for $\Xi_2 = [0,0,0,\frac{1}{6},\frac{2}{3},\frac{2}{3},1,1,1]$

The basis functions for this open non-uniform knot vector are computed the same way as for Ξ_1, and shown in Figures 2.5 to 2.7. The length of the vector, $n+p+1 = 9$, indicates $n = 6$ quadratic shape functions, and C^0-continuity at $\xi = 2/3$ due to the repeated knot, which is easily recognized as a corner.

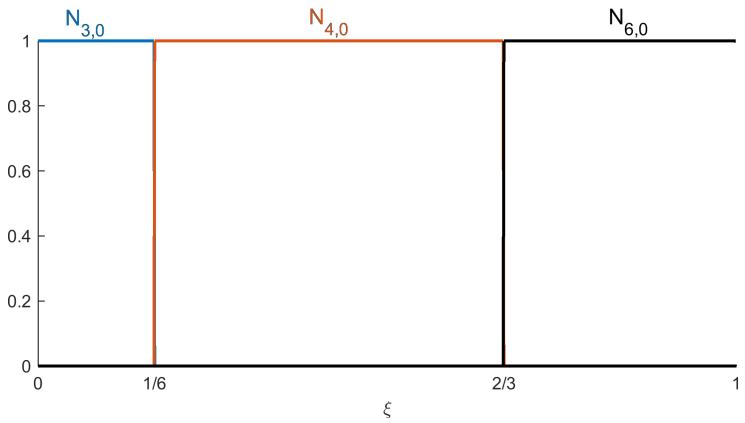

Figure 2.5: Constant basis functions for Ξ_2.

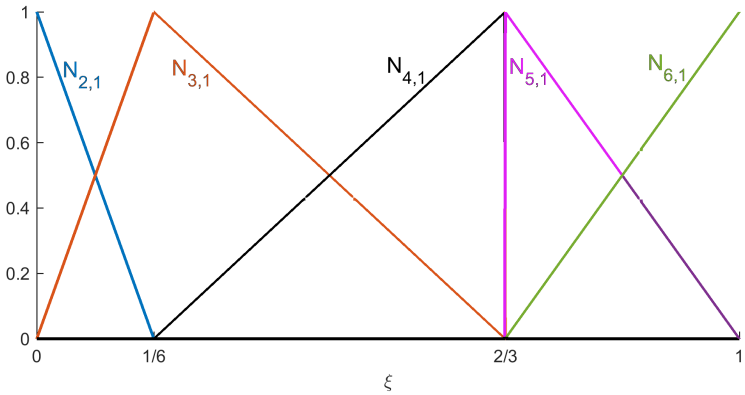

Figure 2.6: Linear basis functions for Ξ_2.

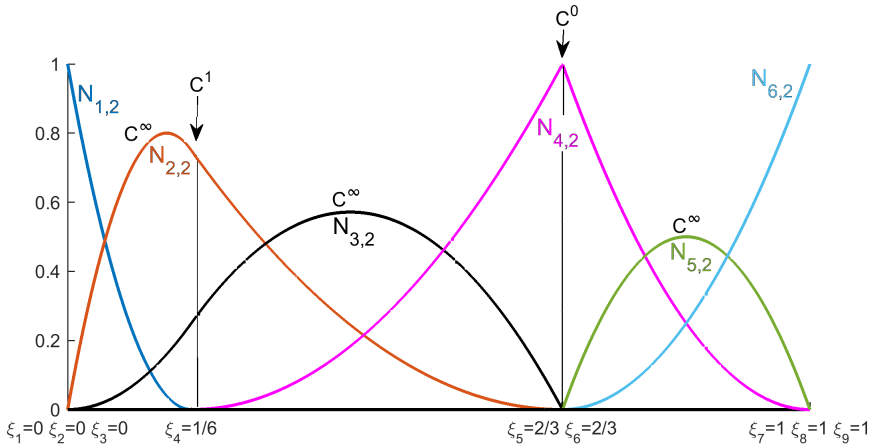

Figure 2.7: Quadratic basis functions for Ξ_2.

Derivatives of basis functions

Derivatives of quantities are essential in numerical analyses. The variable in NURBS-geometries is found in the basis functions, and the derivatives of these are given in terms of the lower order basis functions. For shape function i and polynomial degree p, the kth derivative is gives as:

$$\frac{d^k N_{i,p}}{d\xi^k} = \frac{p}{\xi_{i+p} - \xi_i}\left(\frac{d^{k-1} N_{i,p-1}}{d\xi^{k-1}}\right) - \frac{p}{\xi_{i+p+1} - \xi_{i+1}}\left(\frac{d^{k-1} N_{i+1,p-1}}{d\xi^{k-1}}\right) \tag{2.5}$$

Figures 2.8 and 2.9 show the $1st$ derivatives of the two bases. Note the continuity across $\xi = 2/3$ for the two bases.

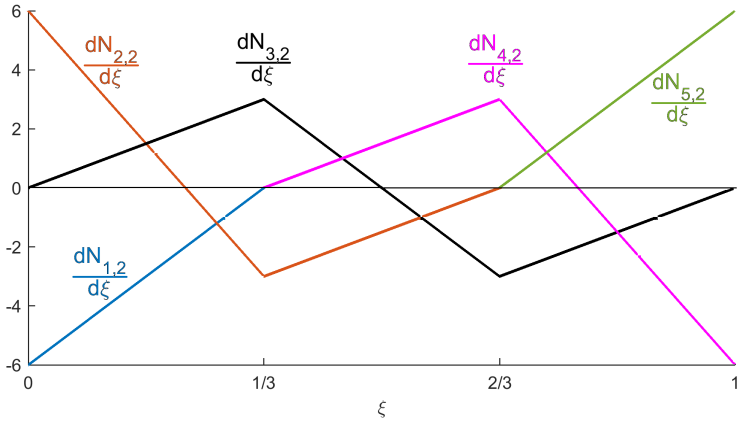

Figure 2.8: $1st$ derivative of the Ξ_1-basis.

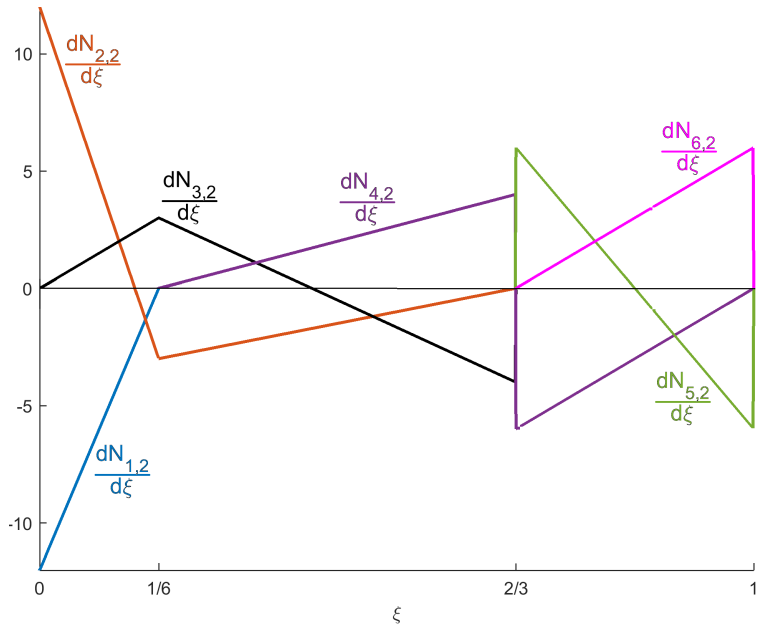

Figure 2.9: $1st$ derivative of the Ξ_2-basis.

2.4 NURBS geometry

A NURBS geometry in $\mathbb{R}^d$ is obtained by a projective transformation of a B-spline geometry in $\mathbb{R}^{d+1}$. Therefore, a natural starting point understanding NURBS geometries is to look into B-spline geometries. It will be focused on curves, as this thesis is limited to beam elements.

2.4.1 B-spline curves

As in standard FEA, a B-spline curve is constructed from a linear combination of the basis functions and a set of vector-valued coefficients, called *control points* in IGA.

Given n basis functions, $N_{i,p}$ and their corresponding control points, $\mathbf{B}_i$, $i = 1,2,...,n$, a B-spline curve, consisting of piecewise polynomials connected at the knot values, is given by:

$$\mathbf{C}(\xi) = \sum_{i=1}^{n} N_{i,p}(\xi)\mathbf{B}_i \tag{2.6}$$

The control points, whose piecewise linear interpolation is called the *control polygon*, are analogous to nodes in FEA. However, an important difference is that they are in general

non-interpolatory.

The curve in Figure 2.10 are constructed from the quadratic Ξ_1-basis. The control points are denoted by ●, and the knot locations, which partition the curve into elements, are denoted ■.

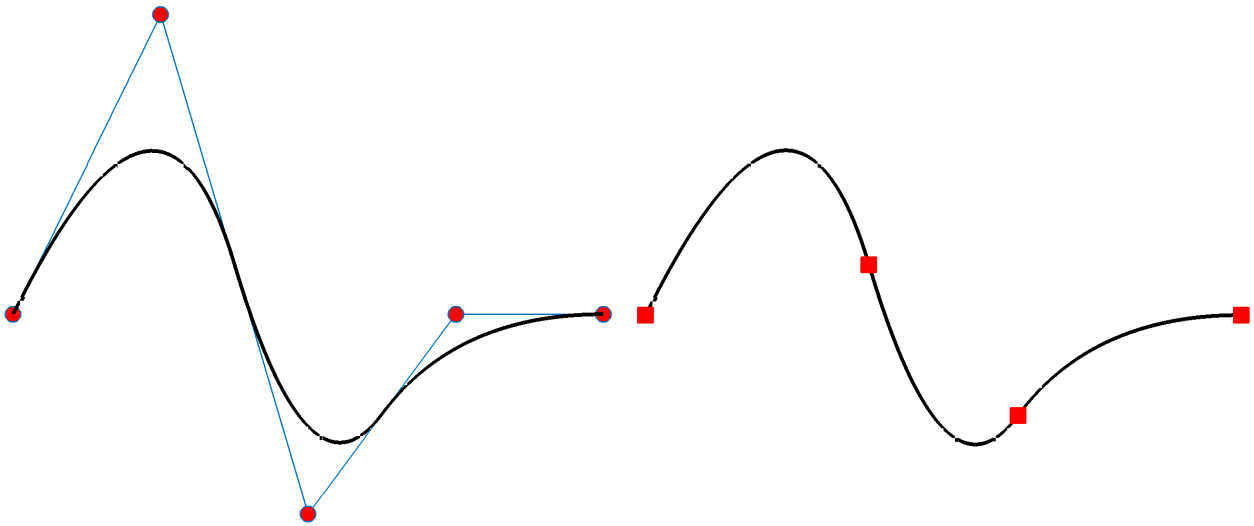

(a) Curve and control polygon

(b) Curve and knot locations

Figure 2.10: Quadratic B-spline curve in $\mathbb{R}^2$ constructed from Ξ_1 and $\mathbf{B} = [(0,0),(1,3),(2,-2),(3,0),(4,0)]$.

Another curve, constructed from the Ξ_2-basis are shown in Figure 2.11. Note that at the C^0-continuity at $\xi = 2/3$, the element boundary coincides with the control point, $\mathbf{B}_4$, which becomes interpolatory. Another important property of B-spline curves (and NURBS curves) is that at the control polygon coincides with the endpoint tangents of the curve [26].

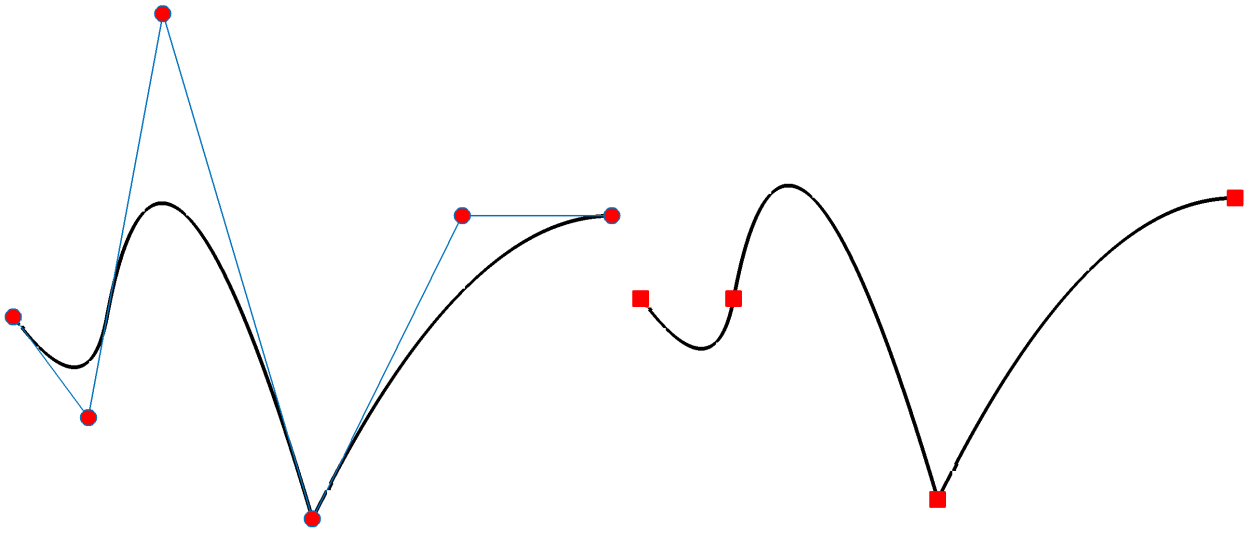

(a) Curve and control polygon

(b) Curve and knot locations

Figure 2.11: Quadratic B-spline curve in $\mathbb{R}^2$ constructed from Ξ_2 and $\mathbf{B} = [(0,0),(0.5,-1),(1,3),(2,-2),(3,1),(4,1)]$.

2.4.2 Refinement

An important aspect of IGA, as well as FEA, is how the basis may be enriched without changing the geometry or the parameterization, allowing control of the discrete solution space. In addition to order elevation and h-refinement, which are known mechanisms from FEA, one may also control the continuity of the basis. This makes the refinement space of IGA much richer.

In IGA, there are three basic refinement mechanisms:

- Knot insertion
- Order elevation
- k-refinement

which in this section are briefly presented. For more detailed descriptions and algorithms, the reader is referred to [32, 25].

Knot insertion

Recalling that element boundaries are found at the knots, insertion of new knots partition the domain into several elements. This is known as knot insertion, and is similar to h-refinement in FEA. It differs, however, in the continuity across the element boundaries created (C^{p-1}). To perfectly replicate h-refinement, the new knot would have to be inserted p times, so that C^0-continuity is obtained.

Insertion of new knots requires recomputation of both the basis functions and the control points. Having an original knot vector, $\Xi = [\xi_1, \xi_2, ..., \xi_{n+p+1}]$, an extended knot vector, $\overline{\Xi} = [\xi_1, \overline{\xi}_2, ..., \overline{\xi}_{m+n+p+1} = \xi_{n+p+1}]$ is introduced, such that $\Xi \subset \overline{\Xi}$. The basis is still formed by equations 2.3 and 2.4. To leave the geometry geometrically and parametrically unchanged, the new control points, $\overline{\mathbf{B}}_i$, $i = 1, ..., n+m$, must satisfy the condition:

$$\mathbf{C}(\xi) = \sum_{i=1}^{n} N_{i,p}(\xi)\mathbf{B}_i = \sum_{i=1}^{n+m} \overline{N}_{i,p}(\xi)\overline{\mathbf{B}}_i \tag{2.7}$$

Which will lead to system of linear combinations of the original control points. For a knot which has an initial multiplicity of s and is to be inserted r times, the ith control point in the rth insertion, denoted $\overline{\mathbf{B}}_{i,r}$, is given as:

$$\overline{\mathbf{B}}_{i,r} = \alpha_{i,r}\overline{\mathbf{B}}_{i,r-1} + (1 - \alpha_{i,r})\overline{\mathbf{B}}_{i-1,r-1} \tag{2.8}$$

where $\overline{\mathbf{B}}_{i,0} = \mathbf{B}_i$ and

$$\alpha_{i,r} = \begin{cases} 1 & i \leq (k-p+r-1) \\ \frac{\overline{\xi} - \xi_i}{\xi_{i+p-r+1} - \xi_i} & (k-p+r) \leq i \leq (k-s) \\ 0 & i \geq (k-s+1) \end{cases}$$

k represents the position index of the new knot. An efficient algorithm for Equation 2.8 is given in Piegl and Tiller [32], A5.1.

In Figure 2.12, knot insertion is performed on the curve from Figure 2.10. In the new knot vector, $\overline{\Xi}_1 = [0, 0, 0, \frac{1}{6}, \frac{2}{6}, \frac{3}{6}, \frac{4}{6}, \frac{5}{6}, 1, 1, 1]$, the knot spans in Ξ_1 is split in half by introducing the knots $\overline{\xi}_4 = \frac{1}{6}, \overline{\xi}_6 = \frac{3}{6}$, and $\overline{\xi}_8 = \frac{5}{6}$. The curves are clearly identical, but the refined curve has got more degrees of freedom and thus a richer solution space.

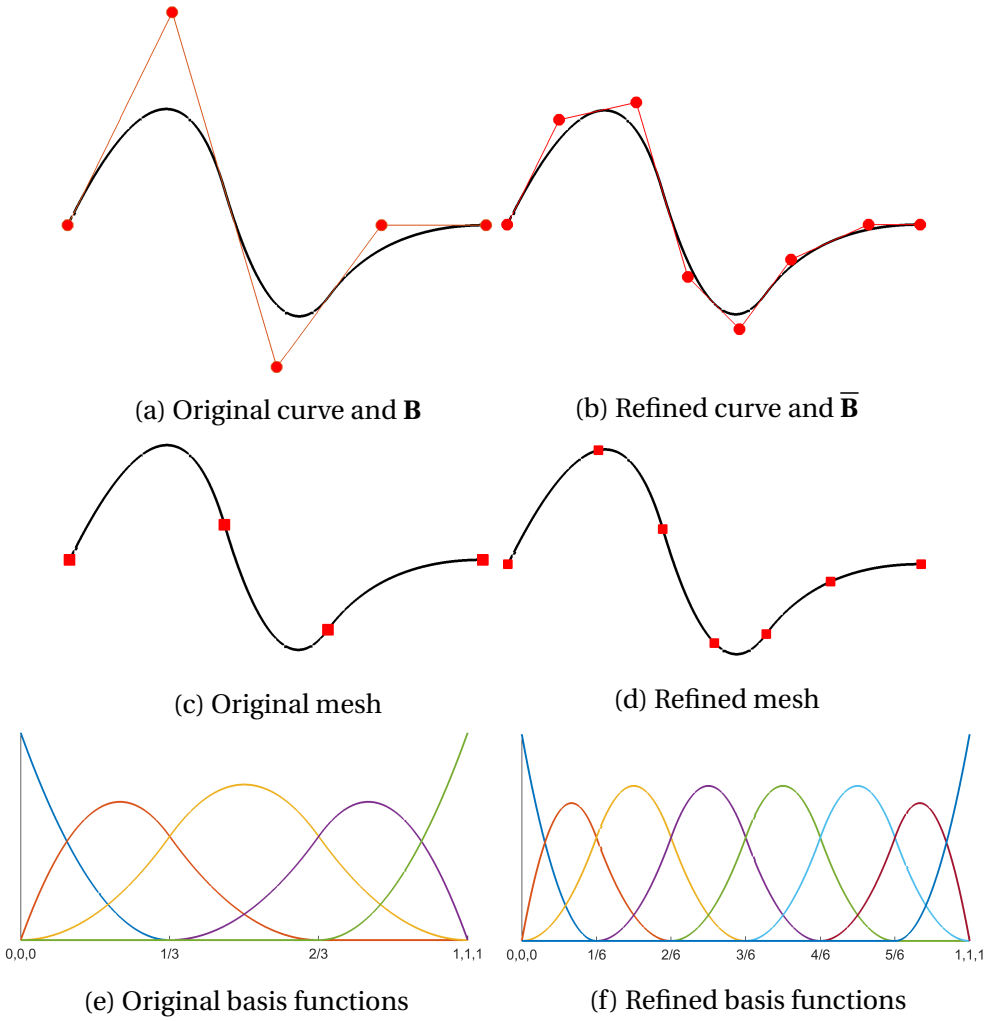

(a) Original curve and $\mathbf{B}$ (b) Refined curve and $\overline{\mathbf{B}}$

(c) Original mesh (d) Refined mesh

(e) Original basis functions (f) Refined basis functions

Figure 2.12: Knot insertion: $\Xi_1 = [0,0,0,\frac{2}{6},\frac{4}{6},1,1,1] \longrightarrow \overline{\Xi}_1 = [0,0,0,\frac{1}{6},\frac{2}{6},\frac{3}{6},\frac{4}{6},\frac{5}{6},1,1,1]$.

Order elevation

Another mechanism to enrich the basis is by order elevation (p- refinement in FEA). Recalling that the first and last knot value appears $p+1$ times for open knot vectors, the order is raised by adding new knots here. To preserve the C^{p-m_i}-continuity, the existing knots must be repeated simultaneously.

In short, order elevation is done by increase the multiplicity of each knot. No new knot values are introduced.

The higher order curve, $\mathbf{C}_{p+1}$, is simply computed by embedding the lower order curve, $\mathbf{C}_p$, to a higher dimensional space. Thus, there must exist control points, $\widehat{\mathbf{B}}$, and a knot vector, $\widehat{\Xi}$, such

that:

$$\mathbf{C}_p(\xi) = \sum_{i=1}^{n} N_{i,p}(\xi)\mathbf{B}_i = \mathbf{C}_{p+1}(\xi) = \sum_{i=1}^{\hat{n}} \hat{N}_{i,p+1}(\xi)\hat{\mathbf{B}}_i \tag{2.9}$$

Order elevation requires computation of the new basis functions, $\hat{\mathbf{N}}$. The new control points, $\hat{\mathbf{B}}$, are obtained in a similar way as for knot insertion.

A detailed description can be read in [32], where also the implemented algorithm A5.9 is given.

Figure 2.13 illustrates this refinement method. Again, the Ξ_1 basis and geometry from Figure 2.10 is used. Increasing the knot multiplicity by 1, the new knot vector becomes $\hat{\Xi}_1 = [0,0,0,0,\frac{1}{3},\frac{1}{3},\frac{2}{3},\frac{2}{3},1,1,1,1]$.

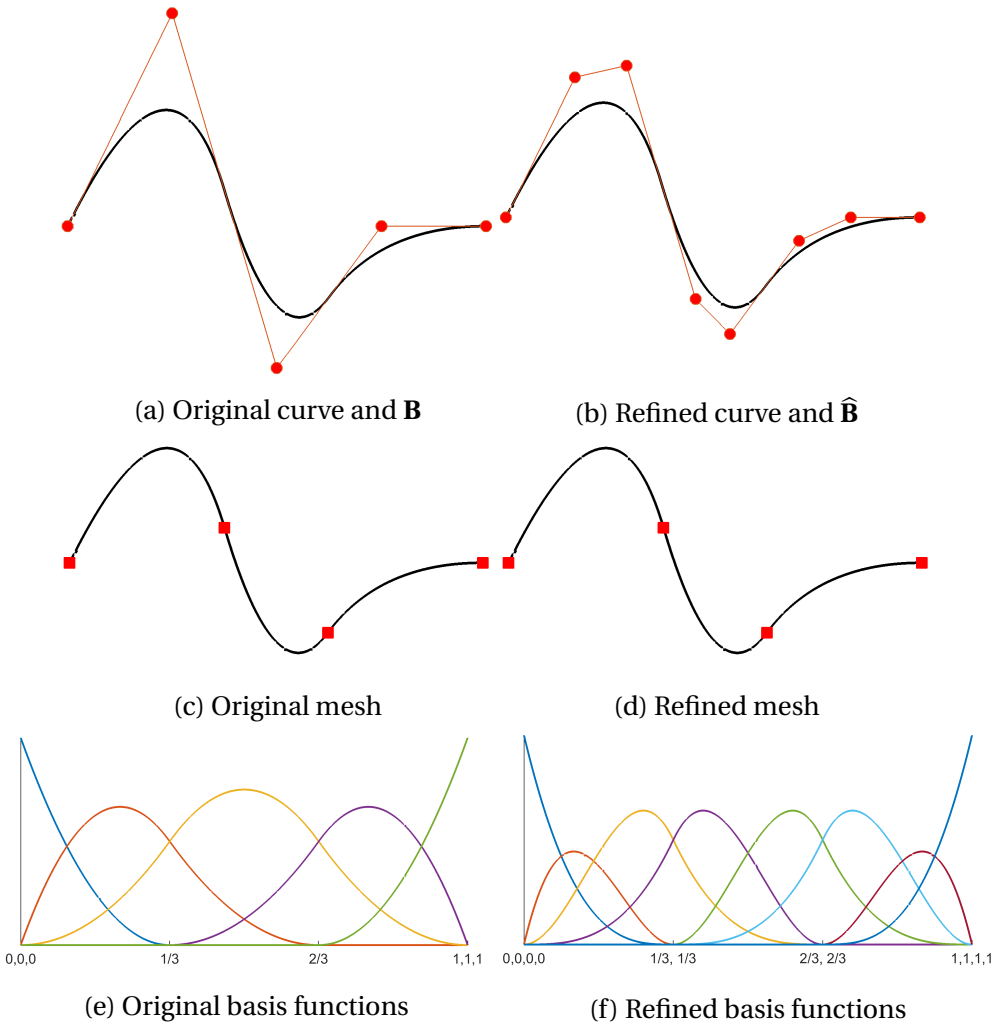

(a) Original curve and $\mathbf{B}$ (b) Refined curve and $\hat{\mathbf{B}}$

(c) Original mesh (d) Refined mesh

(e) Original basis functions (f) Refined basis functions

Figure 2.13: Order elevation: $\Xi_1 = [0,0,0,\frac{2}{6},\frac{4}{6},1,1,1] \rightarrow \hat{\Xi}_1 = [0,0,0,0,\frac{1}{3},\frac{1}{3},\frac{2}{3},\frac{2}{3},1,1,1,1]$.

k- refinement

It is observed that knot insertion generates more elements while keeping the polynomial order constant, and that order elevation raise the polynomial order while keeping number of elements *and* the continuity constant. k -refinement mixes these two methods such that the order is raised while having the maximum continuity available. This method has no analogue in FEA.

The strategy for k-refinement is to first perform order elevation to the desired degree, and then insert additional knot values. For pure p -refinement, these operations are done in the opposite order. Figure 2.14 compares these methods for a case where one linear element shall be refined to three $4th$ order elements. Note that the number of new shape functions generated is significantly lower with k -refinement.

Hughes *et al.* [22] has shown that k-refinement has advantages of robustness and efficiency over p-refinement.

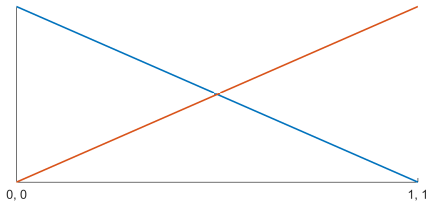

Initial basis, $\Xi = [0,0,1,1]$

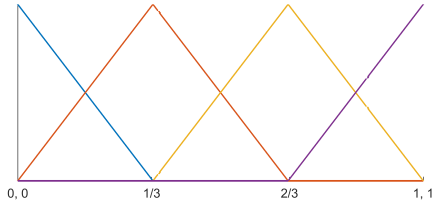

$\Xi = [0,0,\frac{1}{3},\frac{2}{3},1,1]$

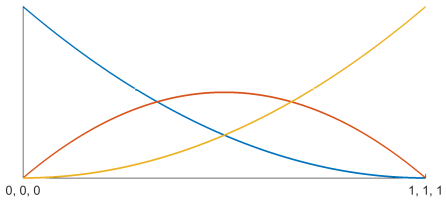

$\Xi = [0,0,0,1,1,1]$

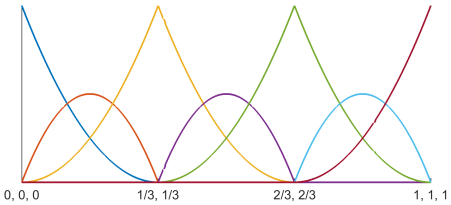

$\Xi = [0,0,0,\frac{1}{3},\frac{1}{3},\frac{2}{3},\frac{2}{3},1,1,1]$

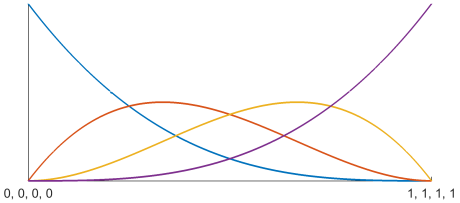

$\Xi = [0,0,0,0,1,1,1,1]$

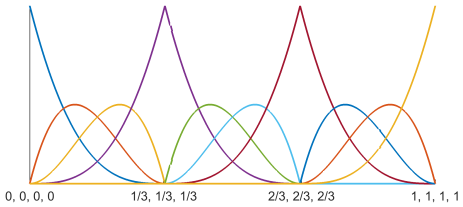

$\Xi = [0,0,0,0,\frac{1}{3},\frac{1}{3},\frac{1}{3},\frac{2}{3},\frac{2}{3},\frac{2}{3},1,1,1,1]$

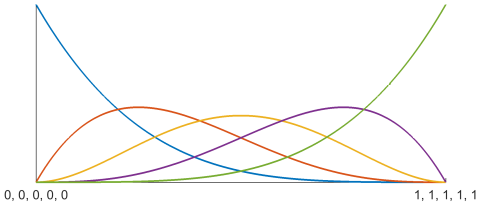

$\Xi = [0,0,0,0,0,1,1,1,1,1]$

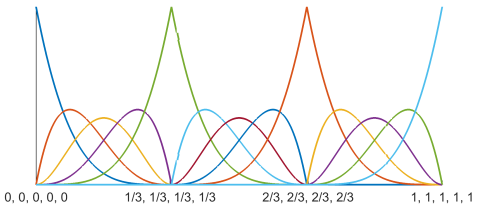

$\Xi = [0,0,0,0,0,\frac{1}{3},\frac{1}{3},\frac{1}{3},\frac{1}{3},\frac{2}{3},\frac{2}{3},\frac{2}{3},\frac{2}{3},1,1,1,1,1]$

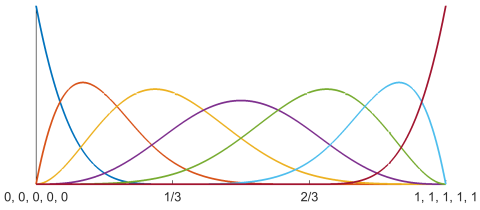

$\Xi = [0,0,0,0,0,\frac{1}{3},\frac{2}{3},1,1,1,1,1]$

Figure 2.14: p-refinement (left) compared to k-refinement (right). Both ending with three $4th$ order elements.

2.4.3 NURBS curves

Having defined the non-rational B-spline curves, non-uniform rational B-splines (NURBS) are now introduced. The motivation is that NURBS allow high geometrical flexibility, such as an exact representation of circular shapes.

From a geometric point of view, a NURBS curve in $\mathbb{R}^d$ is obtained by a projective transformation of a B-spline curve in $\mathbb{R}^{d+1}$ onto a hyperplane $\mathbb{H} = 1$ in $\mathbb{R}^d$. This is easily interpreted for a curve in $\mathbb{R}^2$ constructed from a B-spline curve in $\mathbb{R}^3$. The transformation is then applied by projecting the curve onto the $z = 1$ plane by a ray through the origin, as shown in Figure 2.15. Here, the z- components represents the *weights*, denoted w_i.

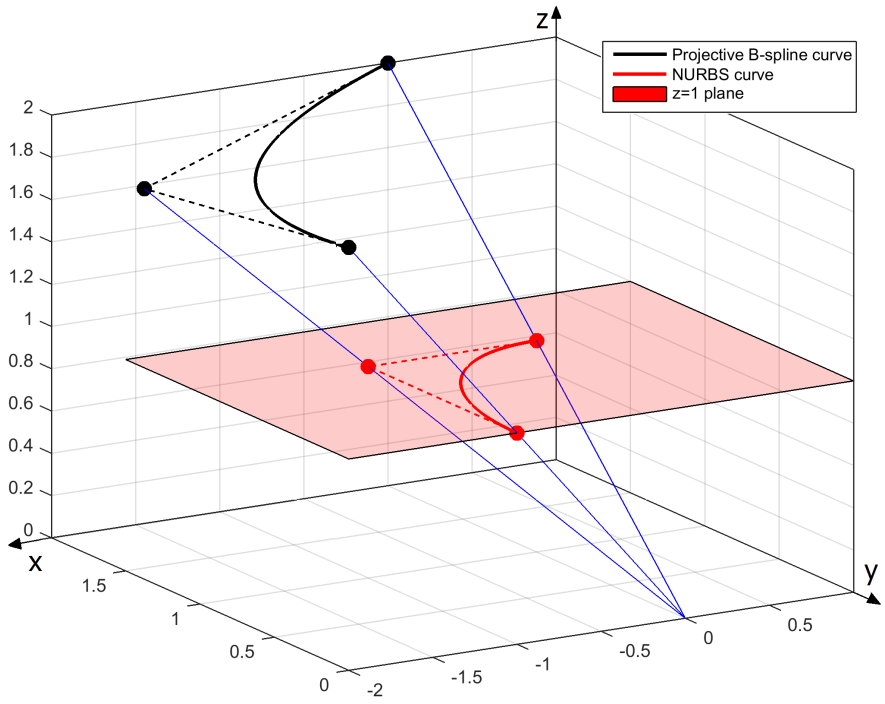

Figure 2.15: A quarter of a circle in $\mathbb{R}^2$ constructed by the projective transformation of a non-rational B-spline curve in $\mathbb{R}^3$

This projection is expressed mathematically by introducing a *weighting function*, $W(\xi)$, given as the sum of the basis functions multiplied with their associated weight:

$$W(\xi) = \sum_{i=1}^{n} N_{i,p}(\xi)\, w_i \tag{2.10}$$

where $N_{i,p}$ is the B-spline basis functions. The NURBS curve, $\mathbf{C}(\xi)$ is then given as:

$$\mathbf{C}(\xi) = \frac{\mathbf{C}^w(\xi)}{W(\xi)} \tag{2.11}$$

where $\mathbf{C}^w(\xi)$ refers to a projective B-spline curve from Equation 2.6.
For IGA, it is more effective to compute the basis for the NURBS space directly. The NURBS basis is given by the B-spline basis and the weights:

$$R_{i,p}(\xi) = \frac{N_{i,p}(\xi)\, w_i}{W(\xi)} \tag{2.12}$$

which leads to the equation for the NURBS curve:

$$\mathbf{C}(\xi) = \sum_{i=1}^{n} R_{i,p}(\xi)\mathbf{P}_i \tag{2.13}$$

where $\mathbf{P}_i$ are the NURBS control points, obtained by the relation: $\mathbf{P}_i = \mathbf{B}_i / w_i$.

All the essential properties discussed earlier are retained in NURBS (linear independence, local support, etc.).

Derivatives of NURBS basis functions

The derivatives of the non-rational basis given in Equation 2.5 are still valid, but as the rational basis contains the weighting function $W(\xi)$, the chain rule must be applied:

$$\frac{d}{d\xi} R_{i,p}(\xi) = w_i \frac{W(\xi)\frac{dN_{i,p}(\xi)}{d\xi} - \frac{dW(\xi)}{d\xi} N_{i,p}(\xi)}{(W(\xi))^2} \tag{2.14}$$

where

$$\frac{dW(\xi)}{d\xi} = \sum_{i=1}^{n} \frac{dN_{i,p}(\xi)}{d\xi} w_i \tag{2.15}$$

Effective algorithms for computing first and higher order derivatives of the rational basis functions are given in [32].

2.4.4 Circular curves

Due to the non-interpolatory properties of NURBS-geometries, obtaining control points and weights for general shapes are not straight forward, and not emphasized in this thesis. However, as circular shapes frequently show up in numerical analyses, a brief description of how these may be modeled in $\mathbb{R}^2$ is given.

Circular arcs with a sweep angle less than 180° may be constructed from one quadratic element, built from the knot vector $\Xi = [0,0,0,1,1,1]$, giving three basis functions control points. Recalling that the first and the last control point is interpolatory and that the end tangents coincide with the control polygon, the control points are easily obtained. For the weights, they are given as $w_i = [1, \cos\frac{\beta}{2}, 1]$, where β is the sweep angle [17]. Figure 2.16 illustrates this for $\beta = 90°$. The third coordinate in $\mathbf{P}_i^w$ refers to the weight number.

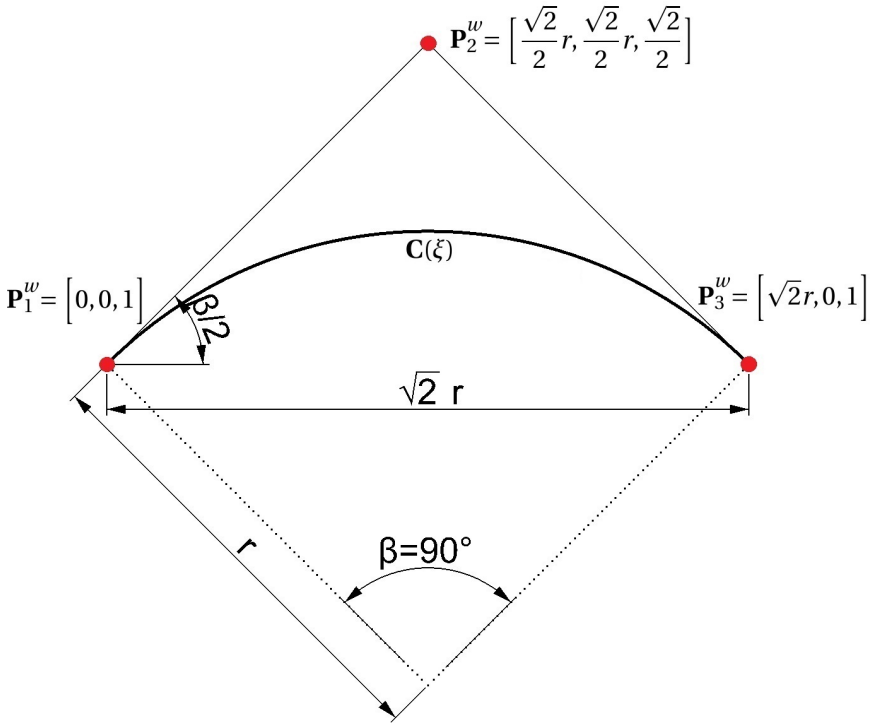

Figure 2.16: 90 °circular arc in $\mathbb{R}^2$ with associated control points and weights, constructed from one quadratic NURBS element.

Refinement of NURBS-geometries

The refinement strategies presented in Section 2.4.2 may also be used NURBS geometries. However, in addition to the new control points, new weights must also be computed.
Having a curve in $\mathbb{R}^d$ from Equation 2.13 to be refined, conditions in Equations 2.8 and 2.9 are valid if the weights are treated as component number $d+1$ in the control polygon.

The code in Appendix D performs k-refinement of a 90° circular arc. It may also be used for other NURBS (and B-spline) geometries by changing the initial geometry.

Chapter 3

Timoshenko beam theory

In contrast to Euler-Bernoulli beam theory, Timoshenko (often referred to as Mindlin-Reissner) beam theory includes shear deformations, which become more significant as the slenderness ratio, *(L/h)*, decreases.
In this chapter a linear, straight beam element is derived from the classical Timoshenko beam theory [43, 44] in Section 3.1, and discretized with the Lagrangian and the NURBS basis in Sections 3.2 and 3.3, respectively. In Section 3.4 the beam elements are implemented and verified through a few numerical examples. Lastly, transverse shear locking is highlighted in Section 3.5.
Note that this element is restricted to linear analyses and linear geometries.

3.1 Governing equations

The displacement based theory assumes independent fields for rotations, θ_i, and translations, u_i, $i = x, y, z$. According to the fundamental hypothesis for beams, it is assumed that the cross-section remain plane under deformation, but not necessarily normal to the line of centroids. The difference between the rotation of the cross-section and the slope defines the transverse shear strains. For a beam with the local axis in x-direction and a cross-section symmetric about

the y- and z-axis, the transverse shear strains are defined as:

$$\gamma_{xz} = u_{z,x} + \theta_y \tag{3.1}$$

$$\gamma_{xy} = u_{y,x} - \theta_z \tag{3.2}$$

where θ_i denotes the rotation about axis i, and $u_{j,x} = \frac{\partial u_j}{\partial x}$ the slope in j- direction wrt. to the local coordinate x. This is illustrated for the xz- plane in Figure 3.1. The minus-sign in Equation 3.2 comes from the definition of the right-handed coordinate system.

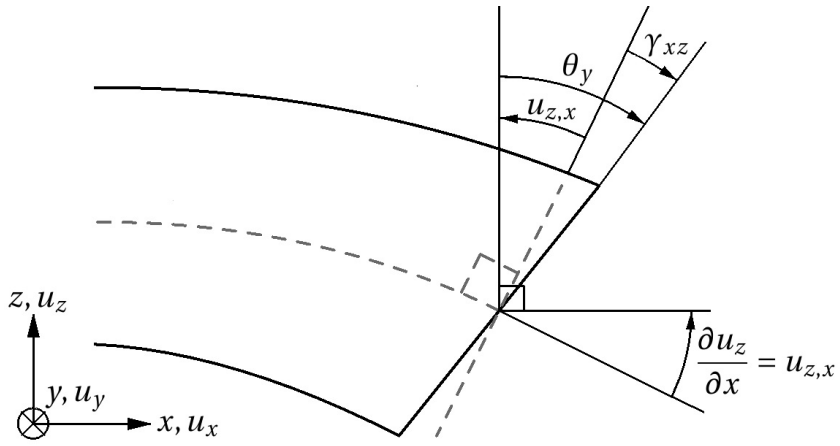

Figure 3.1: Transverse shear strain in the xz- plane, γ_{xz}.

Restricting the model to double-symmetric cross-sections, such that the shear center coincides with the cross-section centroid, axial force is decoupled from bending moments and torsional moment decoupled from shear forces and can thus be handled independently. The other strain components: axial strain, torsional strain and bending strains are given respectively as:

$$\begin{aligned} \varepsilon_x &= u_{x,x} \\ \varphi &= \theta_{x,x} \\ \kappa_y &= \theta_{z,x} \\ \kappa_z &= \theta_{y,x} \end{aligned} \tag{3.3}$$

Assuming a linear elastic material with Young's modulus, E, and shear modulus, G, the

corresponding forces and moments are given:

$$\begin{aligned} N &= EA\varepsilon_x \\ V_y &= GA_{sy}\gamma_{xy} \\ V_z &= GA_{sz}\gamma_{xz} \end{aligned} \tag{3.4}$$

$$\begin{aligned} T &= GI_T\varphi \\ M_y &= EI_z\kappa_z \\ M_z &= EI_y\kappa_y \end{aligned} \tag{3.5}$$

where A denotes the cross-section area, A_{si} the reduced cross-section shear area in the direction of i. I_T is the torsional stiffness and I_i is the cross-section second moment of area about axis i. The forces and moments are illustrated in Figure 3.2.

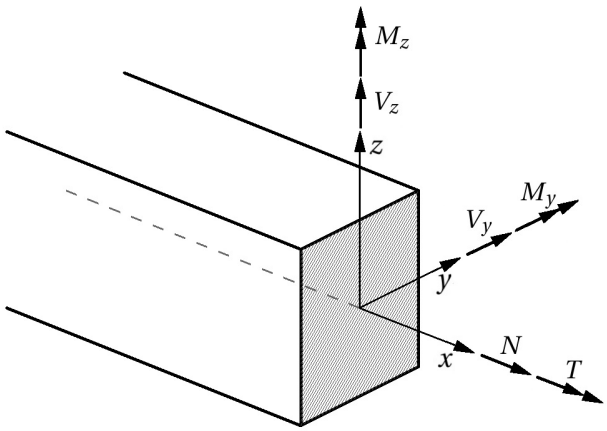

Figure 3.2: Forces and moments from Eqs. 3.3 and 3.4.

The total strain energy, U, may then be expressed as:

$$\begin{aligned} &U = U_N + U_{V_y} + U_{V_z} + U_T + U_{M_y} + U_{M_z} = \\ &\frac{1}{2}\left(EA\int_L \varepsilon_x^2 dx + GA_{sy}\int_L \gamma_{xy}^2 dx + GA_{sz}\int_L \gamma_{xz}^2 dx + GI_T\int_L \varphi^2 dx + EI_y\int_L \kappa_z^2 dx + EI_z\int_L \kappa_y^2 dx\right) \end{aligned} \tag{3.6}$$

3.2 Linear FEA of straight Timoshenko beams

For comparison and reference, the Timoshenko beam has been implemented using the standard Lagrangian shape functions for discretization. As this is a well known element, only a brief summary of the derivation is given. For more details, see [7].
This element has six unknown fields: translations, $\mathbf{u}$, and rotations, $\boldsymbol{\theta}$, written as:

$$\mathbf{u} = \begin{bmatrix} u_x \\ u_y \\ u_z \end{bmatrix}, \quad \boldsymbol{\theta} = \begin{bmatrix} \theta_x \\ \theta_y \\ \theta_z \end{bmatrix} \tag{3.7}$$

with the indices x, y, z referring to the local axes of the element.

Using Galerkin's method, the weak formulation of these fields are obtained by interpolation between the nodal degrees of freedom, $\mathbf{v}$:

$$\mathbf{u}^h = \widehat{\mathbf{N}}_{\mathbf{0}} \mathbf{v}_u \tag{3.8}$$

$$\boldsymbol{\theta}^h = \widehat{\mathbf{N}}_{\mathbf{0}} \mathbf{v}_\theta \tag{3.9}$$

where

$$\widehat{\mathbf{N}}_{\mathbf{0}} = \begin{bmatrix} \mathbf{N} & \mathbf{0} & \mathbf{0} \\ \mathbf{0} & \mathbf{N} & \mathbf{0} \\ \mathbf{0} & \mathbf{0} & \mathbf{N} \end{bmatrix}, \qquad \mathbf{v}_u = \begin{bmatrix} \mathbf{v}_x \\ \mathbf{v}_y \\ \mathbf{v}_z \end{bmatrix}, \qquad \mathbf{v}_\theta = \begin{bmatrix} \mathbf{v}_{\theta_x} \\ \mathbf{v}_{\theta_y} \\ \mathbf{v}_{\theta_z} \end{bmatrix} \tag{3.10}$$

and $\mathbf{N} = [N_1, N_2, ...N_n]$ are the Lagrangian interpolation functions. $\mathbf{u}^h$ represents the weak form approximation of $\mathbf{u}$, such that $\mathbf{u}^h \subset \mathbf{u}$ (and similar for $\boldsymbol{\theta}^h$).

By introducing

$$\widehat{\mathbf{u}}^h = \begin{bmatrix} \mathbf{u}^h \\ \boldsymbol{\theta}^h \end{bmatrix}, \qquad \widehat{\mathbf{N}} = \begin{bmatrix} \widehat{\mathbf{N}}_0 & \mathbf{0} \\ \mathbf{0} & \widehat{\mathbf{N}}_0 \end{bmatrix}, \text{and} \qquad \widehat{\mathbf{v}} = \begin{bmatrix} \mathbf{v}_u \\ \mathbf{v}_\theta \end{bmatrix} \tag{3.11}$$

the interpolation may be expressed in compact form:

$$\widehat{\mathbf{u}}^h = \widehat{\mathbf{N}}\widehat{\mathbf{v}} \tag{3.12}$$

The displacement fields are obviously uncoupled, due to the diagonal properties of $\widehat{\mathbf{N}}$. Thus, the strain energy contributions can be computed separately.
Using Equations 3.8 and 3.9 the integrands (strains and curvatures) in Equation 3.6 become:

$$\varepsilon_x = u_{x,x} = \begin{bmatrix}\mathbf{N}_{,x} & \mathbf{0} & \mathbf{0} & \mathbf{0} & \mathbf{0} & \mathbf{0}\end{bmatrix}\widehat{\mathbf{v}} = \mathbf{B}_N\widehat{\mathbf{v}} \tag{3.13}$$

$$\gamma_{xy} = u_{y,x} - \theta_z = \begin{bmatrix}\mathbf{0} & \mathbf{0} & \mathbf{N}_{,x} & \mathbf{0} & -\mathbf{N} & \mathbf{0}\end{bmatrix}\widehat{\mathbf{v}} = \mathbf{B}_{V_y}\widehat{\mathbf{v}} \tag{3.14}$$

$$\gamma_{xz} = u_{z,x} + \theta_y = \begin{bmatrix}\mathbf{0} & \mathbf{N}_{,x} & \mathbf{0} & \mathbf{0} & \mathbf{0} & \mathbf{N}\end{bmatrix}\widehat{\mathbf{v}} = \mathbf{B}_{V_z}\widehat{\mathbf{v}} \tag{3.15}$$

$$\varphi = \theta_{x,x} = \begin{bmatrix}\mathbf{0} & \mathbf{0} & \mathbf{0} & \mathbf{N}_{,x} & \mathbf{0} & \mathbf{0}\end{bmatrix}\widehat{\mathbf{v}} = \mathbf{B}_T\widehat{\mathbf{v}} \tag{3.16}$$

$$\kappa_y = \theta_{y,x} = \begin{bmatrix}\mathbf{0} & \mathbf{0} & \mathbf{0} & \mathbf{0} & \mathbf{N}_{,x} & \mathbf{0}\end{bmatrix}\widehat{\mathbf{v}} = \mathbf{B}_{M_y}\widehat{\mathbf{v}} \tag{3.17}$$

$$\kappa_z = \theta_{z,x} = \begin{bmatrix}\mathbf{0} & \mathbf{0} & \mathbf{0} & \mathbf{0} & \mathbf{0} & \mathbf{N}_{,x}\end{bmatrix}\widehat{\mathbf{v}} = \mathbf{B}_{M_z}\widehat{\mathbf{v}} \tag{3.18}$$

Where $\mathbf{B}$ is the strain-displacement matrix. Inserting these in Eq. 3.6, the strain energy for the weak formulation in terms of the element stiffness matrix, $\mathbf{k}$ becomes:

$$\begin{aligned} U &= \frac{1}{2}\widehat{\mathbf{v}}^T\Big(EA\int_{L_e}\mathbf{B}_N^T\mathbf{B}_N dx + GA_{sy}\int_{L_e}\mathbf{B}_{V_y}^T\mathbf{B}_{V_y}dx + GA_{sz}\int_{L_e}\mathbf{B}_{V_z}^T\mathbf{B}_{V_z}dx \\ &+ GI_T\int_{L_e}\mathbf{B}_T^T\mathbf{B}_T dx + EI_y\int_{L_e}\mathbf{B}_{M_y}^T\mathbf{B}_{M_y}dx + EI_z\int_{L_e}\mathbf{B}_{M_z}^T\mathbf{B}_{M_z}dx\Big)\widehat{\mathbf{v}} \\ &= \frac{1}{2}\widehat{\mathbf{v}}^T\mathbf{k}\widehat{\mathbf{v}} \end{aligned} \tag{3.19}$$

The same shape functions are used to distribute the loads. This consistent element load vector, $\mathbf{S}^0$, is given as:

$$\mathbf{S}^0 = -\int_{L_e}\widehat{\mathbf{N}}\mathbf{q}(x)dx \tag{3.20}$$

where $\mathbf{q}(x)$ is the load function.

By equilibrium considerations, the well known element stiffness relation is obtained:

$$\mathbf{k}\hat{\mathbf{v}} + \mathbf{S}^0 = \mathbf{S} \tag{3.21}$$

which is finally assembled to the global system.

3.3 Linear IGA of straight Timoshenko beams

The element derived in Section 3.2 is now discretized with the NURBS basis. Most of the steps are identical as for the Lagrange basis, but a distinct difference, however, is that the parameter space is no longer local to elements, but rather to patches. Furthermore, the control points (analogue to nodes in FEA) are in general not interpolatory.

Starting from the continuous displacement fields in Equation 3.7, they are now discretized by the definition of NURBS-curves from Equation 2.13, written on matrix form as:

$$\hat{\mathbf{u}}^h = \hat{\mathbf{R}}\hat{\mathbf{d}} \tag{3.22}$$

which is identical to Equation 3.12 for FEA, apart from $\hat{\mathbf{R}}$, which is a diagonal matrix containing the NURBS basis functions, $\mathbf{R} = [R_{1,p}, R_{2,p}, ..., R_{n,p}]$, and $\hat{\mathbf{d}} = [\mathbf{d}_x, \mathbf{d}_y, \mathbf{d}_z, \mathbf{d}_{\theta_x}, \mathbf{d}_{\theta_y}, \mathbf{d}_{\theta_z}]^T$, representing the control point displacements.

The strain-displacement relations are obtained from Equations 3.13 - 3.18 by replacing the Lagrange basis with the NURBS basis. Because the Gaussian quadrature rule for numerical integration is convenient for knot spans (or spline elements) [25], the stiffness matrix and consistent load vector are computed knot span-wise. As with FEA, these contributions are finally assembled to a global system (i.e. the patch). For the assembly, it is important to remember that each basis function has support over the half-open interval $[\xi_i, \xi_{i+p+1}\rangle$, and the elements may thus 'overlap' each other. Connectivity arrays can be found in Hughes *et al.*[25].

3.4 Verification of the straight Timoshenko beam element

To verify the implementation of the Timoshenko theory for linear analyses of straight beams, a few classical numerical tests have been carried out, where the Lagrangian and the NURBS elements (referred to as FEA and IGA) have been tested in parallel. The errors in displacements are expected to be in the range of $e = \mathcal{O}(h^{p+1})$. Furthermore, the discretizations should predict the analytical solution exactly if the solution space is contained within the approximation space, i.e. $\widehat{\mathbf{u}} \subset \widehat{\mathbf{u}}^h$.

The impact of full and reduced integration has also been studied. Full, or exact integration corresponds to an element-wise Gaussian quadrature rule of order $p+1$, and reduced integration to one order lower, i.e. p Gauss points per element.

As the displacements directly determine strains and forces, only convergence of the displacements are investigated. On the horizontal axis in the convergence plots, "nDOFS" refers to the number of free DOFs, i.e. 3 per free node for planar beams.

For the 2D straight beam problems considered in this section, the analytical solutions are computed from a superposition of the Euler- Bernoulli solution, solved from the differential equation:

$$\frac{d^2}{dx^2}\left(EI_y \frac{du_z}{dx^2}\right) = q_z(x) \tag{3.23}$$

and the shear deformation δ_s, given as:

$$\delta_s = \int_0^x \frac{V_z(x)(4+5\nu)k_z h^2}{24EI_y} dx \tag{3.24}$$

where $V_z(x)$ is the shear force distribution.

With the analytical solution at hand, the relative error of $\bullet$ is computed either pointwise as:

$$|e_\bullet| = \frac{|\bullet^{exact} - \bullet^h|}{|\bullet^{exact}|} \tag{3.25}$$

or over a domain, L, in terms of the classical L^2-norm:

$$||e_\bullet||_{L^2} = \sqrt{\frac{\int_L \left(\bullet^{ex}(x) - \bullet^h(x)\right)^2 dx}{\int_L \left(\bullet^{ex}(x)\right)^2 dx}} \tag{3.26}$$

3.4.1 Cantilever beam subjected to tip shear

The first example is a straight cantilever beam subjected to a transverse load at the free end. Input data is given in Table 3.1.

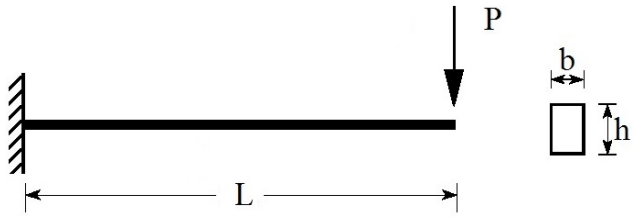

Figure 3.3: Cantilever beam

Length	Young's modulus	Poisson's ratio	Width	Thickness	Load
$L = 10$	$E = 1000$	$\nu = 0$	$b = 1$	$h = 1$	$P = 1$

Table 3.1: Geometry and material data for cantilever beam subjected to tip shear.

The analytical solution for the displacements, including shear deformations is given:

$$u_z = \frac{P}{6EI_y}\left[(3L - x)x^2 + (4 + 5\nu)\frac{k_z h^2 x}{4}\right] \tag{3.27}$$

The beam is discretized with linear and quadratic basis functions for both FEA and IGA. The cubic displacement field is exactly reproduced with elements of equal order. With exact, or full integration, the relative error in displacements in terms of the L^2-norm, computed from Equation 3.26, is shown in Figure 3.4.

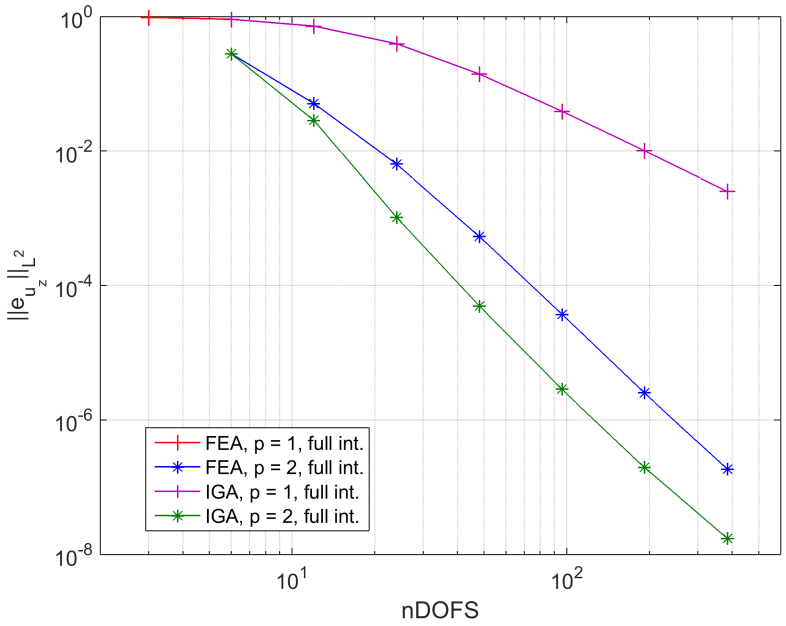

Figure 3.4: L^2-norm of the relative error in displacements for IGA and FEA with exact integration.

IGA coincides with FEA for $p = 1$ as the linear bases are identical. Further, they produce the same convergence rates with quadratic elements, but for IGA the absolute error is approximately one order less.

For reduced integration, the relative error in the displacement field is shown in Figure 3.5. As for full integration, quadratic IGA produce the same convergence rate and less absolute error than FEA. All elements exhibit optimal convergence.

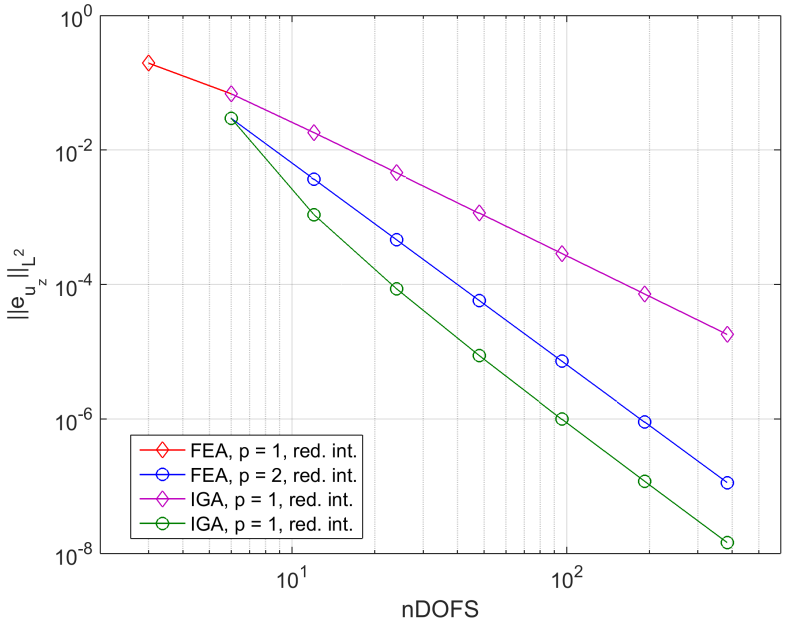

Figure 3.5: L^2-norm of the relative error in displacements for IGA and FEA with reduced integration.

3.4.2 Cantilever beam subjected to distributed load

The cantilever beam from Section 3.4.1 is now subjected to a uniformly distributed load, $q = 0.1$, taken into account with a consistent load vector.

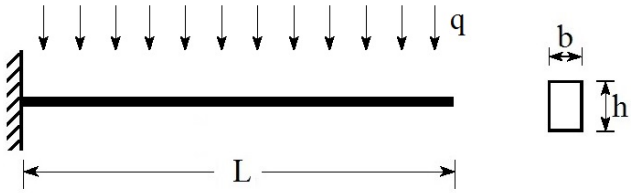

Figure 3.6: Cantilever beam subjected to distributed load

Here, the analytical solution for the transverse displacements is given:

$$u_z = \frac{qx^2}{24EI_y}\left(2L^2 + (2L-x)^2\right) + \frac{qk_z h^2(4+5\nu)}{24EI_y}\left(Lx - \frac{x^2}{2}\right) \tag{3.28}$$

The convergence is studied for FEA and IGA for elements up to cubic order. Quartic elements

produce the analytical solution. As error measurement, the L^2-norm of the relative error in transverse displacements has been computed from Eqs. 3.28 and 3.26. The results are reported in Figures 3.7 and 3.8 for full and reduced integration, respectively.

Again it is confirmed that the linear bases coincide. For $p \geq 2$, IGA produce errors approximately one order less than FEA for both integration regimes. With reduced integration, the errors from the linear basis is shifted approximately two orders, which indicates presence of transverse shear locking with full integration. This phenomenon is discussed in Section 3.5. The errors are also shifted with quadratic and cubic elements, but not nearly as significantly as for the linear elements.

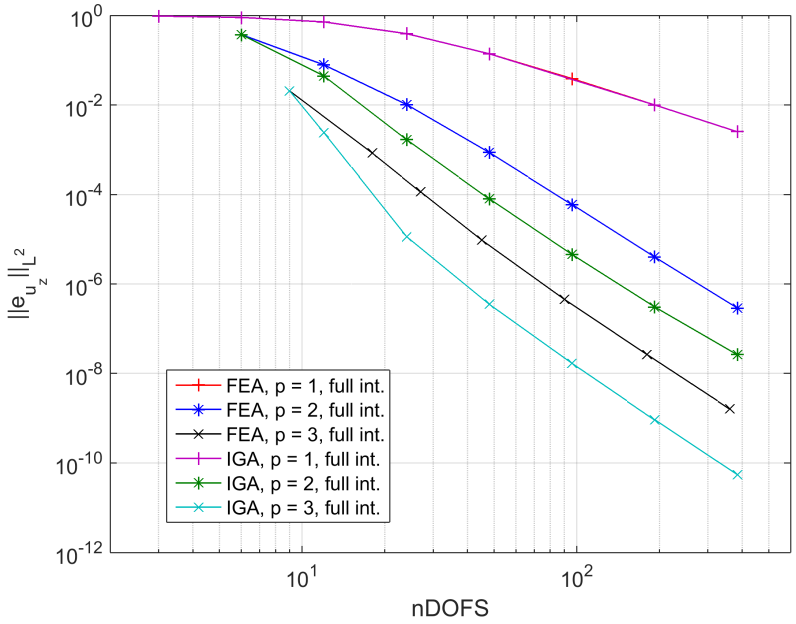

Figure 3.7: L^2-norm of the relative error in displacements for FEA and IGA with full integration.

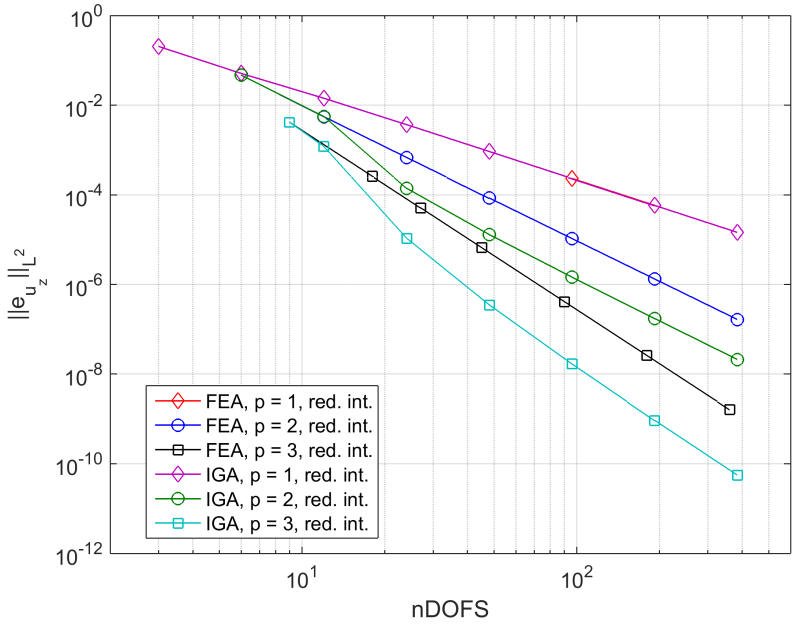

Figure 3.8: L^2-norm of the relative error in displacements for FEA and IGA with reduced integration.

3.4.3 Double cantilever beam subjected to transverse point load

In the next example, a beam is clamped in both ends and subjected to a transverse point load at the center, as shown in Figure 3.9a. Geometry and material data are given in Table 3.2. Due to symmetry, only half of the beam is considered. Zero rotation and no shear are assumed at the midspan. Figure 3.9b shows the problem setup.

Length	Young's modulus	Poisson's ratio	Width	Thickness	Load
$L = 10$	$E = 1000$	$\nu = 0$	$b = 1$	$h = 1$	$P = 1$

Table 3.2: Geometry and material data for clamped beam subjected to transverse load at the center.

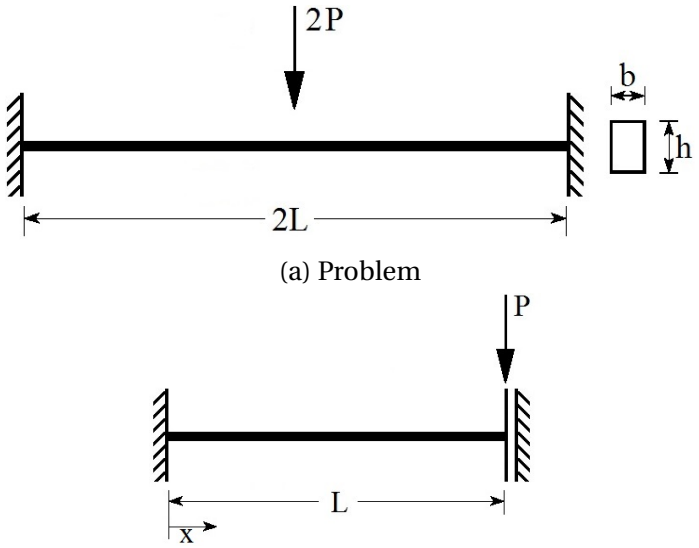

(a) Problem

(b) Idealized system

Figure 3.9: Double cantilever beam subjected to transverse point load.

Again the L^2-norm of the relative error in transverse displacements is used as measure. For this problem, the analytical solution is given:

$$u_z = \frac{P}{12EI_y}\left((3L-2x)x^2 + \frac{(4+5\nu)k_z h^2 x}{2}\right) \tag{3.29}$$

Figures 3.10 and 3.11 compare FEA and IGA for full and reduced integration, respectively. In Figure 3.12, IGA with both integration regimes is compared. For this beam the convergence rates for $p = 2$ are initially higher with full integration, but as seen from Figure 3.12, they converge towards the same rate and errors as reduced integration. Otherwise the behavior is similar as the previous tests.

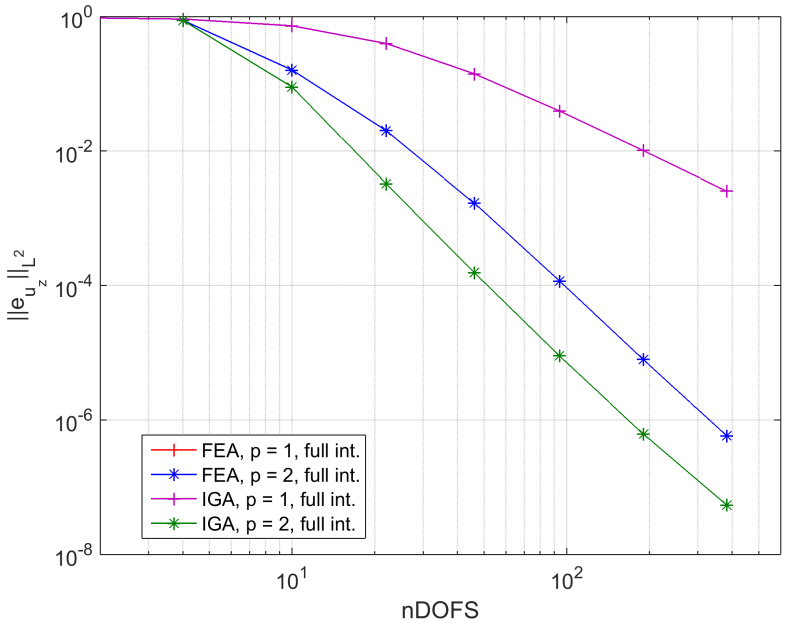

Figure 3.10: L^2-norm of relative error in transverse displacements for FEA and IGA with full integration.

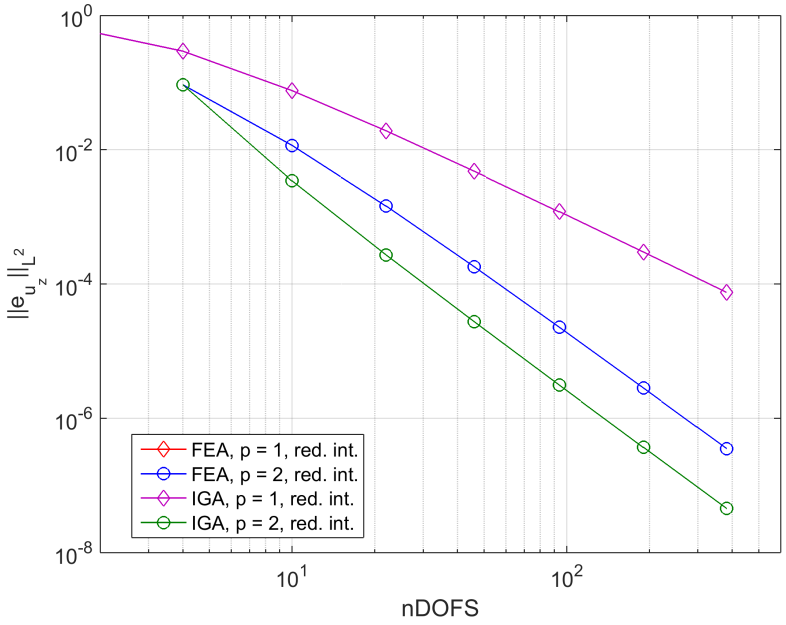

Figure 3.11: L^2-norm of relative error in transverse displacements for FEA and IGA with reduced integration.

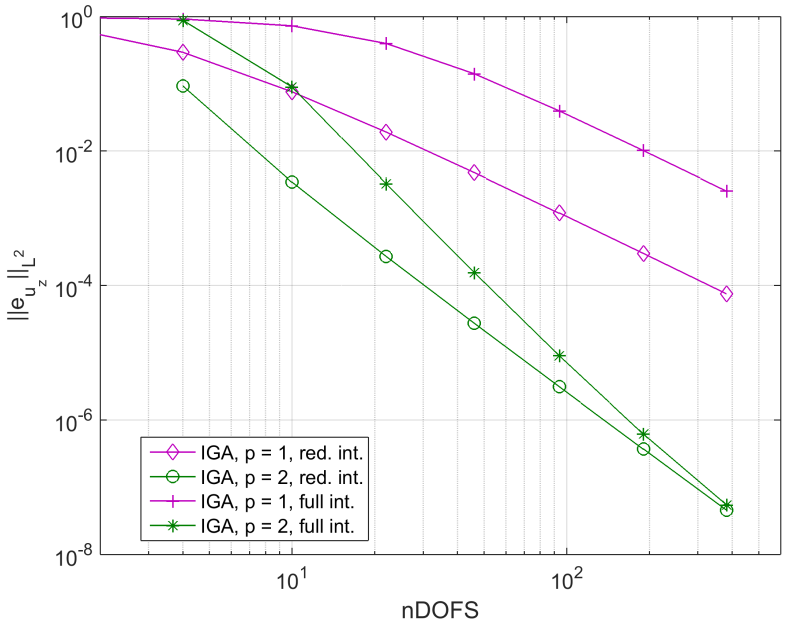

Figure 3.12: L^2-norm of relative error in transverse displacements for IGA with full and reduced integration.

3.4.4 Double cantilever beam subjected to distributed load

The beam from Section 3.4.3 is now subjected to a uniformly distributed transverse load, $q = 0.1$. Due to symmetry, only half the beam is considered. Problem setup is shown in Figure 3.13, and the analytical solution is given:

$$u_z = \frac{qx^2}{24EI_y}(2L-x)^2 + \frac{qk_zh^2(4+5\nu)}{24EI_y}\left(Lx - \frac{x^2}{2}\right) \tag{3.30}$$

from which the L^2-norm of the relative error is computed and used as measure.

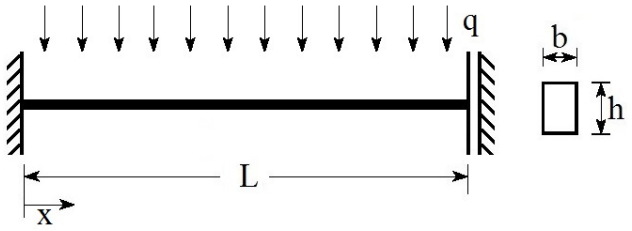

Figure 3.13: Double cantilever beam subjected to uniformly distributed load.

As the strong form solution is of $4th$ order, the convergence study is carried out for elements up to cubic order. Figures 3.14 and 3.15 compare FEA and IGA for full and reduced integration, respectively. The same results are shown in Figures 3.16 and 3.17, but now full and reduced integration are compared for the Lagrangian and the NURBS bases, respectively.

For $p \geq 2$ IGA still produces errors approximately one order less than FEA. Furthermore, both bases have initially faster convergence with full integration, but they seem to stabilize to the same rates and errors as with reduced integration. Lastly, it is observed that the errors with FEA is shifted slightly more than for IGA with reduced integration.

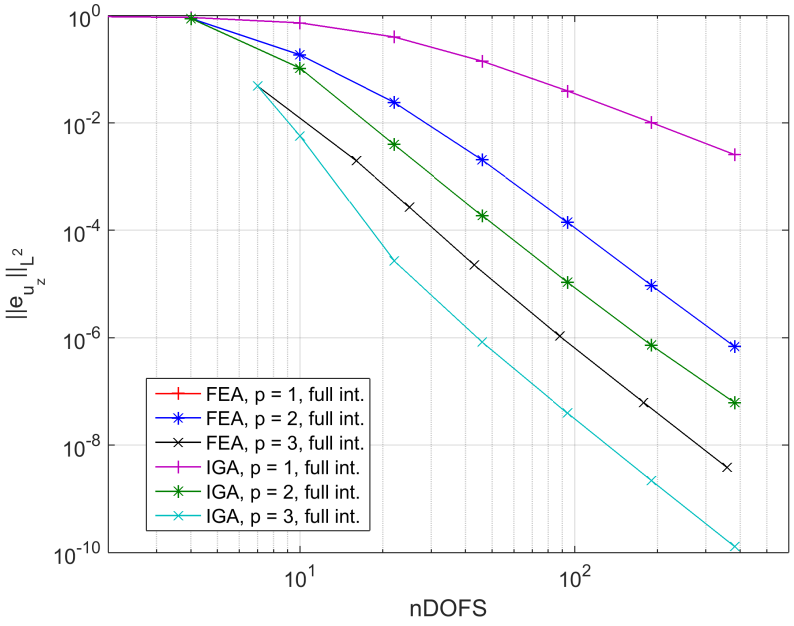

Figure 3.14: L^2-norm of relative error in transverse displacements for FEA and IGA with full integration.

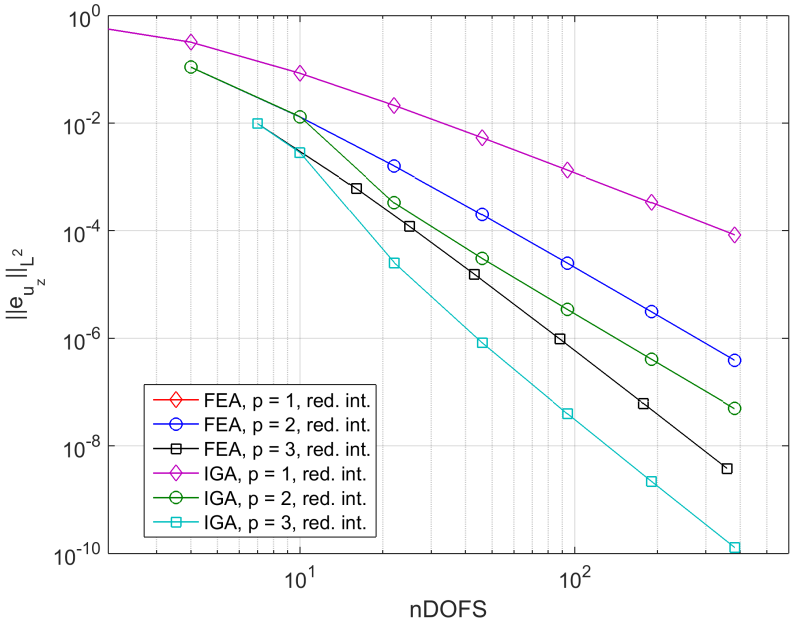

Figure 3.15: L^2-norm of relative error in transverse displacements for FEA and IGA with reduced integration.

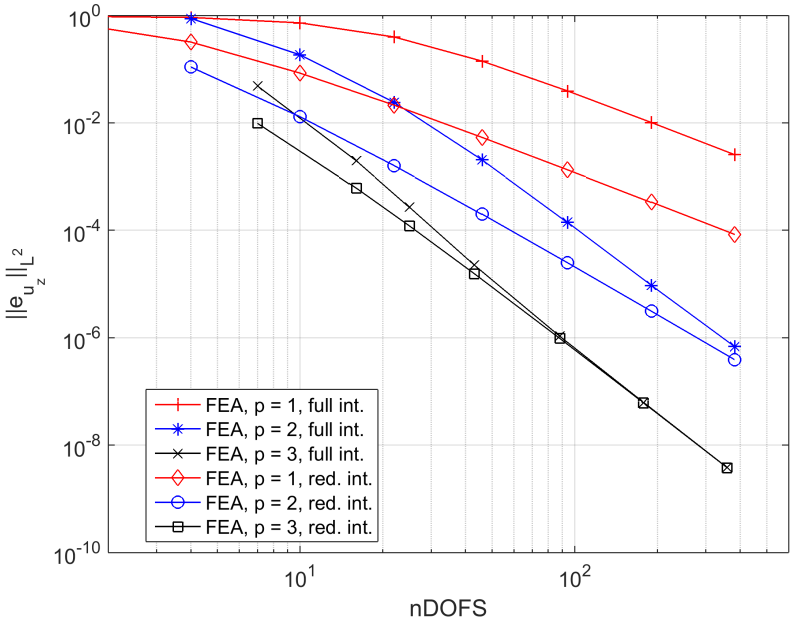

Figure 3.16: L^2-norm of relative error in transverse displacements for FEA and IGA with reduced integration.

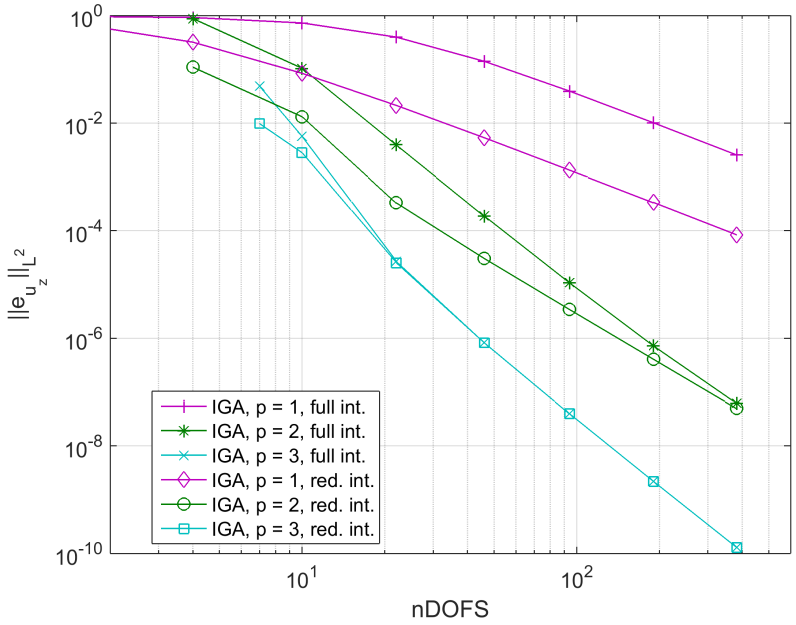

Figure 3.17: L^2-norm of relative error in transverse displacements for FEA and IGA with reduced integration.

3.4.5 Concluding remarks

The numerical tests have shown that both IGA and FEA exhibit optimal convergence and produce the exact solution when the approximation space is a superset of the solution space, $\hat{\mathbf{u}} \subset \hat{\mathbf{u}}^h$. Thus, the implementation of the Lagrangian and the NURBS discretizations to the straight, linear Timoshenko beam has been successful.

The numerical results suggest that for $p \geq 2$, IGA produce errors approximately one order less than FEA for linear, straight beam problems. Furthermore, it has been observed that reduced integration has slightly more impact on FEA than IGA, as seen from e.g. Figure 3.16 and 3.17.

For all analyses reduced integration shows less errors than exact integration, which indicates presence of spurious strains and numerical locking.

3.5 Locking effects in straight beam elements

It may turn out that the numerical analyses provide slow convergence and large errors due to strains which are not present in the analytical solution. These spurious strains will absorb strain energy and give artificial stiffness, which in literature is referred to as *locking*. For this thesis, the relevant locking phenomena are *transverse shear locking* and *membrane locking*. The latter will only occur in curved beam elements and is described in Section 4.5. Other types of locking, as *poisson locking* and *volumetric locking* are not discussed any further here.

Transverse shear locking may appear in both IGA and FEA for displacement-based straight Timoshenko beam elements. The ratio between bending and shear stiffness, $\frac{EI}{GA_s}$, is proportional to the square of the thickness, h. As the thickness decreases, this ratio converges quadratically towards zero and the response becomes dominated by bending. However, if spurious shear strains are produced under deformation, these will absorb strain energy and consequently give over-stiffening behavior. This is known as transverse shear locking.

Recalling from Section 3.1 the kinematic equations for curvature and transverse shear strain are given in terms of the independent fields for rotation and displacement as:

$$\kappa_y = \theta_{y,x}$$
$$\gamma_{xz} = u_{z,x} - \theta_y$$

respectively. Interpolated with equal order, the highest order term in θ_y cannot be balanced by $u_{z,x}$ in the expression for γ_{xz}. This is illustrated in Figure 3.18, where the transverse strain field, γ_{xy}^h, for the beam in Figure 3.19 discretized with 5 quadratic elements. The unbalanced term is of equal order and turns up as parabolas in the strain field. It does not coincide with the analytical solution, γ_{xy}, and hence, spurious shear strains are present.

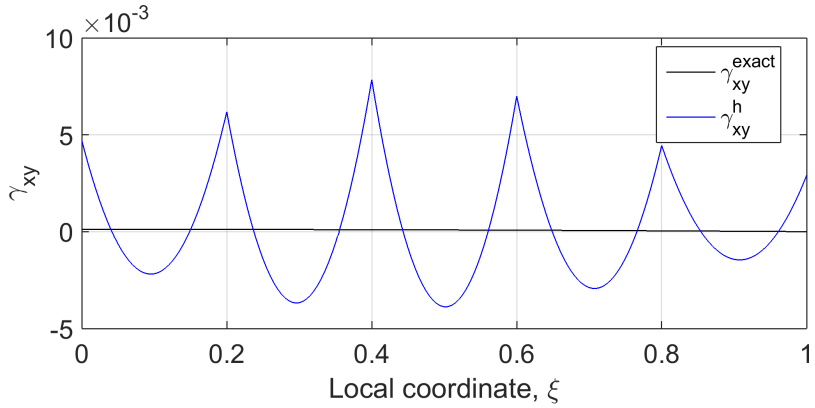

Figure 3.18: Spurious transverse shear strains.

An analytical study of transverse shear locking is carried out for the cantilever beam from section 3.4.1, keeping the thickness symbolic. For $\nu = 0$ and $A_{sz} = A$, the analytical solution for the displacement and rotation can be written respectively as:

$$u_z = w = \frac{2\widehat{P}}{Eb}\Big((3L - x)x^2 + xh^2\Big) \tag{3.31}$$

$$u_{\theta_y} = \theta = -\frac{6\widehat{P}}{Eb}\Big((2L - x)x\Big) \tag{3.32}$$

Where $\widehat{P}$ is scaled with h^3 such that the bending part of the displacements become independent of the thickness. Note that in the Kirchhoff limit, i.e. $h \to 0$, the Euler-Bernoulli solution is obtained.

The beam is now discretized with one isogeometric element. Starting with $p = 1$ the reduced equation system becomes:

$$\frac{Eb}{12L}\begin{bmatrix} 6h & -3hL \\ -3hL & 2hL^2 + h^3 \end{bmatrix}\begin{bmatrix} w_2 \\ \theta_2 \end{bmatrix} = \begin{bmatrix} Ph^3 \\ 0 \end{bmatrix} \tag{3.33}$$

which gives the displacements at the free control point:

$$\mathbf{v}_{p=1} = \begin{bmatrix} w_2 \\ \theta_2 \end{bmatrix} = \begin{bmatrix} \frac{1}{50}\frac{h^2(h^2+200)}{(h^2+50)} \\ -\frac{3}{5}\frac{h^2}{(h^2+50)} \end{bmatrix} \tag{3.34}$$

where it is obvious that for $h \to 0$, the displacements $[w, \theta] \to 0$ and consequently, the element locks.

Solving for one quadratic and cubic isogeometric element, the free control point displacements become respectively:

$$\mathbf{v}_{p=2} = \begin{bmatrix} w_2 \\ \theta_2 \\ w_3 \\ \theta_3 \end{bmatrix} = \begin{bmatrix} \frac{1}{100}\frac{h^2(h^2+60)}{h^2+10} \\ -\frac{3}{5}\frac{h^2+5}{h^2+10} \\ \frac{1}{50}\frac{h^4+210h^2+1500}{h^2+10} \\ -\frac{3}{5} \end{bmatrix} \qquad \mathbf{v}_{p=3} = \begin{bmatrix} w_2 \\ \theta_2 \\ w_3 \\ \theta_3 \\ w_4 \\ \theta_4 \end{bmatrix} = \begin{bmatrix} \frac{h^2}{150} \\ -\frac{2}{5} \\ \frac{h^2}{75}+2 \\ -\frac{3}{5} \\ \frac{h^2}{50}+4 \\ -\frac{3}{5} \end{bmatrix} \tag{3.35}$$

The rotation at the tip becomes independent of h for quadratic elements, but the interior knot and tip displacement is still dependent of h. Thus, locking effects are still present, but increasing the polynomial order drastically reduces the impact of locking.

For this beam, the analytical solution is exactly reproduced with one cubic elements, and is for that reason locking-free. However, as seen in Figure 3.20, higher order elements also reveal locking.

As a numerical test, the clamped beam subjected to a transverse distributed load shown in Figure 3.19 is considered. The load is increasing linearly from zero in $x = 0$ to q in $x = L$. Otherwise it is identical as the beam in Section 3.4.4. The 5^{th} order analytical solution for transverse displacements reads:

$$u_z(x) = \frac{\widehat{q}}{EI}\left[\frac{x^5}{120L} - \frac{Lx^3}{12} + \frac{5L^2x^2}{48}\right] + \frac{\widehat{q}k_z h^2}{12EIL}\left[L^2x - \frac{x^3}{3}\right] \tag{3.36}$$

where $\widehat{q} = qh^3$.

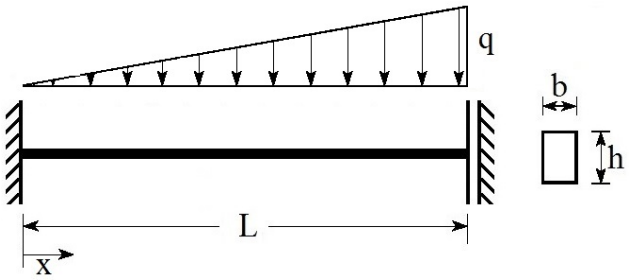

Figure 3.19: Clamped beam subjected to linearly increasing pressure

The beam is discretized with 5 equally sized NURBS elements with the highest continuity available. To include locking of interior control points, the relative error is measured in terms of the L^2-norm of the displacement field, computed from Equation 3.26.

The results for $p = 1,2,3,4$ with exact integration is reported in Table 3.3 and Figure 3.20. $p = 5$ produces the analytical solution.

L_e/h	10^1	10^2	10^3	10^4	10^5
$p = 1$	0.631994	0.994148	0.999941	0.999999	1.000000
$p = 2$	0.014023	0.559620	0.992066	0.999920	0.999999
$p = 3$	0.000050	0.002836	0.038994	0.045177	0.045253
$p = 4$	0.000002	0.000024	0.001184	0.002688	0.002719

Table 3.3: L^2-norm of the relative error in displacements for $p = 1,2,3,4$ with exact integration.

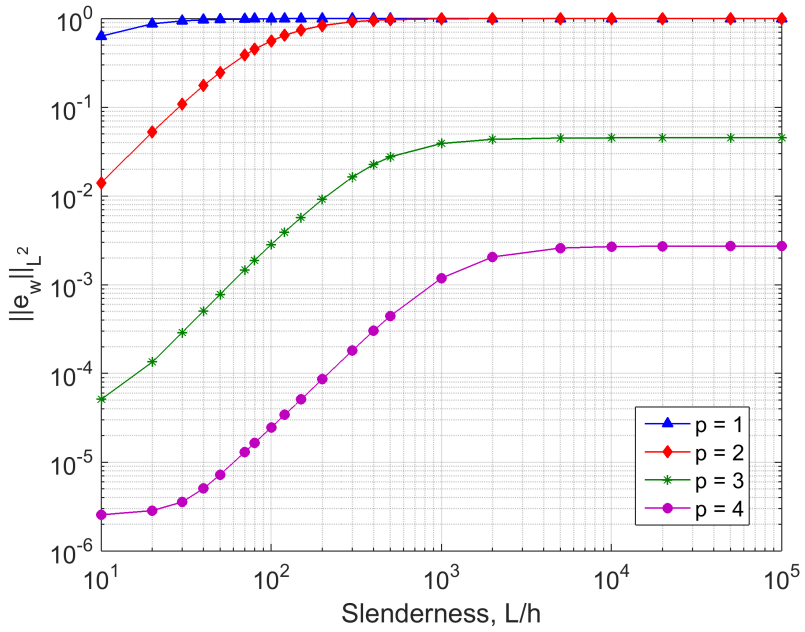

Figure 3.20: Logarithmic plot of relative error in terms of the L^2-norm with respect to the slenderness for the clamped beam subjected to a linearly increasing pressure with exact integrated IGA.

Thickness dependency in all elements are revealed, and linear and quadratic elements lock completely, even for moderate slendernesses.

For the same setup, the effect of reduced integration is studied. The results are reported in Table 3.4 and Figure 3.21. Except for $p = 1$, whose basis is identical as the Lagrangian, the elements still show thickness dependency. Quadratic elements performs better and do not lock completely with reduced integration, but on higher order elements, the impact of reduced integration is vanishingly small.

L_e/h	10^1	10^2	10^3	10^4	10^5
$p=1$	0.068498	0.069789	0.069803	0.069803	0.069802
$p=2$	0.001039	0.022783	0.044860	0.045302	0.045310
$p=3$	0.000045	0.001945	0.036229	0.045137	0.045254
$p=4$	0.000002	0.000024	0.001122	0.002685	0.002715

Table 3.4: L^2-norm of the relative error in displacements for $p = 1,2,3,4$ with reduced integration.

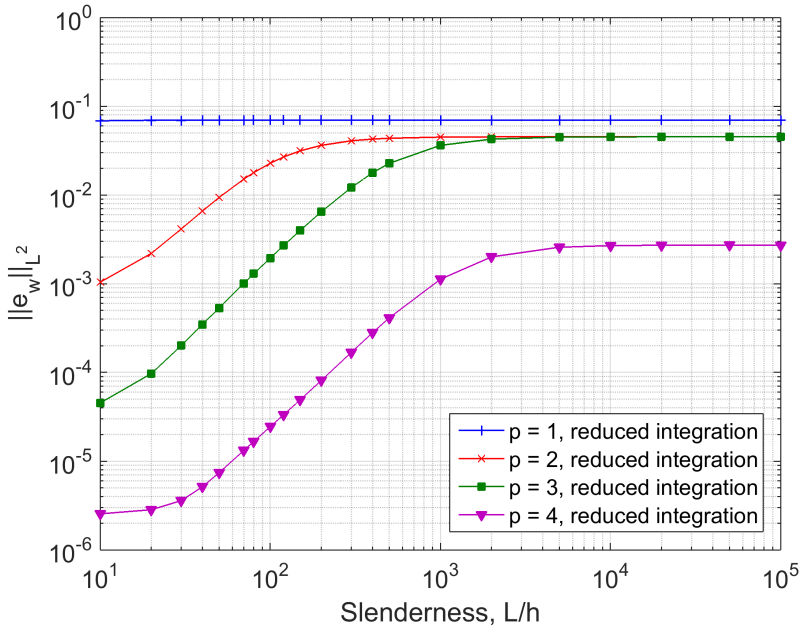

Figure 3.21: Logarithmic plot of relative error in terms of the L^2-norm with respect to the slenderness for the clamped beam subjected to a linearly increasing pressure with reduced integrated IGA.

Chapter 4

The geometrically exact 3D Timoshenko beam model

The element derived in Chapter 3 is limited to linear analyses of straight beams, which limits its versatility. However, it is a good starting point understanding the structure of numerical analyses, and sufficient for many academic purposes.

In this chapter the *geometrically exact 3D beam model*, proposed by Simo [38], Simo and Vu-Quoc [39, 40] and Ibrahimbegović [23] based on Reissner's 3D beam theory [35], is presented. This beam model is able to accommodate large displacements, finite rotations and finite strains, and is thus suitable for not only linear analyses, but also non-linear and dynamic analyses.

In Sections 4.1 and 4.2, the governing kinematic and equilibrium equations are considered at a continuous level. The problem will be discretized using the Lagrangian and the NURBS basis functions in Sections 4.3 and 4.4, respectively. Lastly, in Section 4.5, membrane locking which may occur in initially curved beams is described.

4.1 Governing kinematic equations

A local curvilinear coordinate system is chosen where $\xi_1(t)$ is the parametric variable used to define the reference axis of the beam. t is the time parameter. Let $\mathbf{X}(\xi_1)$ and $\mathbf{x}(\xi_1)$ denote the coordinates of the beam reference axis in the initial, $\mathscr{C}_0$, and current, $\mathscr{C}_n$, configuration, respectively.

In accordance with standard hypothesis for beam,

(i) a straight line that is initially normal to the reference axis remains straight in the deformed configuration, but not necessarily normal to the deformed axis (since transverse shear deformations are considered), and

(ii) the cross-section remain plane and undeformed in the deformed configuration.

The orientation of the cross-section in the initial configuration is defined by the local Cartesian basis vector, $\boldsymbol{i}_1^0(\xi_1)$, and the two cross-section axes $\boldsymbol{i}_2^0(\xi_1)$ and $\boldsymbol{i}_3^0(\xi_1)$.
Without loss of generality, the cross-section is chosen to be initially normal to the beam reference axis, hence:

$$\boldsymbol{i}_1^0(\xi_1) = \mathbf{X}_{,\xi_1} \tag{4.1}$$

The position of the local Cartesian bases in the current configuration, $\boldsymbol{i}_i(\xi_1, t)$, can be defined via the product of the two orthogonal tensors $\mathbf{R}$ and $\mathbf{R}^0$:

$$\boldsymbol{i}_i = \mathbf{R}\,\boldsymbol{i}_i^0 = \mathbf{R}\mathbf{R}^0\,\mathbf{I}_{\boldsymbol{i}} = \overline{\mathbf{R}}\,\mathbf{I}_i \tag{4.2}$$

where $\mathbf{R} = \mathbf{R}(\xi_1, t)$ represents the rotation of the local Cartesian basis from its initial configuration $\boldsymbol{i}_i^0$ to its current (deformed) configuration, $\boldsymbol{i}_i$, whereas $\mathbf{R}^0 = \mathbf{R}^0(\xi_1)$ is the rotation tensor representing the position of the local Cartesian basis, $\boldsymbol{i}_i^0$ with respect to the fixed, global Euclidean base vectors, $\mathbf{I}_i$, respectively.
These relations are illustrated in Figure 4.1.

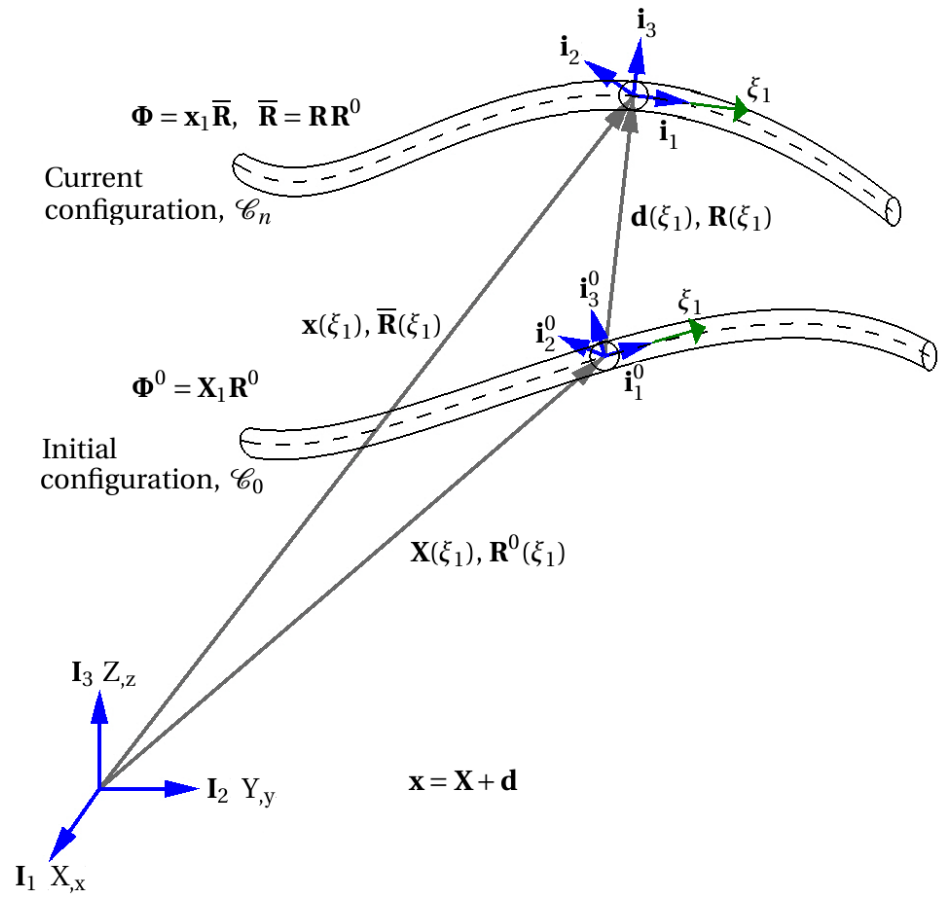

Figure 4.1: Beam segment in initial and current configuration with its governing kinematic relations.

4.2 Governing equilibrium equations

As shown by Antmann [3], Reissner [35], Simo [38] and Ibrahimbegivić [24], the beam balance equations can be obtained without introducing any simplifying hypothesis regarding its geometry or size of the displacement and rotation. Hence, this theory is referred to as *geometrically exact.*

The linear and angular momentum balance equations for the geometrically exact 3D beam for statics reads:

$$\mathbf{n}_{,\xi_1} + \overline{\mathbf{n}} = \mathbf{0} \tag{4.3}$$

$$\mathbf{m}_{,\xi_1} + \mathbf{x}_{,\xi_1} \times \mathbf{n} + \overline{\mathbf{m}} = \mathbf{0} \tag{4.4}$$

where $\mathbf{n}$ and $\mathbf{m}$ are the spatial stress resultants and stress couples (moments), and $\overline{\mathbf{n}}$ and $\overline{\mathbf{m}}$ are the externally applied forces and moments.

It may be shown (Helgedagsrud *et al.* [20]) that the corresponding conjugate axial, shear and bending strain measures can be obtained, respectively, as:

$$\boldsymbol{\varepsilon} = \mathbf{x}_{,\xi_1} - \boldsymbol{i}_1 \tag{4.5}$$

$$\boldsymbol{\kappa} = \boldsymbol{\omega} \tag{4.6}$$

where $\boldsymbol{\omega}$ is the axial vector of the skew-symmetric tensor $\boldsymbol{\Omega}$, defined as:

$$\boldsymbol{\Omega} = \mathbf{R}_{,\xi_1}\mathbf{R}^T \tag{4.7}$$

Assuming a linear elastic material, the spatial stress resultants are related to the finite strain measures through the constitutive equations:

$$\mathbf{n} = \mathbf{R}\mathbf{C}\mathbf{R}^T\boldsymbol{\varepsilon}; \qquad \mathbf{C} = \mathrm{diag}(EA, GA_2, GA_3) \tag{4.8}$$

$$\mathbf{m} = \mathbf{R}\mathbf{D}\mathbf{R}^T\boldsymbol{\kappa}; \qquad \mathbf{D} = \mathrm{diag}(GI_t, EI_2, EI_3) \tag{4.9}$$

The potential energy of the beam can then be written:

$$\Pi = \frac{1}{2}\int_L \Big(\boldsymbol{\varepsilon}\,\mathbf{n} + \boldsymbol{\kappa}\,\mathbf{m}\Big)ds - \Pi_{ext} \tag{4.10}$$

The weak form of the equilibrium equation now reads:

$$\delta\Pi = \int_L \Big(\delta\boldsymbol{\varepsilon}\,\mathbf{n} + \delta\boldsymbol{\kappa}\,\mathbf{m}\Big)ds - \int_L \Big(\delta\mathbf{x}\overline{\mathbf{n}} + \delta\boldsymbol{\omega}\overline{\mathbf{m}}\Big)ds \tag{4.11}$$

where $\delta\mathbf{x}$ and $\boldsymbol{\omega}$ are the vectors of virtual displacements and rotations, respectively.

As shown by Reissner [35], the explicit forms of the virtual displacements may be obtained

from:

$$\delta\boldsymbol{\varepsilon} = \delta\mathbf{x}_{,\xi_1} - \delta\boldsymbol{\omega} \times \mathbf{x}_{,\xi_1} \tag{4.12}$$

$$\delta\boldsymbol{\kappa} = \delta\boldsymbol{\omega}_{,\xi_1} \tag{4.13}$$

4.3 FE-approximation

Let the domain L be approximated with piecewise polynomial functions, i.e. $L \simeq L^h = \sum_{e=1}^{n_{el}} L^e$, and:

$$\mathbf{x}^h\Big|_{L^e} = \sum_{i=1}^{n_{en}} N_i(\xi)\mathbf{x}_i = \mathbf{N}\mathbf{x}^e \tag{4.14}$$

where $N_i(\xi)$ are the standard Lagrange-type polynomials and $\mathbf{x}_i$ are vectors of nodal coordinates.

Similarly the virtual rotations are also obtained by isoparametric interpolation:

$$\delta\boldsymbol{\omega}^h\Big|_{L^e} = \sum_{i=1}^{n_{en}} N_i(\xi)\delta\boldsymbol{\kappa}_i = \mathbf{N}\delta\boldsymbol{\omega}^e \tag{4.15}$$

The matrix component of the discrete form of the weak form now becomes:

$$\sum_{e=1}^{n_{el}} \delta\mathbf{d}^e\left(\mathbf{r}^e - \mathbf{f}^e\right) = 0; \qquad \delta\mathbf{d}^e = \begin{bmatrix} \delta\mathbf{x}^e \\ \delta\boldsymbol{\omega}^e \end{bmatrix} \tag{4.16}$$

where $\sum_{e=1}^{n_{el}}$ denotes the FE assembly procedure accounting for the topology, or the connectivity of the FE-matrices. $\mathbf{f}^e$ denotes the external load vector, $\mathbf{r}^e$ the element residual, and the latter reads:

$$\mathbf{r}^e = \int_{L^e} \begin{bmatrix} \mathbf{N}_{,\xi_1} & \mathbf{x}_{,\xi_1} \times \mathbf{N} \\ \mathbf{0} & \mathbf{N}_{,\xi_1} \end{bmatrix}^T \begin{pmatrix} \mathbf{n} \\ \mathbf{m} \end{pmatrix} ds \tag{4.17}$$

Using the Gaussian quadrature rule for numerical integration, the components in the element residual, r_a^e, is given as:

$$r_a^e = \sum_{g=1}^{n_{gp}} j_w(\xi_g) \begin{bmatrix} N_{a,\xi_1}\mathbf{I}_3 & \widehat{\mathbf{x}}_{,\xi_1} \times N_a\mathbf{I}_3 \\ \mathbf{0} & N_{a,\xi_1}\mathbf{I}_3 \end{bmatrix}^T \begin{pmatrix} \mathbf{n} \\ \mathbf{m} \end{pmatrix} \tag{4.18}$$

where $j_w(\xi) = \det(J)w(\xi)$ is the product of the Jacobian determinant and the weight number for Gaussian quadrature, and $\widehat{\mathbf{x}}_{,\xi_1}$ is the skew-symmetric tensor of $\mathbf{x}_{,\xi_1}$.

The material part of the tangent stiffness now reads:

$$\mathbf{K}_m^e = \int_{L^e} \begin{bmatrix} \mathbf{N}_{,\xi_1} & \mathbf{x}_{,\xi_1} \times \mathbf{N} \\ \mathbf{0} & \mathbf{N}_{,\xi_1} \end{bmatrix}^T \begin{bmatrix} \mathbf{R}^T\mathbf{C}\mathbf{R} & \mathbf{0} \\ \mathbf{0} & \mathbf{R}^T\mathbf{D}\mathbf{R} \end{bmatrix} \begin{bmatrix} \mathbf{N}_{,\xi_1} & \mathbf{x}_{,\xi_1} \times \mathbf{N} \\ \mathbf{0} & \mathbf{N}_{,\xi_1} \end{bmatrix} \tag{4.19}$$

written on component form as:

$$K_{m_{ab}}^e = \begin{bmatrix} N_{a,\xi_1}\mathbf{I}_3 & \widehat{\mathbf{x}}_{,\xi_1} \times N_a\mathbf{I}_3 \\ \mathbf{0} & N_{a,\xi_1}\mathbf{I}_3 \end{bmatrix}^T \begin{bmatrix} \mathbf{R}^T\mathbf{C}\mathbf{R} & \mathbf{0} \\ \mathbf{0} & \mathbf{R}^T\mathbf{D}\mathbf{R} \end{bmatrix} \begin{bmatrix} N_{b,\xi_1}\mathbf{I}_3 & \widehat{\mathbf{x}}_{,\xi_1} \times N_b\mathbf{I}_3 \\ \mathbf{0} & N_{b,\xi_1}\mathbf{I}_3 \end{bmatrix} \tag{4.20}$$

4.4 Isogeometric approximation

The domain,L, is now approximated using NURBS. For single-patch problems, the parameter space is relative to the entire domain. Thus, the weak form now reads:

$$\mathbf{x}^h = \sum_{i=1}^{n_{CP}} N_i(\xi)\mathbf{p}_i = \mathbf{N}\mathbf{p} \tag{4.21}$$

where $N_i(\xi)$ are the NURBS basis functions (denoted $R_{i,p}$ in Chapter 3 and 2), and $\mathbf{p}_i$ are vectors of weighted control point coordinates.
Similarly, the virtual rotations are obtained using the NURBS basis functions for interpolation:

$$\delta\boldsymbol{\omega}^h = \sum_{i=1}^{n_{CP}} N_i(\xi)\delta\boldsymbol{\kappa}_i = \mathbf{N}\delta\boldsymbol{\omega} \tag{4.22}$$

Apart from the topology, the IGA-approximation is from this point identical to the FE-approximation, and the element residual, r_a^e, and the tangent stiffness, $K_{m_{ab}}^e$, are computed from Equations 4.16 to 4.20.

4.5 Locking effects in curved beam elements

Using the same notation as in Chapter 3, initial curvature is taken into account by an additional term in the kinematic equations from Eqs. 3.1 to 3.3, which in 2D now reads:

$$\varepsilon_1 = u_{1,1} + \frac{u_3}{R} \tag{4.23}$$

$$\gamma_{13} = u_{3,1} - \theta_2 \tag{4.24}$$

$$\kappa_2 = \theta_{2,1} - \frac{u_{1,1}}{R} \tag{4.25}$$

where 1, 2 and 3 refer to the local axes. Recalling from Section 3.5, the curved element will also be sensible to transverse shear locking, seen from the same inconsistency in polynomial terms in the expression for γ_{12}. In a similar way the introduced $\frac{1}{R}$-term gives rise to *membrane locking*, which may take place in curved elements with both membrane and bending action.

As for the shear stiffness, the ratio between bending and axial stiffness, $\frac{EI}{EA}$, converges quadratically towards zero. For high slendernesses the beam will then exhibit inextensional bending, giving the *inextensibility condititon*:

$$\varepsilon_1 = u_{1,1} + \frac{u_3}{R} = 0 \tag{4.26}$$

A linear beam with curvature $\frac{1}{R}$ is now considered with the following interpolation:

$$u_1 = a_1 + a_2 s \tag{4.27}$$

$$u_3 = b_1 + b_2 s \tag{4.28}$$

$$\theta_2 = c_1 + c_2 s \tag{4.29}$$

where a_i, b_i, c_i are generalized DOFs, and s the mid-line coordinate. The inextensibility condition then reads:

$$\varepsilon_1 = a_2 + \frac{b_1}{R} + \frac{b_2}{R} s = 0 \tag{4.30}$$

The constraint $b_2 \to 0$ implies from Equation 4.28 that $u_{3,1} \to 0$. From the Kirchoff limit for slender beams, $\gamma_{13} = u_{3,1} - \theta_2 = 0$, it is then seen that $\theta_2 \to 0$, and thus the element tend to lock. This locking phenomenon is referred to as membrane locking.

The same field-inconsistency may cause locking in higher order elements. For a quadratic element with curvature $\frac{1}{R}$, the interpolation reads:

$$u_1 = a_1 + a_2 s + a_3 s^2 \tag{4.31}$$

$$u_3 = b_1 + b_2 s + b_3 s^2 \tag{4.32}$$

$$\theta_2 = c_1 + c_2 s + c_3 s^2 \tag{4.33}$$

giving the inextensibility condition:

$$\varepsilon_1 = a_2 + \frac{b_1}{R} + \left(2a_3 + \frac{b_2}{R}\right)s + \frac{b_3}{R}s^2 = 0 \tag{4.34}$$

The spurious constraint is now $b_3 \to 0$, which from Equation 4.32 implies that $u_{3,11} \to 0$. By the derivative of the Kirchhoff limit, $\gamma_{13,1} = u_{3,11} - \theta_{2,1} = 0$, it is seen that $\theta_{2,1} \to 0$, and locking is also present in quadratic elements.

A spurious constraint will in fact appear in all higher order elements and give excessive stiffness in bending action. However, as the spurious constraint increases with one order per order elevation, the corresponding effect will be reduced by approximately two orders (since $K^e_{m_{11}} \propto \int_{L^e} \varepsilon_1^2 ds$). For more details on membrane locking, the reader is referred to [14, 33].

Chapter 5

Verification of spatial Timoshenko beam

The element derived in Chapter 4 is tested through a number of numerical tests with different load types and boundary conditions. The aim is to verify that the elements provide the expected convergence, study the impact of full and reduced integration and determine any locking or other weaknesses of the isogeometric elements.
The number of elements are chosen to give approximately the same number of nodes for the different element types. This relation is given in Appendix A.
For comparison, the tests have also been analyzed with standard Lagrangian finite elements.
Note that in this chapter "nDOFS" in the convergence plots refers to the total number of degrees of freedom (i.e. $6(n_{els}+p)$ for IGA).

5.1 Curved cantilever subjected to axial tip load

Figure 5.1 shows geometry and material data for a planar 90° circular cantilever beam subjected to an axial tip load, F_x. The load is proportional to the bending stiffness, such that the bending part of the response is independent of the thickness.

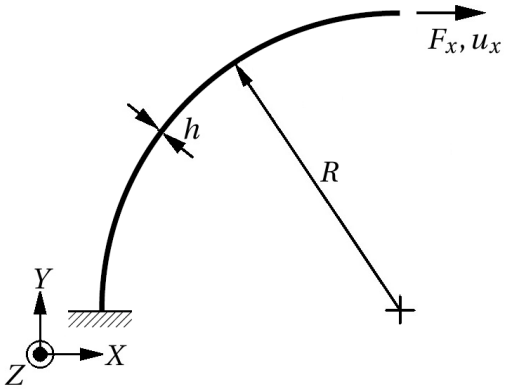

Young's modulus:	$E = 1000$
Poisson's ratio:	$\nu = 0$
Radius:	$R = 10$
Width:	$b = 1$
Thickness:	$h = 1$
Shear factor:	$k_s = 6/5$
Load:	$P = 0.1h^3$

Figure 5.1: Geometry and material data for curved beam subjected to axial tip load.

From Roark *et al.* [37], the analytical solution for the tangential tip displacement, $u_x(\xi = 1)$, which is energy conjugate with the imposed load, is given:

$$u_x = \frac{F_x R^3}{EI}\left[\frac{3\pi}{4} - 2\right] + \frac{F_x R}{EA}\left[2k_s(1-\nu) + \frac{8}{\pi} - 1\right] \tag{5.1}$$

which evaluated for the input data reads: $u_x = 0.4313798673$. However, they have used a simplified expression for the radial shear force and the solution will consequently not coincide with Timoshenko theory. Therefore, a reference solution is computed from 32 quintic Lagrangian elements with reduced integration which gives $u_x = 0.4301037419$. The relative error , $|e_{u_x}|$, is then computed from Eq. 3.25.

Firstly, a convergence study is carried out for a fixed thickness of $h = 1$. The beam is discretized with equally sized knot-span elements and the highest continuity available. The number of elements is chosen in accordance with Table A.1 in order to keep the number of unknowns (nearly) equal. The results for full and reduced integration is reported in Table 5.1. n_{nodes} refers to the (approximate) number of free nodes or control points.

n_{nodes}		4	8	16	32	64
FEA	$p=2$	0.711296	0.145560	0.011335	0.000743	0.000047
	$p=3$	0.036070	0.004564	0.000245	0.000004	0.000000
	$p=4$		0.000270	0.000002	0.000000	
IGA	$p=2$	0.394649	0.019841	0.000929	0.000051	0.000003
	$p=3$	0.083866	0.000272	0.000001	0.000000	
	$p=4$		0.000020	0.000000		
FEA	$p=2$, red. int.	0.003702	0.000234	0.000015	0.000001	0.000000
	$p=3$, red. int.	0.000025	0.000003	0.000000		
	$p=4$, red. int.		0.000000			
IGA	$p=2$, red. int.	0.086941	0.000786	0.000010	0.000000	
	$p=3$, red. int.	0.047582	0.000199	0.000001	0.000000	
	$p=4$, red. int.		0.000020	0.000000		

Table 5.1: Relative error in axial tip displacement for full and reduced integration

The logarithmic plots in Figures 5.2 and 5.3 show the convergence for IGA and FEA with full and reduced integration, respectively.

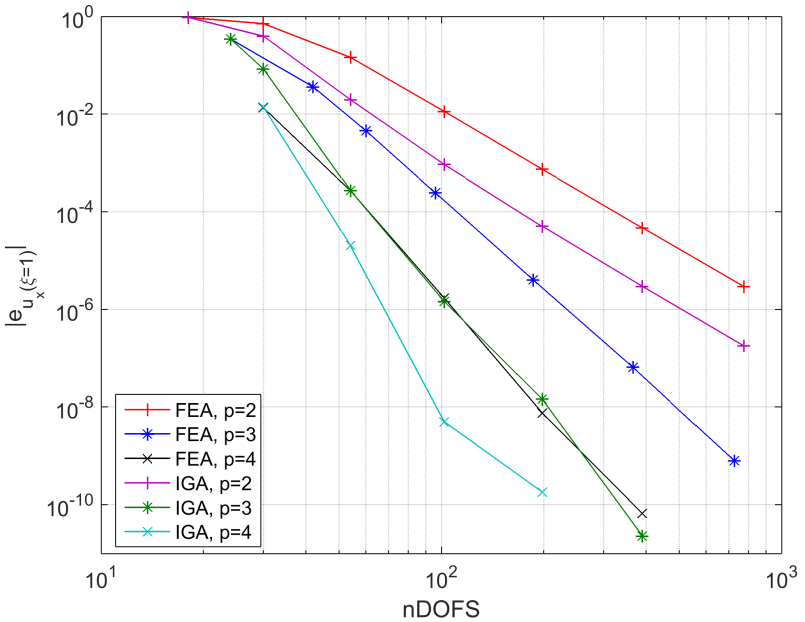

Figure 5.2: Relative error in axial tip displacement for IGA and FEA with full integration.

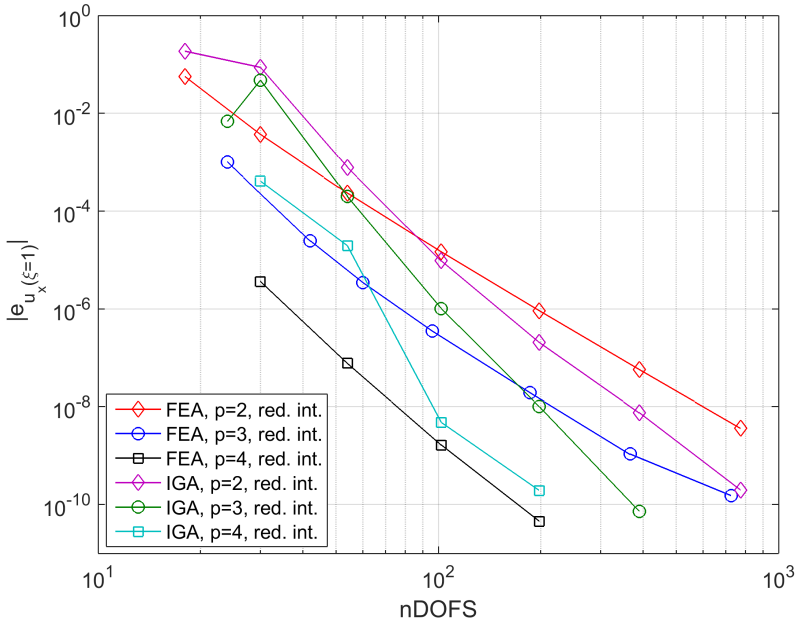

Figure 5.3: Relative error in axial tip displacement for IGA and FEA with reduced integration.

For full integration, FEA exhibits optimal convergence. IGA performs significantly better with less error and faster convergence for $p = 3$ and $p = 4$. Quadratic elements converge with the same speed, but the errors for IGA is approximately one order less.
With reduced integration, cubic and quartic Lagrangian elements show slightly slower convergence, but the absolute errors are considerably reduced. Convergence rates are maintained with IGA, but only the quadratic elements show less errors. It is also observed that with IGA and reduced integration, the errors increase going from 1 to 2 elements for $p = 2$.

Thickness dependency is now studied for a fixed number of 5 elements, varying the slenderness ratio, R/h, from 10^0 to 10^5. Figure 5.4 shows the tangential tip displacement for IGA and FEA with both integration regimes together with the Kirchhoff solution.

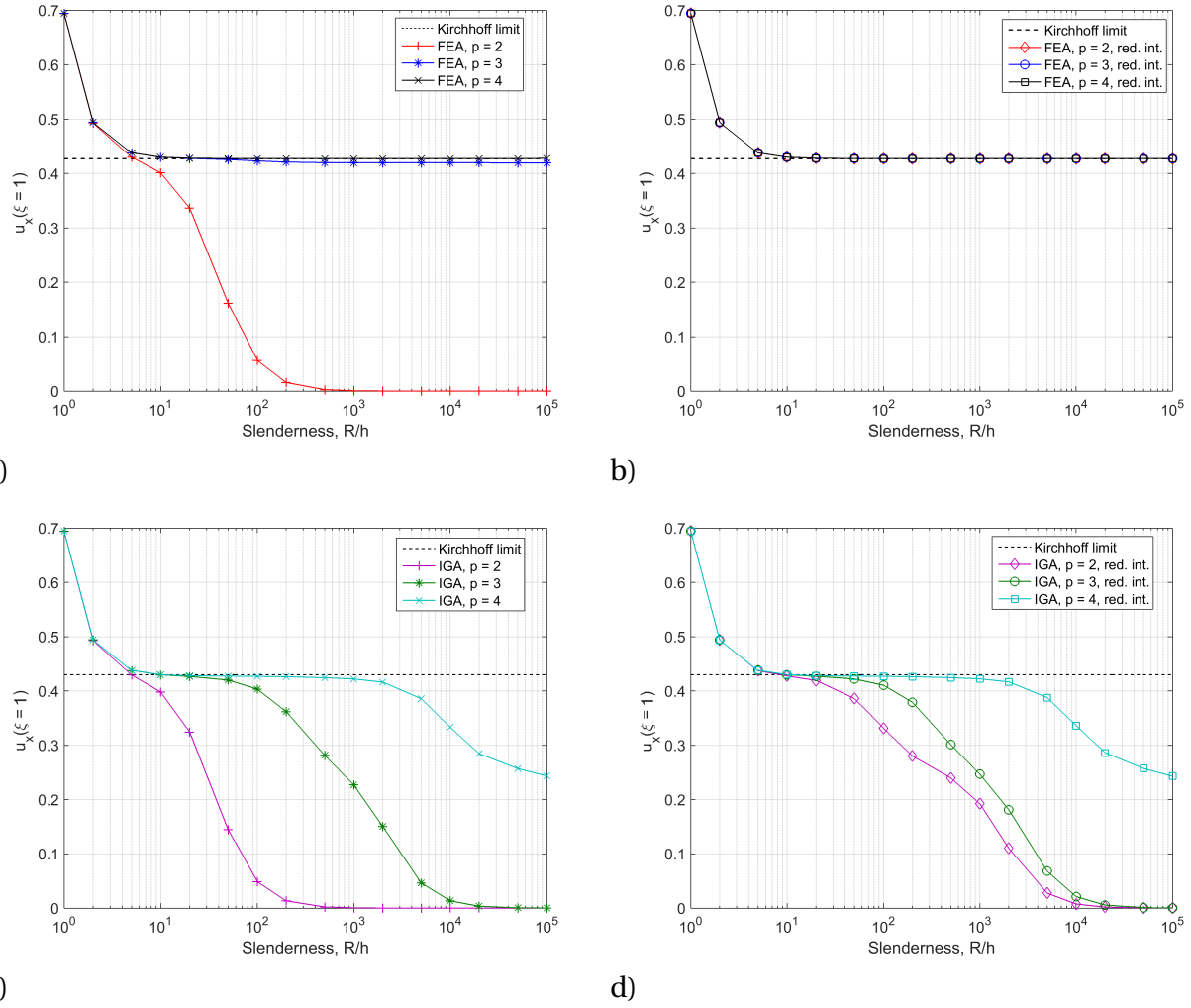

Figure 5.4: Thickness dependency of tangential tip displacement: a) FEA, full int., b) FEA, red. int., c) IGA, full int., d) IGA, red. int.

IGA shows more severe locking than FEA, and while reduced integration appear to make FEA completely locking-free, only the quadratic IGA-element show any significant improvement. The amount of locking in isogeometric elements emphasize the severity of membrane locking.

5.2 45° bend subjected to an out-of-plane load

To check the implementation for a spatial response, a circular 45° bend is subjected to an out-of-plane end load, $P = 60$, as shown in Figure 5.5. The bend has an average radius, R, of 100 and a cross-sectional area of 1.

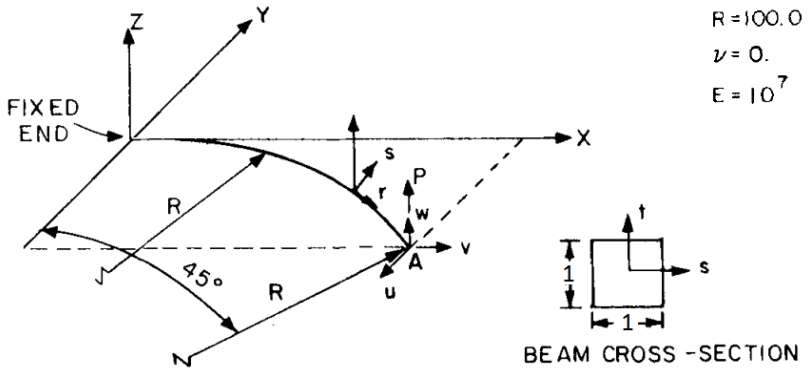

Figure 5.5: Geometry and material data for a circular 45° bend [5].

The convergence of the displacement parallel to P is studied for quadratic to quintic order IGA and FEA. A reference solution is computed from 32 quintic Lagrangian elements with reduced integration and reads $u_z = 11.27509000$, from which the relative errors are computed and reported in Table 5.2.

n_{nodes}		4	8	16	32
FEA	$p=2$	0.042591	0.010477	0.002406	0.000452
	$p=3$	0.002902	0.000048	0.000006	0.000000
	$p=4$	0.000077	0.000001	0.000000	
IGA	$p=2$	0.140419	0.028865	0.001708	0.000096
	$p=3$	0.001093	0.000028	0.000000	
	$p=4$	0.000079	0.000000		
FEA	$p=2$, red. int.	0.000495	0.000031	0.000002	0.000000
	$p=3$, red. int.	0.000086	0.000001	0.000000	
	$p=4$, red. int.	0.000001	0.000000		
IGA	$p=2$, red. int.	0.000546	0.000044	0.000001	0.000000
	$p=3$, red. int.	0.001052	0.000019	0.000000	
	$p=4$, red. int.	0.000002	0.000000		

Table 5.2: Relative error in $u_z(\xi = 1)$ for full and reduced integration.

Figures 5.6 and 5.7 show convergence plots for full and reduced integration. respectively.

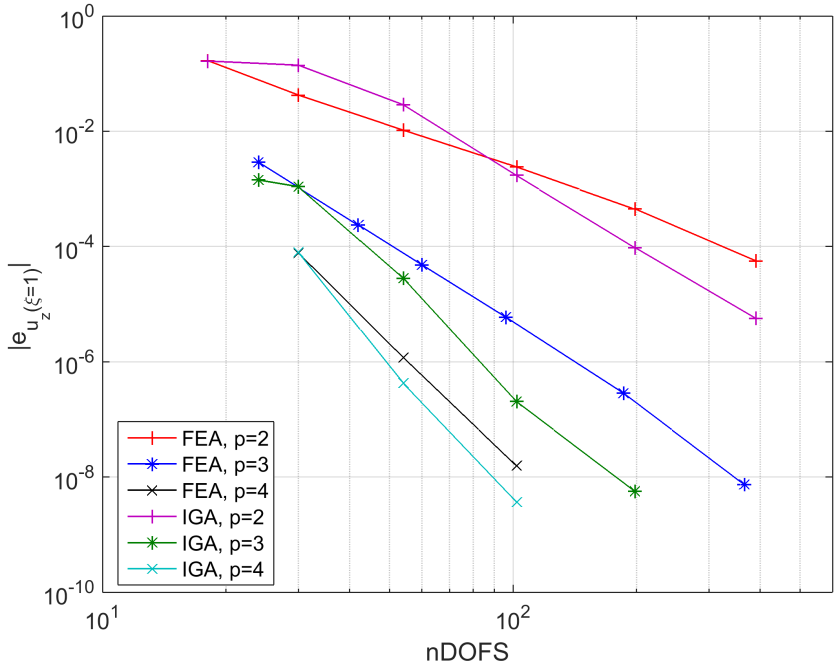

Figure 5.6: Convergence of tip displacement for full integration.

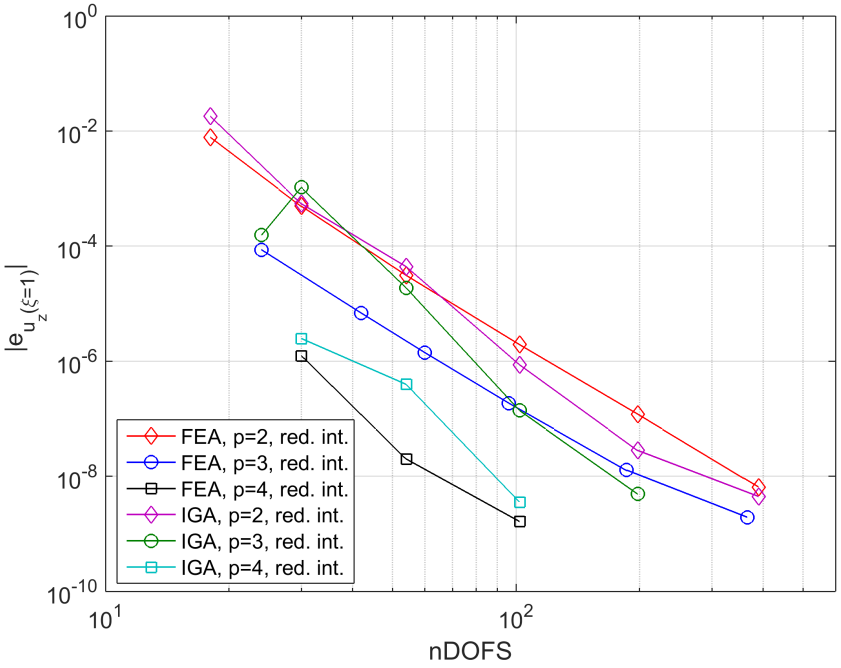

Figure 5.7: Convergence of tip displacement for reduced integration.

FEA exhibit optimal convergence except for cubic and quartic order with reduced integration, which converge one order slower. For IGA, convergence rates are contained with reduced integration. However, only the quadratic NURBS elements show significantly better performance with reduced integration, while Lagrangian elements are improved for all p. This is clearly seen in Figure 5.8, where IGA with full and reduced integration are compared.

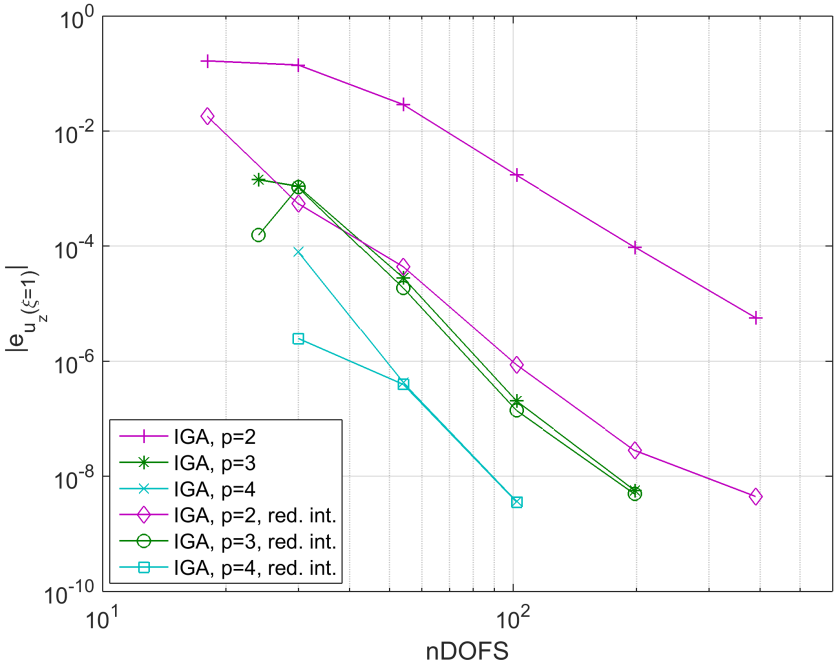

Figure 5.8: Convergence of tip displacement for isogeometric elements.

5.3 Pipe subjected to internal pressure

A pipe with infinitely extent in z-direction subjected to an internal pressure, q, is considered. With Poisson's ratio equal to zero, the problem can be idealized with beam elements. Further, by utilizing the polar symmetry, only a quarter of the pipe is considered, using shear-free boundaries. The pipe cross-section and its calculation model is shown in figure 5.9. Input data is given in Table 5.3.

From [37], the reference solution for axial force and radial displacement is given respectively as:

$$N_\theta = qR, \quad \text{and} \quad u_r = \frac{qR^2}{Eh} \tag{5.2}$$

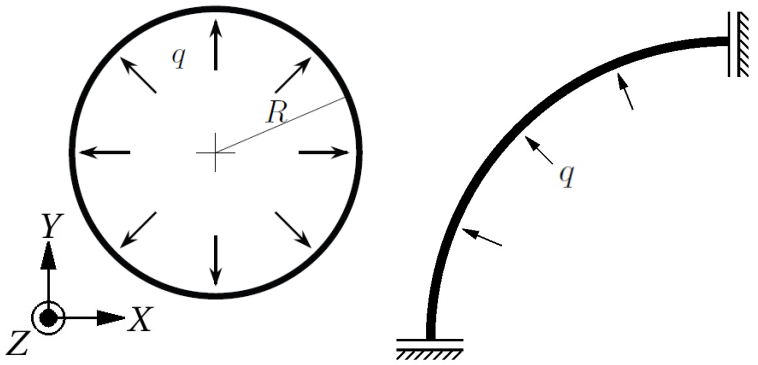

a) b)

Figure 5.9: Pipe subjected to internal pressure: a) xy- plane, b) Idealized system.

Radius	Young's modulus	Poisson's ratio	Width	Thickness	Pressure
$R = 10$	$E = 1e5$	$\nu = 0$	$b = 1$	$h = 1$	$q = 1000h$

Table 5.3: Geometry and material data for pipe subjected to internal pressure.

Firstly, the thickness dependency has been investigated. For this study, the model is discretized with 8 equally sized elements with a slenderness, R/h varying from 10^0 to 10^4. The radial displacements is reported in Table 5.4 for quadratic to quartic order FEA and IGA with full and reduced integration.

	R/h	10^0	10^1	10^2	10^3	10^4
FEA	$p = 2$	0.999995	0.999995	0.999995	0.999995	0.999995
FEA	$p = 3$	1.000001	1.000001	1.000002	1.000002	1.000000
FEA	$p = 4$	1.000000	1.000000	1.000000	1.000000	0.999996
IGA	$p = 2$	1.000000	0.999999	0.999980	0.999974	0.999974
IGA	$p = 3$	1.000000	1.000000	1.000000	0.999993	0.999992
IGA	$p = 4$	1.000000	1.000000	1.000000	1.000000	1.000000
FEA	$p = 2$, red. int.	1.000004	1.000004	1.000004	1.000004	1.000004
FEA	$p = 3$, red. int.	1.000001	1.000001	1.000019	1.001780	1.177838
FEA	$p = 4$, red. int.	1.000000	1.000000	1.000000	1.000001	1.000062
IGA	$p = 2$, red. int.	1.000021	1.000353	1.023155	1.072501	1.074081
IGA	$p = 3$, red. int.	1.000000	1.000003	1.000296	1.007236	1.009394
IGA	$p = 4$, red. int.	1.000000	1.000000	1.000000	1.000037	1.000782

Table 5.4: FEA and IGA of pipe under internal pressure: radial displacement varying the slenderness and polynomial order.

Under pure axial loading, the pipe (beam) does not show any thickness dependency. However, with reduced integration both IGA and FEA show a rather unexpected softening behavior.
The slenderness is now kept fixed to $R/h = 10$, and the convergence of the radial displacement is studied. Numerical results for u_r are reported in Tables 5.5 and 5.6 for full and reduced integration, respectively.

n_{nodes}		4	8	16	32
FEA	$p = 2$	0.998785	0.999918	0.999995	1.000000
	$p = 3$	1.006896	1.000071	1.000007	1.000000
	$p = 4$	0.999163	0.999985	1.000000	
IGA	$p = 2$	0.999913	0.999998	1.000000	
	$p = 3$	0.999928	1.000000		
	$p = 4$	0.998988	1.000000		

Table 5.5: Radial displacement for fully integrated elements with FEA and IGA.

n_{nodes}		4	8	16	32
FEA	$p = 2$, red. int.	1.000917	1.000058	1.000004	1.000000
	$p = 3$, red. int.	1.065975	1.000106	1.000008	1.000000
	$p = 4$, red. int.	1.001538	1.000007	1.000000	
IGA	$p = 2$, red. int.	1.010557	1.000616	1.000027	1.000001
	$p = 3$, red. int.	1.004127	1.000018	1.000000	
	$p = 4$, red. int.	1.086771	1.000000		

Table 5.6: Radial displacement for reduced integrated elements with FEA and IGA.

Figures 5.10 and 5.11 show convergence plots for the relative error in radial displacement, $|e_{u_r}|$, for full and reduced integration, respectively. With no locking, FEA performs similar with both integration rules. IGA, however shows better results with full integration.

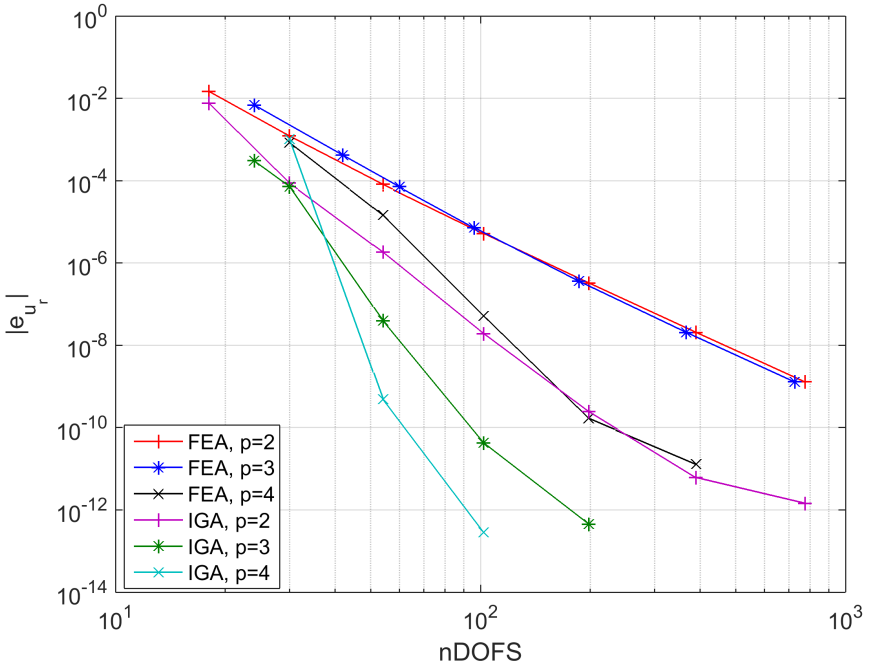

Figure 5.10: Relative error in radial displacement for IGA and FEA, full integration

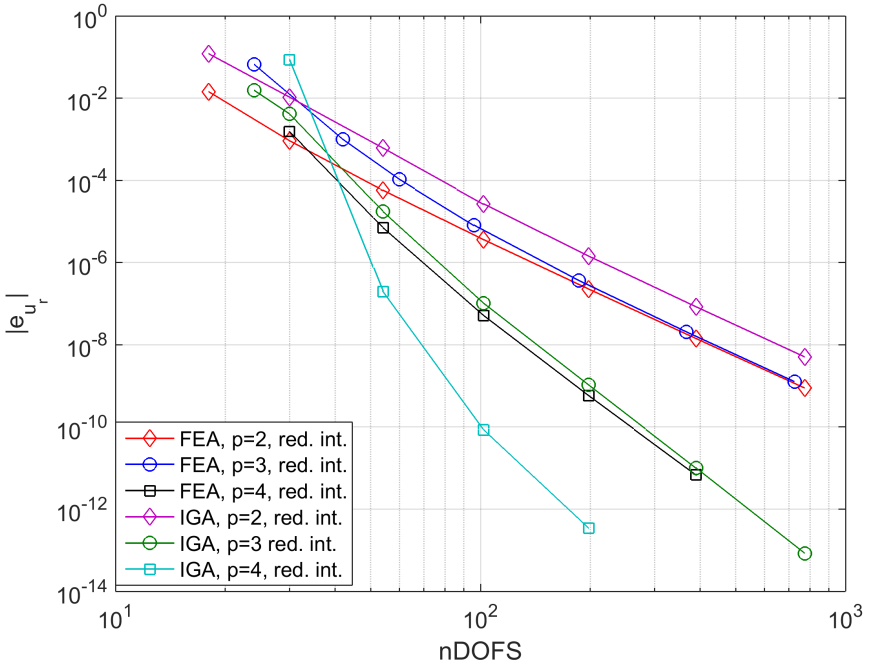

Figure 5.11: Relative error in radial displacement for IGA and FEA, reduced integration

5.4 Cantilever circular arch under tip shear at the free end

A circular arch is subjected to a unit tip shear, P. Geometry and material data are given in Figure 5.12. Depicted in [13], the analytical solution, governed from equilibrium and kinematic compatibility equations for the Timoshenko beam problem, is given in terms of the radial angle, ψ, as:

$$u_t = -P(c_1(\sin\psi + \psi\cos\psi) + c_2\sin\psi), \quad u_n = Pc_1\psi\sin\psi, \quad \theta = -Pc_3\sin\psi \tag{5.3}$$

for the tangential displacement, radial displacement and cross-section rotation, respectively. The compliance coefficients, c_1, c_2 and c_3, are given as:

$$c_1 = \frac{1}{2}\Big(\frac{R}{EA} + \frac{R}{GA_s} + \frac{R^3}{EI}\Big), \quad c_2 = \Big(\frac{R}{GA_s} + \frac{R^3}{EI}\Big), \quad c_3 = \frac{R^2}{EI} \tag{5.4}$$

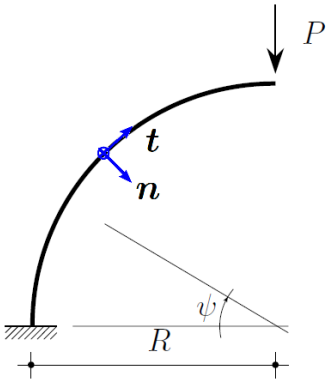

Young's modulus:	$E = 80GPa$
Poisson's ratio:	$\nu = 0.2$
Radius:	$R = 2m$
Width:	$b = 0.2m$
Thickness:	$h = 0.01m$

Figure 5.12: Geometry and material data for cantilever circular arch subjected to tip shear.

For the convergence study, Tables 5.7 and 5.8 report the vertical (radial) displacement at the free end $u_n|_{\pi/2}$, for full and reduced integration, respectively. The analytical solution for vertical tip displacement reads $u_n^{ex}|_{\pi/2} = 4.712427mm$.

n_{nodes}		4	8	16	32	64
FEA	$p=2$	0.004961	0.074084	0.951099	3.775064	4.639796
	$p=3$	3.428906	4.601622	4.679388	4.710067	4.712377
	$p=4$	4.550928	4.702476	4.711904	4.712417	4.712427
IGA	$p=2$	0.020455	0.561629	3.484100	4.622241	4.707040
	$p=3$	1.717781	4.487901	4.710410	4.712406	4.712427
	$p=4$	4.544019	4.697776	4.712419	4.712427	

Table 5.7: Radial tip displacement, $u_n(\psi = \pi/2)$ $[mm]$, for FEA and IGA with full integration.

n_{nodes}		4	8	16	32	64
FEA	$p=2$	4.705746	4.712002	4.712400	4.712425	4.712427
	$p=3$	4.723278	4.712588	4.712448	4.712428	4.712427
	$p=4$	4.712932	4.712435	4.712427		
IGA	$p=2$	3.057595	4.297819	4.702897	4.712300	4.712425
	$p=3$	2.642291	4.543190	4.711010	4.712413	4.712426
	$p=4$	4.712629	4.698559	4.712418	4.712427	

Table 5.8: Radial tip displacement, $u_n(\psi = \pi/2)$ $[mm]$, for FEA and IGA with reduced integration.

The relative error, computed from Equation 3.25, is shown with respect to the number of degrees of freedom in Figures 5.13 and 5.14 for FEA and IGA, respectively. Again, FEA with full integration exhibit the optimal congvergence rates. With reduced integration, cubic or higher order Lagrangian elements converge one order slower, similarly as in Sections 5.1 and 5.2. For IGA, the convergence rates are maintained with reduced integration, but again, FEA shows better performance here, indicating that they are free for locking. As in Section 5.1, IGA with reduced integration show increasing errors going from 1 to 2 elements, but now for all polynomial orders.

The same results are presented in Figures 5.15 and 5.16, but here IGA and FEA is compared with full and reduced integration, respectively.

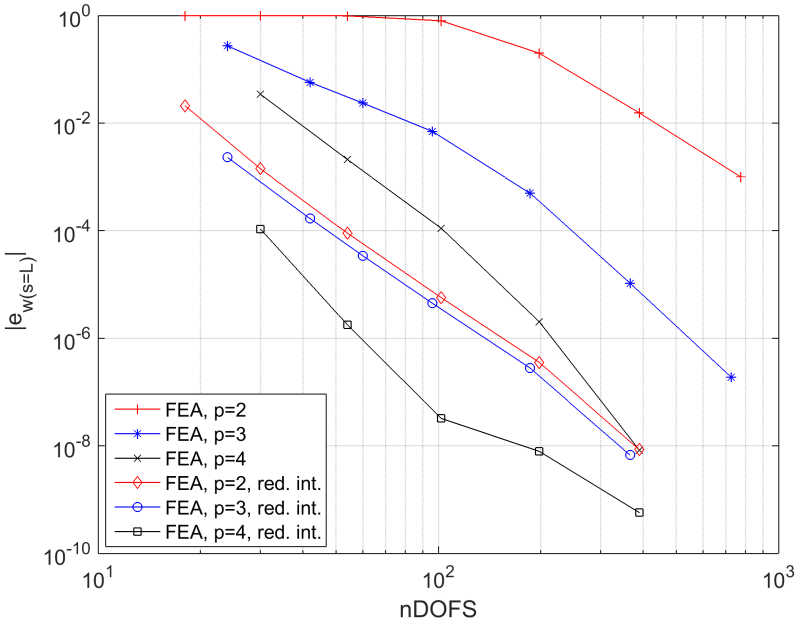

Figure 5.13: Relative error in vertical tip displacement for FEA with full and reduced integration.

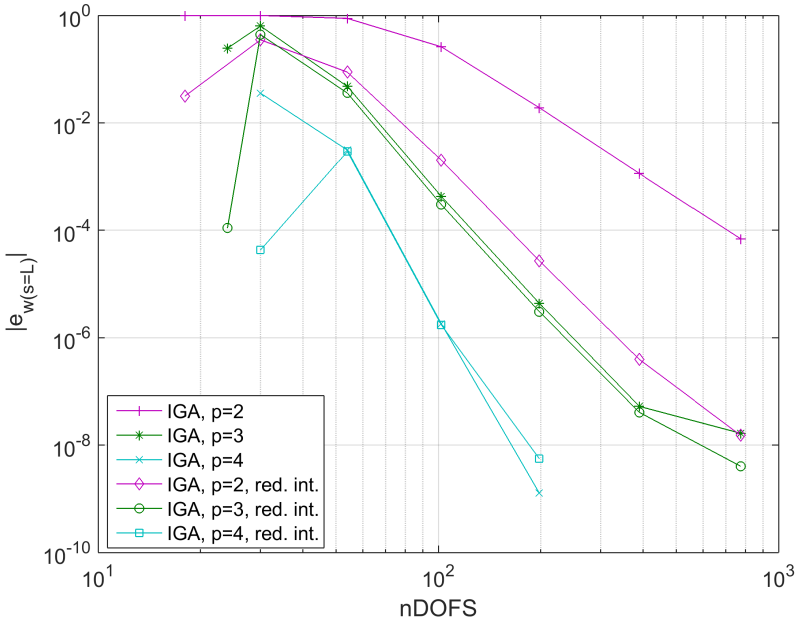

Figure 5.14: Relative error in vertical tip displacement for IGA with full and reduced integration.

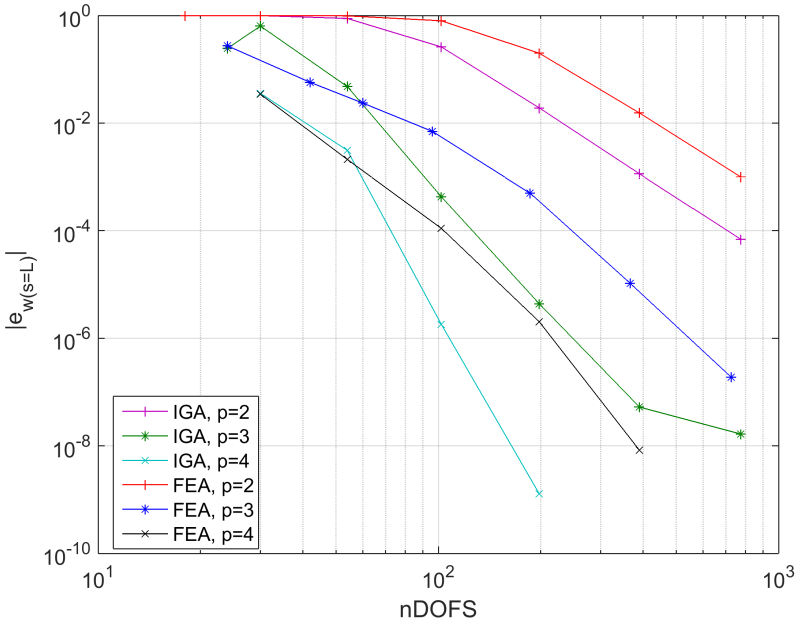

Figure 5.15: Relative error in tip displacement: comparison of FEA and IGA with full integration.

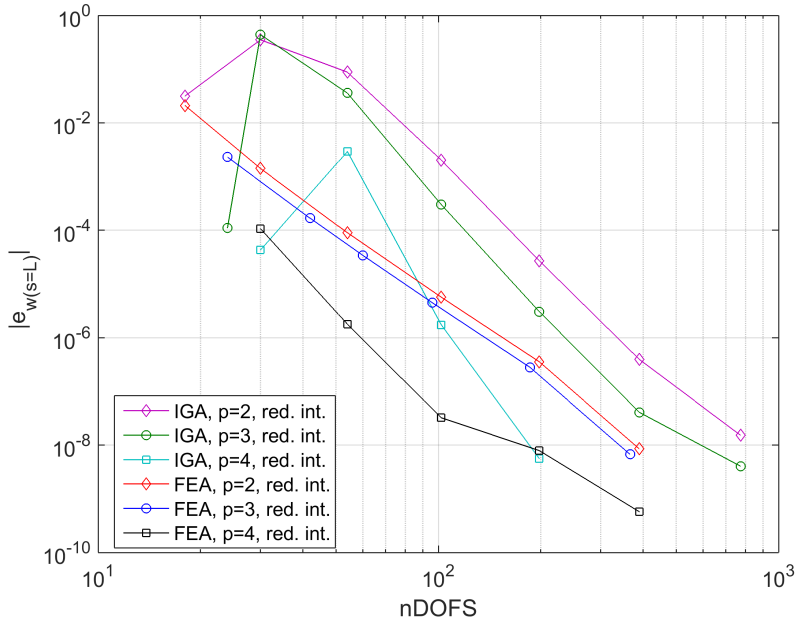

Figure 5.16: Relative error in tip displacement: comparison of FEA and IGA with reduced integration.

Thickness dependency is now studied for a uniform mesh of 5 elements, using the thickness, h, as variable. The relative error in radial tip displacement is reported in Tables 5.9 and 5.10 for full and reduced integration, respectively. The results are also illustrated in logarithmic plots in Figure 5.17. FEA with reduced integration appears to be locking free. The disorders for high slendernesses are due to computer precision and a worsen condition of the stiffness matrix. With full integration, locking is revealed in both IGA and FEA. However, the latter shows less sensibility. For IGA with reduced integration, any noticeable improvement is only seen in quadratic elements.

	R/h	10^1	10^2	10^3	10^4	10^5
FEA	$p=2$	0.0635	0.8661	0.9985	1.0000	1.0000
	$p=3$	0.0002	0.0047	0.0083	0.0084	0.0084
	$p=4$	0.0000	0.0000	0.0001	0.0000	0.0011
	$p=5$	0.0000	0.0000	0.0000	0.0000	0.0059
IGA	$p=2$	0.0726	0.8793	0.9986	1.0000	1.0000
	$p=3$	0.0007	0.0399	0.3211	0.9587	0.9996
	$p=4$	0.0000	0.0011	0.0230	0.1289	0.2499
	$p=5$	0.0000	0.0000	0.0010	0.0094	0.0337

Table 5.9: Relative error in tip displacement w.r.t the slenderness, full integration

	R/h	10^1	10^2	10^3	10^4	10^5
FEA	$p=2$	0.0000	0.0000	0.0001	0.0000	0.0002
	$p=3$	0.0000	0.0000	0.0001	0.0000	0.0003
	$p=4$	0.0000	0.0000	0.0001	0.0000	0.0002
	$p=5$	0.0000	0.0000	0.0001	0.0000	0.0008
IGA	$p=2$	0.0039	0.1203	0.3979	0.9763	0.9998
	$p=3$	0.0005	0.0297	0.2734	0.9349	0.9993
	$p=4$	0.0000	0.0010	0.0222	0.1257	0.2520
	$p=5$	0.0000	0.0000	0.0010	0.0093	0.0338

Table 5.10: Relative error in tip displacement w.r.t the slenderness, reduced integration

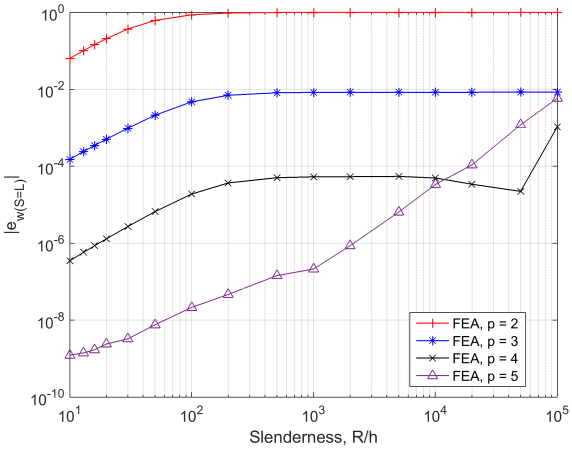

a)

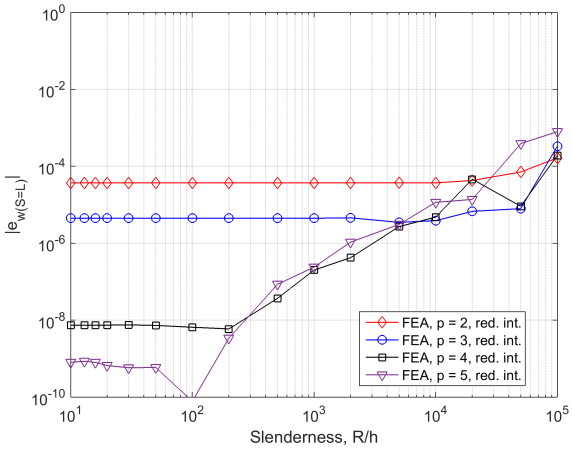

b)

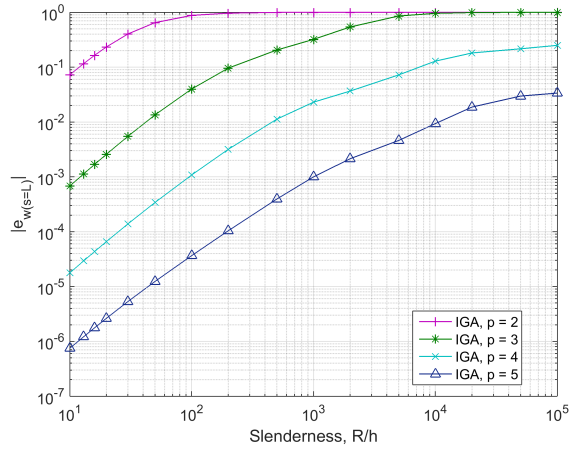

c)

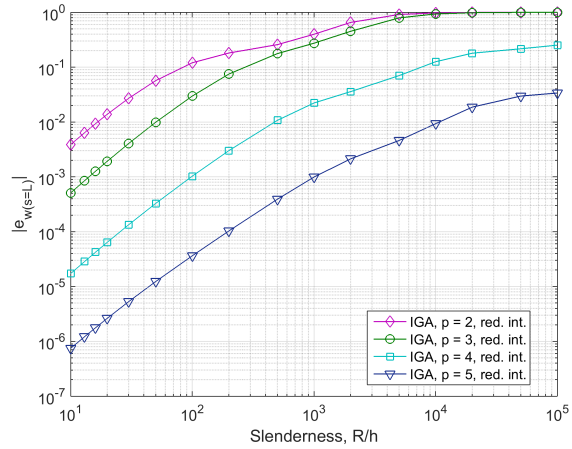

d)

Figure 5.17: Thickness dependency of vertical tip displacement: a) FEA, full int., b) FEA, red int., c) IGA, full. int., d) IGA, red. int.

5.5 Pinched ring

In this example a pinched ring is considered. Due to double symmetry, only one quarter of the structure is modeled. The problem setup is shown in Figure 5.18 and the input data is given in Table 5.11 From [27] the analytical solution for displacements in point A and B is given respectively as:

$$v_A = -\frac{PR^3}{EI}\left(\frac{\pi^2-8}{4\pi}\right) - \frac{\pi PR}{4GA_s} - \frac{\pi PR}{4EA} \tag{5.5}$$

$$u_B = \frac{PR^3}{EI}\left(\frac{4-\pi}{2\pi}\right) + \frac{PR}{2GA_s} - \frac{PR}{2EA} \tag{5.6}$$

Equilibrium considerations give the corresponding bending moments:

$$M_A = \frac{2PR}{\pi} \tag{5.7}$$

$$M_B = PR\left(\frac{2}{\pi} - 1\right) \tag{5.8}$$

Evaluated for the input data, the analytical solution reads:

$$v_A = -1.520035 \qquad u_B = -1.386732$$

$$M_A = 6.366198 \qquad M_B = 3.633802$$

However, the displacements do not converge towards this solution. Lee and Sin [27], explain this by that Castigliano's theorem, from which the analytical solution obtained, is in a thickness range there the response is not entirely beam-like. Therefore, a reference solution is computed from 32 quintic Lagrangian elements with reduced integration:

$$v_A = -1.513964 \qquad u_B = -1.374531$$

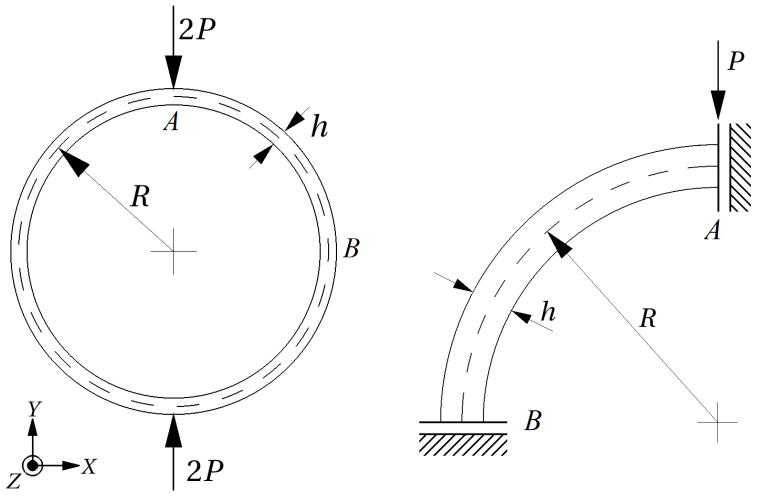

a) b)

Figure 5.18: Pipe subjected to internal pressure: a) xy- plane, b) Problem setup.

Raduis	Young's modulus	Poisson's ratio	Width	Thickness	Load
$R = 10$	$E = 1200$	$\nu = 0.25$	$b = 1$	$h = 1$	$P = 1$

Table 5.11: Geometry and material data for the pinched ring problem.

The numerical results for the vertical displacement and its corresponding relative error in pt. A, v_A and $|e_{v_A}|$, and the bending moment in pt. A and B, M_A and M_B, are reported in Tables 5.12 and 5.13 for FEA, and in 5.14 and 5.15 for IGA with full and reduced integration, respectively.

p	n_{els}	n_{nodes}	v_A	$\lvert e_{v_A}\rvert$	M_A	M_B
2	2	4	-0.429556	0.716271	6.336564	3.663436
	4	8	-1.276267	0.157003	6.364202	3.635798
	8	16	-1.494466	0.012879	6.366070	3.633930
	16	32	-1.512662	0.000860	6.366190	3.633810
3	1	3	-0.249262	0.835358	6.231203	3.768796
	3	9	-1.497760	0.010703	6.365382	3.634617
	5	15	-1.513099	0.000571	6.366150	3.633850
	10	30	-1.513950	0.000009	6.366197	3.633802
4	2	8	-1.512600	0.000901	6.365652	3.634348
	4	16	-1.513956	0.000005	6.366195	3.633805
	8	32	-1.513964	0.000000	6.366198	3.633802
Reference	-	-	-1.513964	-	6.366198	3.633802

Table 5.12: FEA of pinched ring, full integration

p	n_{els}	n_{nodes}	v_A	$\lvert e_{v_A} \rvert$	M_A	M_B
2	2	4	-1.501941	0.007941	6.367055	3.632945
	4	8	-1.513201	0.000504	6.366251	3.633749
	8	16	-1.513916	0.000032	6.366201	3.633799
	16	32	-1.513961	0.000002	6.366198	3.633802
3	1	3	-1.515118	0.000762	6.371934	3.628066
	3	9	-1.514011	0.000031	6.366271	3.633728
	5	15	-1.513970	0.000004	6.366207	3.633792
	10	30	-1.513964	0.000000	6.366198	3.633801
4	2	8	-1.513967	0.000002	6.366201	3.633799
	4	16	-1.513964	0.000000	6.366198	3.633802
Reference	-	-	-1.513964	-	6.366198	3.633802

Table 5.13: FEA of pinched ring, reduced integration

p	n_{els}	n_{nodes}	v_A	$\lvert e_{v_A} \rvert$	M_A	M_B
2	3	4	-0.806318	0.467413	6.309809	3.690191
	9	8	-1.478345	0.023527	6.363465	3.636535
	15	16	-1.512351	0.001066	6.366090	3.633910
	31	32	-1.513877	0.000058	6.366192	3.633808
3	2	4	-1.188560	0.214935	6.328144	3.671856
	6	8	-1.512890	0.000709	6.366038	3.633962
	14	16	-1.513958	0.000004	6.366196	3.633803
	30	32	-1.513963	0.000000	6.366198	3.633802
4	1	4	-1.429186	0.055997	6.322715	3.677284
	5	8	-1.513880	0.000055	6.366180	3.633820
	13	16	-1.513964	0.000000	6.366198	3.633802
Reference	-	-	-1.513964	-	6.366198	3.633802

Table 5.14: IGA of pinched ring, full integration

p	n_{els}	n_{nodes}	v_A	$\lvert e_{v_A}\rvert$	M_A	M_B
2	3	4	-1.183452	0.218309	6.343344	3.656655
	9	8	-1.510913	0.002015	6.365881	3.634119
	15	16	-1.513929	0.000023	6.366196	3.633804
	31	32	-1.513963	0.000000	6.366198	3.633802
3	2	4	-1.313656	0.132307	6.327180	3.672820
	6	8	-1.513176	0.000520	6.366078	3.633921
	14	16	-1.513960	0.000003	6.366197	3.633803
	30	32	-1.513964	0.000000	6.366198	3.633802
4	1	4	-1.513083	0.011247	6.366745	3.633254
	5	8	-1.513882	0.000053	6.366180	3.633819
	13	16	-1.513964	0.000000	6.366198	3.633802
Reference	-	-	-1.513964	-	6.366198	3.633802

Table 5.15: IGA of pinched ring, reduced integration

For the displacements, FEA and IGA behave as in the previous examples. Comparison of FEA and IGA is illustrated in Figures 5.19 and 5.20 for full and reduced integration, respectively. In Figure 5.21, IGA is shown with both integration schemes.

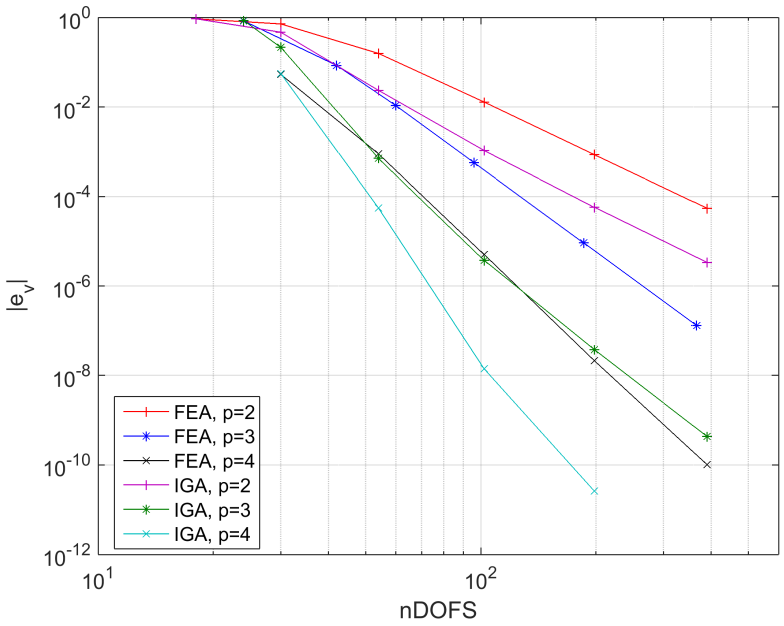

Figure 5.19: Relative error in displacement in A, full integration

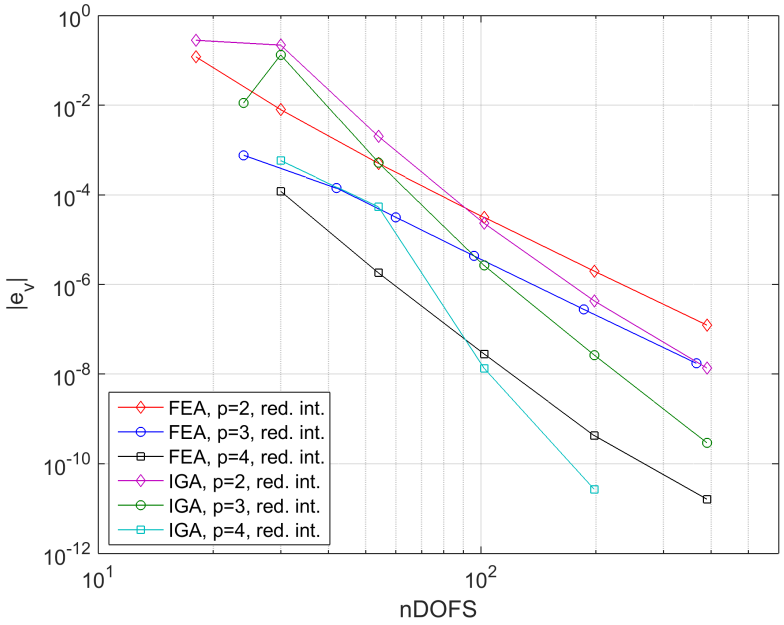

Figure 5.20: Relative error in displacement in A, reduced integration

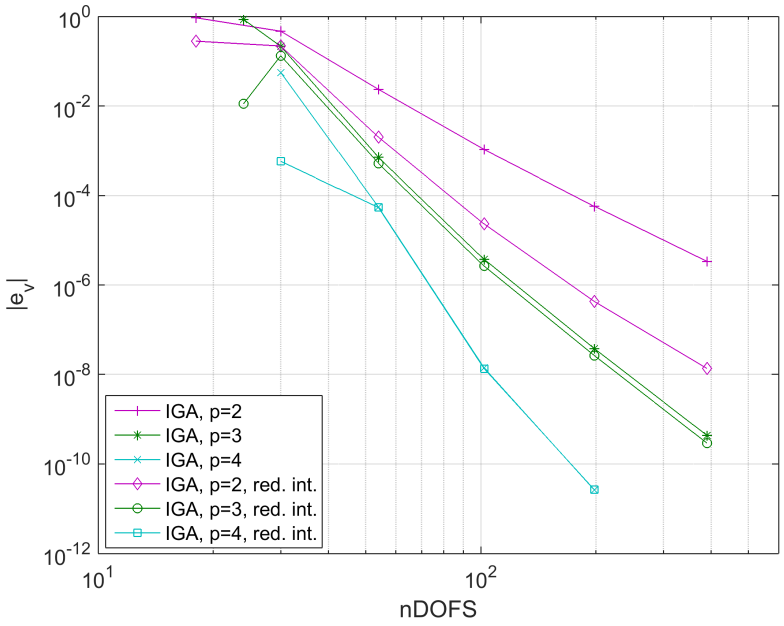

Figure 5.21: Relative error in displacement in A, IGA

Figures 5.22 - 5.24 show convergence plots for the relative error in bending moment in point *A*. Firstly, FEA is compared to IGA for full integration. As for the displacements, IGA shows better

performance and faster convergence than FEA for higher order elements. Secondly, in the comparison of reduced integration, convergence rates for cubic and quartic FEA is reduced, but they show small errors and perform better than IGA for coarse discretizations.

Lastly, isogeometric elements with full and reduced integration is shown in the same figure, and again, significant improvements are only seen in quadratic elements.

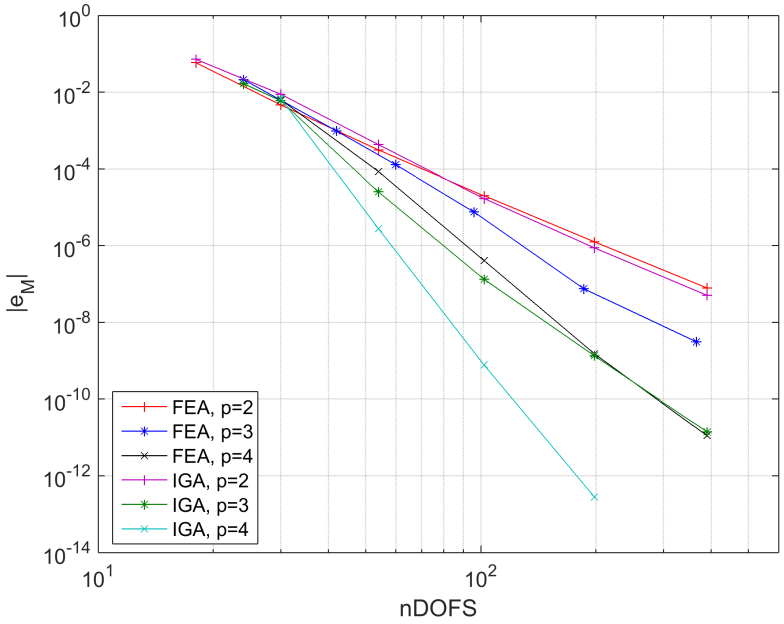

Figure 5.22: Relative error in bending moment in A, full integration

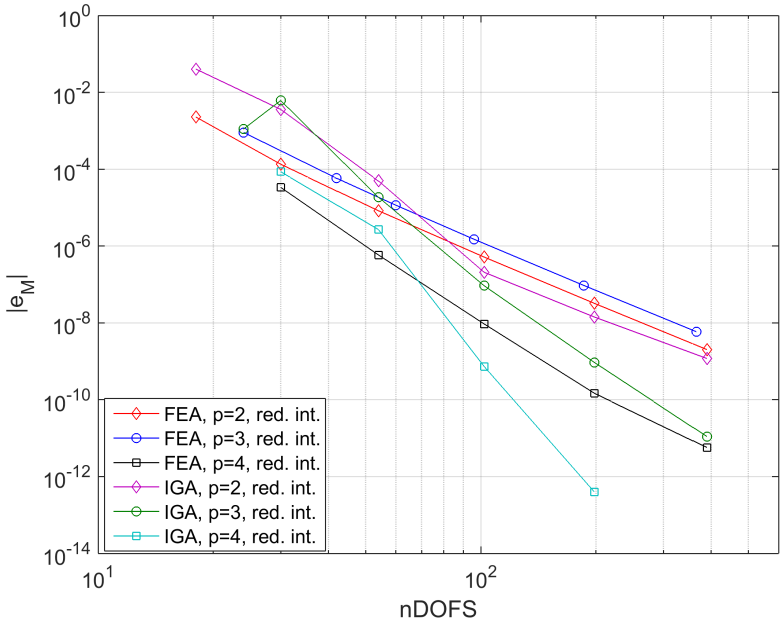

Figure 5.23: Relative error in bending moment in A, reduced integration

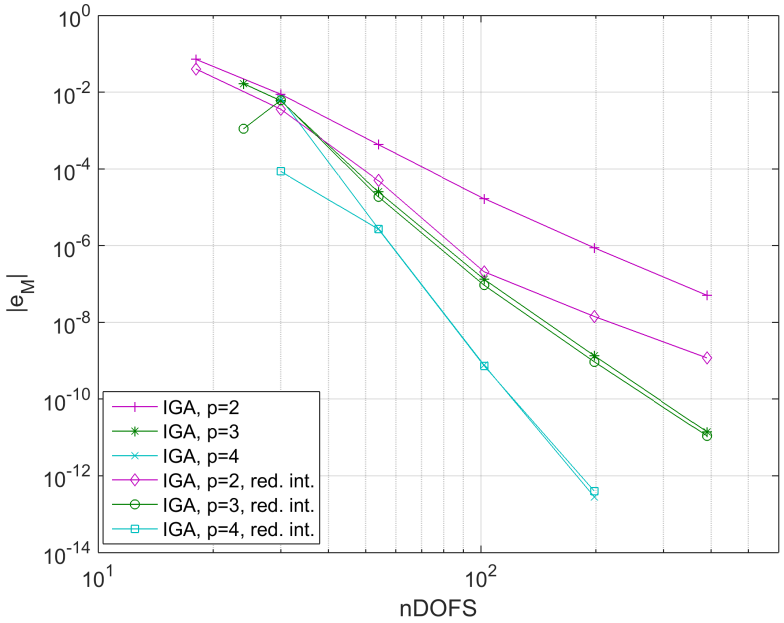

Figure 5.24: Relative error in bending moment in A, IGA

5.6 Hinged arc under self-weight

The hinged arch in Figure 5.25 is taken into consideration with the data given in Table 5.16. The self-weight is applied as a uniformly distributed load, q_0, per unit arc length. Utilizing the symmetry, only half the structure, $A-C$, is considered. The imposed boundary conditions assume moment-free hinges and no shear force in the arch tip, C.

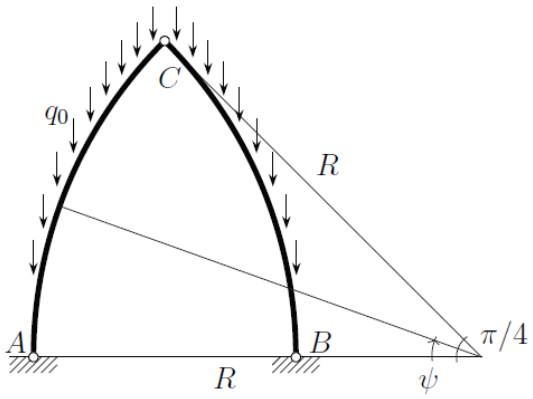

Figure 5.25: Hinged arch under self-weight, taken from [13].

Raduis	Young's modulus	Poisson's ratio	Width	Thickness	Self-weight
$R=1m$	$E=1GPa$	$\nu=0.2$	$b=0.2m$	$h=0.01m$	$q_0=-1kN/m$

Table 5.16: Geometry and material data for the beam in Figure 5.12.

From [13], the analytical solution for vertical displacement, v, is given:

$$\begin{aligned} v = v(\psi) = & A_1\big[-c_1\psi\sin\psi + c_3R(1-\cos\psi)\big] - A_4\sin\psi + \\ & A_2\big[c_1(\psi\cos\psi-\sin\psi) + c_2\sin\psi - c_3R\sin\psi\big] + A_6R\sin\psi + \\ & q_0\Big[\frac{(c_2-c_1)}{4}R(2\psi\cos\psi-\sin\psi) - c_1R\frac{\psi^2}{2}\sin\psi + c_3R^2(\sin\psi-\psi\cos\psi)\Big] \end{aligned} \tag{5.9}$$

where c_i is given in Equation 5.4, and the constants A_1, A_2, A_4 and A_6 reads:

$$
\begin{aligned}
A_1 &= -q_0 R\frac{\pi}{4},\\
A_2 &= q_0 R\Big(1-\frac{\pi}{\sqrt{8}}\Big),\\
A_4 &= q_0 R\Big[2c_3 R+\frac{(c_2-c_1)}{4}\Big],\\
A_6 &= -q_0\Big[c_1\frac{\pi^2}{8}+(c_1-c_2)\Big(\frac{\sqrt{2}}{2}-\frac{\pi}{4}\Big)-(c_1+c_2)\frac{\pi}{4\sqrt{2}}+c_3 R\Big(1+\frac{\pi}{4}+\frac{\pi^2}{16}-\frac{\pi}{2\sqrt{2}}+\frac{\sqrt{2}}{2}\Big)\Big]
\end{aligned}
\tag{5.10}
$$

Evaluated in $\psi = \frac{\pi}{4}$, the reference solution for the vertical displacement in point C reads $v_c = -5.4780240mm$. Further, by equilibrium considerations of the statically determined system, the reactions in point A gives $H_A = 0.1107207kN$ and $V_A = 0.7853982kN$ for horizontal and vertical force components, respectively.

The numerical results for H_A and relative error in v_c are reported in Tables 5.17 and 5.18 and in 5.19 and 5.20 for FEA and IGA with full and reduced integration, respectively.

p	n_{els}	n_{nodes}	$\lvert e_{v_c}\rvert$	H_A
2	2	4	0.918832	0.1107427
	4	8	0.503512	0.1107221
	8	16	0.066682	0.1107208
	16	32	0.005719	0.1107207
	32	64	0.000469	0.1107207
3	1	3	0.184135	0.1106743
	3	9	0.031595	0.1107201
	5	15	0.002568	0.1107207
	10	30	0.000054	0.1107207
	20	60	0.000001	0.1107207
4	1	4	0.156950	0.1107202
	2	8	0.007100	0.1107207
	4	16	0.000061	0.1107207
	8	32	0.000000	0.1107207
Analytical	-	-	-	0.1107207

Table 5.17: FEA of hinged arch, full integration

p	n_{els}	n_{nodes}	$\lvert e_{v_c} \rvert$	H_A
2	2	4	0.013407	0.1107115
	4	8	0.000753	0.1107202
	8	16	0.000046	0.1107207
	16	32	0.000003	0.1107207
	32	64	0.000000	0.1107207
3	1	3	0.029763	0.1106690
	3	9	0.000176	0.1107201
	5	15	0.000021	0.1107207
	10	30	0.000001	0.1107207
	20	60	0.000000	0.1107207
4	1	4	0.000084	0.1107202
	2	8	0.000002	0.1107207
	4	16	0.000000	0.1107207
Analytical	-	-	-	0.1107207

Table 5.18: FEA of hinged arch, reduced integration

p	n_{els}	n_{nodes}	$\lvert e_{v_c} \rvert$	H_A
2	3	4	0.772983	0.1107207
	7	8	0.154730	0.1107207
	15	16	0.010898	0.1107207
	31	32	0.000632	0.1107207
	63	64	0.000037	0.1107207
3	2	4	0.161980	0.1107207
	6	8	0.004274	0.1107207
	14	16	0.000030	0.1107207
	30	32	0.000000	0.1107207
4	1	4	0.157484	0.1107207
	5	8	0.000125	0.1107207
	13	16	0.000000	0.1107207
Analytical	-	-	-	0.1107207

Table 5.19: IGA of hinged arch, full integration

p	n_{els}	n_{nodes}	$\lvert e_{v_c} \rvert$	H_A
2	3	4	0.151605	0.1107206
2	7	8	0.016941	0.1107207
	15	16	0.000240	0.1107207
	31	32	0.000003	0.1107207
	63	64	0.000000	0.1107207
3	2	4	0.157414	0.1107207
	6	8	0.002761	0.1107207
	14	16	0.000020	0.1107207
	30	32	0.000000	0.1107207
4	1	4	0.000127	0.1107208
	5	8	0.000116	0.1107207
	13	16	0.000000	0.1107207
Analytical	-	-	-	0.1107207

Table 5.20: IGA of hinged arch, reduced integration

Convergence plots for displacement in C are shown in Figures 5.26 to 5.28 and for horizontal reaction forces in A in Figures 5.29 and 5.30.

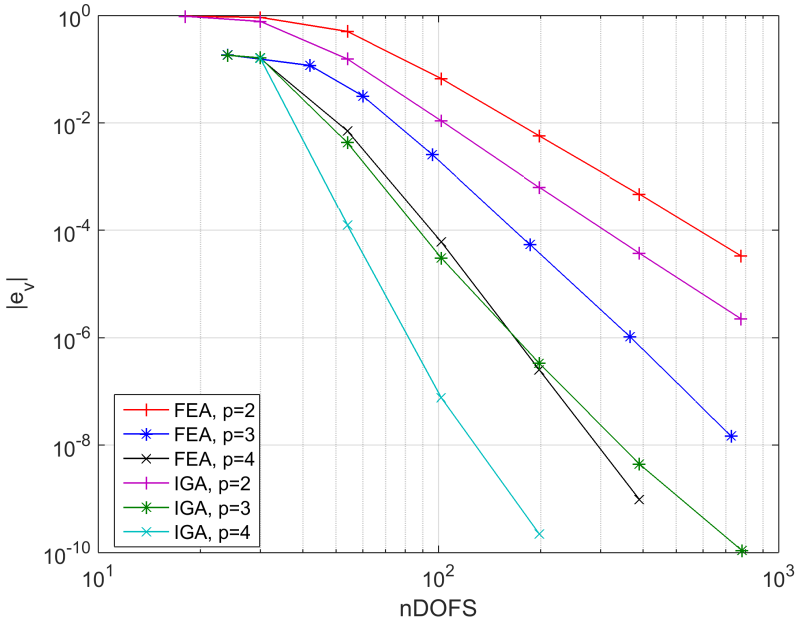

Figure 5.26: Relative error in vertical displacement for full integration.

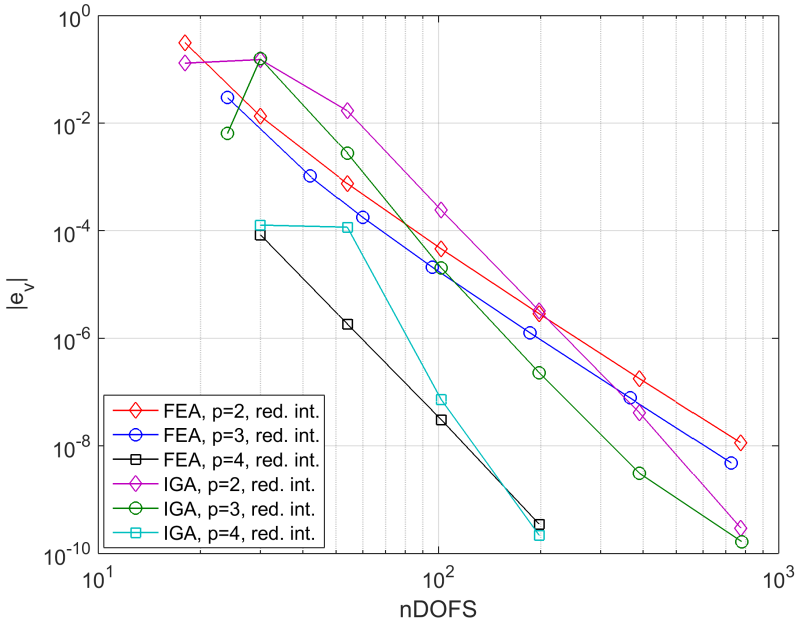

Figure 5.27: Relative error in vertical displacement reduced integration.

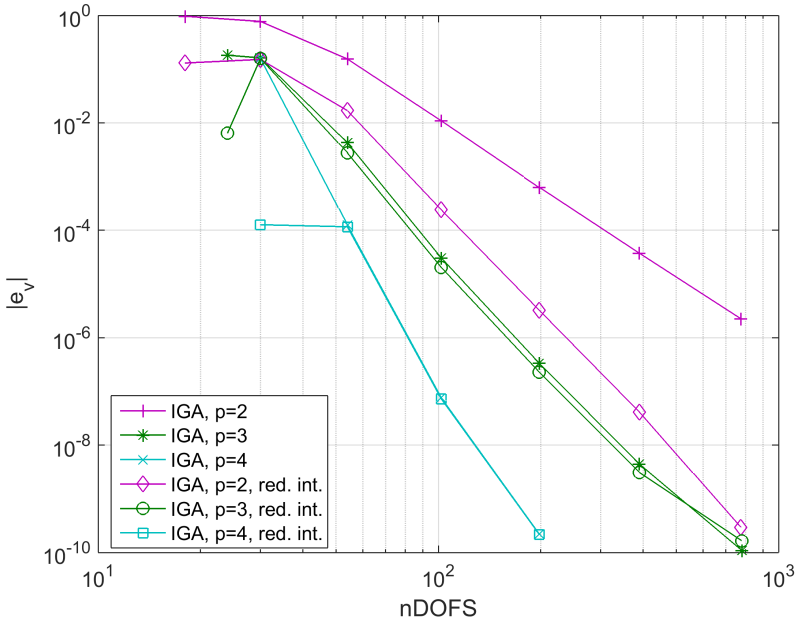

Figure 5.28: Relative error in vertical displacement for IGA, full and reduced integration.

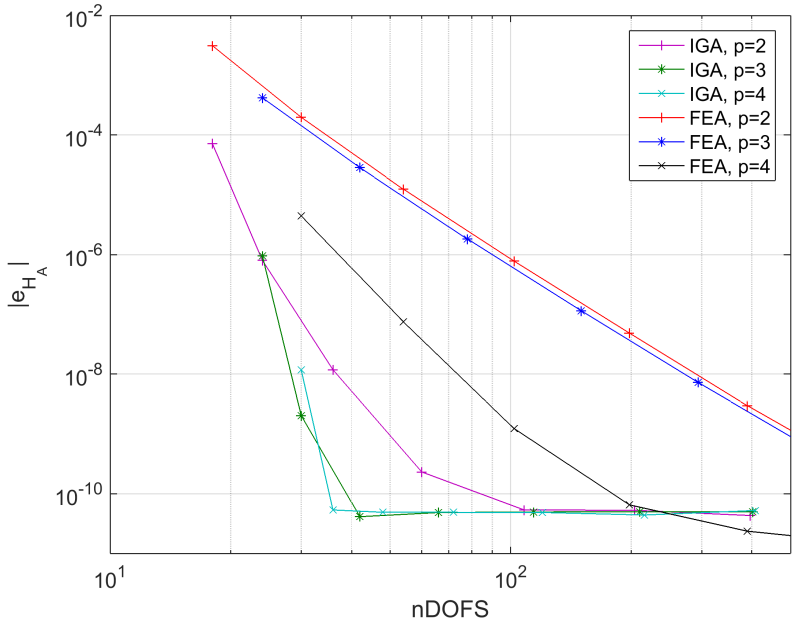

Figure 5.29: Relative error in horizontal reaction force, full integration.

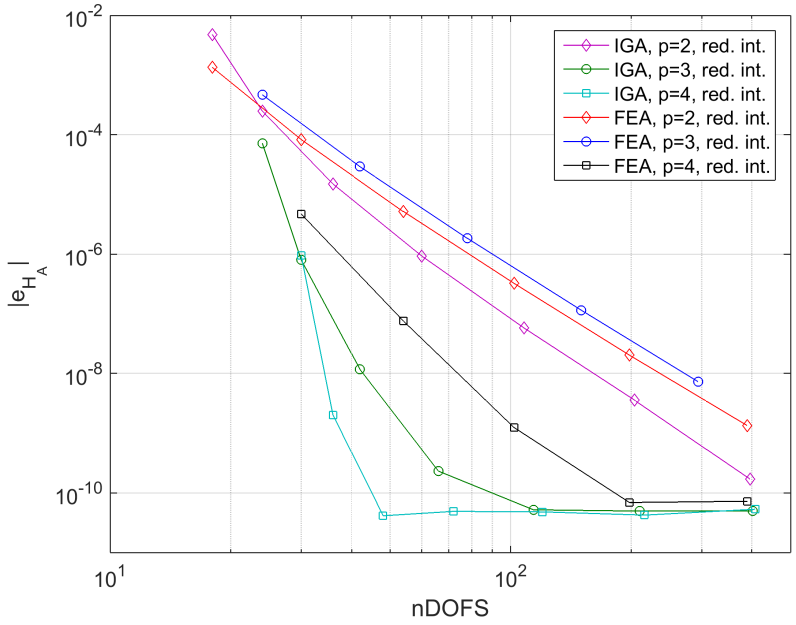

Figure 5.30: Relative error in horizontal reaction force, reduced integration.

FEA and IGA behave as in the previous examples for the displacements. In Figures 5.29 and 5.30, where the relative error in horizontal reaction forces in A are shown for full and reduced

integration, respectively, IGA outperforms FEA with both less errors and faster convergence. As in Section 5.5, cubic Lagrangian elements shows slightly larger errors than the quadratic ones for this problem. Note that the convergence is terminated by the computer precision.

5.7 Straight beam subjected to distributed moment

In the last example, a straight beam subjected to a sinusoidally distributed moment $m(s) = h^3 \sin(\pi s/2L)$, as shown in Figure 5.31, is analyzed with the spatial beam element. Unlike the numerical tests in Chapter 3, the closed form solution for the sinusoidal loading is not contained within the approximation space.

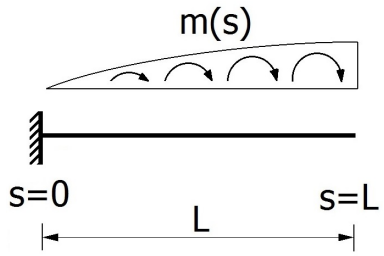

Young's modulus:	$E = 1000$
Poisson's ratio:	$\nu = 0$
Length:	$L = 1$
Width:	$b = 0.2$
Thickness:	$h = 0.01$

Figure 5.31: Geometry and material data for a straight beam under sinusoidally moment loading.

The analytical solution is given by [1, 9]:

$$u_z(s) = \frac{96L^3}{Eb\pi^3}\left(1 - \cos\left(\frac{\pi}{2L}s\right)\right) \tag{5.11}$$

$$u_x(s) = 0 \tag{5.12}$$

$$\theta(s) = \frac{48L^2}{Eb\pi^2}\sin\left(\frac{\pi}{2L}s\right) \tag{5.13}$$

for the vertical and horizontal displacement and rotation fields, respectively.

The convergence is studied for elements up to $5th$ order. As the initial geometry is linear, also linear elements are included in the analysis. The relative error is in terms of the L^2-norm of the vertical displacements, computed from Eq. 3.26, are shown in Figure 5.32 for IGA and FEA with

full and reduced integration.

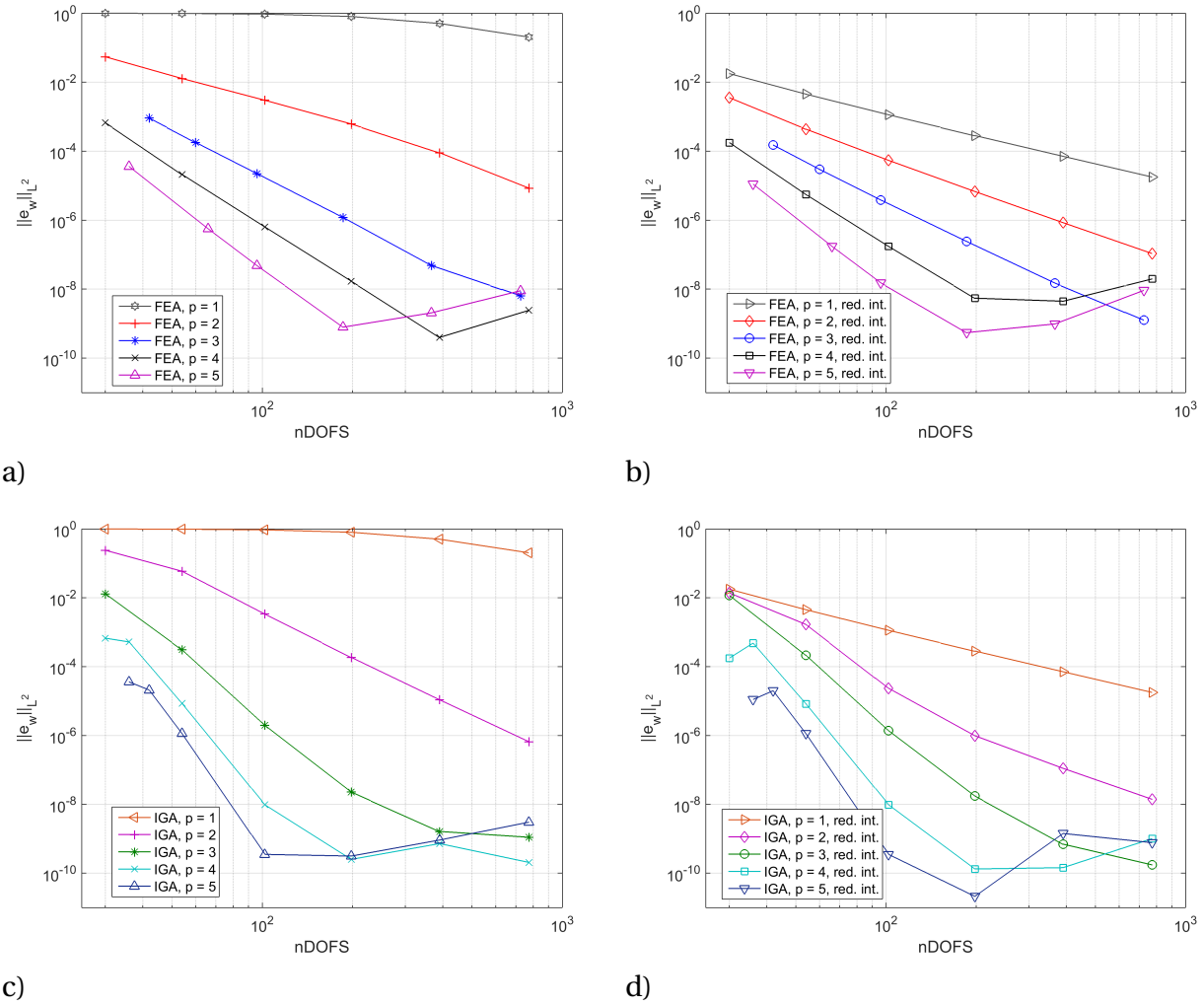

Figure 5.32: Convergence plots of straight beam under sinusoidally moment loading: a) FEA, full. int., b) FEA, red int., c) IGA, full int., d) IGA, red. int.

Unlike the initially curved beams, FEA does not show slower convergence with reduced integration here. The shift in absolute errors for all element orders indicate presence of transverse shear locking. For IGA, the convergence rates are also maintained, but only linear and quadratic order elements show less error, indicating presence of spurious shear strains in higher order elements.

Further, the thickness dependency is investigated with a uniform mesh of 5 elements, shown in Figure 5.33. The same error measurement as for the convergence study is used. All elements show thickness dependency with exact integration. Locking is however more severe in IGA. As

expected, FEA with reduced integration is locking-free, while IGA show the same thickness dependency. Note that for $p = 1$, IGA is equivalent to FEA and thus locking-free with reduced integration.

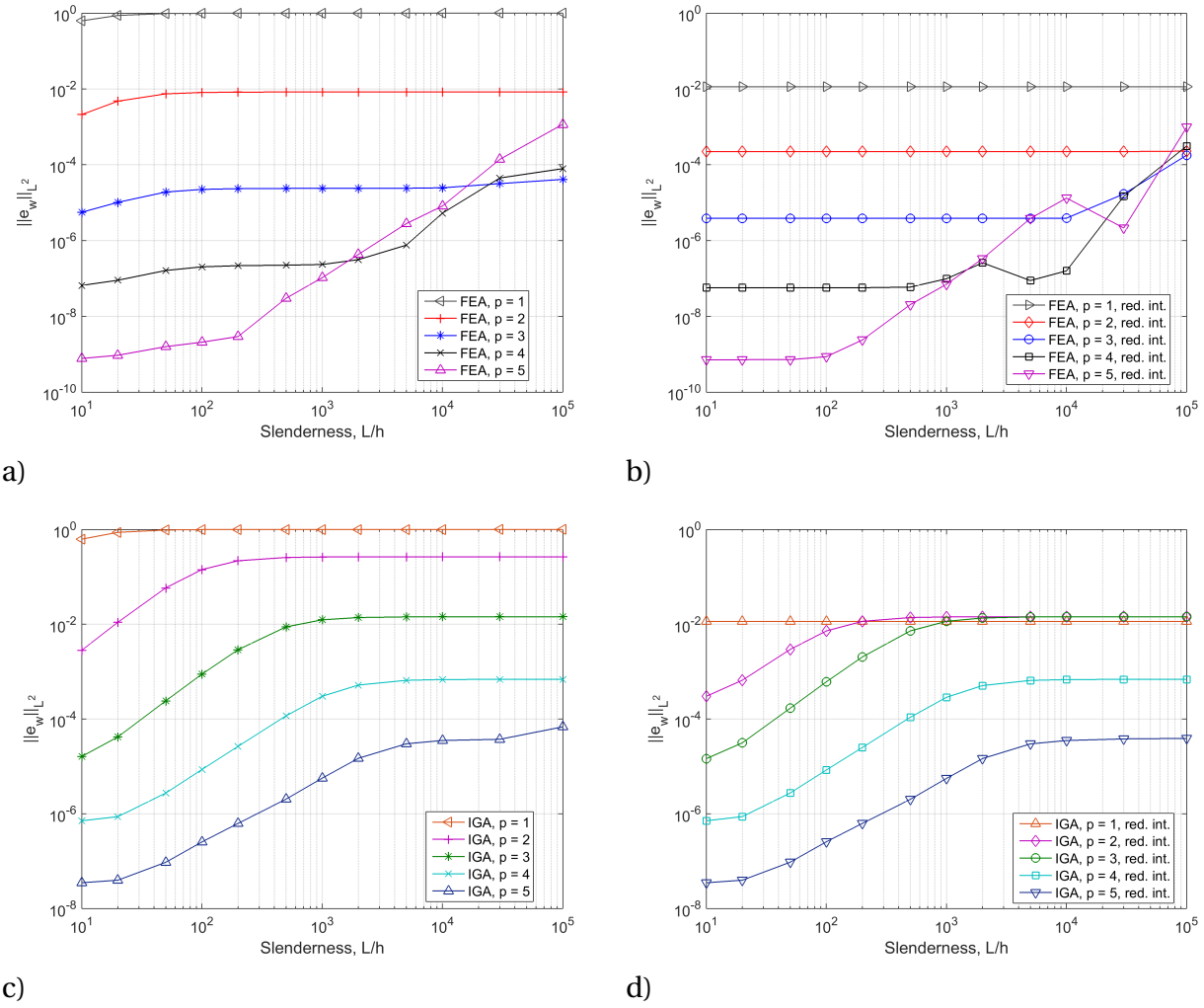

Figure 5.33: Thickness dependency in a straight beam under sinusoidally moment loading: a) FEA, full int., b) FEA, red int., c) IGA, full int., d) IGA, red. int.

5.8 Concluding remarks

Through the numerical tests in this chapter, it has been proven that the implementation of the geometrical exact 3D Timoshenko beam has been successfully implemented using Lagrangian and NURBS basis functions for discretization. The latter has shown superior performance for exact integration of the stiffness matrix, producing both less errors and faster convergence, see e.g. Figures 5.2, 5.15 and 5.26.

Reduced integration, which has proven to eliminate (or at least alleviate) numerical locking in FEA, does however not remove locking in the NURBS elements (except for $p = 1$). Improvements are seen for quadratic elements, but for higher order elements, the impact is negligible (see Figures 5.4, 5.17 and 5.33). This confirms that IGA with reduced integration still capture spurious strains.

An interesting feature of IGA with reduced integration is that 1 element produce less errors than 2, which may indicate that the equation system becomes over-constrained: The ratio between free nodes and Gauss points for a single-element patch is $\frac{p}{p} = 1$. Adding one C^{p-1}-continuous element will add 1 node and p Gauss points, and the ratio now becomes $\frac{p+1}{2p} \leq 1$ and thus over-constrained for $p \geq 2$. For C^0-elements however, there will be added p free nodes and the ratio remains constant.

Chapter 6

Locking removal

From the verification tests in Chapter 5 it was proven that isogeometric elements suffer from the same locking phenomena as Lagrangian elements, and that they do not resolve with the conventional element-wise reduced integration rule. As a consequence, the elements fail to reproduce bending properly approaching the Kirchhoff limit.

One remedy to overcome this problem is to apply reduced and selective reduced integration rules by a patch-wise approach, which has recently been successfully applied by Adam *et al.* [1] and Bouclier *et al.* [9]. However, these studies were limited to linear elastic analyses and polynomial orders, $p \leq 3$, while the geometrically exact beam formulation presented herein is able to accommodate large displacement analyses and is valid for all polynomial orders.

In this chapter, the connection between spurious strains and locking will be highlighted in Section 6.1 In Section 6.2 follows an investigation of one elements propensity to lock, resulting in two proposed integration schemes, which are implemented and tested on a selection of numerical examples in Section 6.3. Section 6.4 summarize the observations from the numerical tests.

6.1 Spurious strains and locking

In curved beams, there exists an interrelationship between transverse shear and membrane locking, as pointed out in [41]. Thus, these locking phenomena must be considered simultaneously.

Recalling from Section 3.5 and 4.5, spurious axial and transverse shear strains, or membrane strains, may rise from the unbalanced terms in the interpolation functions in the translational part. However, the strains do have the correct value in a discrete set of points with in the patch (or between two C^0-continuities [1]), and if these coincide with the integration points, locking may be avoided.

To show how the strains may reveal locking, the 90° bend subjected to a axial load at the free end from Section 5.1 is considered again. Figure 6.1 shows the resulting distribution of axial strains obtained with 3 C^0 Lagrangian and 5 C^1 NURBS elements of quadratic order (and thus an equal number of unknowns) with full and reduced integration. It is clearly seen that with the Gaussian quadrature rule corresponding to full integration, both elements sample the strains erroneously, and thus reveal locking. The Lagrangian element with reduced integration, however, which has proven to be locking free, shows perfect match between the Gauss points and the reference solution. This cannot be said for IGA with the same integration rule. Improvements are seen, but spurious strains are still captured. The verification tests in Section 3.4 and Chapter 5 support this.

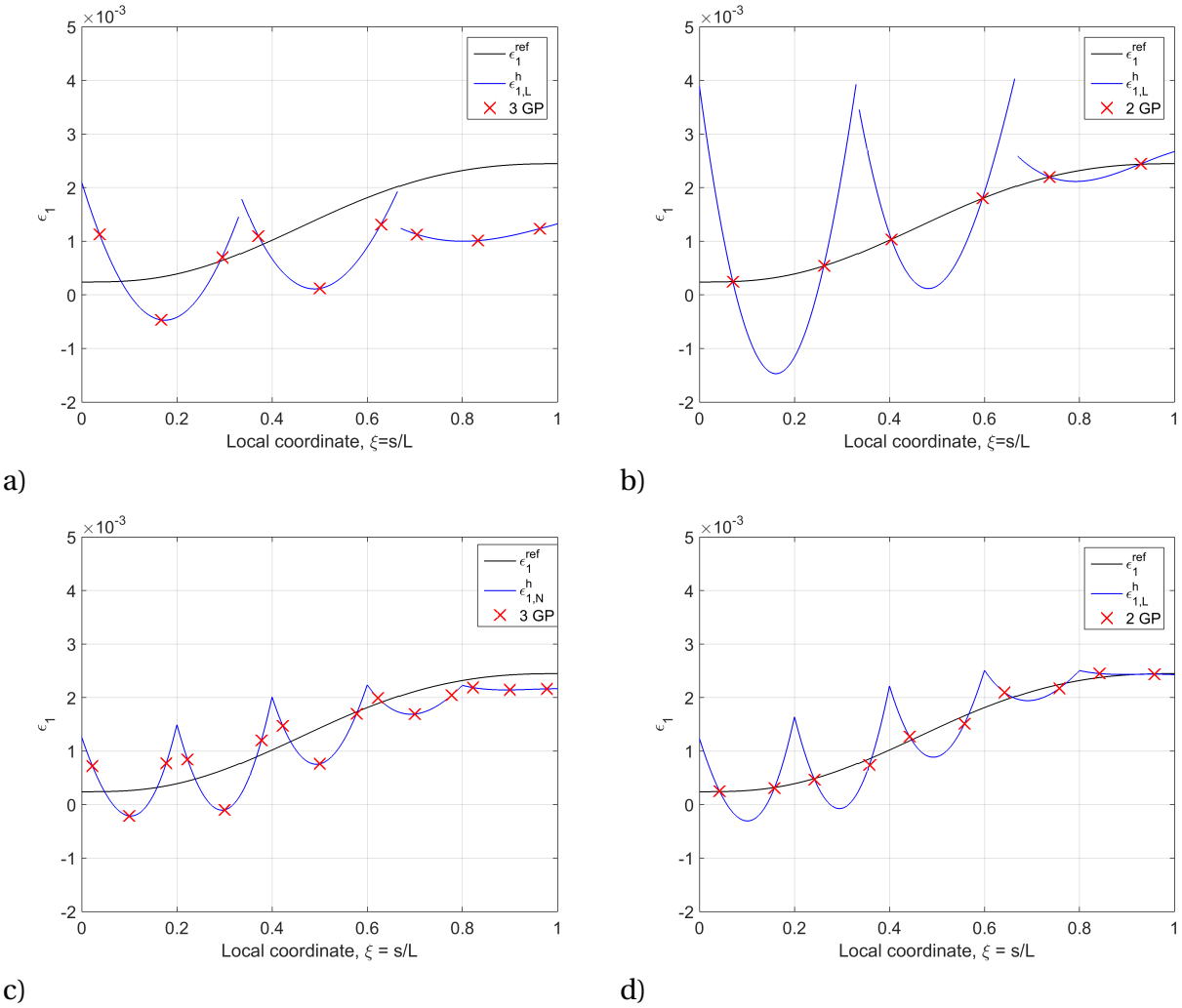

Figure 6.1: Axial strain distribution with the corresponding quadrature points for: a) 3 Lagrange elements with full integration, b) 3 Lagrange elements with reduced integration, c) 5 NURBS elements with full integration and d) 5 NURBS elements with reduced integration.

6.2 Selective Gaussian-based integration

In order to evaluate an element's propensity of locking, Hughes [21] introduced a heuristic approach, the so-called *constraint count* method. This method relies on the constraint ratio, r, which is defined as the ratio between the total number of equilibrium equations, n_{eq} and the total number of constraint equations, n_c:

$$r = \frac{n_{eq}}{n_c} \tag{6.1}$$

To investigate whether an element is prone to locking, the constraint ratio for the continuous problem is compared with the constraint ratio of the discretized problem, r^h, in the limit of an infinite number of elements, $n_e \to \infty$:

$$r^h = \lim_{n_e \to \infty} \frac{n_u^e}{n_c^e} \tag{6.2}$$

Here n_u^e denotes the number of unknowns added to the system by adding one more element to an infinitely large mesh, while n_c^e is the corresponding number of constraints introduced by this element. Thus, n_c^e is related to the number of quadrature points, n_{GP}, where the constraints are evaluated.

For an element with $r^h < r$, and especially with $r^h < 1$ (which implies that there are added more constraints than unknowns), the propensity of locking is high. In contrast when $r^h > r$, this indicate that there are too few constraints to approximate the equations accurately. Consequently, the optimal element satisfy the criterion $r^h = r$.

Without loss of generality a 2D beam is considered, for which the constraint ratio for the continuous problem is

$$r_{2D} = \frac{3}{2} \tag{6.3}$$

If the beam is discretized with C^0- Lagrange elements and C^{p-1} NURBS elements, the constraint ratio becomes respectively

$$r_{2D,L}^h = \frac{3p}{2n_{GP}} \quad \text{and} \quad r_{2D,N}^h = \frac{3}{2n_{GP}} \tag{6.4}$$

from which it is seen that the optimal constraint ratio is obtained with $n_{GP} = p$ for Lagrange elements. For NURBS however, there should be added only one Gauss point per added element in order to obtain the optimal constraint ratio.

Recalling from Chapter 4 and Equation 4.10, the strain energy of the beam consist of one membrane part, $\frac{1}{2}\int_L \boldsymbol{\varepsilon}\,\mathbf{n}ds$, and one bending part, $\frac{1}{2}\int_L \boldsymbol{\kappa}\,\mathbf{m}ds$, each contributing to the material part of the stiffness matrix, $\mathbf{K}_m$:

$$\mathbf{K}_m = \mathbf{K}_n + \mathbf{K}_b \tag{6.5}$$

$\mathbf{K}_n$ and $\mathbf{K}_b$ denote the membrane and the bending stiffness matrix, respectively. To avoid zero-energy modes, the global stiffness matrix must be rank sufficient. If the number of free DOFs is n_F, the rank of $\mathbf{K}_m$ is given:

$$\text{rank}(\mathbf{K}_m) = \min(n_F, n_\varepsilon n_{GP}) \tag{6.6}$$

where n_ε represents the number of strain components, which for this beam is 6. I.e. each Gauss point adds n_ε to rank($\mathbf{K}_m$) up to the maximum number og n_F. To solve a system of n_F free DOFs, $\mathbf{K}_m$ must be of equal rank. Otherwise the system is rank deficient and becomes singular. While the number of Gauss points corresponding to the optimal constraint ratio with Lagrangian elements may be achieved without rank deficiency, applying only one Gauss point on all elements will not give a sufficient number of constraints, and thus produce zero-energy modes in the analysis. However, using a patch-wise approach, rather than evaluating the integrals element-by-element, the zero-energy modes may be stabilized by adding Gauss points to *some* elements. Governed by Eq. 6.6, rank-sufficiency is obtained with a total number of $n_{GP} = n_{els} + p - 1$ Gauss points within the patch.

The above investigation has resulted in two proposed integration schemes, reported in Table 6.1, which will be referred to as SRI-1 and URI-1, and SRI-2 and URI-2, respectively. In URI-1 and URI-2, both the membrane and the bending stiffness matrix is integrated with the proposed rule, while for SRI-1 and SRI-2, the integration scheme is applied to the membrane stiffness matrix only and the bending stiffness is integrated with $n_{GP} = p$ per NURBS element. URI and SRI refer to *uniform* and *selective* reduced integration, and unless URI is labeled with a number, it refers to the conventional reduced integration rule. The motivation for using SRI is that the terms giving rise to locking occur in the translational part.

p	SRI-1/URI-1	SRI-2/URI-2
1	$n_{GP} = 1$	$n_{GP} = 1$
2	$n_{GP} = 1 \setminus e = (1 + n_e)/2 : n_{GP} = 2$	$n_{GP} = 1 \setminus e = n_e : n_{GP} = 2$
3	$n_{GP} = 1 \setminus e = 2, n_e - 1 : n_{GP} = 2$	$n_{GP} = 1 \setminus e = 1, n_e : n_{GP} = 2$
4	$n_{GP} = 1 \setminus e = 2, (1 + n_e)/2, n_e - 1 : n_{GP} = 2$	$n_g = 1 \setminus e = 1, n_e : n_{GP} = 3$
5	$n_{GP} = 1 \setminus e = 2, n_e - 1 : n_{GP} = 2 \wedge e = (1 + n_e)/2 : n_{GP} = 3$	$n_{GP} = 1 \setminus e = 1, n_e : n_{GP} = 4$

Table 6.1: Selective reduced integration schemes.

6.3 Numerical tests

The purpose of the numerical tests is to study how isogeometric analysis performs with the different integration regimes for uniform and selective reduced integration. They are also compared with standard Lagrangian finite elements and NURBS elements with conventional reduced integration.

Comparison of the strain fields obtained from the numerical analyses with their respective Gauss points and the analytical fields has been emphasized, as locking occurs from incorrectly sampled strains. Convergence and thickness dependency are also studied.

The strain components are computed from the Lagrangian and the NURBS basis functions using the kinematic equations presented in Chapter 3 and Chapter 4 for straight and curved beams, respectively. However, all analyses are performed using the geometrically exact beam model, including the straight beams. Note that when this non-linear beam model is used to compute the strains, they are given in the current configuration and will consequently not show the linear solution exactly.

6.3.1 Cantilever beam subjected to tip shear

The first test is a straight cantilever beam subjected to a transverse tip load, similar as in Section 3.4.1. The material and cross-section properties are given in Table 6.2. The thickness is expressed in terms of a slenderness parameter, ρ, such that the slenderness, L/h is given as 10^{ρ}. Furthermore, the dimensionless load is scaled with the bending stiffness.

Young's modulus	Poisson's ratio	Length	Width	Thickness	Load,
$E = 4000$	$\nu = 0$	$L = 10$	$b = 1$	$h = L/10^{\rho}$	$P = Eh^3/400L$

Table 6.2: Geometry and material data for cantilever beam subjected to tip shear at the free end.

The analytical solution for the transverse displacement field, $w(x)$, is given in Equation 3.27, and may be written:

$$w(x) = \frac{L}{20}\left[-\left(\frac{x}{L}\right)^3 + 3\left(\frac{x}{L}\right)^2 + \frac{6}{5}\left(\frac{x}{L}\right)\left(\frac{h}{L}\right)^2 \right] \tag{6.7}$$

The analytical solution for the rotation field, $\theta(x)$, may be found from the unit-load method.

Note that the rotations are independent of the transverse shear stiffness, GA_s:

$$\theta(x) = \frac{Px^2}{2EI} - \frac{PLx}{EI} = \frac{6P}{EA}\left[\left(\frac{x}{h}\right)^2 - 2\left(\frac{L}{h}\right)\left(\frac{x}{h}\right)\right] = \frac{3}{20}\left[\left(\frac{x}{L}\right)^2 - 2\left(\frac{x}{L}\right)\right] \tag{6.8}$$

From the kinematic equations, the nonzero strain components, γ_{xy} and κ_z, are obtained:

$$\gamma_{xy} = w_{,x} + \theta = \frac{3h^2}{500Lb} \tag{6.9}$$

$$\kappa_z = \theta_{,x} = \frac{3}{10L}\left(\frac{x}{L} - 1\right) \tag{6.10}$$

The beam is discretized with 5 equally sized NURBS elements, and the strain fields for ε_x (axial strain), γ_{xy} (transverse shear strain) and κ_z (bending strain) are studied for the different integration models.

Firstly, the strains obtained with conventional reduced integration (URI) are compared for quadratic Lagrangian and isogeometric elements. In order to keep the number of approximation functions n equal for Lagrange ($n \propto n_e p$) and NURBS ($n \propto n_e + p - 1$) based solutions, a uniform mesh of 3 quadratic Lagrange elements is used. The strains are reported in Figure 6.2 for slendernesses of $\rho = 1$ and $\rho = 3$. Both elements sample the strains correctly, and thus appear to be locking free. NURBS elements with URI seem to be able to produce a constant membrane strain distribution correctly.

With a fixed slenderness of $\rho = 3$, the beam is now analyzed with the proposed integration regimes. Figure 6.3 shows the strain fields obtained with SRI-1 and SRI-2, and Figure 6.4 with URI-1 and URI-2 for quadratic elements. Similarly, Figures 6.5 and 6.6 show the strains for $p = 3$, and Figures 6.7 and 6.8 for $p = 4,5$. Note the scale of the vertical axis! For $p = 2$, the membrane part is sampled with good accuracy for all integration regimes, while they show increasing errors and divergence for higher order elements with SRI-1 and URI-1. The rotational part is represented with good accuracy for quadratic SRI-1 and all orders of SRI-2, while it is more inaccurately represented with URI-1 and URI-2.

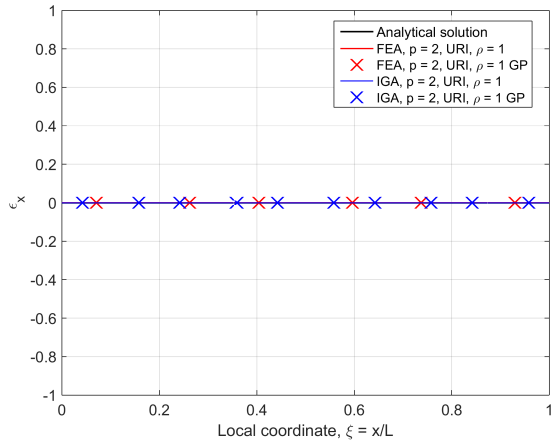

a)

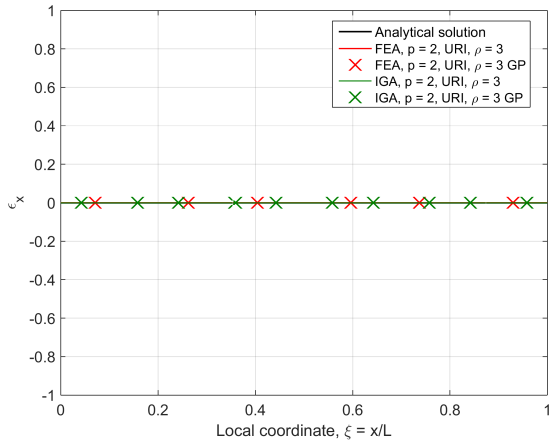

b)

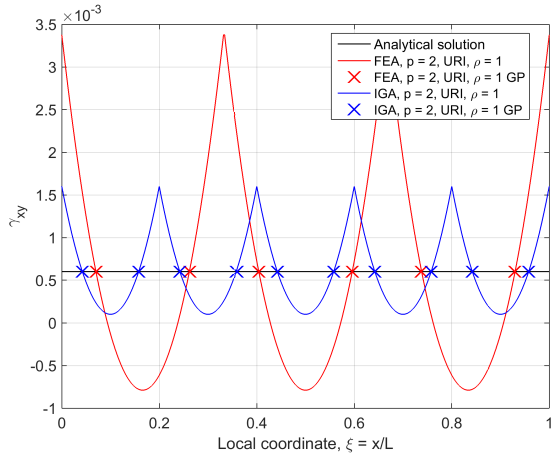

c)

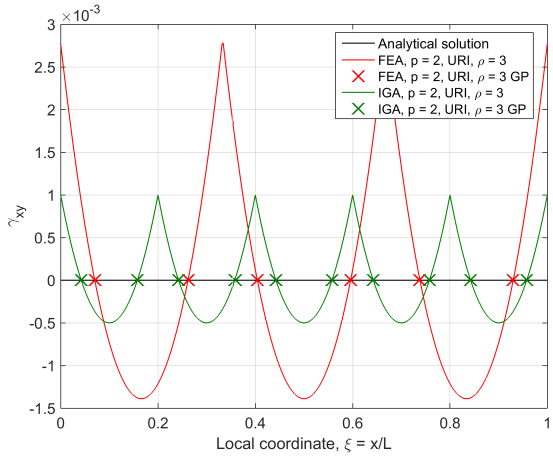

d)

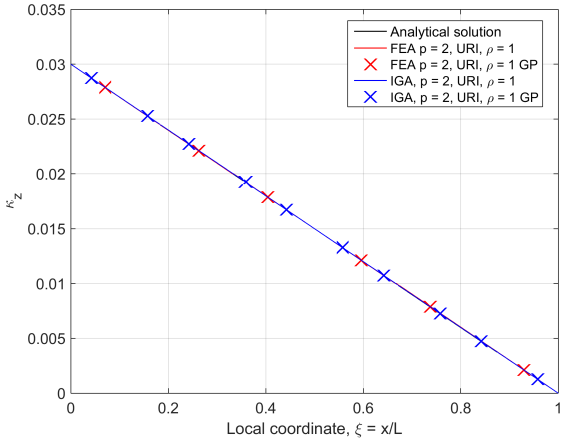

e)

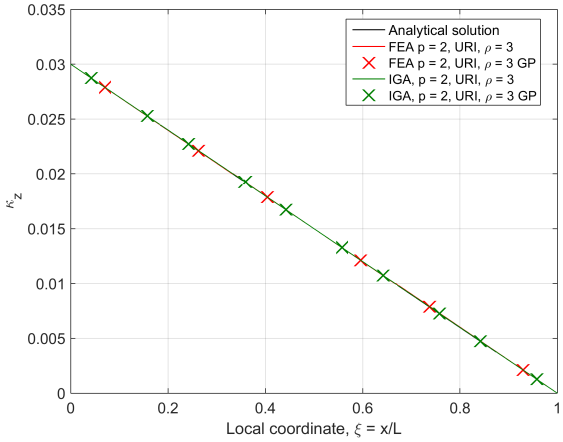

f)

Figure 6.2: Comparison of Lagrange (FEA) and NURBS (IGA) based solutions applying conventional reduced integration (URI) for $p = 2$: a) Axial strain, $\rho = 1$, b) axial strain, $\rho = 3$, c) transverse shear strain, $\rho = 1$, d) transverse shear strain, $\rho = 3$, e) bending strain, $\rho = 1$, and f) bending strain, $\rho = 3$.

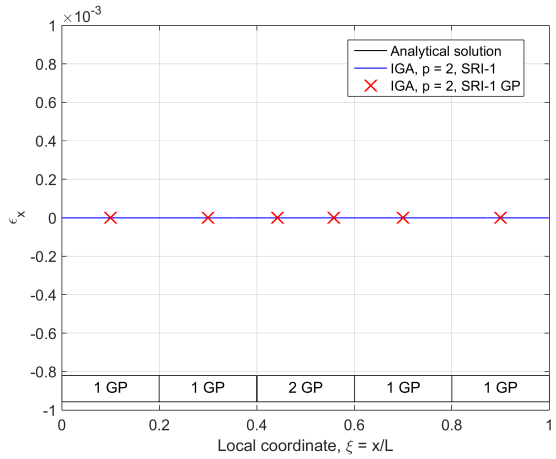

a)

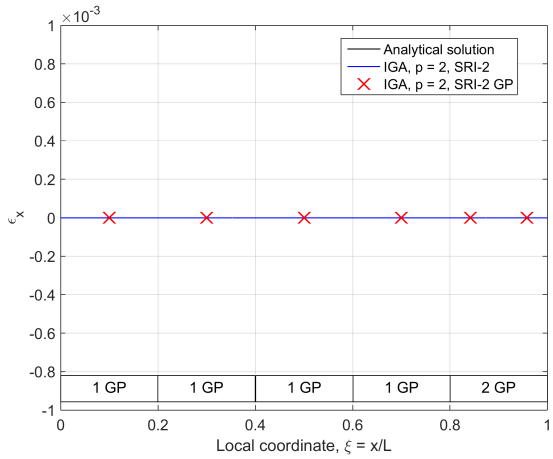

b)

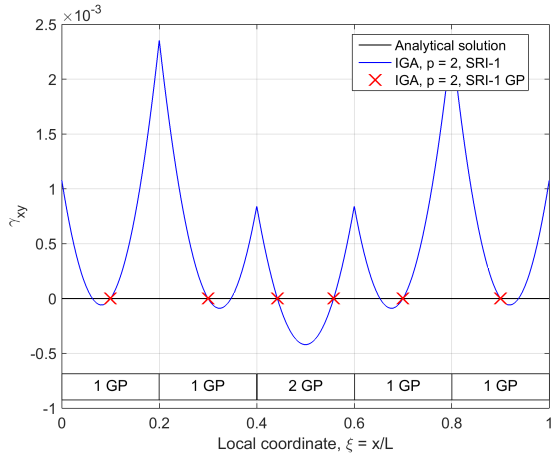

c)

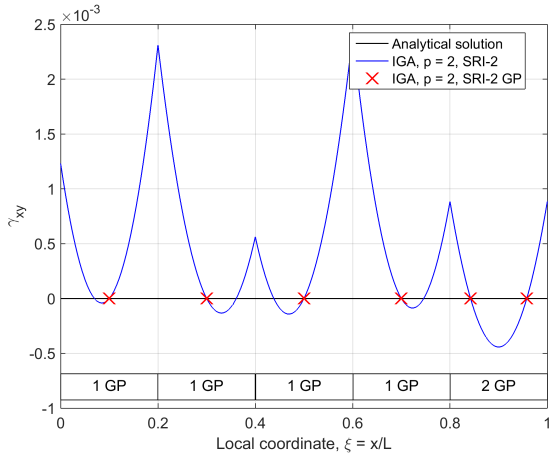

d)

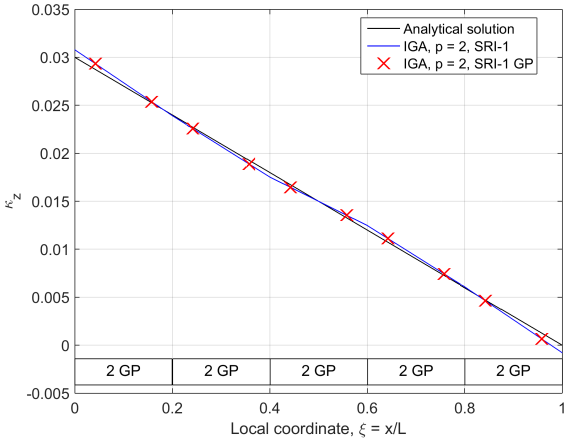

e)

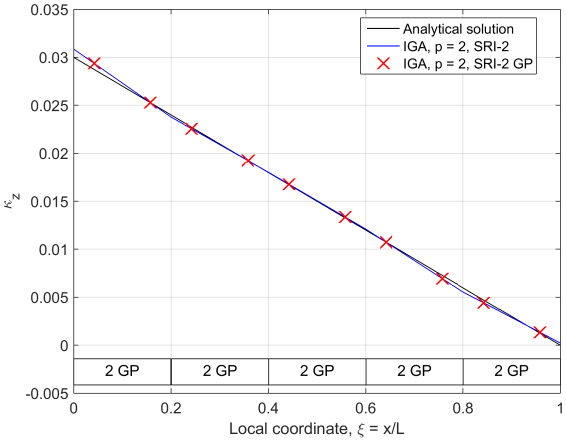

f)

Figure 6.3: Strain fields obtained with SRI-1 and SRI-2 for $p = 2$ and $\rho = 3$ compared with the analytical solutions: a) Axial strain (SRI-1), b) axial strain (SRI-2), c) transverse shear strain (SRI-1), d) transverse shear strain (SRI-2), e) bending strain (SRI-1), and f) bending strain (SRI-2).

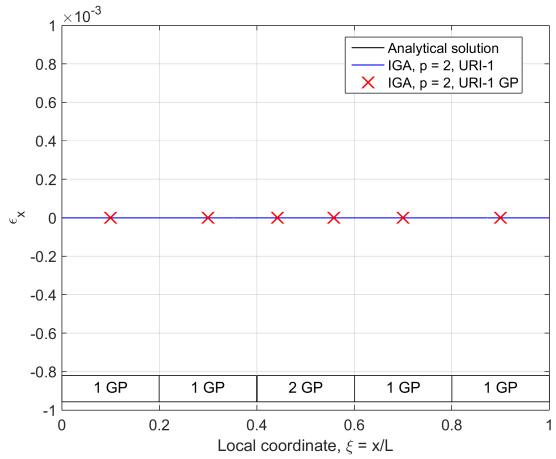

a)

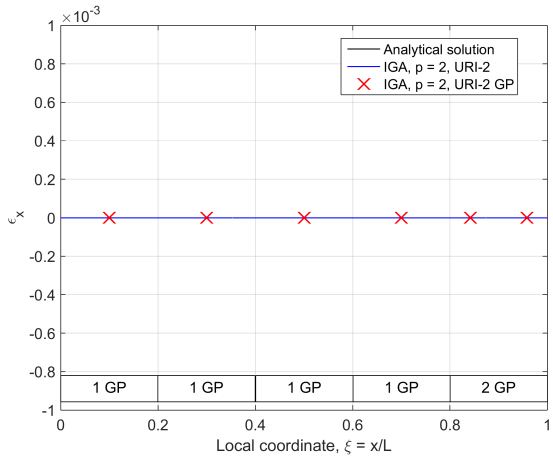

b)

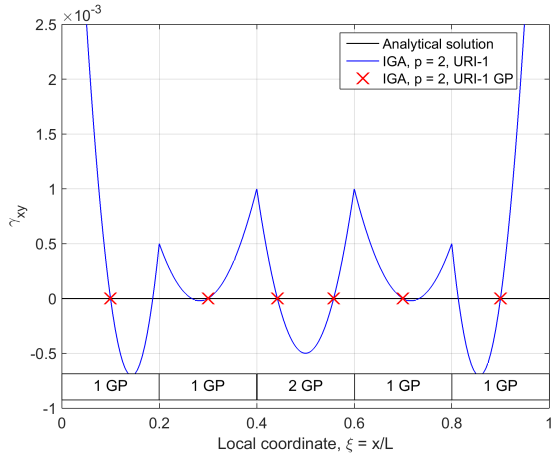

c)

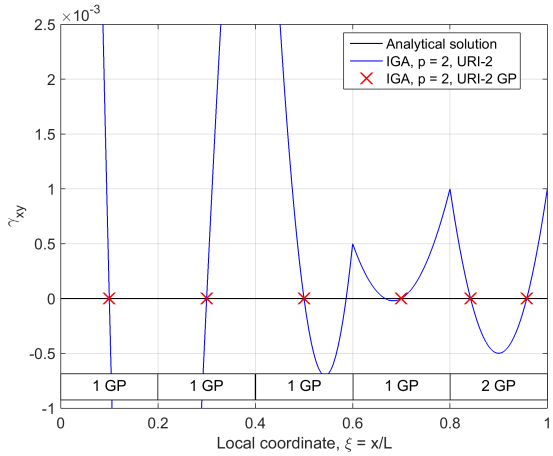

d)

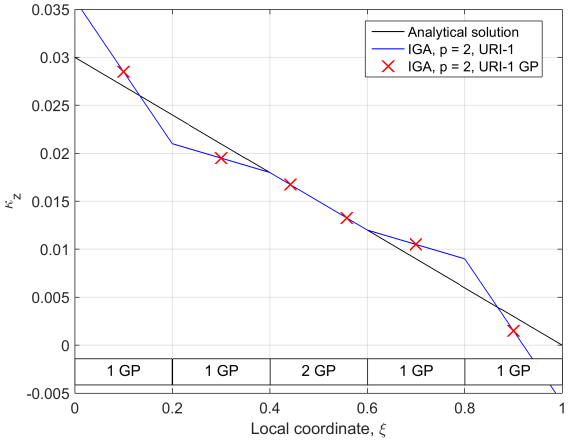

e)

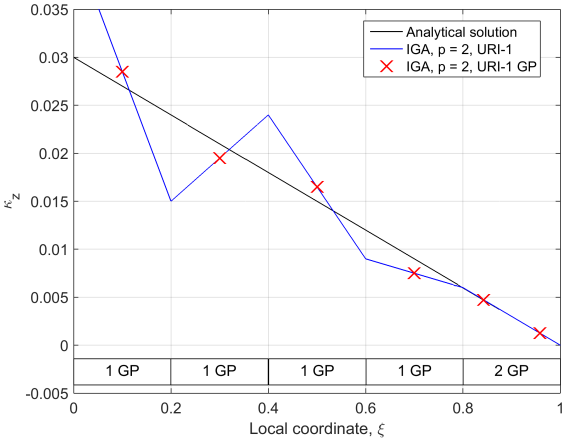

f)

Figure 6.4: Strain fields obtained with URI-1 and URI-2 for $p = 2$ and $\rho = 3$ compared with the analytical solutions: a) Axial strain (URI-1), b) axial strain (URI-2), c) transverse shear strain (URI-1), d) transverse shear strain (URI-2), e) bending strain (URI-1), and f) bending strain (URI-2).

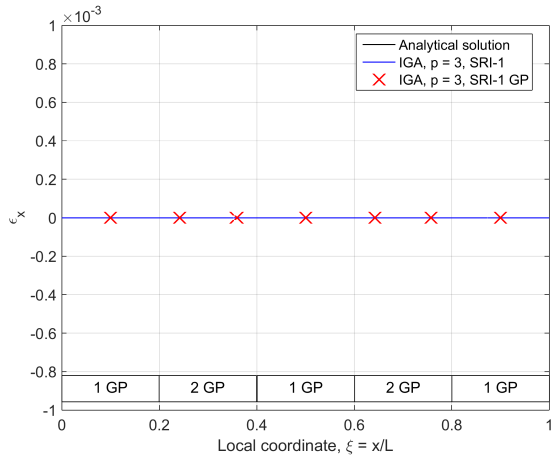

a)

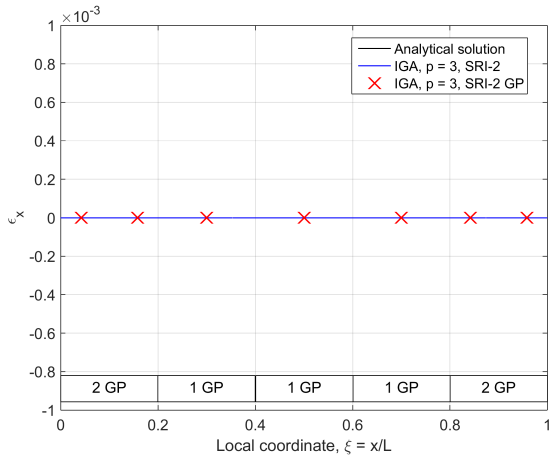

b)

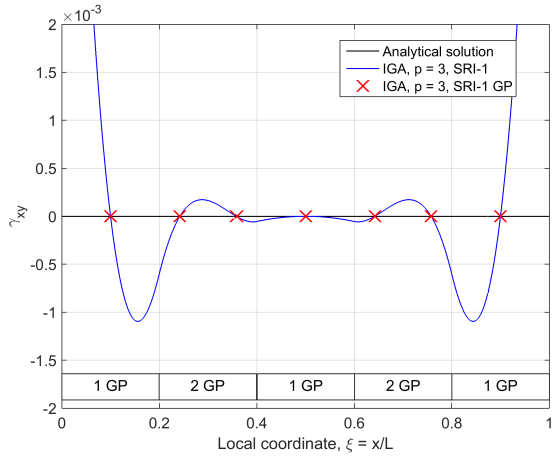

c)

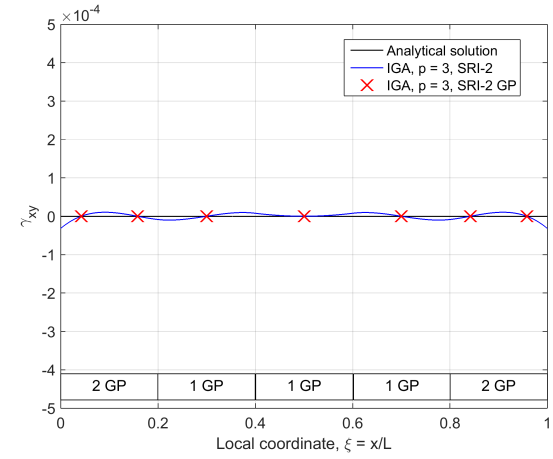

d)

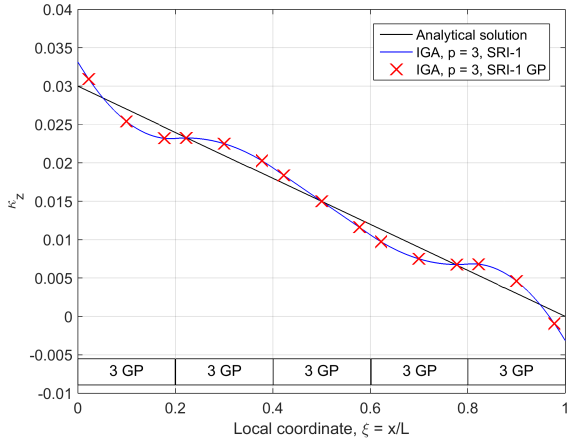

e)

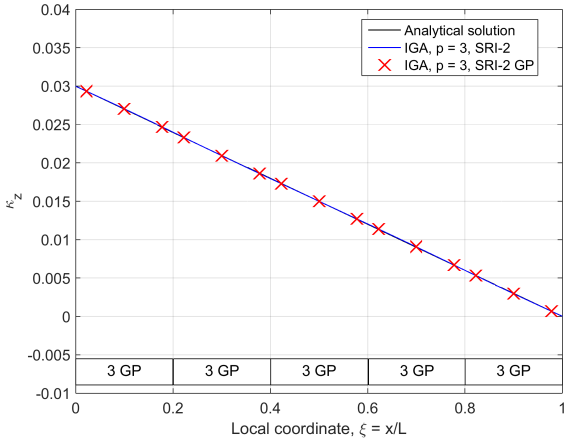

f)

Figure 6.5: Strain fields obtained with SRI-1 and SRI-2 for $p = 3$ and $\rho = 3$ compared with the analytical solutions: a) Axial strain (SRI-1), b) axial strain (SRI-2), c) transverse shear strain (SRI-1), d) transverse shear strain (SRI-2), e) bending strain (SRI-1), and f) bending strain (SRI-2).

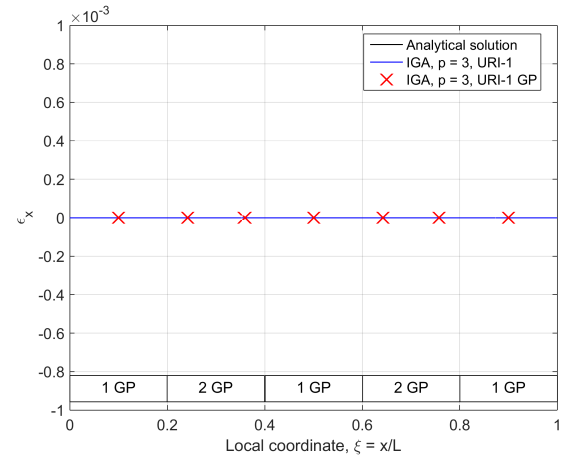

a)

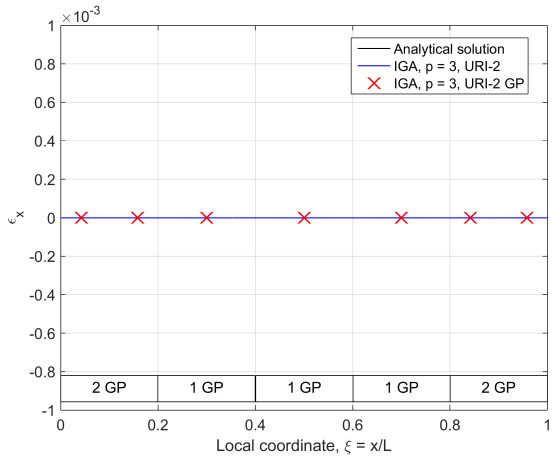

b)

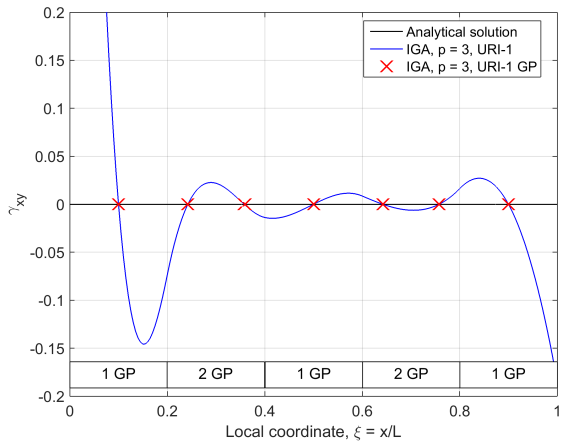

c)

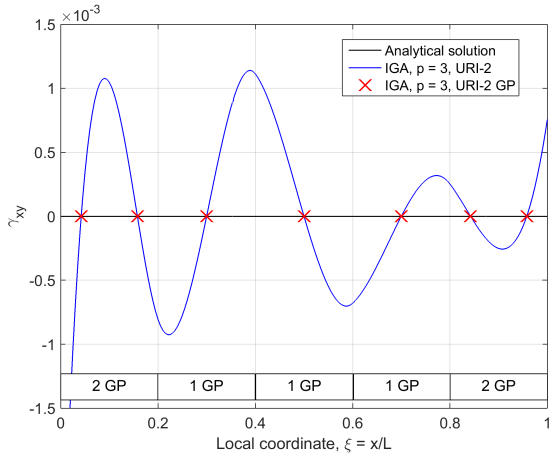

d)

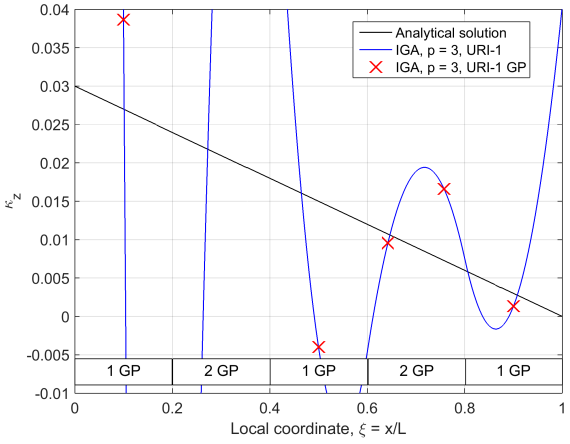

e)

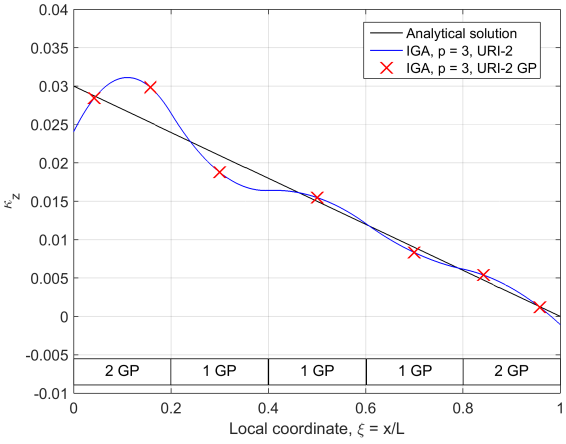

f)

Figure 6.6: Strain fields obtained with URI-1 and URI-2 for $p = 3$ and $\rho = 3$ compared with the analytical solutions: a) Axial strain (URI-1), b) axial strain (URI-2), c) transverse shear strain (URI-1), d) transverse shear strain (URI-2), e) bending strain (URI-1), and f) bending strain (URI-2).

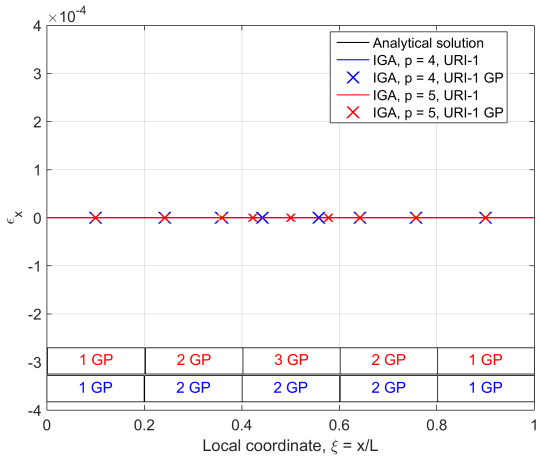

a)

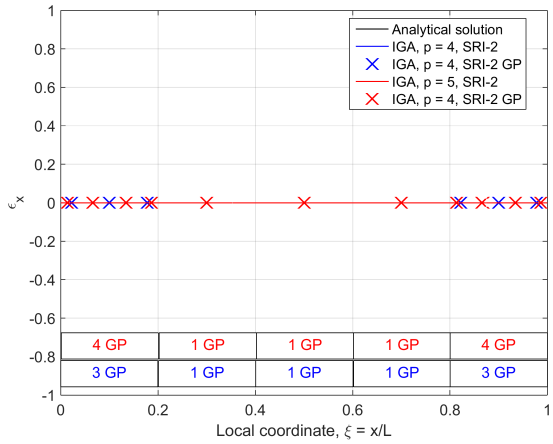

b)

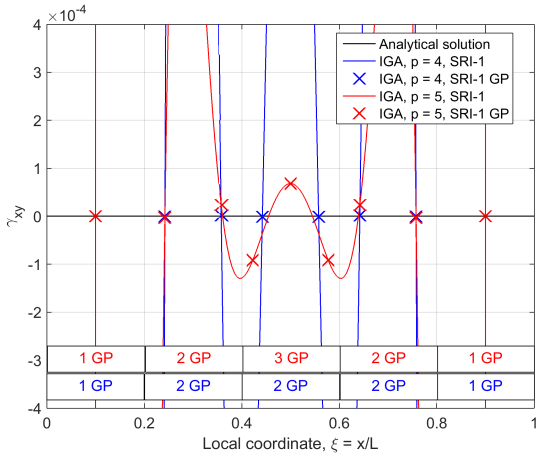

c)

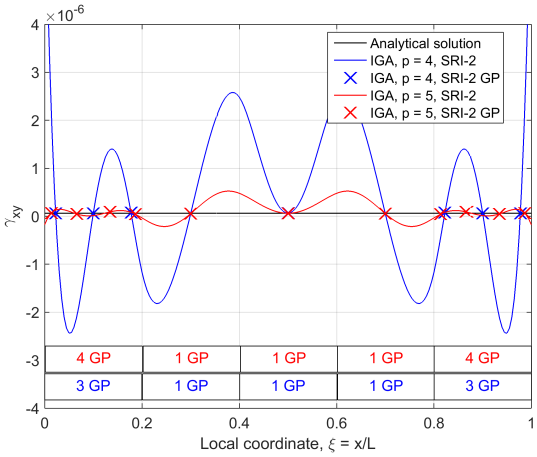

d)

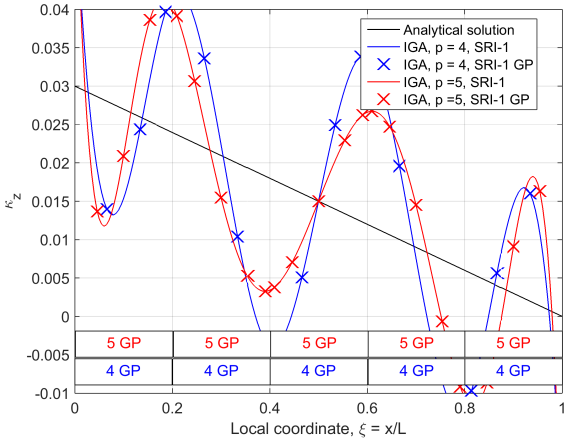

e)

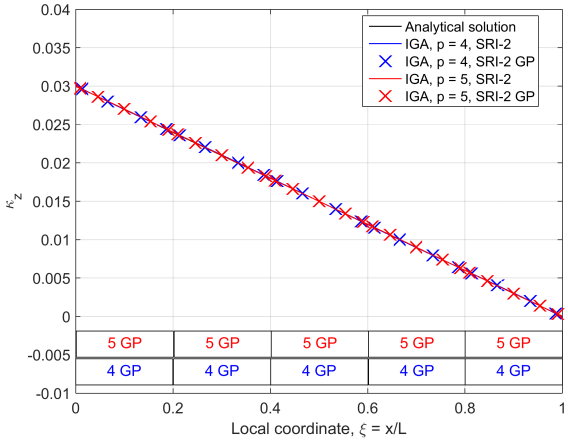

f)

Figure 6.7: Strain fields obtained with SRI-1 and SRI-2 for $p = 4,5$ and $\rho = 3$ compared with the analytical solutions: a) Axial strain (SRI-1), b) axial strain (SRI-2), c) transverse shear strain (SRI-1), d) transverse shear strain (SRI-2), e) bending strain (SRI-1), and f) bending strain (SRI-2).

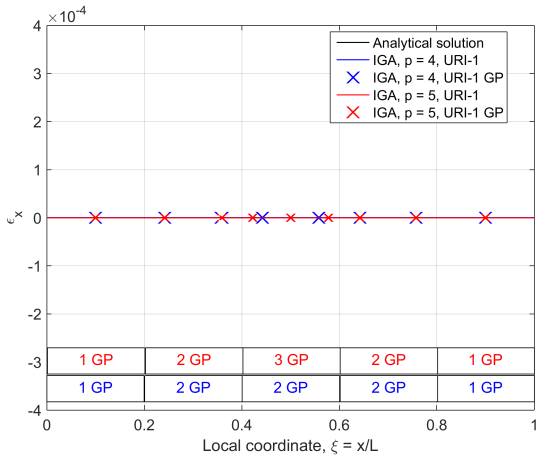

a)

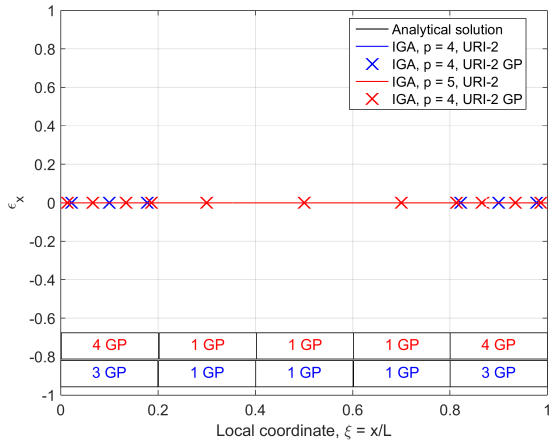

b)

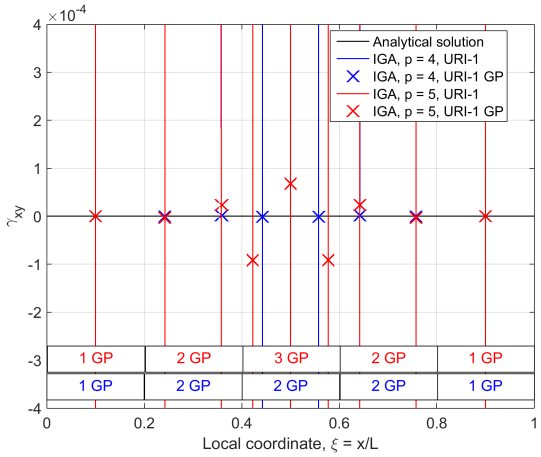

c)

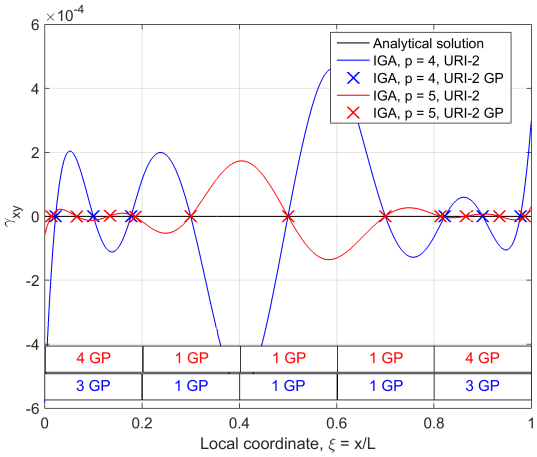

d)

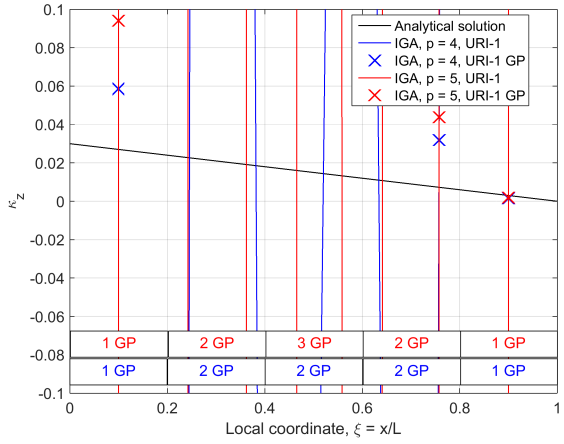

e)

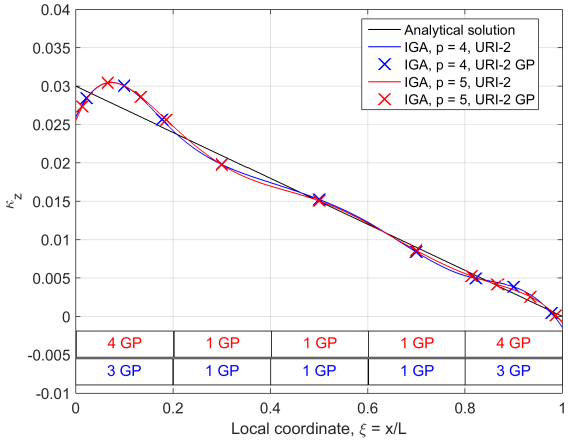

f)

Figure 6.8: Strain fields obtained with URI-1 and URI-2 for $p = 4,5$ and $\rho = 3$ compared with the analytical solutions: a) Axial strain (URI-1), b) axial strain (URI-2), c) transverse shear strain (URI-1), d) transverse shear strain (URI-2), e) bending strain (URI-1), and f) bending strain (URI-2).

Furthermore, a convergence study is carried out to see how the various quadrature rules affect the accuracy. For error measure, the L^2 relative error norm of the displacement field, computed from Eq. 3.26, is used. Note that cubic elements with conventional reduced integration produce the exact solution. The convergence plots in Figure 6.9 reveal slower convergence with the new quadrature rules. Further, it is observed that quadratic elements with SRI and URI behave very similar as linear elements with reduced integration. The slow convergence and large absolute errors with URI-1 and URI-2 may be due to their inaccurate representation of the rotations. The strong form solution is also lost with the proposed integration rules.

Higher order elements with SRI-1 and URI-1 are omitted due to divergent solutions.

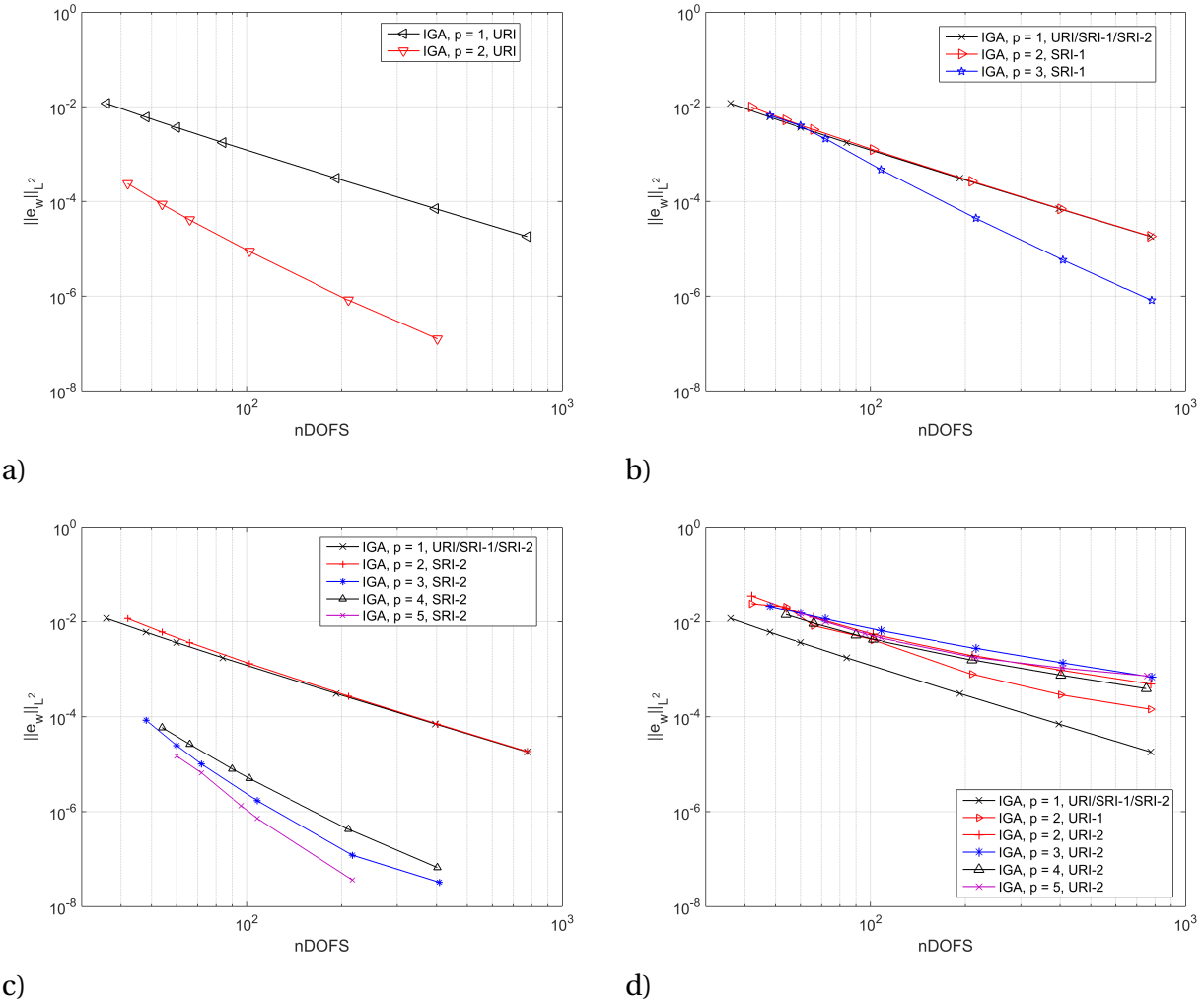

a) b)

c) d)

Figure 6.9: L^2-norm of relative error on displacements for the various quadrature rules and $\rho = 3$: a) Conventional reduced integration (URI), b) SRI-1 c) SRI-2, d) URI-1 ($p = 2$) and URI-2

Finally, in Figure 6.10 the thickness dependency is studied. For this analysis, the L^2-norm of the relative error in displacements is computed with respect to the slenderness parameter, ρ which is varied from 1 to 5 with a fixed number of 5 elements. Conventional reduced integrated elements (URI) are included for comparison. It appears that all elements (URI included) are locking-free. Cubic elements with URI, whose solution space is a superset of the analytical solution, serve here as a measure of the condition of the stiffness matrix. As the slenderness increases and the equation system becomes more badly scaled, the computational precision decreases.

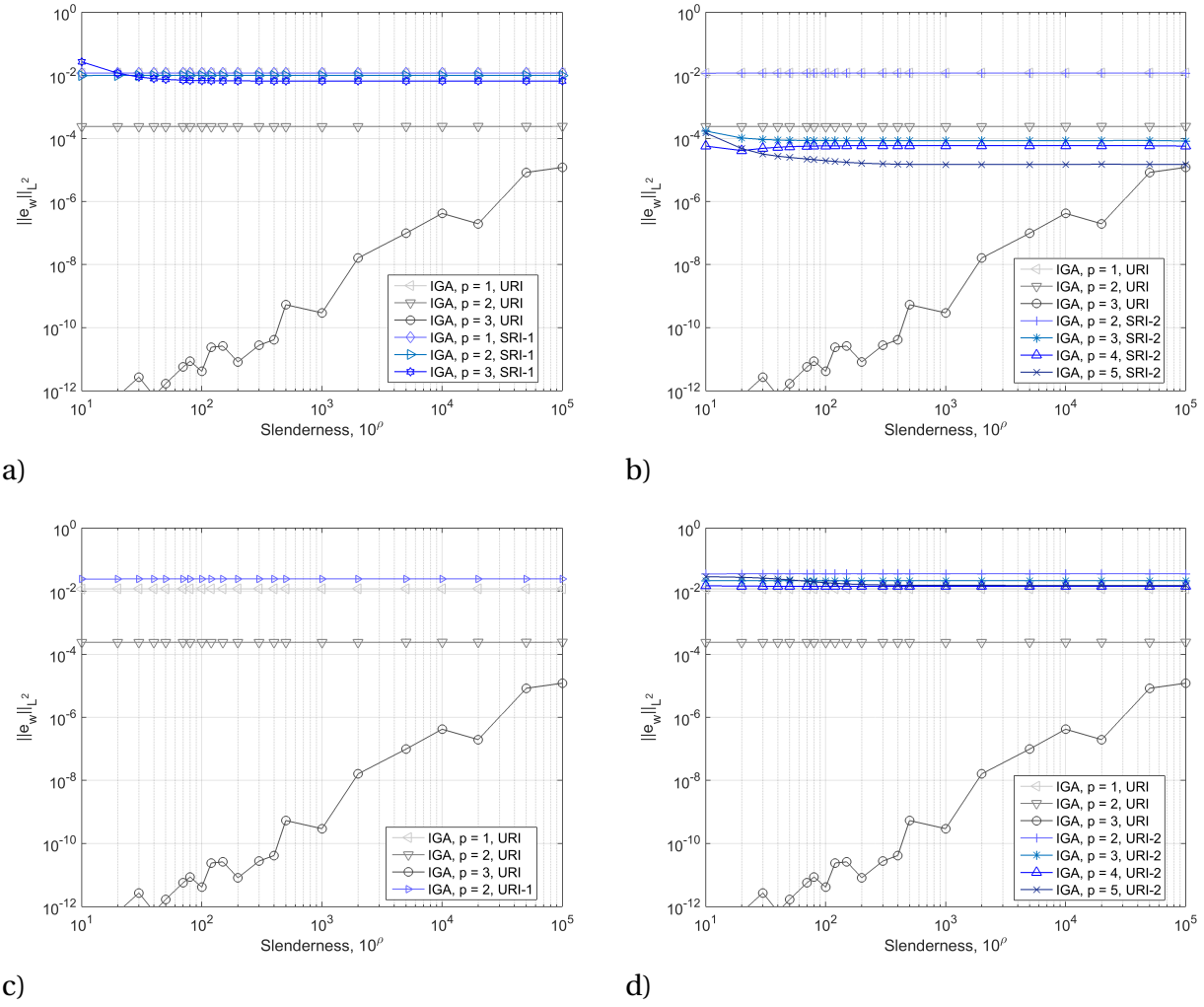

a) b)

c) d)

Figure 6.10: L^2-norm of relative error on displacements with respect to slenderness for the various quadrature rules and $\rho = 3$: a) SRI-1, b) SRI-2, c) URI-1, d) URI-2.

6.3.2 Clamped beam subjected to linearly distributed transverse load

As the previous example, with constant membrane strain distributions, already was locking-free for the conventional quadrature rule, it did not serve as a very good test for transverse shear locking. Therefore, a straight beam with a higher order solution space has been analyzed.

Figure 6.11 shows the geometry and material data for the clamped beam with linearly increasing pressure from Section 3.5. Again, the thickness is expressed in terms of the slenderness parameter, ρ, and the load is scaled with the bending stiffness.

Governed from the unit-load method, the vertical displacements and rotations are given respectively as:

$$w = w(x) = \frac{q}{EI}\Big[\frac{x^5}{120L} - \frac{Lx^3}{12} + \frac{5L^2x^2}{48}\Big] + \frac{q\kappa_y h^2}{12EIL}\Big[L^2x - \frac{x^3}{3}\Big] \tag{6.11}$$

$$\theta = \theta(x) = \frac{q}{EI}\Big[-\frac{x^4}{24L} + \frac{Lx^3}{4} - \frac{5L^2x}{24}\Big] \tag{6.12}$$

from which the strains may be computed.

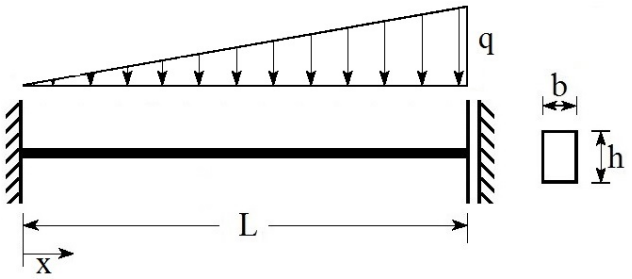

Young's modulus:	$E = 1000$
Poisson's ratio:	$\nu = 0$
Length:	$L = 10$
Width:	$b = 1$
Thickness:	$h = L/10^{\rho}$
Load:	$q = h^3$

Figure 6.11: Geometry and material data for the clamped beam subjected to linearly increasing pressure.

Comparison of transverse shear and bending strains obtained with Lagrange and NURBS-elements with conventional reduced integration is shown in Figure 6.12 for $\rho = 1$ and $\rho = 3$. While Lagrangian elements sample the transverse shear strains correctly, they are slightly wrong with IGA, causing increasing errors in the curvatures.

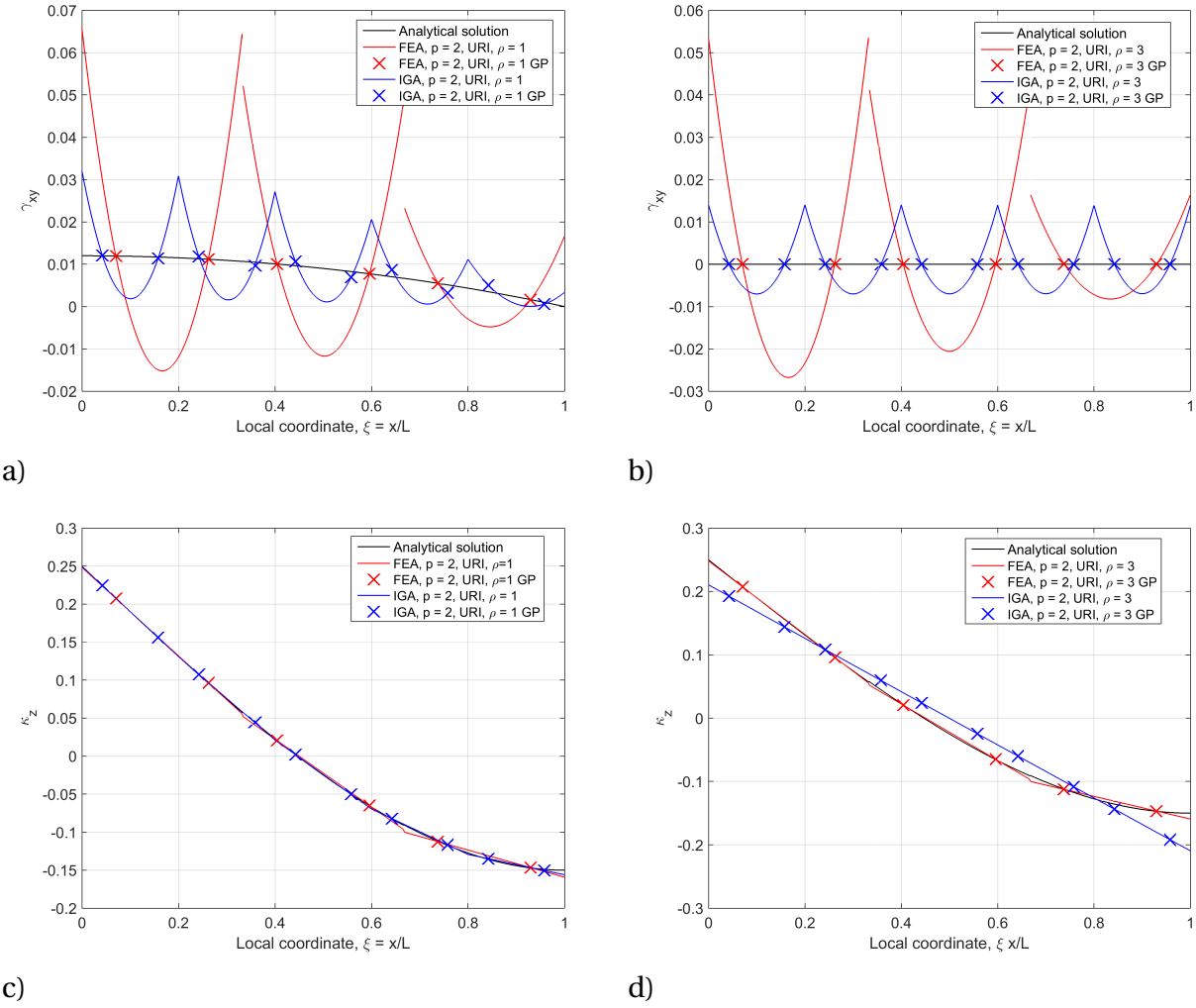

Figure 6.12: Comparison of Lagrange (FEA) and NURBS (IGA) based solutions applying conventional reduced integration (URI) for $p = 2$: a) Transverse shear strain, $\rho = 1$, b) transverse shear strain, $\rho = 3$, c) bending strain, $\rho = 1$, and d) bending strain, $\rho = 3$.

The transverse shear and curvature fields are now analyzed with the different integration rules for a fixed slenderness of $\rho = 3$. The axial strains become exactly zero for all analyses, similar as in Section 6.3.1, and are therefore not shown.

The quadratic elements are depicted in Figures 6.13 and 6.14 for the selective and uniform integration rules, respectively. URI-1 and URI-2 do not represent the bending strains accurately. Otherwise the strains are represented with good accuracy. For $p = 2$, adding Gauss points near the center of the patch leads to less amplitudes in strains and a better conditioned system, and consequently better accuracy.

Cubic elements are shown in Figure 6.15, and quartic and quintic in Figure 6.16. Only SRI-2

and URI-2 are considered, as the oscillations in strains leads to unstable systems for higher order elements with SRI-1/URI-1. As for quadratic elements, the strains are represented with good accuracy, except for URI-2, which leaves the rotational part incorrectly.

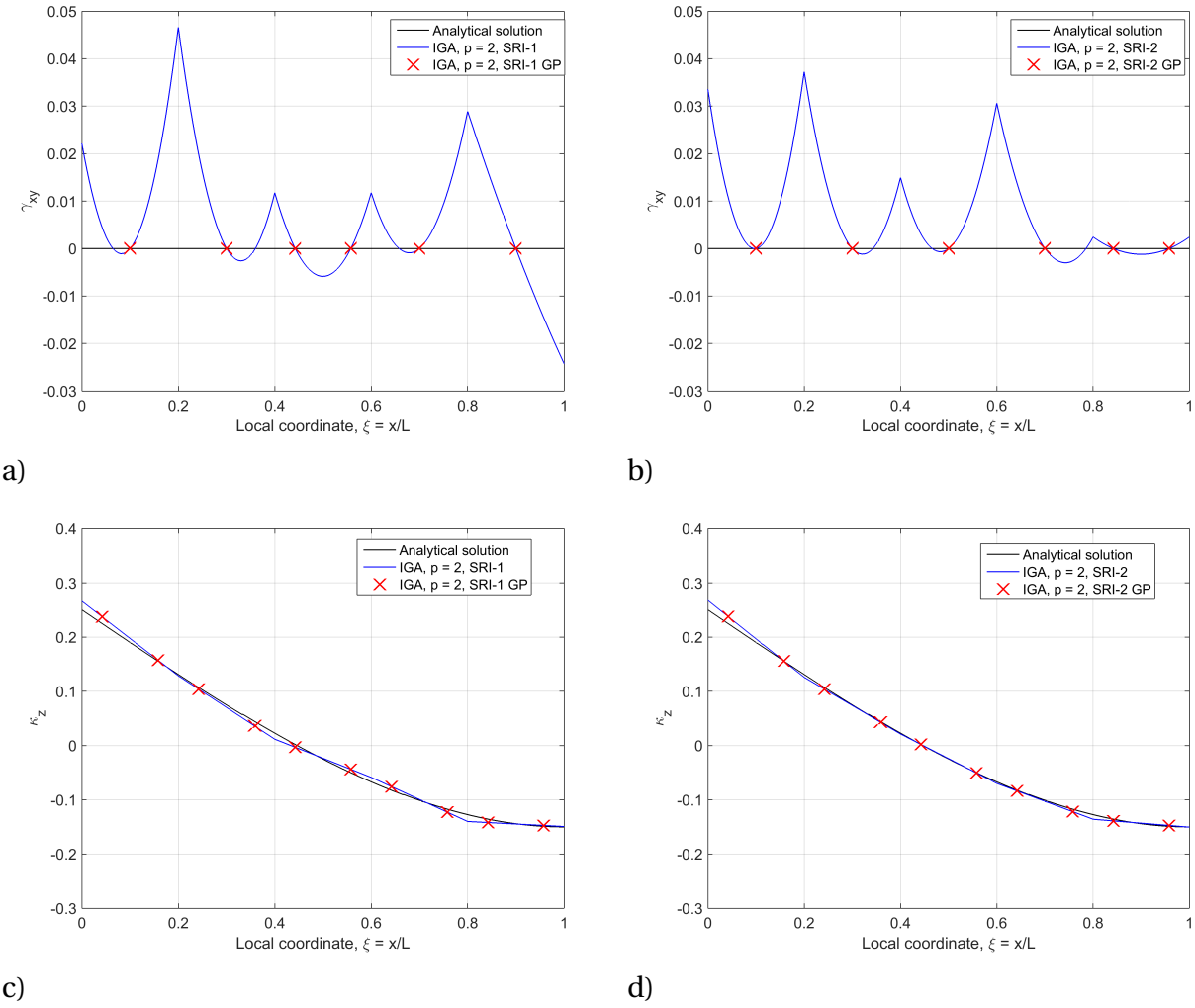

Figure 6.13: Strain fields obtained with SRI-1 and SRI-2 for $p = 2$ and $\rho = 3$ compared with the analytical solutions: a) Transverse shear strain (SRI-1), b) transverse shear strain (SRI-2), c) bending strain (SRI-1), and d) bending strain (SRI-2).

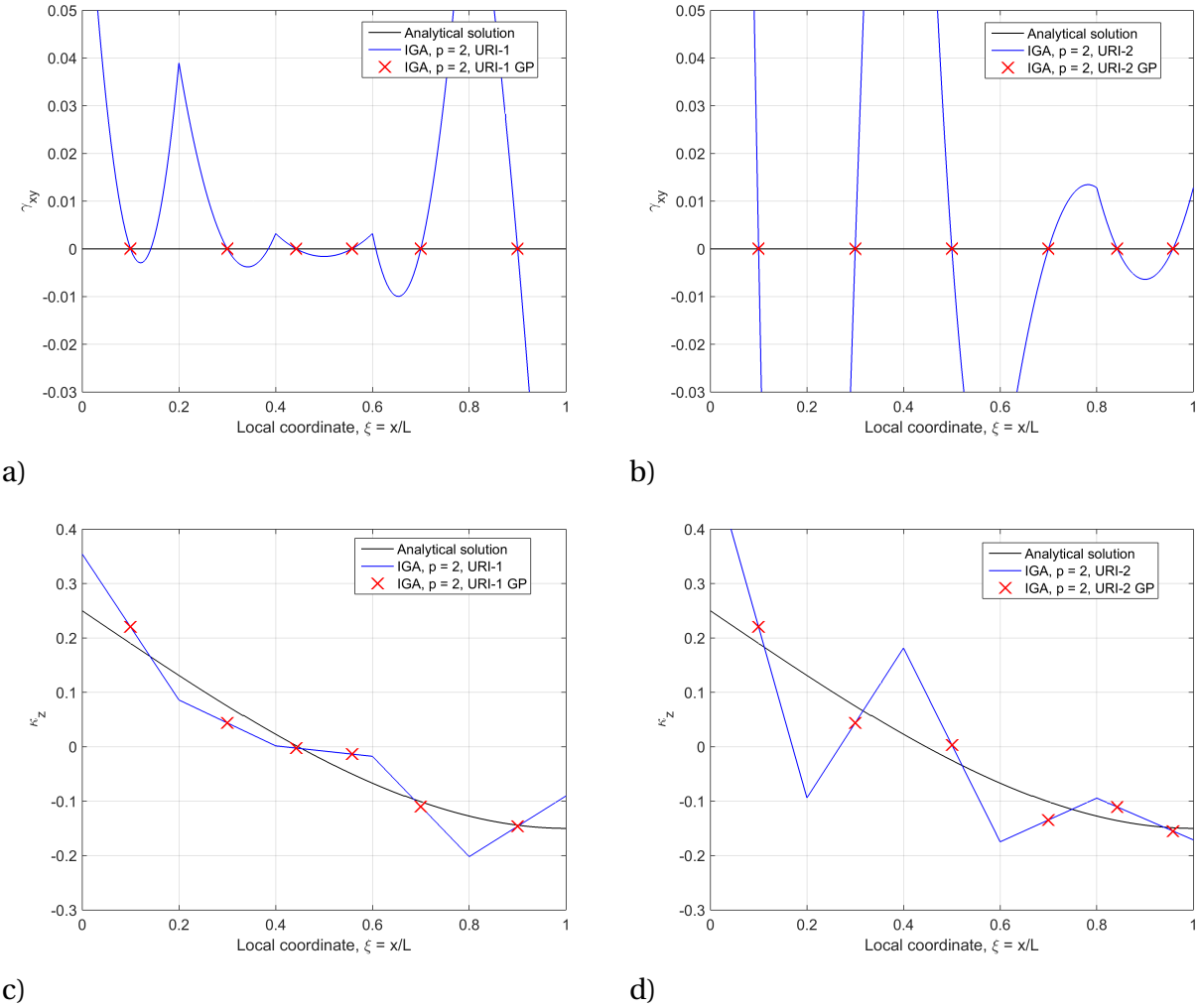

a) b)

c) d)

Figure 6.14: Strain fields obtained with URI-1 and URI-2 for $p = 2$ and $\rho = 3$ compared with the analytical solutions: a) Transverse shear strain (URI-1), b) transverse shear strain (URI-2), c) bending strain (URI-1), and d) bending strain (URI-2).

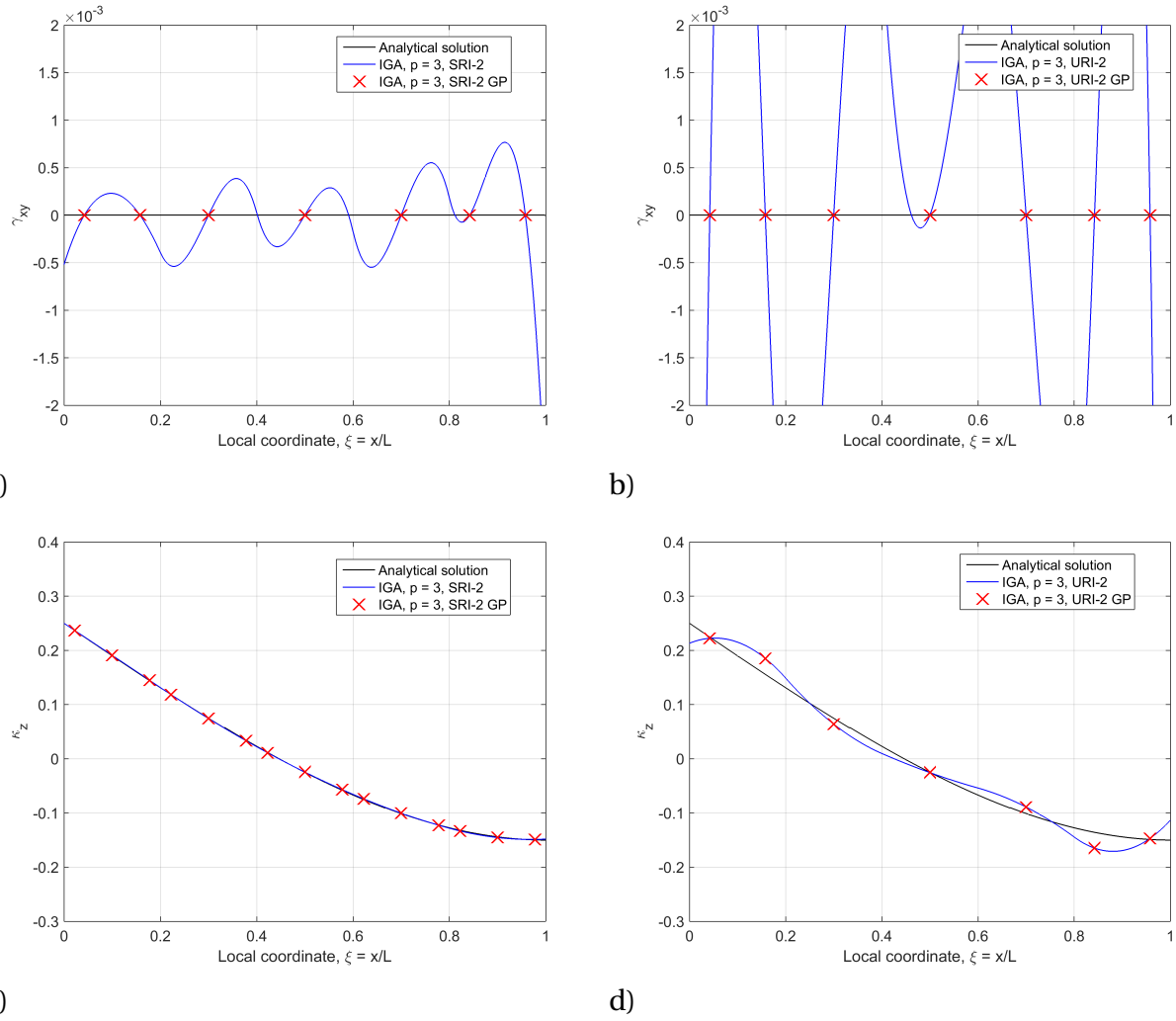

Figure 6.15: Strain fields obtained with SRI-2 and URI-2 for $p = 3$ and $\rho = 3$ compared with the analytical solutions: a) Transverse shear strain (SRI-2), b) transverse shear strain (URI-2), c) bending strain (SRI-2), and d) bending strain (URI-2).

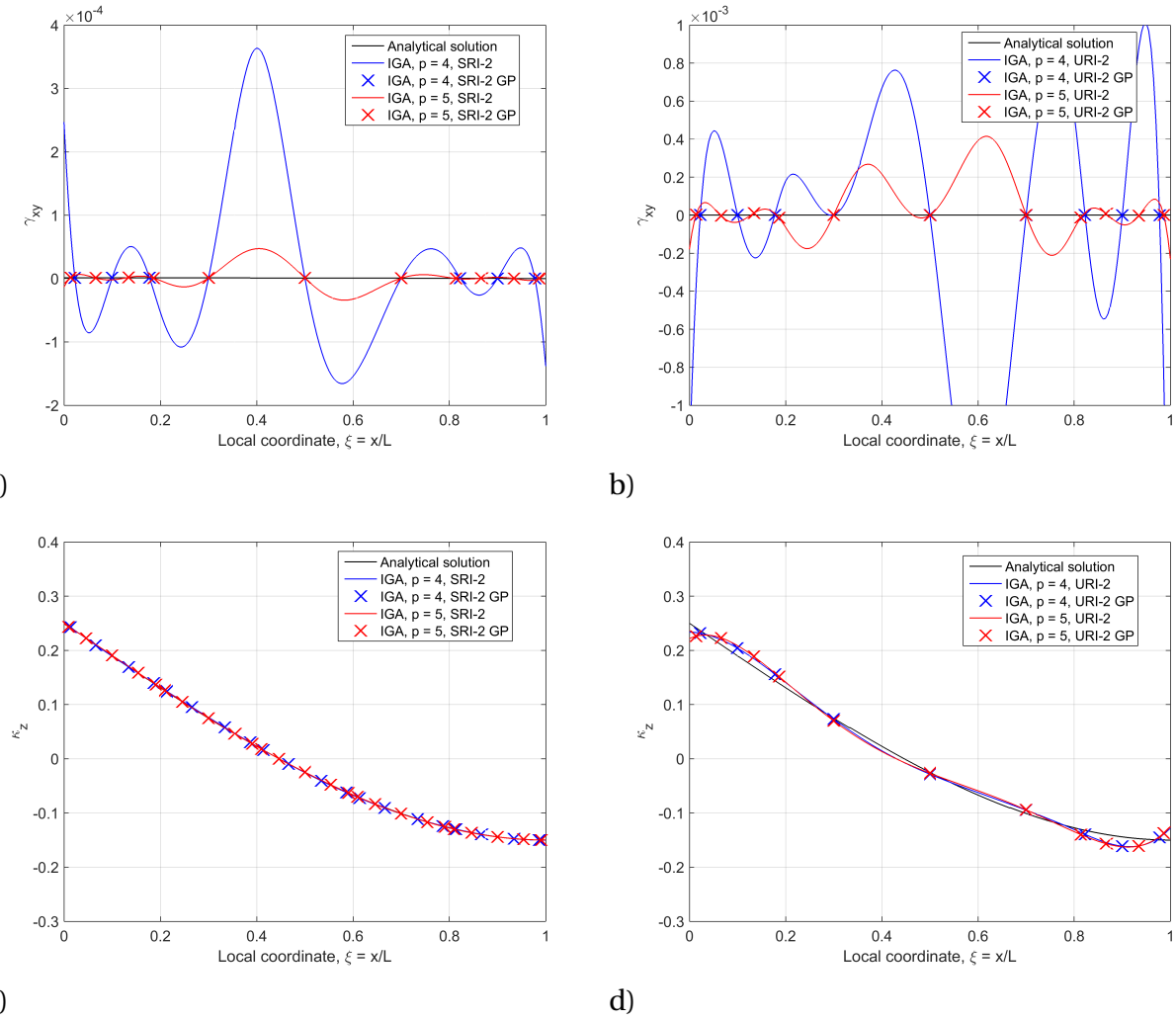

Figure 6.16: Strain fields obtained with SRI-2 and URI-2 for $p = 4,5$ and $\rho = 3$ compared with the analytical solutions: a) Transverse shear strain (SRI-2), b) transverse shear strain (URI-2), c) bending strain (SRI-2), and d) bending strain (URI-2).

Convergence of the L^2-norm of the relative error in transverse displacements is now studied with a slenderness of $\rho = 3$, reported in Figure 6.17. Similar behavior as for the tip-loaded cantilever beam is seen: slower convergence, loss of strong form ($5th$ order for this beam) and poor performance of higher order elements with URI-2.

Thickness dependency is studied with a uniform mesh of 5 elements. Figure 6.18 reveals that unlike the elements with conventional reduced integration, SRI and URI show no thickness dependency and are thus free of transverse shear locking.

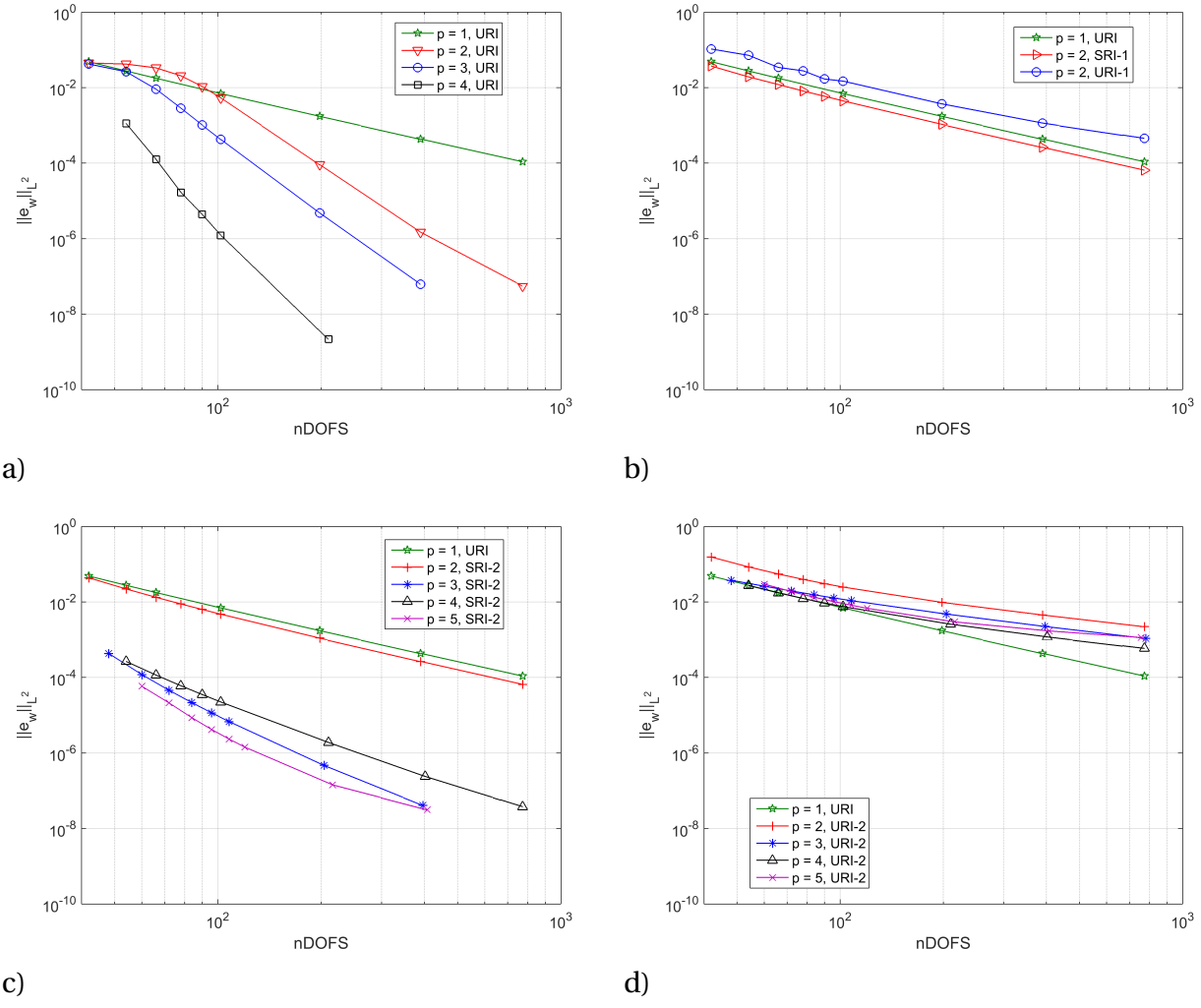

Figure 6.17: L^2-norm of relative error in displacements for the different quadrature rules, $\rho = 3$: a) Conventional reduced integration (URI), b) SRI-1 and URI-1 for $p = 2$, c) SRI-2, and d) URI-2.

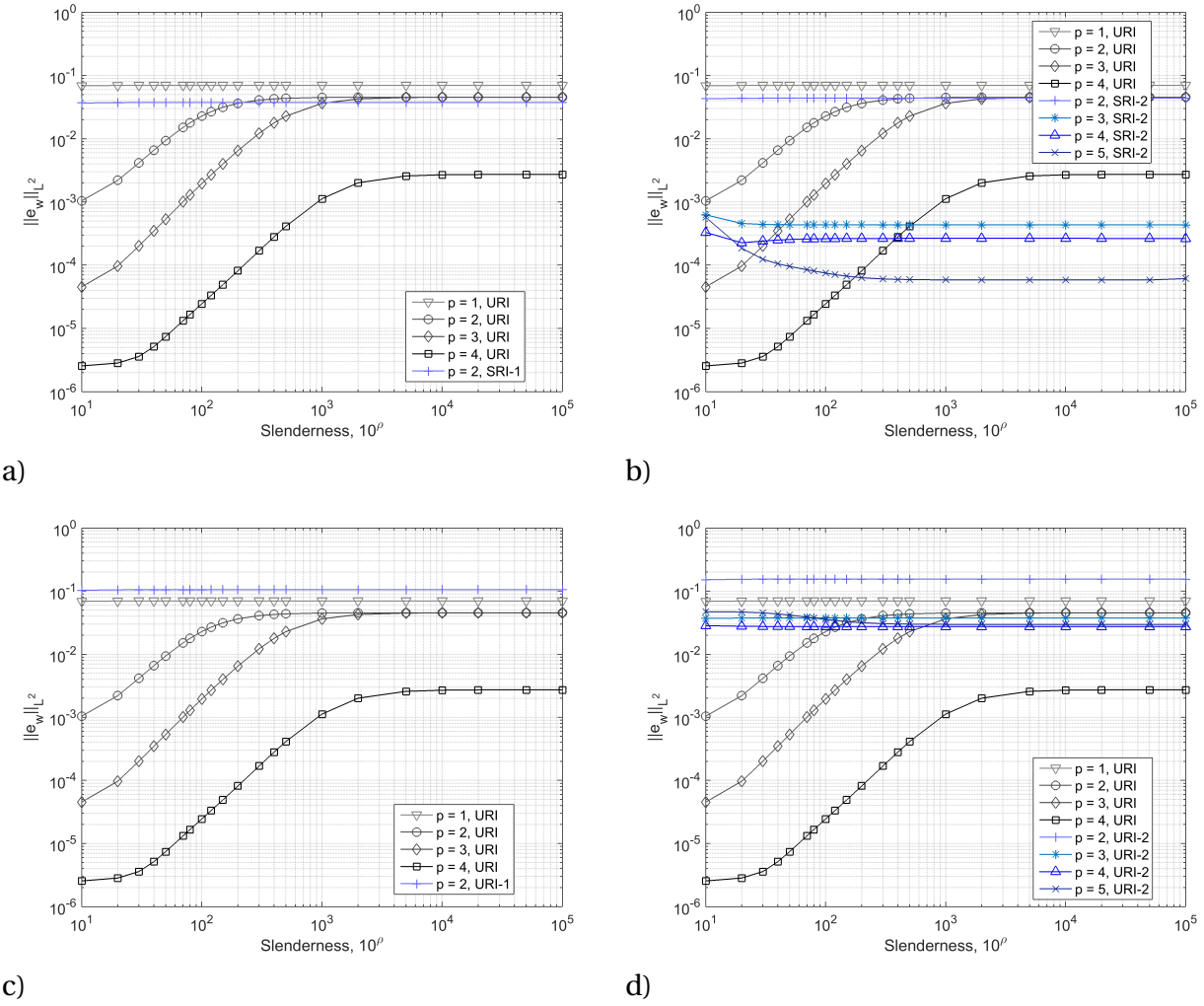

a) b)

c) d)

Figure 6.18: L^2-norm of relative error in displacements with respect to ρ: a) SRI-1, b) SRI-2, c) URI-1, and d) URI-2.

6.3.3 Curved beam subjected to sinusoidally distributed moment

Figure 6.19 shows geometry and material properties for a planar 90° circular arc subjected to a sinusoidally distributed moment $m(s) = h^3 \sin(\pi s/2L)$. This load imposes a state of pure bending with no membrane and transverse shear energy and is therefore a severe test for membrane and transverse shear locking. Also note that by choosing a sinusoidally distributed moment, the closed form solution is obviously not contained in the approximation space. The load is proportional with the bending stiffness such that the displacements and rotations are independent of the thickness.

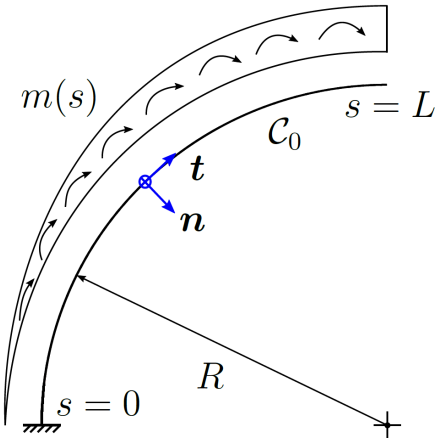

Young's modulus:	$E = 1000$
Poisson's ratio:	$\nu = 0$
Radius:	$R = 1$
Width:	$b = 0.2$
Thickness:	$h = R/10^{\rho}$

Figure 6.19: Geometry and material data for a curved beam under sinusoidally moment loading.

Denoting $u_t(s)$ and $u_n(s)$ displacements parallel to the local Cartesian bases, $\boldsymbol{i}_1^0$ and $\boldsymbol{i}_3^0$, respectively, the analytical solution may be obtained by solving the strong form governed by Eqs. 4.3 and 4.4, and is given by [1, 9]:

$$u_n(s) = \frac{6R^2}{Eb} s \sin\left(\frac{s}{R}\right) \tag{6.13}$$

$$u_t(s) = \frac{6R^3}{Eb}\left[\sin\left(\frac{s}{R}\right) - \frac{s}{R}\cos\left(\frac{s}{R}\right)\right] \tag{6.14}$$

$$\theta(s) = \frac{12R^2}{Eb}\sin\left(\frac{s}{R}\right) \tag{6.15}$$

The three nonzero strain fields, ε_1, γ_{12}, and κ_3, for the different integration models are studied for the slenderness ratios $\rho = 1$ and $\rho = 3$, using a mesh of $n_e = 5$ equally sized knot-span elements with the maximum continuity available. Since the strains are now computed in the

current configuration and consequently not show the linear solution, the analytical solution is approximated with a reference solution obtained with 32 quintic isogeometric elements each integrated with p Gauss points ($n_{GP} = p$). The sinusoidally varying moment is taken into consideration with a consistent load vector, numerically integrated with $n_{GP} = 5p$.

Firstly, the beam has been analyzed and compared with quadratic C^0-continuous Lagrangian elements applying the conventional uniform reduced integration rule (URI). The strain fields for ε_1, γ_{12} and κ_3, reported in Fig. 6.20, confirms that the strains sampled at the Gauss points for the Lagrangian elements coincide with the reference solution for both $\rho = 1$ and $\rho = 3$ for all strain fields, and thus appear to be locking-free. However, for the NURBS elements of equal order and with the same quadrature rules, i.e. URI with $n_{GP} = p$ within each element, it is observed that all of the three strain fields when sampled at the Gauss points deviate from the reference solution. Further, the deviation increase with increased slenderness, and thus, the elements reveal both membrane and transverse shear locking.

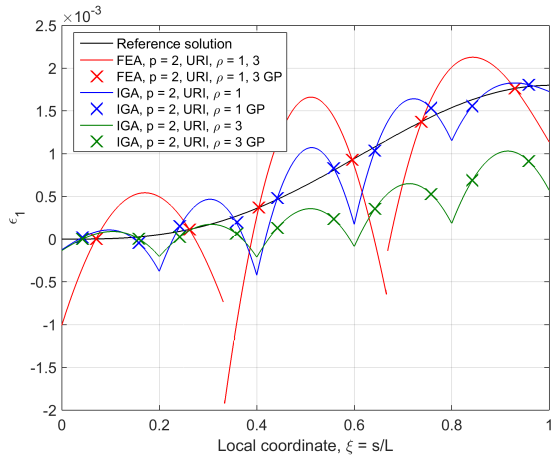

a)

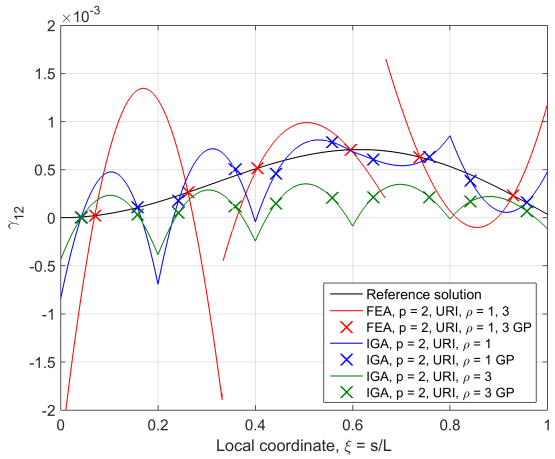

b)

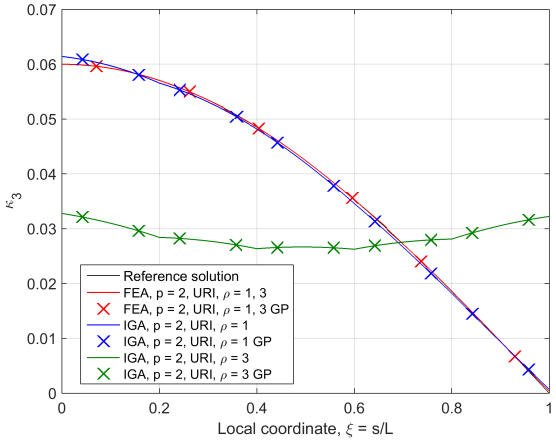

c)

Figure 6.20: Comparison of Lagrange (FEA) and NURBS (IGA) based solutions applying conventional URI for $p = 2$: a) Axial strain, b) transverse shear strain, and c) bending strain.

With a fixed slenderness of $\rho = 3$, the beam is now analyzed with the proposed integration rules. The strain fields obtained with quadratic and cubic NURBS elements with the two SRI rules are depicted in Figures 6.21 and 6.22, respectively. Now all three strain fields coincide with the reference solution when sampled at the Gauss points for both SRI-1 and SRI-2, and consequently yields a precise approximation of the corresponding curvature field. These observation are also valid for higher order elements (see Fig. 6.23). However, for SRI-1, where the additional Gauss points are not located at the boundary elements, the translational strains show oscillations when the polynomial order is increased.

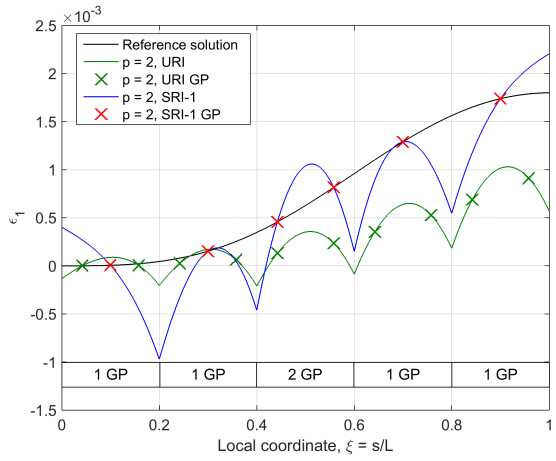

a)

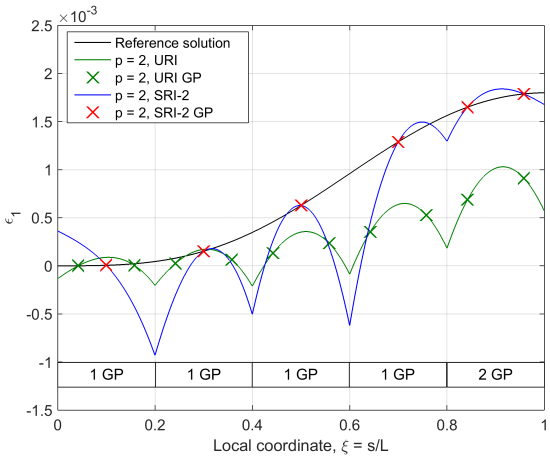

b)

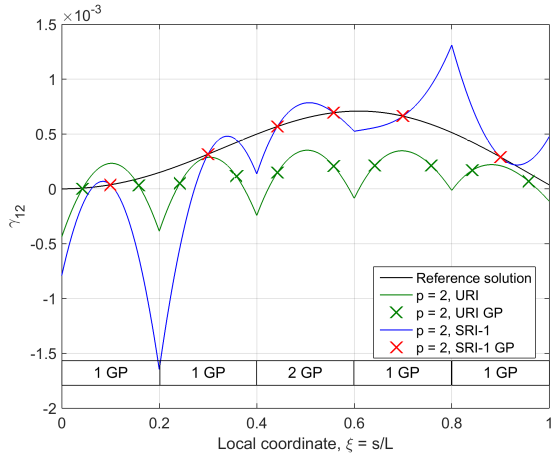

c)

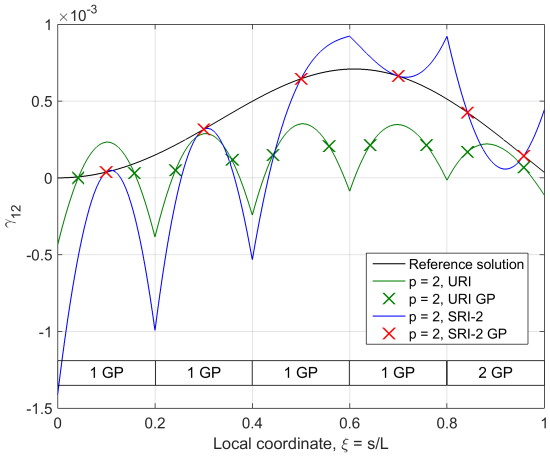

d)

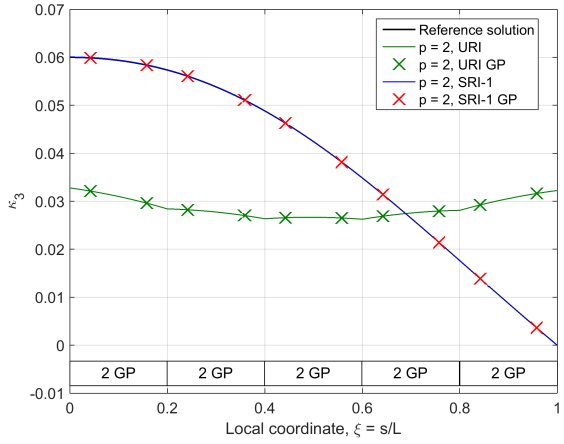

e)

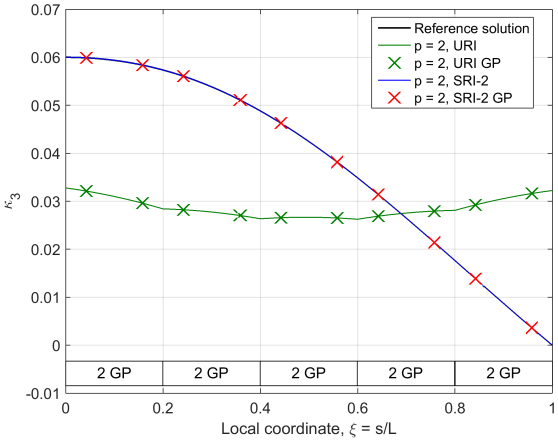

f)

Figure 6.21: Comparison of the solutions obtained with the various SRI rules applied to the translational part only, for $p = 2$: a) Axial strain (SRI-1), b) axial strain (SRI-2), c) transverse shear strain (SRI-1), d) transverse shear strain (SRI-2), e) bending strain (SRI-1), and f) bending strain (SRI-2).

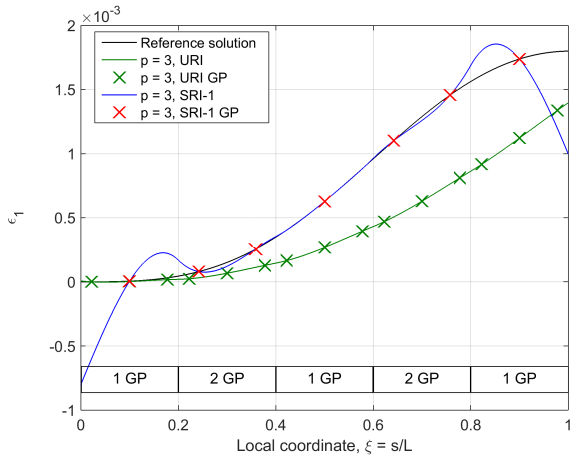

a)

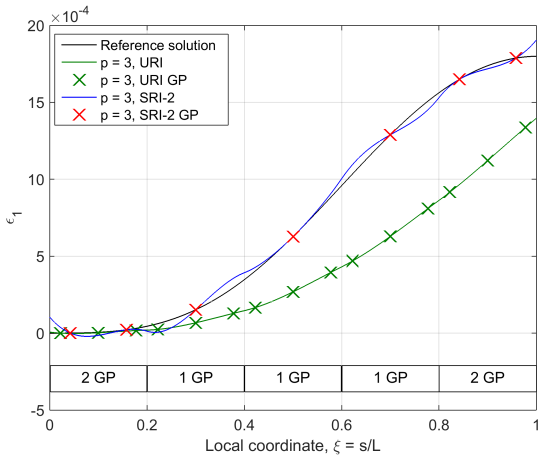

b)

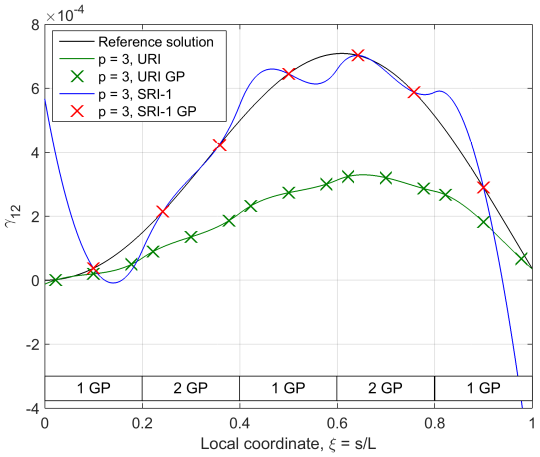

c)

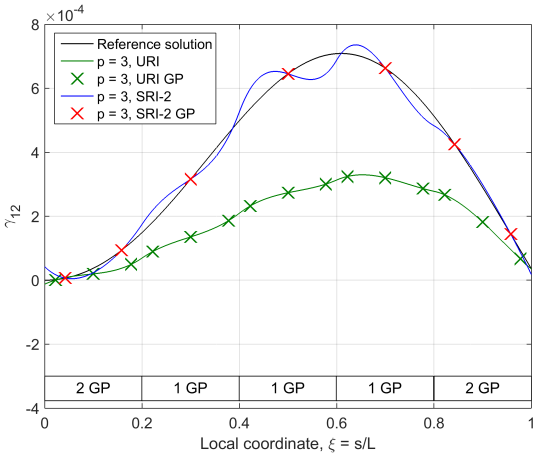

d)

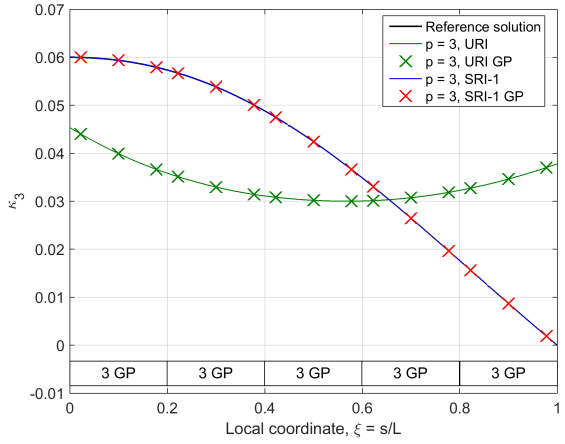

e)

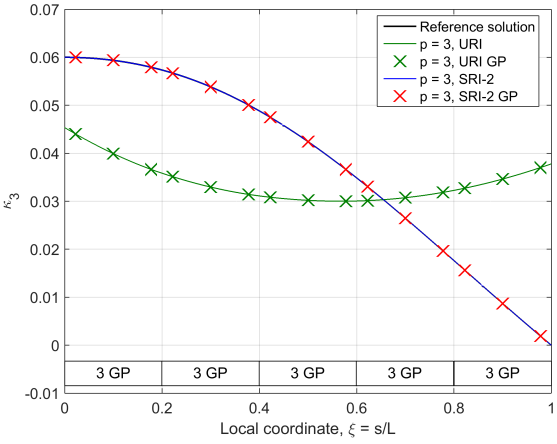

f)

Figure 6.22: Comparison of the solutions obtained with the various SRI rules applied to the translational part only, for $p = 3$: a) Axial strain (SRI-1), b) axial strain (SRI-2), c) transverse shear strain (SRI-1), d) transverse shear strain (SRI-2), e) bending strain (SRI-1), and f) bending strain (SRI-2).

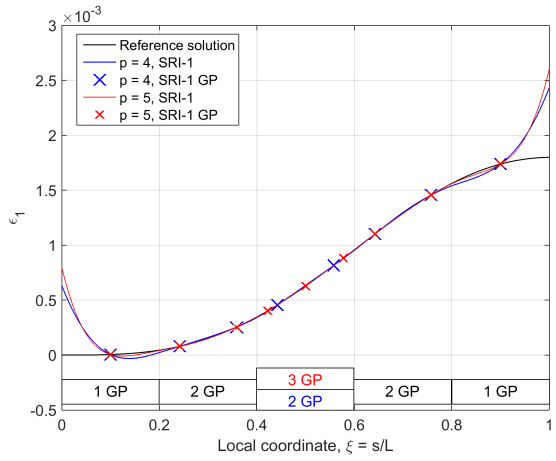

a)

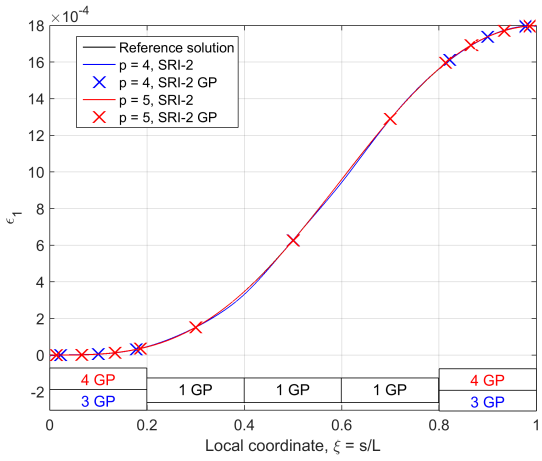

b)

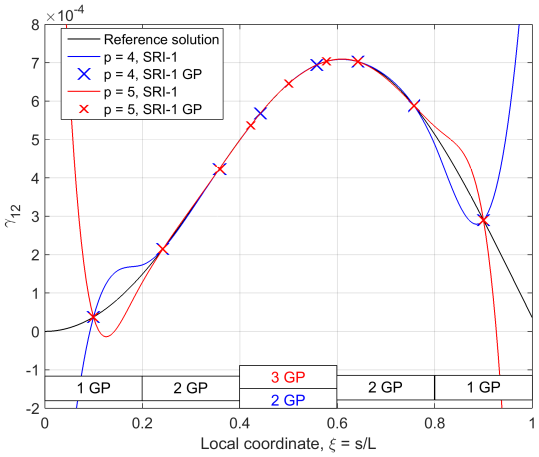

c)

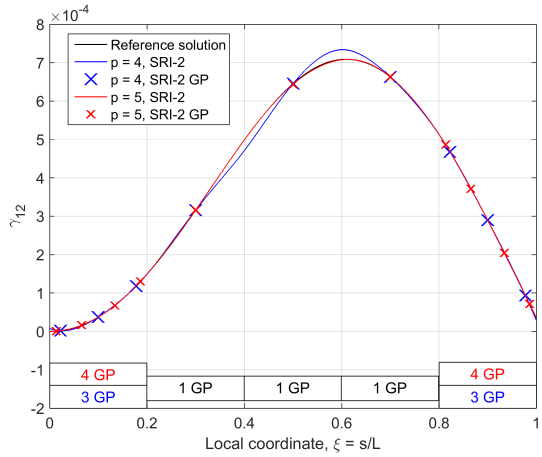

d)

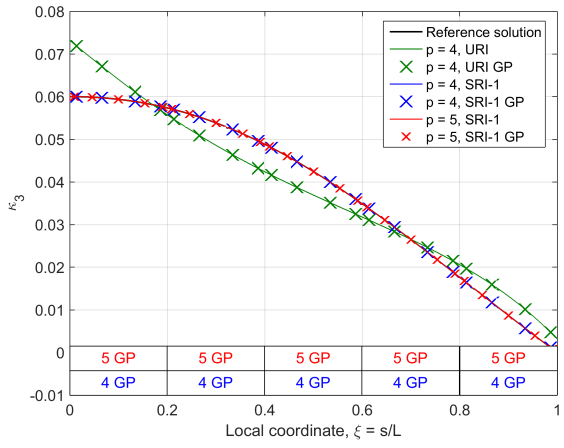

e)

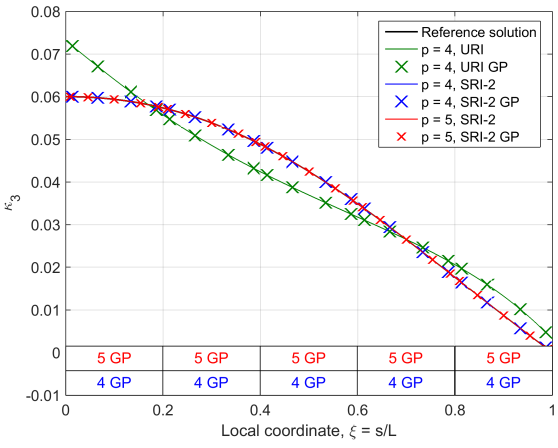

f)

Figure 6.23: Comparison of the solutions obtained with the various SRI rules applied to the translational part only, for quartic and quintic order elements: a) Axial strain (SRI-1), b) axial strain (SRI-2), c) transverse shear strain (SRI-1), d) transverse shear strain (SRI-2), e) bending strain (SRI-1), and f) bending strain (SRI-2).

The beam is analyzed once more applying the proposed integration schemes on both the translational and rotational parts (URI-1 and URI-2). The corresponding strain field solutions are reported in Figs. 6.24 and 6.25 for the quadratic and cubic elements, respectively. For $p = 3$ or higher, the solution is not convergent unless the additional Gauss points are added to the boundary elements (URI-2). Results obtained for the quartic and quintic order elements are not reported here, but they behave similar to the cubic elements.

Again, strains sampled at the Gauss points coincide with the reference solution for the translational strains. However, applying less than $n_{GP} = p$ on the rotational part does not produce accurate results for the bending strains.

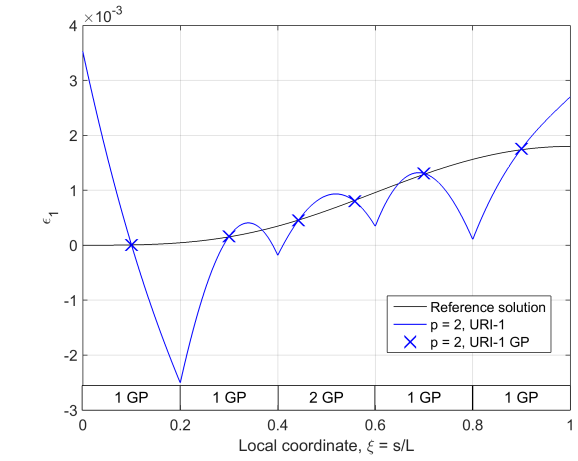

a)

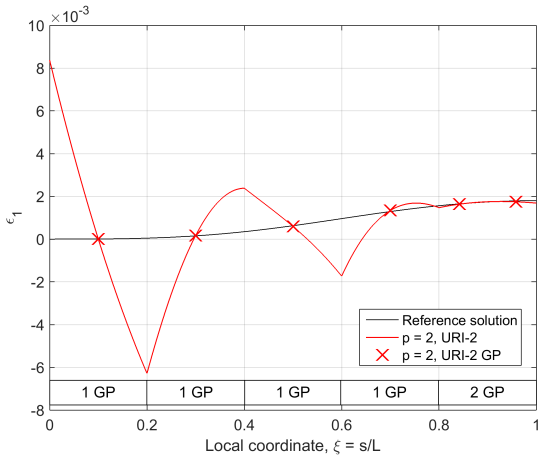

b)

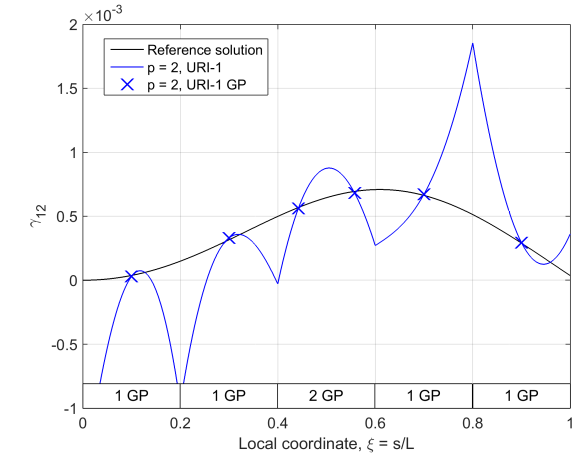

c)

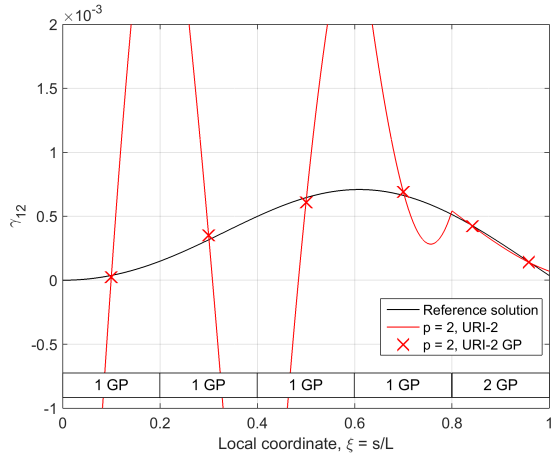

d)

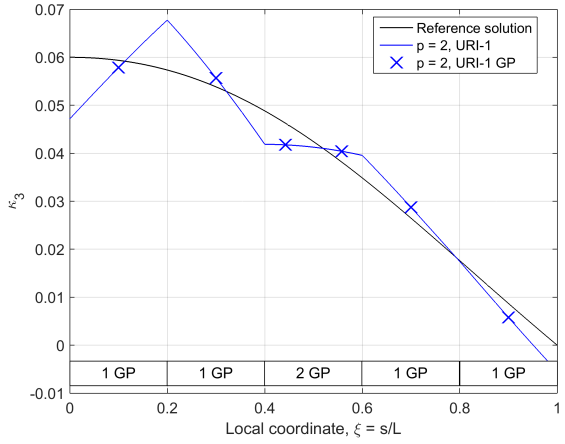

e)

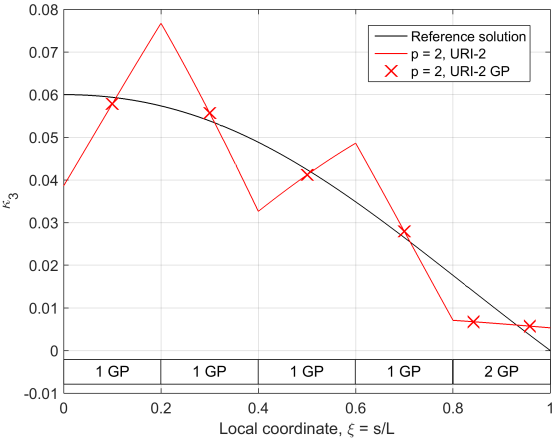

f)

Figure 6.24: Comparison of solutions obtained with the various URI rules applied to both the translational and the rotational parts, for $p = 2$: a) Axial strain (SRI-1), b) axial strain (SRI-2), c) transverse shear strain (SRI-1), d) transverse shear strain (SRI-2), e) bending strain (SRI-1), and f) bending strain (SRI-2).

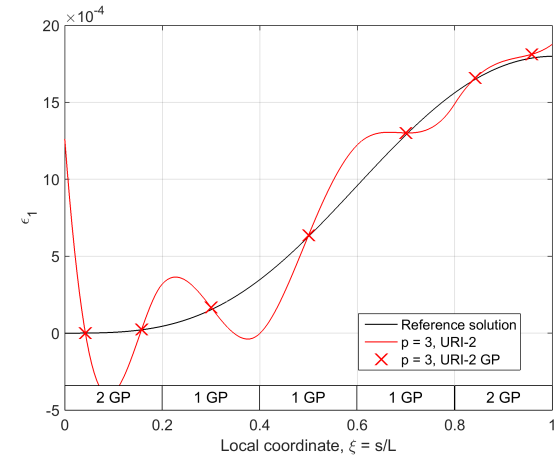

a)

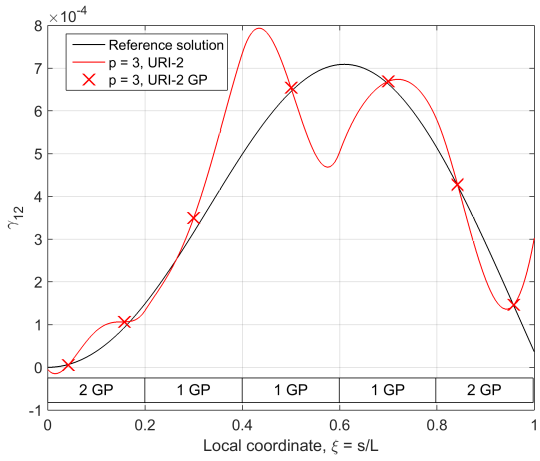

b)

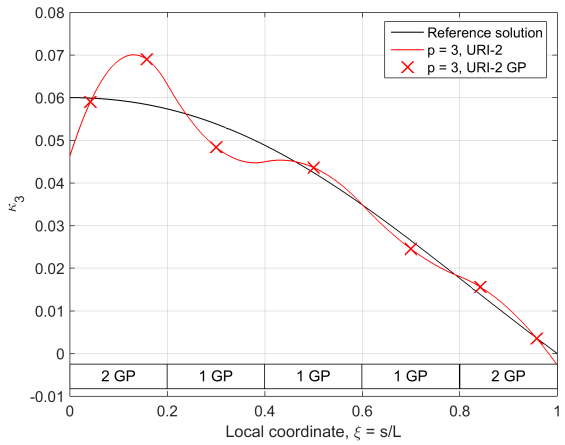

c)

Figure 6.25: Comparison of solutions obtained with the URI-2 rule applied to both the translational and the rotational parts, for $p = 3$: a) Axial strain, b) transverse shear strain, and c) bending strain.

Furthermore, a convergence study is carried out to study the impact of the various reduced quadrature rules on accuracy. The tangential tip displacement is chosen as measurement, and the relative error is computed from Eq. 3.25, where u^{ex} represents $u_t(s = L)$ from Eq. (6.14). Figures 6.26 and 6.27 show convergence plots for the various reduced integration rules with NURBS, for $\rho = 1$ and $\rho = 3$, respectively. Firstly, it is seen that the absolute errors from the conventional URI elements shift with approximately 4 orders, going from $\rho = 1$ to $\rho = 3$ which strongly indicate locking. Elements with SRI provide slower convergence, but the absolute errors are small for coarse discretizations and they are not shifted with ρ. Apparently, quadratic elements integrated with URI-1 or URI-2 performs similar to the associated SRI-1 and SRI-2

elements for which the reduced quadrature rules are only applied to the translational part, while the associated cubic and higher order elements has rather poor performance with slow convergence and large errors.

Lastly the thickness dependency is studied. For this analysis, ρ is varied from 1 to 5, keeping a fixed number of 5 NURBS elements. Figures 6.28 and 6.29 show logarithmic plots of the relative error and the numerical values for tangential tip displacements and tip rotations for the various reduced integration regimes, respectively. Elements with conventional reduced integration (URI) are included for comparison.

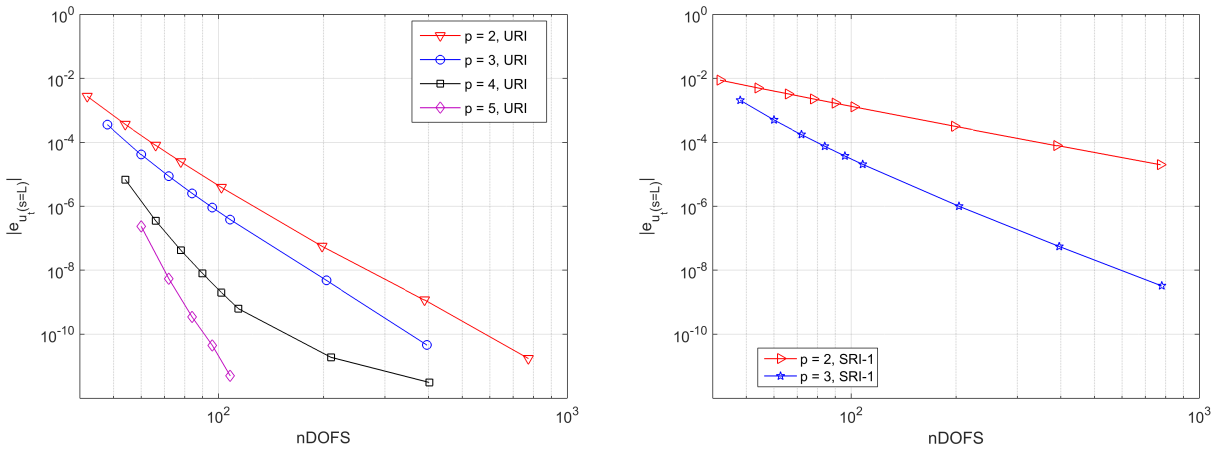

Figure 6.26: Relative error in tangential tip displacement for the various reduced quadrature rules with NURBS, for $\rho = 1$: a) URI, b) SRI-1, c) SRI-2, d) URI-1 and URI-2.

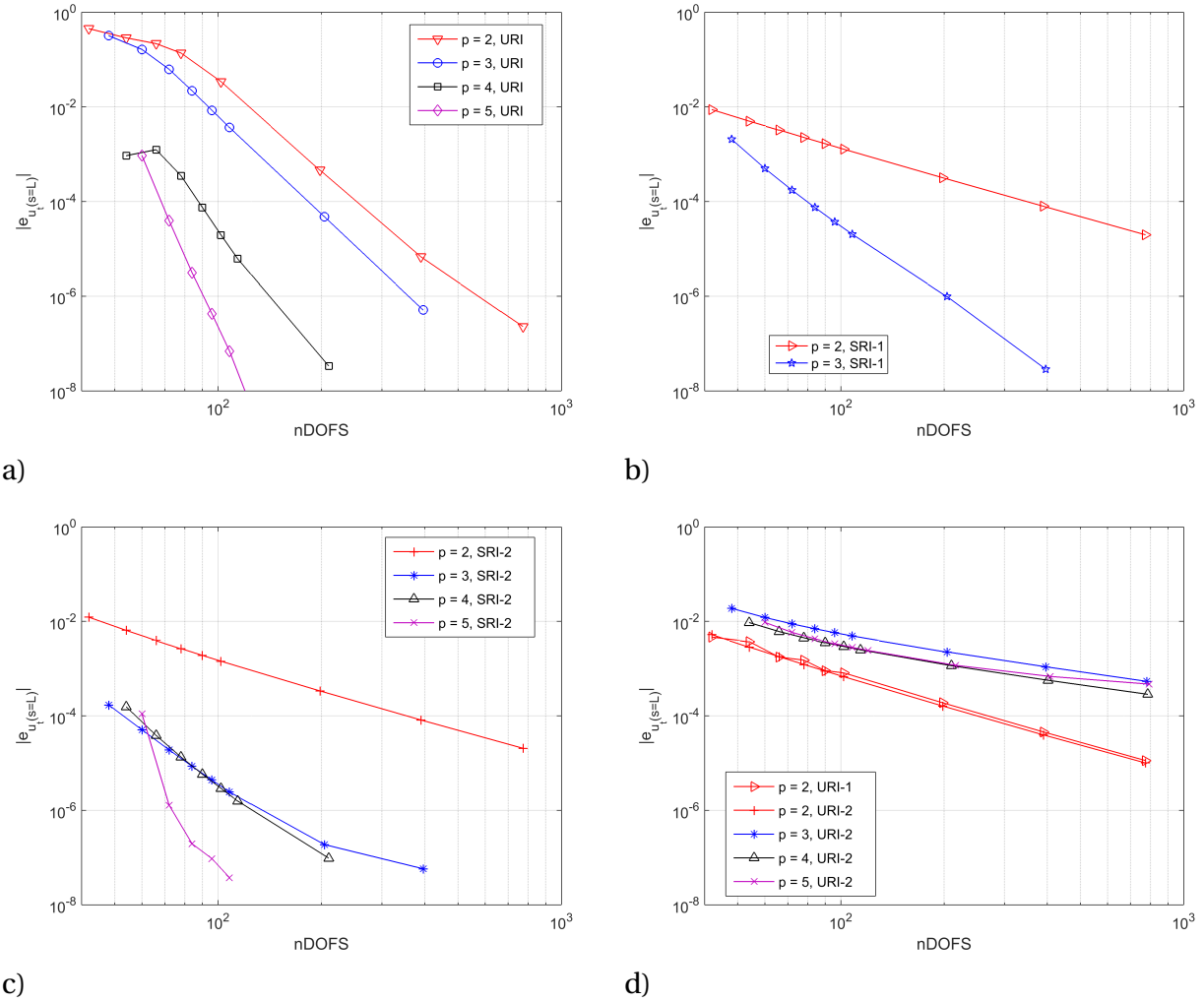

Figure 6.27: Relative error in tangential tip displacement for the various reduced quadrature rules with NURBS, for $\rho = 3$: a) URI, b) SRI-1, c) SRI-2, d) URI-1 and URI-2.

Apart from $p = 5$, all elements appear to be locking-free. The slight thickness dependency of the quintic elements may be due to the fact that the proposed quadrature rule adds two more Gauss points than needed to avoid rank deficiency and thus creates an over-constrained system. Note how this curved beam locks completely with URI, even with cubic elements. The dotted line in Fig. 6.29 represents the limit in computer precision.

A closer investigation of the kink in $4th$ order elements with URI is carried out in Appendix B, where also the thickness dependency of the L^2 relative error norm is considered.

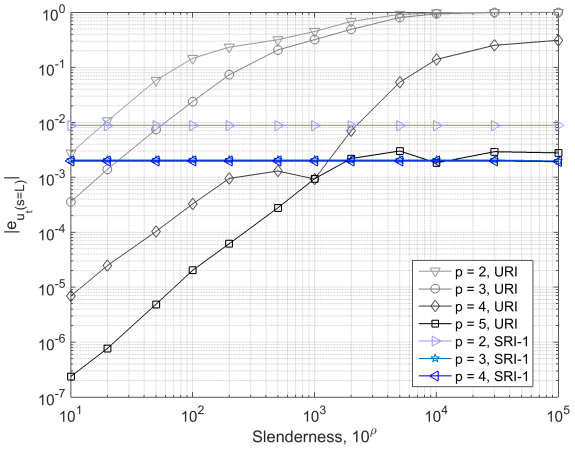

a)

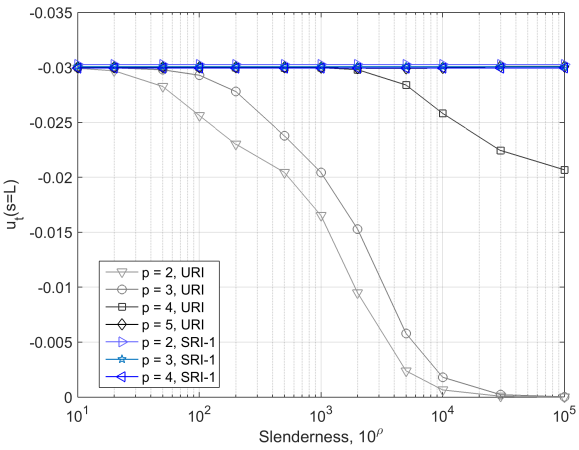

b)

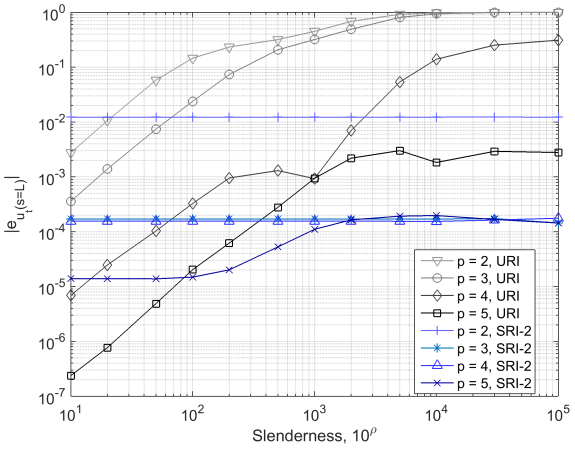

c)

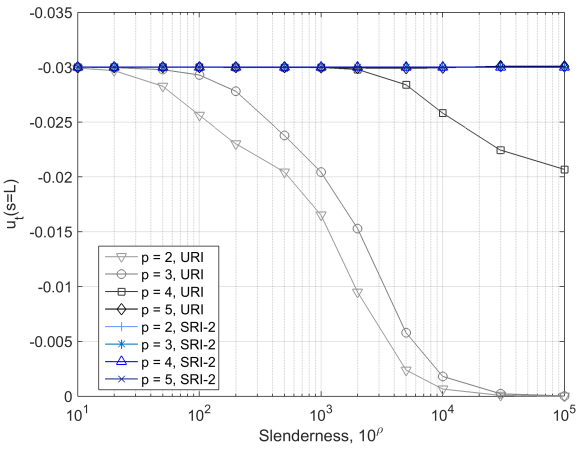

d)

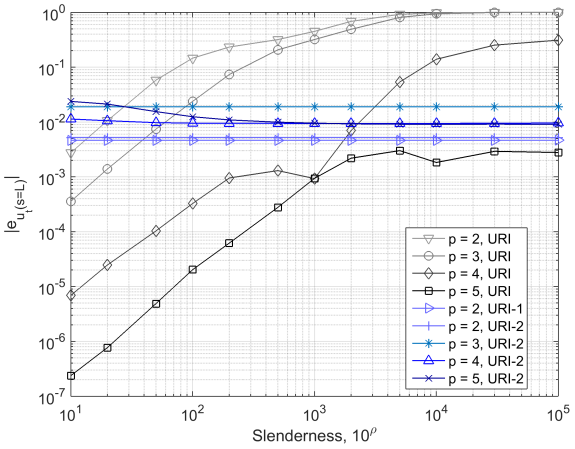

e)

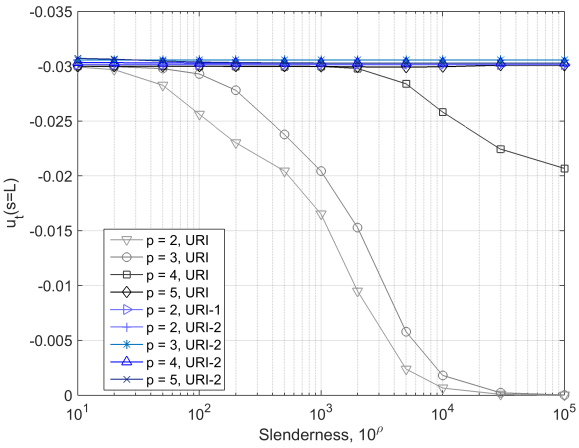

f)

Figure 6.28: Convergence of the tangential tip displacement with respect to the slenderness of the beam for NURBS: a) Relative error (SRI-1), b) displacement (SRI-1), c) relative error (SRI-2), d) displacement (SRI-2), e) relative error (URI-1 and URI-2), and f) displacement (URI-1 and URI-2).

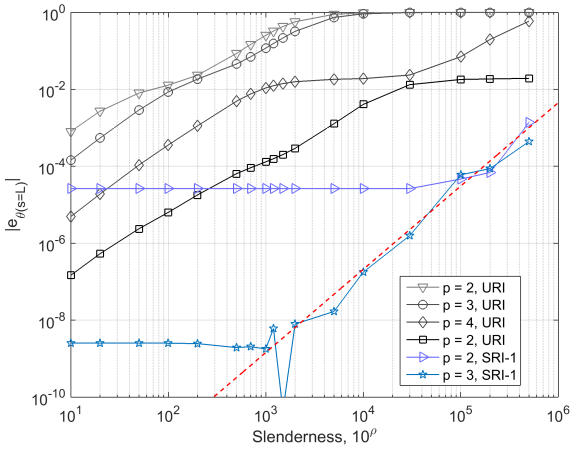

a)

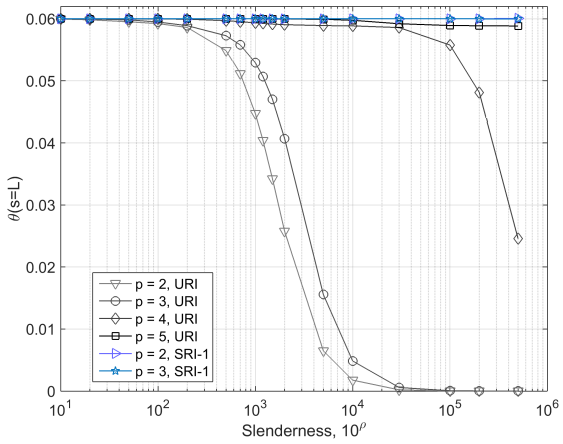

b)

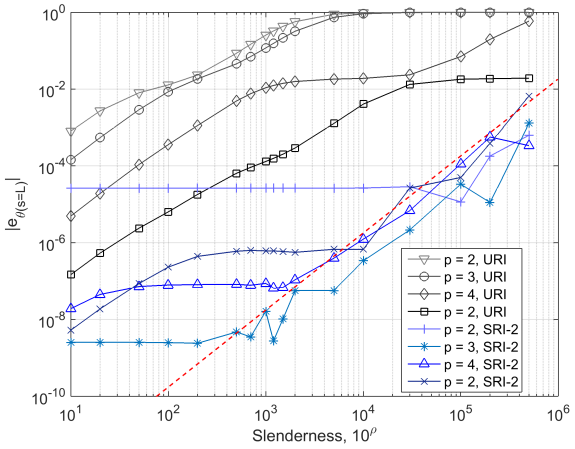

c)

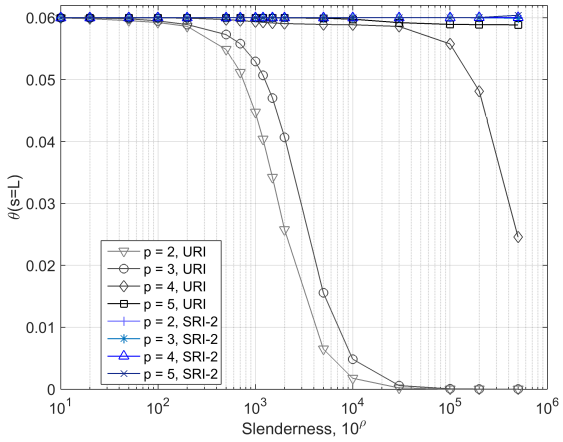

d)

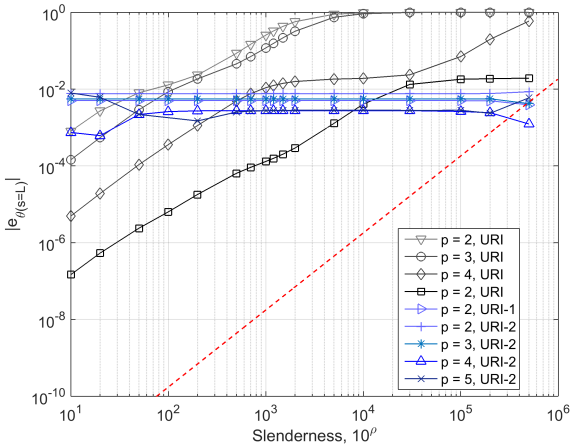

e)

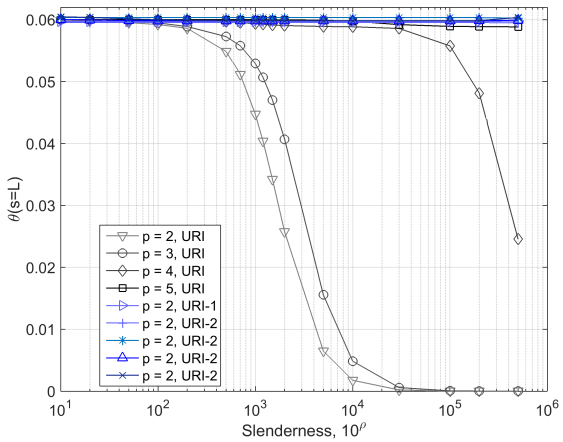

f)

Figure 6.29: Convergence of the tip rotation with respect to the slenderness of the beam for NURBS: a) Relative error (SRI-1), b) rotation (SRI-1), c) relative error (SRI-2), d) rotation (SRI-2), e) relative error (URI-1 and URI-2), and f) rotation (URI-1 and URI-2).

6.3.4 Curved beam subjected to tip shear

In this last example, the beam from Section 5.4 is analyzed with the proposed integration regimes in Table 6.1. Figure 6.30 shows geometry and material properties. Unlike the moment loaded beam from the previous section, this load imposes strain energy contributions from not only bending, but also axial- and transverse shear strains.

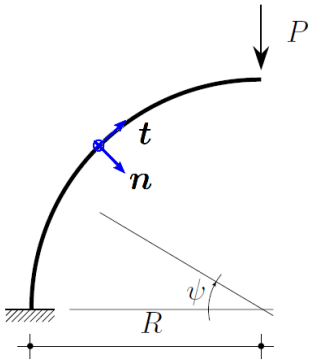

Young's modulus:	$E = 1000$
Poisson's ratio:	$\nu = 0$
Radius:	$R = 10$
Width:	$b = 1$
Thickness:	$h = R/10^{\rho}$
Load:	$P = 0.1h^3$

Figure 6.30: Geometry and material data for a curved beam under sinusoidally moment loading.

Again, the nonzero strain fields, ε_1, γ_{12} and κ_3, which may be computed from the analytical solution given in Eq. 5.3 have been studied with the different integration regimes. A comparison of Lagrange and NURBS elements of quadratic order and conventional reduced integration (URI) is shown in Figure 6.31 for slendernesses of $\rho = 1$ and $\rho = 3$. In order to match the number of unknowns, a uniform mesh of 3 and 5 elements is used for FEA and IGA, respectively. The strains are obtained from the current configuration, and for that reason the analytical (linear) solution is approximated with a reference solution obtained with 32 quintic isogeometric elements each integrated with p Gauss points ($n_{GP} = p$). These figures confirm that URI removes locking of the Lagrangian elements, while IGA, on the other hand, show increasing errors with the slenderness and consequently tends to lock.

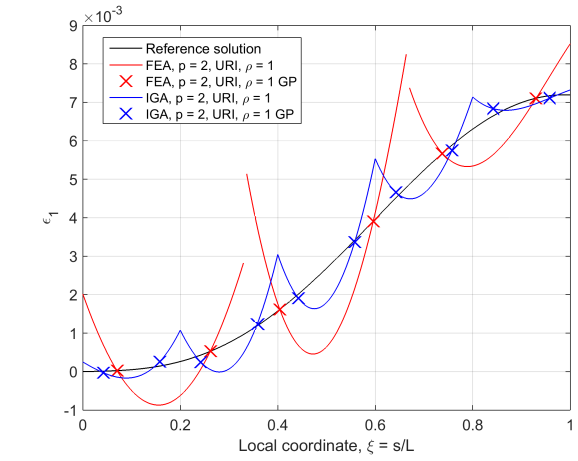

a)

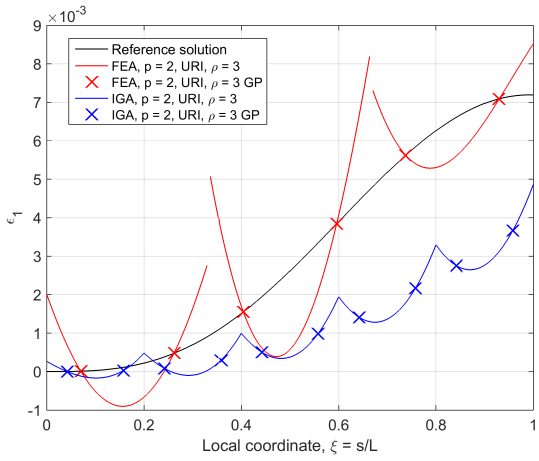

b)

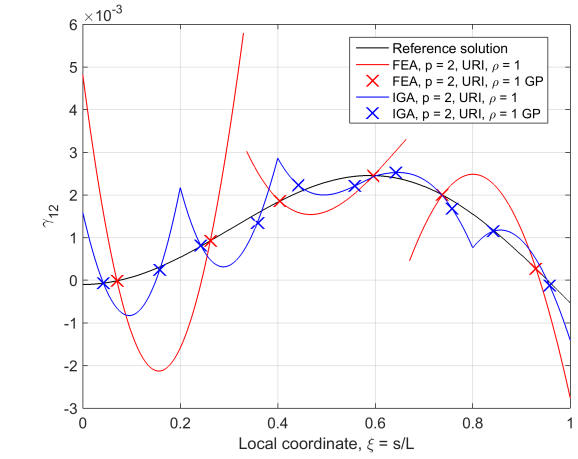

c)

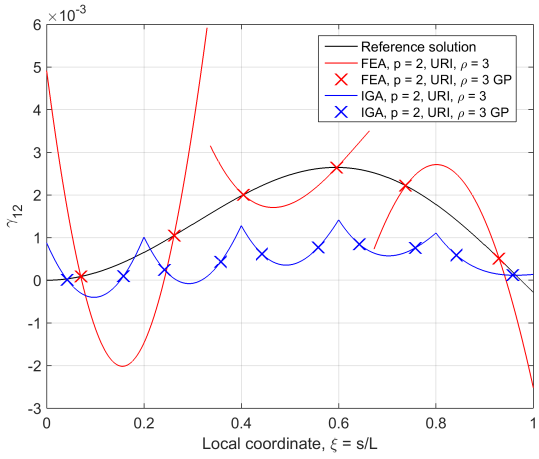

d)

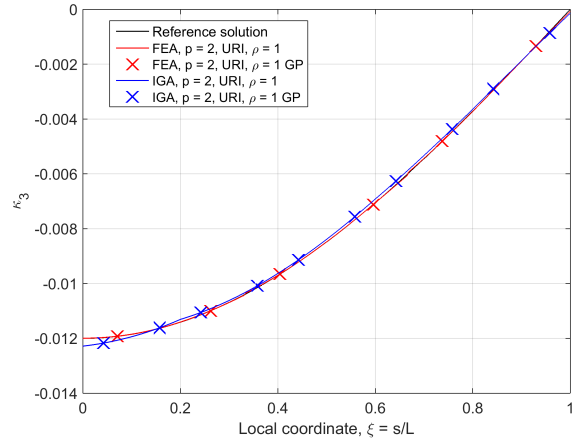

e)

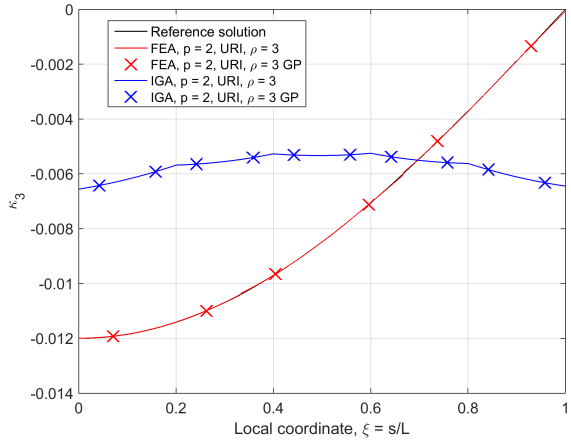

f)

Figure 6.31: Comparison of Lagrange (FEA) and NURBS (IGA) based solutions applying conventional URI for $p = 2$: a) and b) Axial strain, $\rho = 1$ and $\rho = 3$, c) and d) transverse shear strain, $\rho = 1$ and $\rho = 3$ and e) and f) bending strain, $\rho = 1$ and $\rho = 3$.

The slenderness is now kept fixed to $\rho = 3$ and the beam is analyzed using selective reduced integration, SRI-1 and SRI-2. The strain fields obtained with 5 equally sized $2nd$ and $3rd$ order elements are depicted in Figures 6.32 and 6.33, respectively. For the quadratic elements all three strain fields sample the reference solution with good accuracy, yielding an accurate approximation of the corresponding curvature field. However, for cubic elements with SRI-1, instabilities in the translational strains at the boundaries leads and incorrect representation of the curvatures. For SRI-2, where the Gauss points are located at the boundary elements, these instabilities are avoided.

The proposed integration schemes are now applied to the entire stiffness matrix (URI-1 and URI-2), and the corresponding strain fields are reported in Figures 6.34 and 6.35 for quadratic and cubic elements, respectively. For $p = 2$, the translational strains are sampled with fair accuracy, but the rotational part is left incorrect. For $p = 3$, the solution is not convergent unless the additional Gauss points are added to the boundary elements (URI-2), and these behave similar as for $p = 2$: fair accuracy for the translational part, incorrect representation of the curvatures.

Figure 6.36 shows the strains obtained for $p = 4$ and $p = 5$ with SRI-2 and URI-2. Due to oscillating strain fields and non-convergent solution with SRI-1/URI-1, these are omitted. Note how the curvatures for URI-2 are inaccurately represented even for quintic order elements.

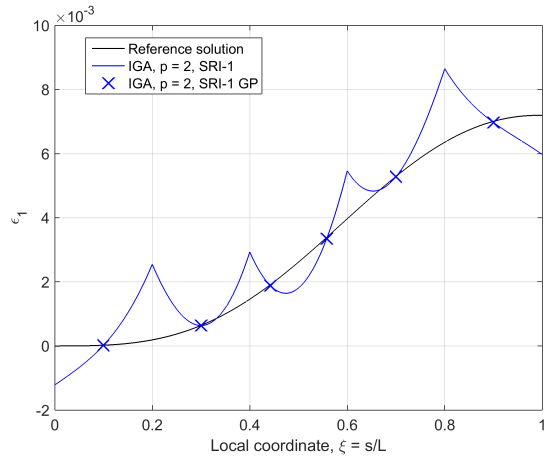

a)

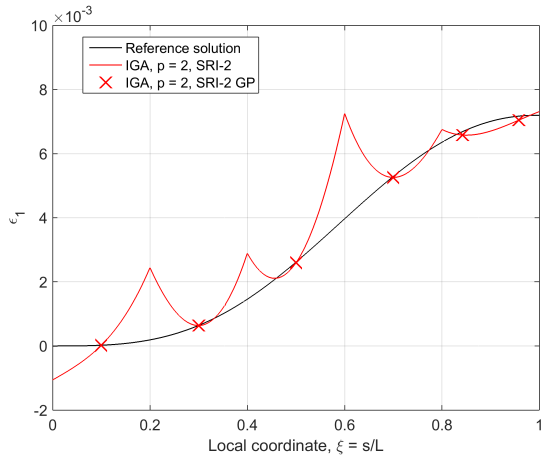

b)

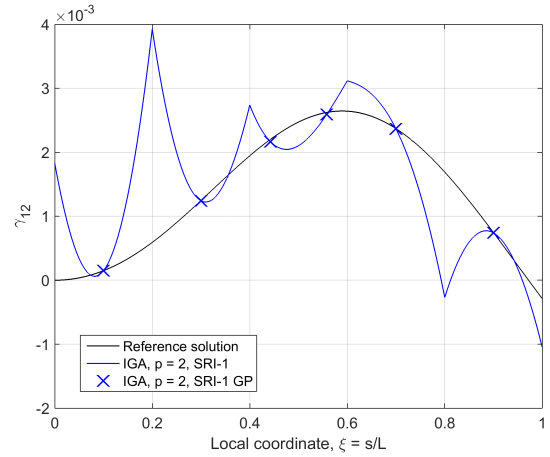

c)

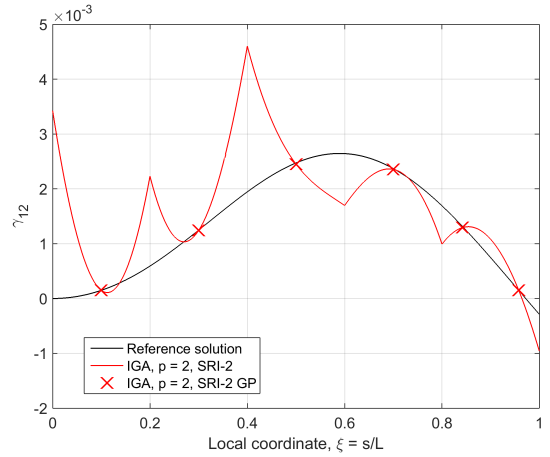

d)

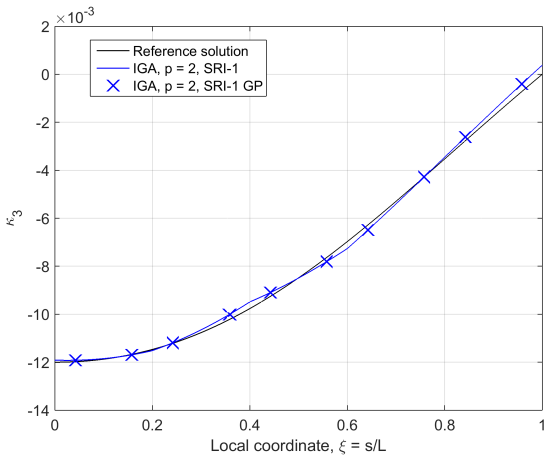

e)

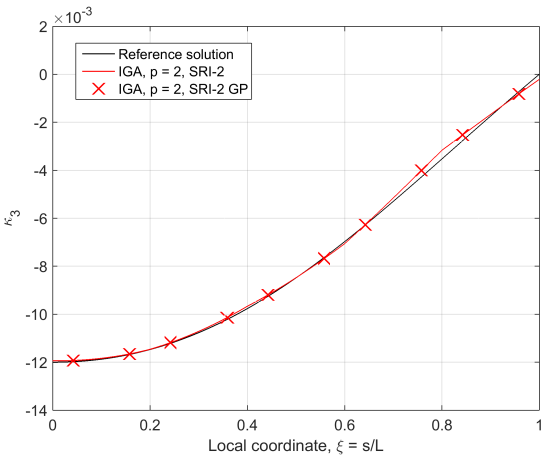

f)

Figure 6.32: Solutions obtained with SRI rules applied to the translational part only, for $p = 2$ and $\rho = 3$: a) ε_1, SRI-1, b) ε_1, SRI-2, c) γ_{12}, SRI-1, d) γ_{12}, SRI-2, e) κ_3, SRI-1 and f) κ_3, SRI-2.

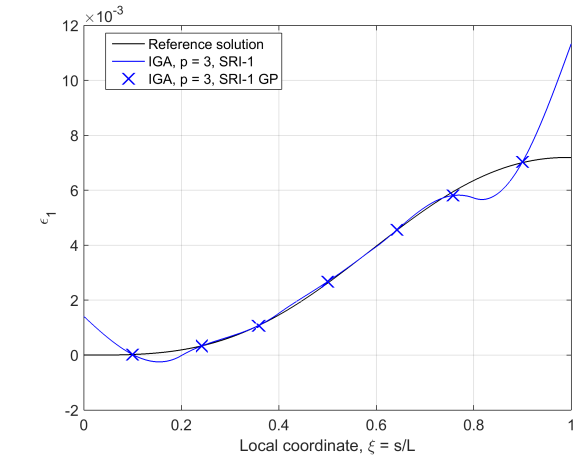

a)

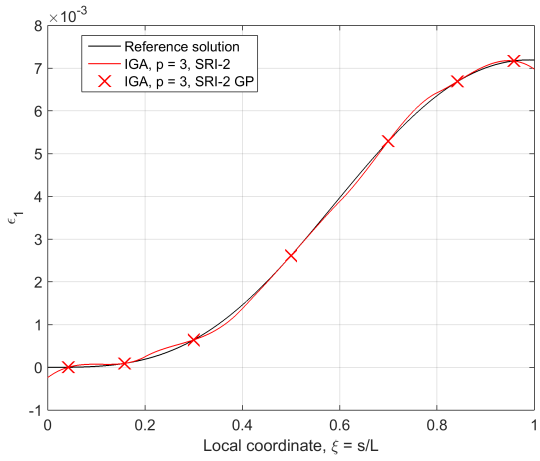

b)

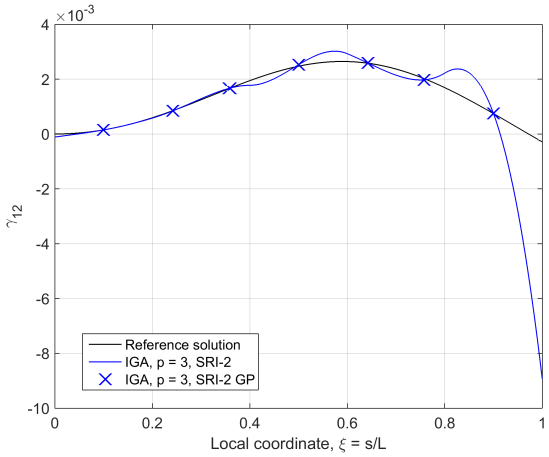

c)

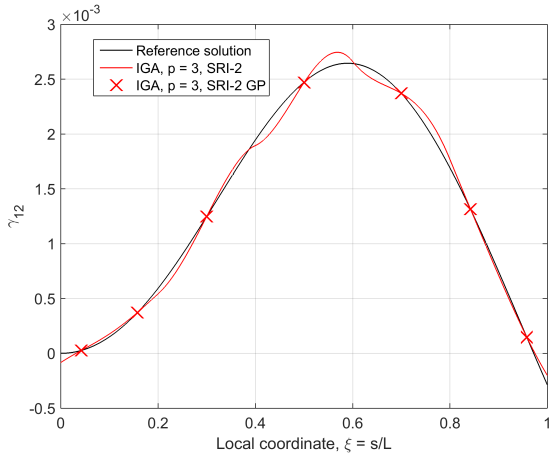

d)

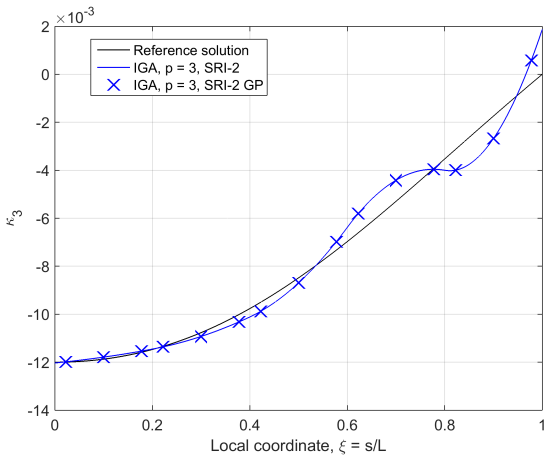

e)

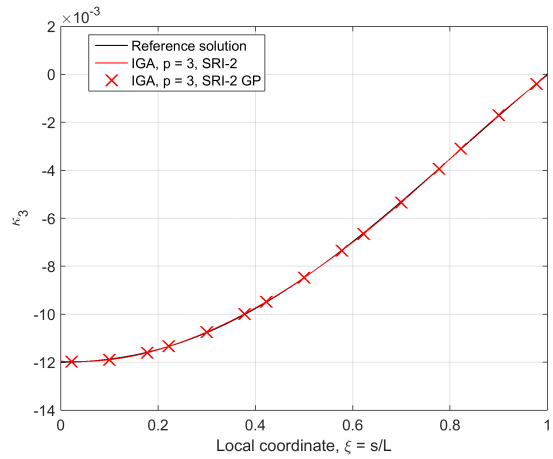

f)

Figure 6.33: Solutions obtained with SRI rules applied to the translational part only, for $p = 3$ and $\rho = 3$: a) ε_1, SRI-1, b) ε_1, SRI-2, c) γ_{12}, SRI-1, d) γ_{12}, SRI-2, e) κ_3, SRI-1 and f) κ_3, SRI-2.

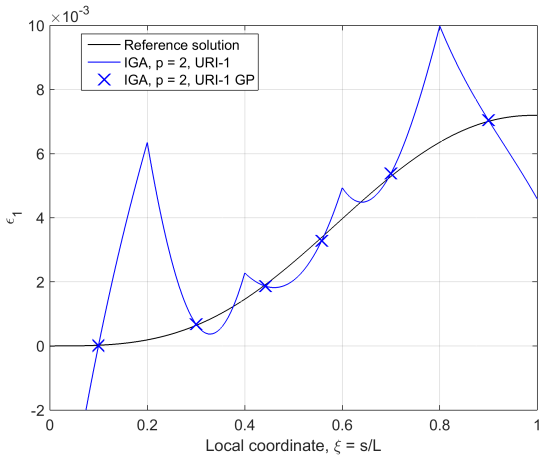

a)

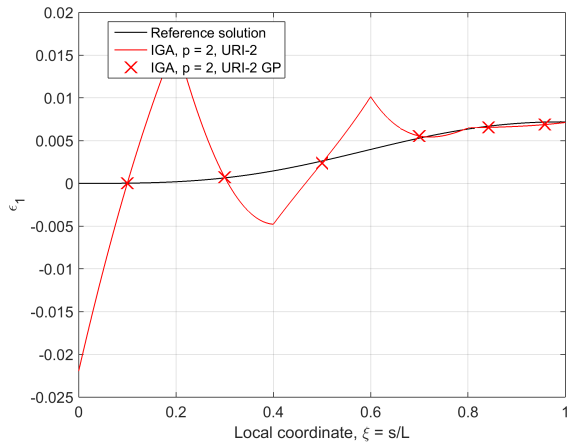

b)

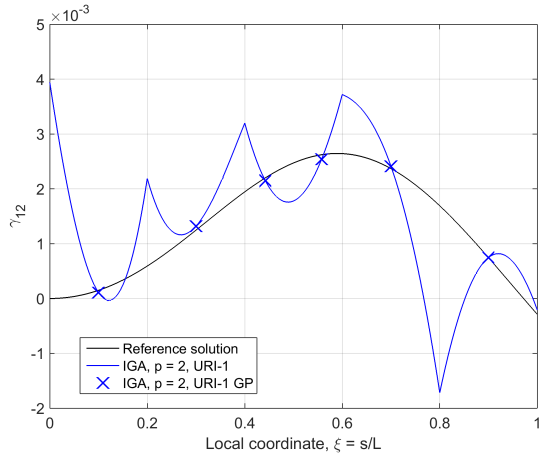

c)

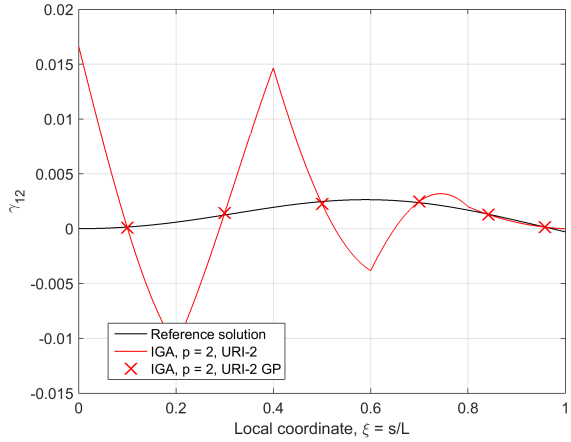

d)

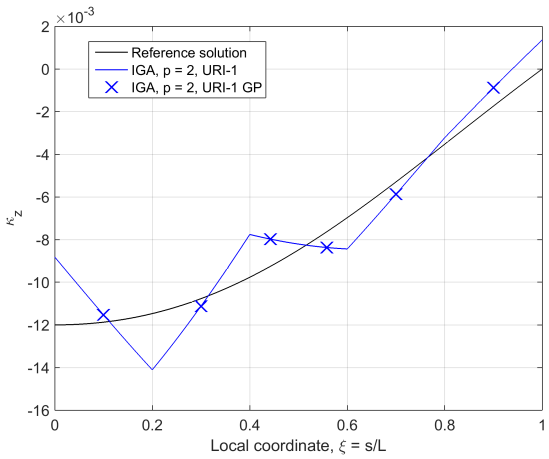

e)

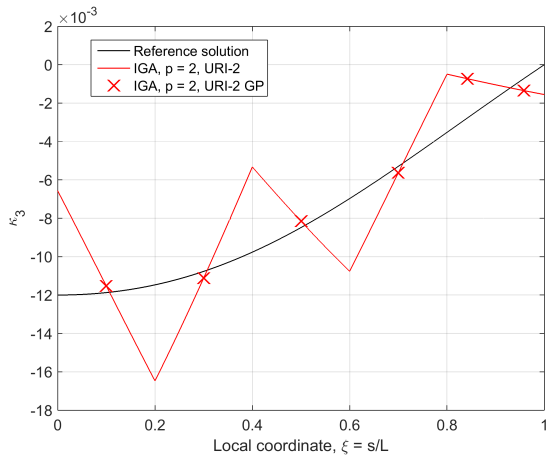

f)

Figure 6.34: Solutions obtained with URI rules applied to both the translational part and the bending part, for $p = 2$ and $\rho = 3$: a) ε_1, URI-1, b) ε_1, URI-2, c) γ_{12}, URI-1, d) γ_{12}, URI-2, e) κ_3, URI-1 and f) κ_3, URI-2.

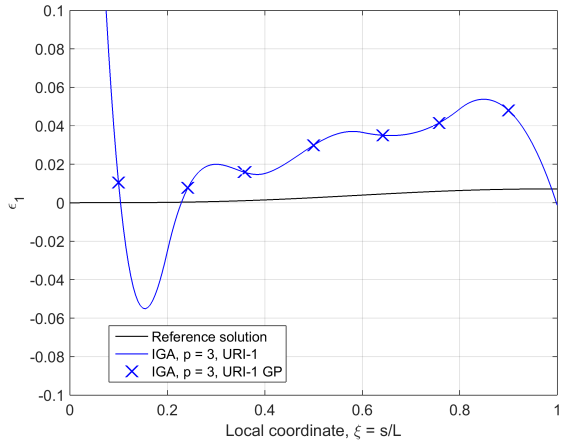

a)

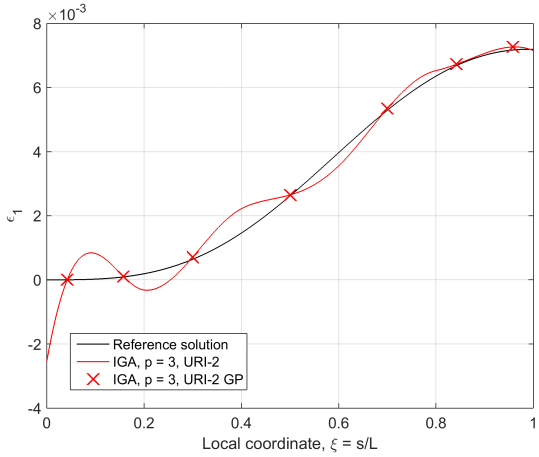

b)

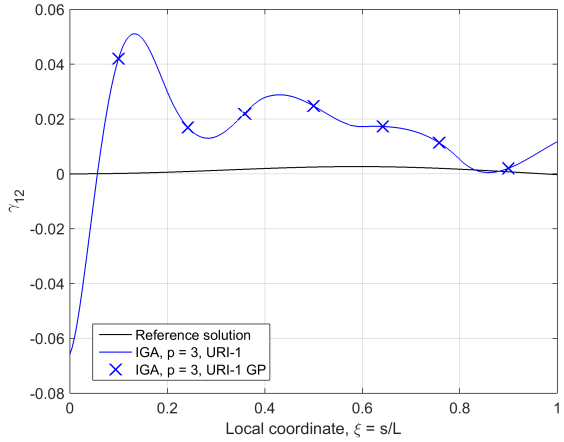

c)

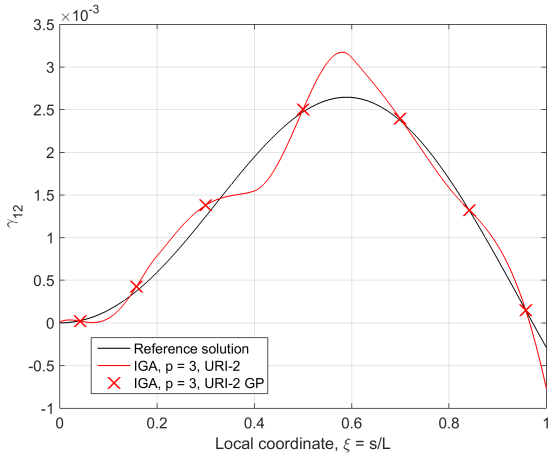

d)

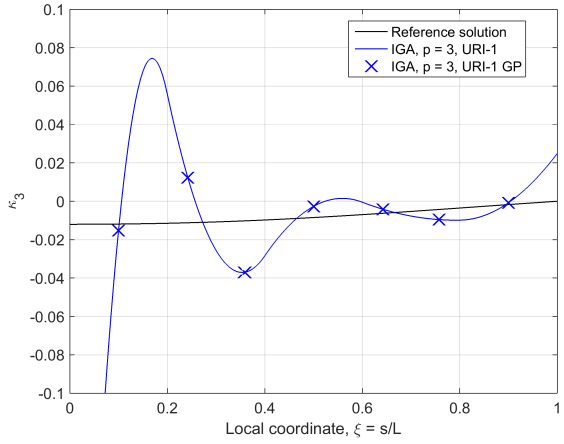

e)

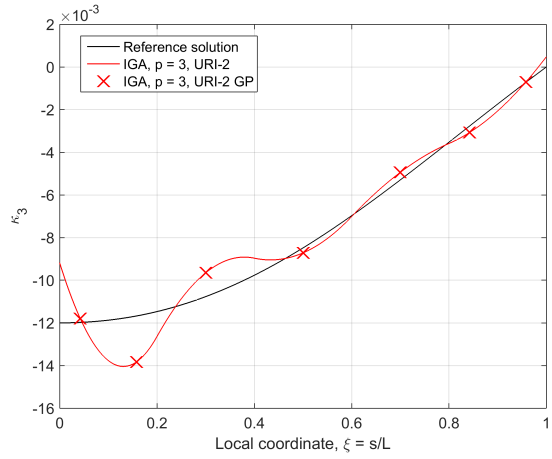

f)

Figure 6.35: Solutions obtained with URI rules applied to both the translational part and the bending part, for $p = 3$ and $\rho = 3$: a) ε_1, URI-1, b) ε_1, URI-2, c) γ_{12}, URI-1, d) γ_{12}, URI-2, e) κ_3, URI-1 and f) κ_3, URI-2.

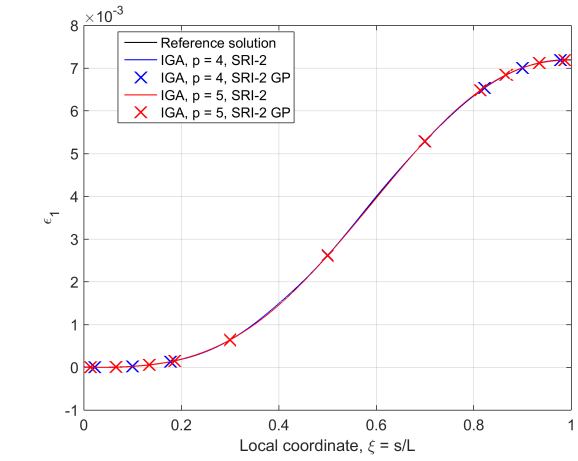

a)

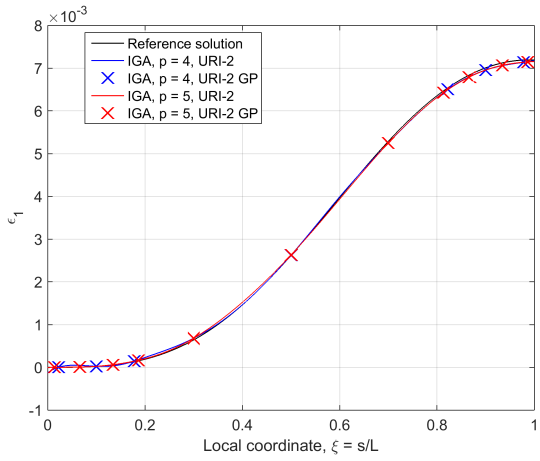

b)

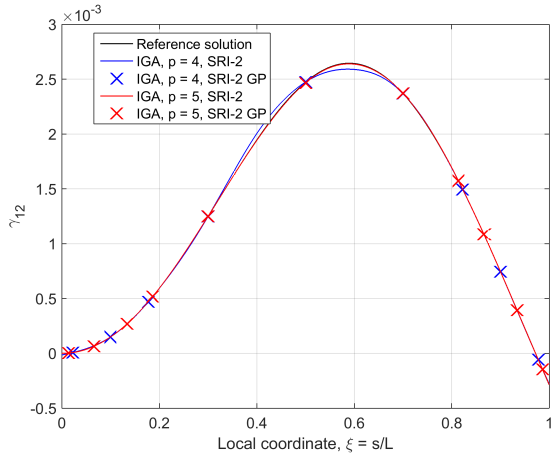

c)

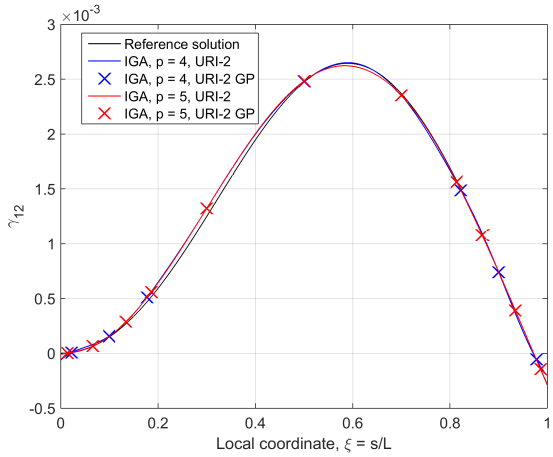

d)

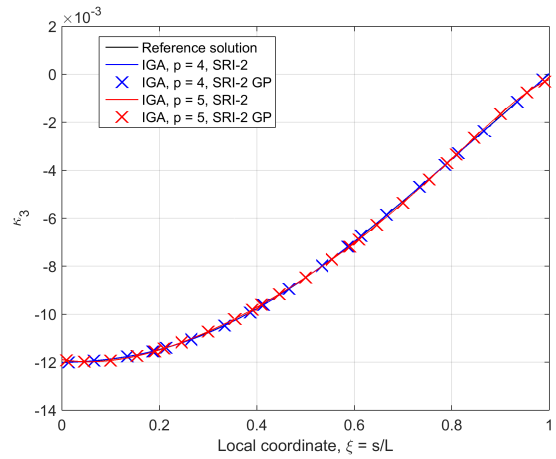

e)

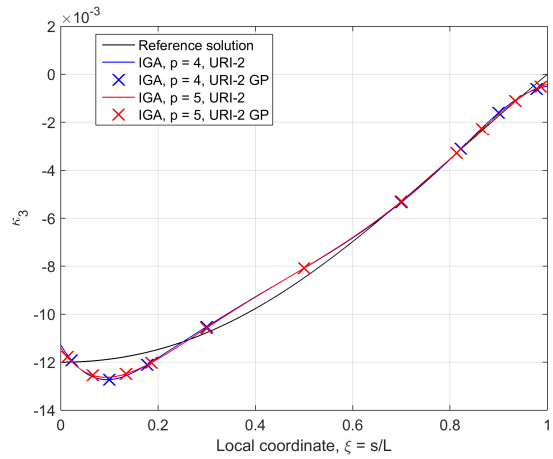

f)

Figure 6.36: Solutions for $4th$ and $5th$ order elements with SRI and URI, for $\rho = 3$: a) ε_1, SRI-2, b) ε_1, URI-2, c) γ_{12}, SRI-2, d) γ_{12}, URI-2, e) κ_3, SRI-2 and f) κ_3, URI-2.

For the convergence study the relative error in normal tip displacement is chosen as measurement, as it is the only contribution to the external energy. Figures 6.37 and 6.38 show convergence plots for the various reduced integration rules, for $\rho = 1$ and $\rho = 3$, respectively. Once again, it is seen that the proposed integration rules provide slower convergence than conventional reduced integration. However, the absolute errors are small for coarse discretizations and they are not shifted with the slenderness, ρ. URI-1 and URI-2 for cubic or higher order elements has rather poor performance with slow convergence and large errors.

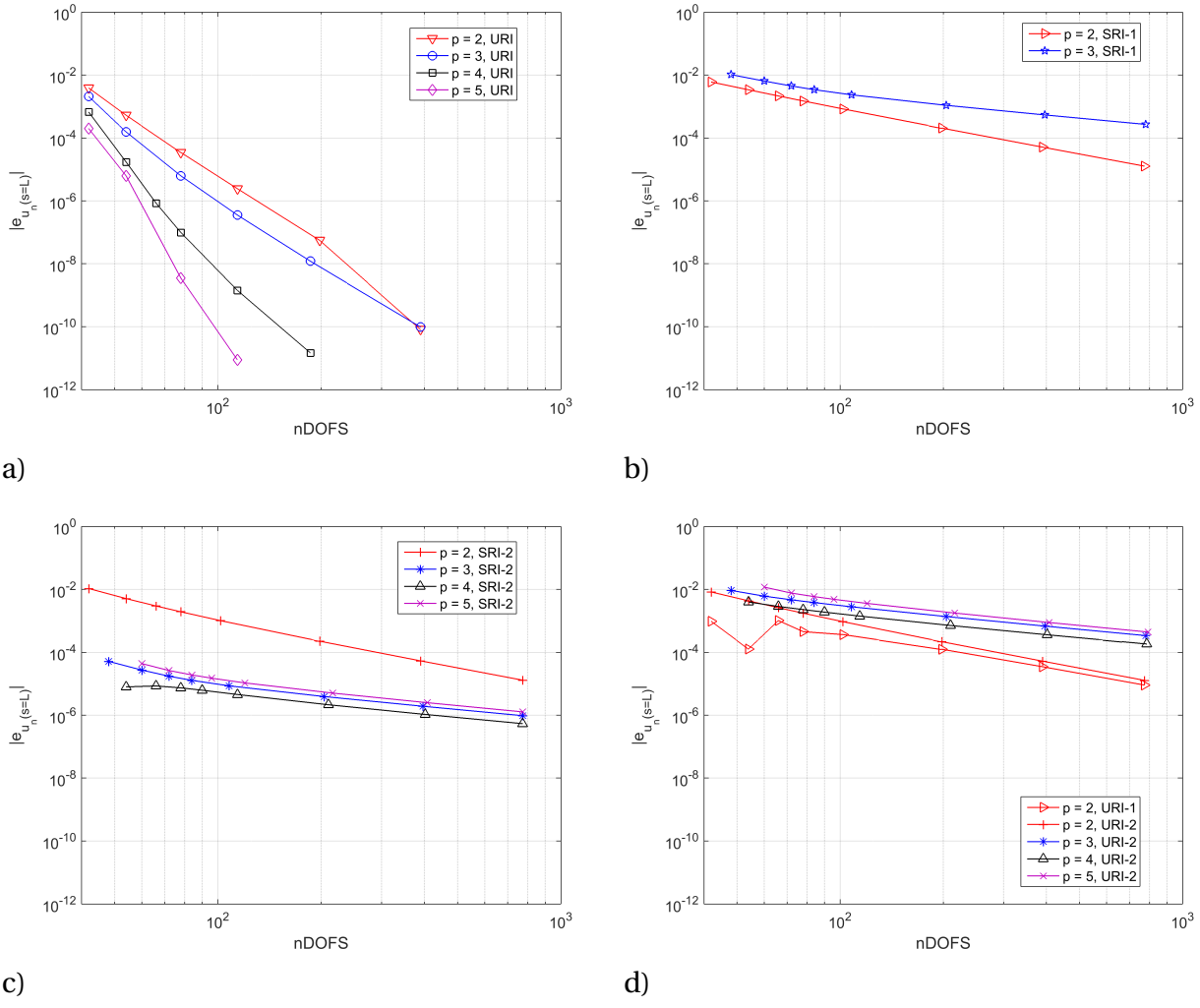

Figure 6.37: Relative error in tangential tip displacement for the various reduced integration rules, for $\rho = 1$: a) URI, b) SRI-1, c) SRI-2 and d) URI-1 and URI-2.

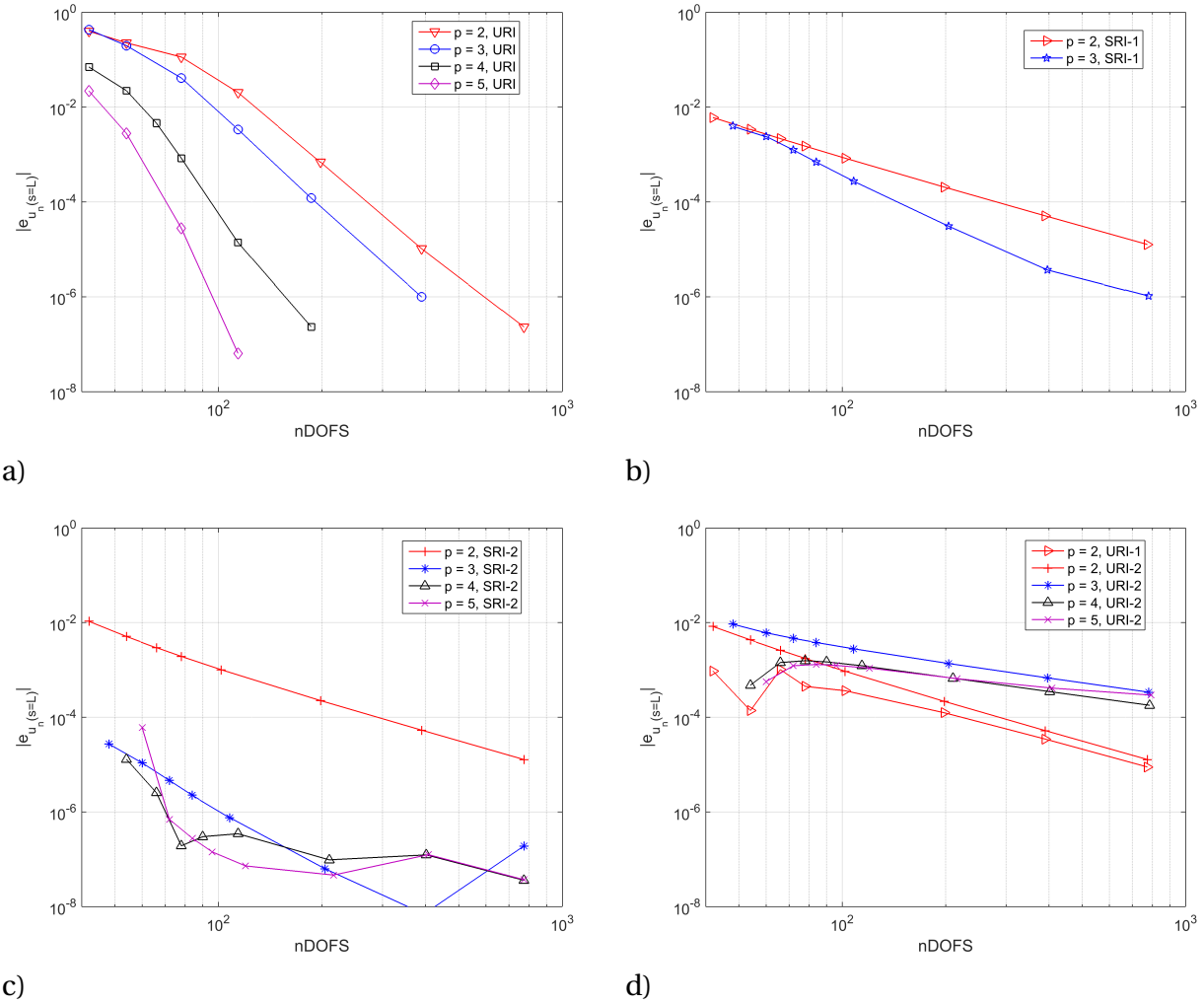

Figure 6.38: Relative error in tangential tip displacement for the various reduced integration rules, for $\rho = 3$: a) URI, b) SRI-1, c) SRI-2 and d) URI-1 and URI-2.

In Figure 6.39 the thickness dependency is studied. The same error measurement is now computed with respect to the slenderness, varying ρ from 1 to 5 with a uniform mesh of 5 elements. Conventional reduced integration is included for comparison. Again the integration models show locking free behavior up to $4th$ order elements. The slight increase in errors for high slendernesses seen in Figure c), might be computational errors, due to an ill-conditioned stiffness matrix.

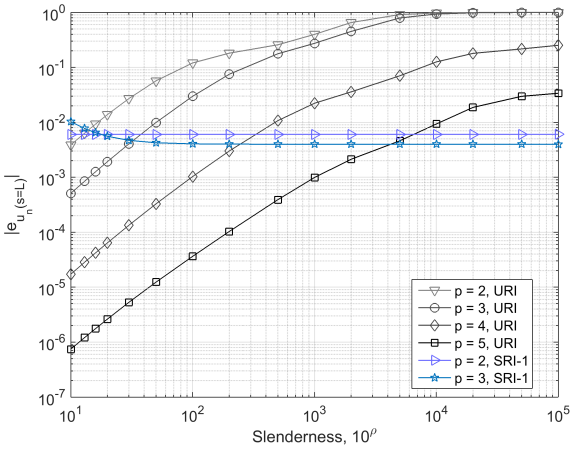

a)

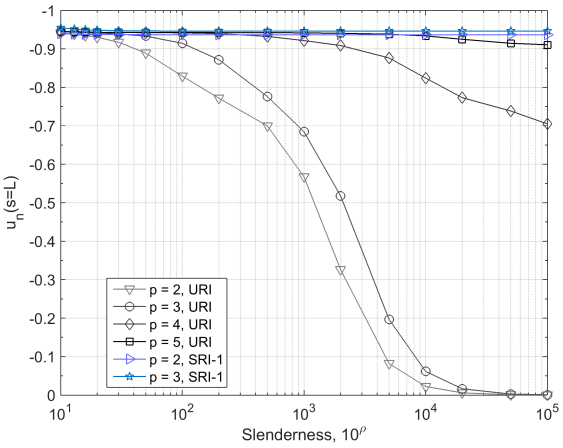

b)

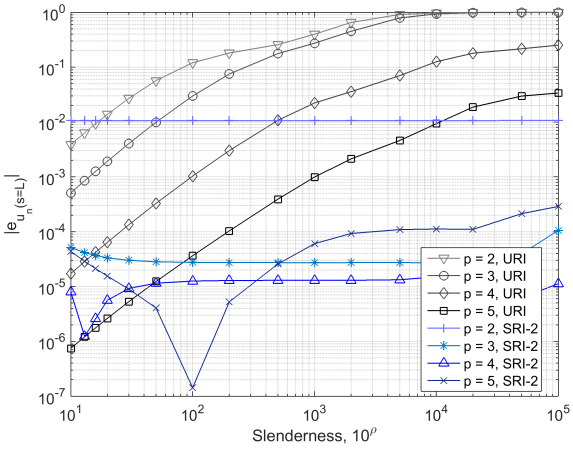

c)

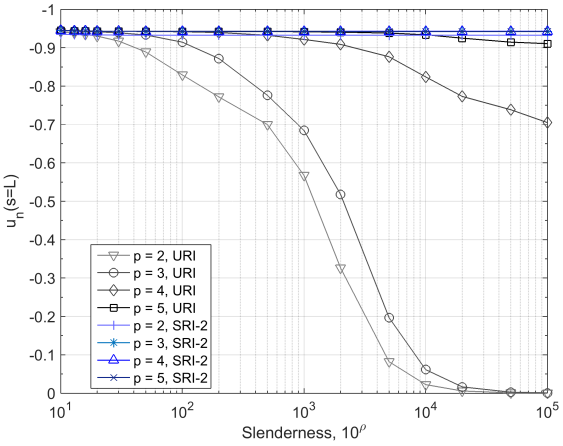

d)

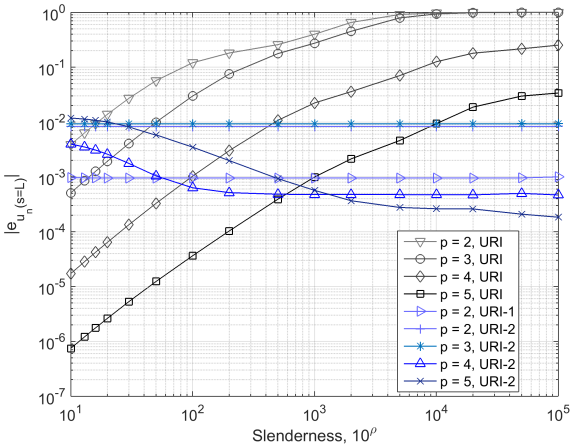

e)

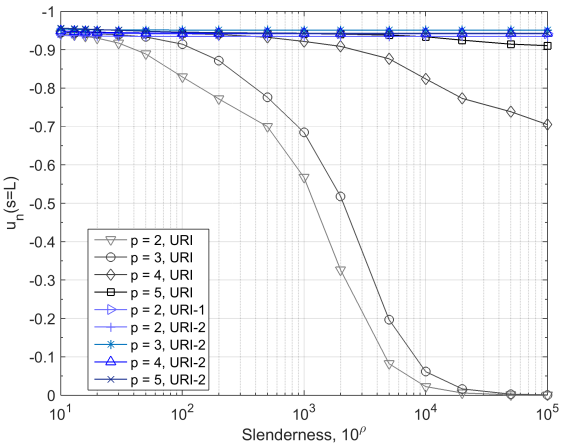

f)

Figure 6.39: Convergence of the normal tip displacement with respect to the slenderness of the beam: a) Relative error (SRI-1), b) displacement (SRI-1), c) relative error (SRI-2), d) displacement (SRI-2), e) relative error (URI-1 and URI-2) and f) displacement (URI-1 and URI-2).

6.4 Concluding remarks

Through the numerical examples it has been proven that a lower order, patch-wise integration rule may be used to alleviate both membrane and transverse shear locking of NURBS elements. The strains obtained from the different integration models indicate that for higher order elements, adding the Gauss points to the boundary elements at both ends stabilize, or support the strain field between. By the same argument, the quadratic elements with only one additional Gauss point are given the best support when it is added near the center, as SRI-1/URI-1 suggests.

Further it is seen that while selective reduced integration (SRI-1 and SRI-2) sample all strain fields with good accuracy, the uniform reduced integration rules (URI-1 and URI-2) leave the rotational part incorrectly, resulting in large errors and slow convergence.

Unfortunately, the convergence rates are reduced with the proposed integration rules, and for cubic and higher order elements, they are also depending on the slenderness. Higher proportion of membrane stiffness gives slower convergence, see e.g. Figure 6.37c and 6.38c. A closer investigation of the thickness dependent convergence rates is carried out in Appendix C.

The initial instabilities seen in the convergence for $p = 2$ with the proposed integration schemes, as seen in e.g. Figures 6.9d and 6.37d, is also studied in Appendix C. Furthermore, any strong form solution is lost with the integration schemes, even if the polynomial order is sufficient.

Note that for $p = 4$ and $p = 5$, the system is still over-constrained by 1 and 2 Gauss points, respectively, which may explain the hint of locking seen for $p = 5$ in e.g. Figure 6.28c.

Chapter 7

Non-linear analysis with SRI

It was proven in Chapter 6 that the patch-wise selective reduced integration rule resulted in a locking-free NURBS element, and the performance in linear analyses was investigated. In this chapter the integration rules which showed the best performance in the linear analyses (i.e. SRI-1 for $p = 2$ and SRI-2 for $p \geq 3$) will be tested in the non-linear regime.

For this study the curved beam subjected to a sinusoidally distributed moment loading, from Section 6.3.3, will be analyzed with the geometry and material data given in Figure 7.1. The red line shows the final configuration.

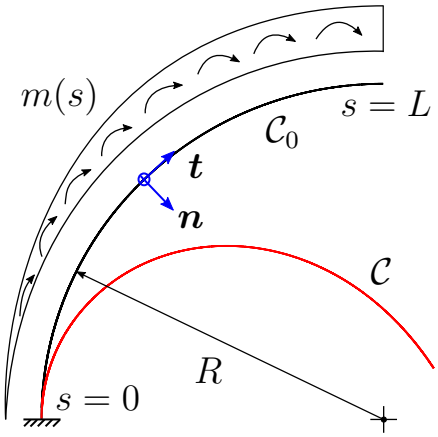

Young's modulus:	$E = 12$
Poisson's ratio:	$\nu = 0$
Radius:	$R = 1$
Width:	$b = 1$
Thickness:	$h = R/10^{\rho}$
Moment loading:	$m(s) = h^3 \sin\left(\frac{\pi s}{2L}\right)$

Figure 7.1: Geometry and material data for a curved beam under sinusoidally moment loading.

The non-linear analysis has been performed with the FENRIS® solver, using 100 load steps. The large number of load steps is chosen to avoid introducing any errors due to path dependency. The convergence of the displacement and the bending moment in terms of the relative L^2 error

norm is studied for quadratic to quartic elements, where the reference solution is computed from 48 octic Lagrangian elements.

Convergence of the displacement is shown in Figures 7.2 and 7.3, where SRI is compared to IGA and FEA with conventional reduced integration, respectively. Figures 7.4 and 7.5 show the corresponding convergence plots for the bending moments.

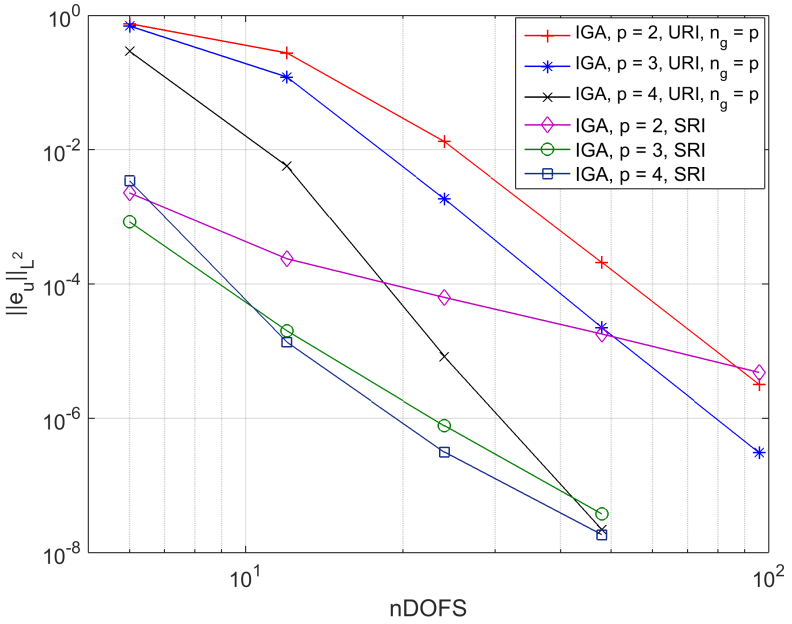

Figure 7.2: Comparison of IGA with URI and SRI for displacement relative error in the L^2-norm for the non-linear analysis.

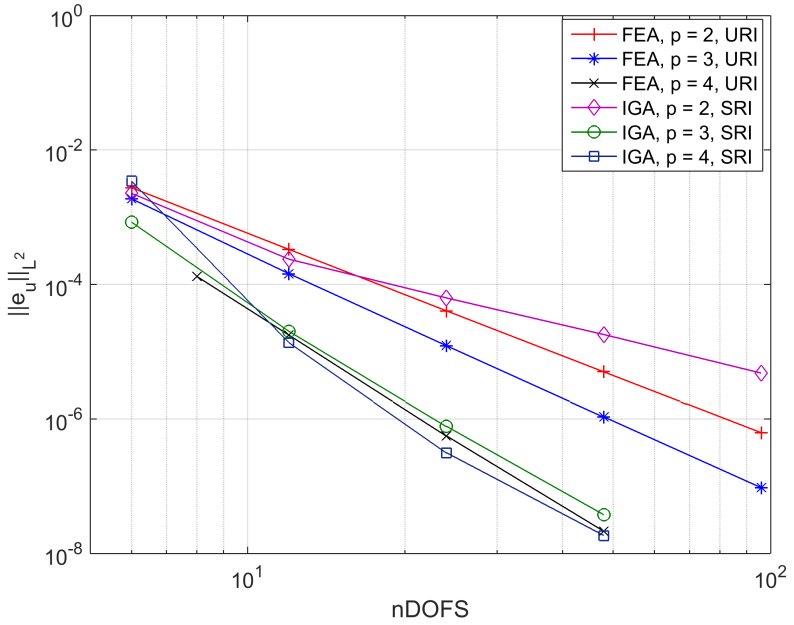

Figure 7.3: Comparison of IGA with SRI and FEA for displacement relative error in the L^2-norm for the non-linear analysis.

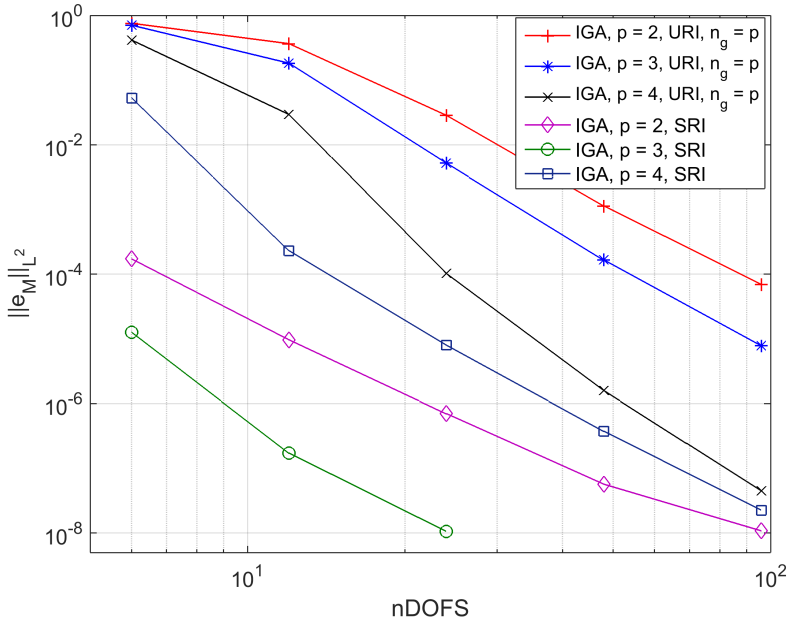

Figure 7.4: Comparison of IGA with URI and SRI for the bending moment relative error in the L^2-norm for the non-linear analysis.

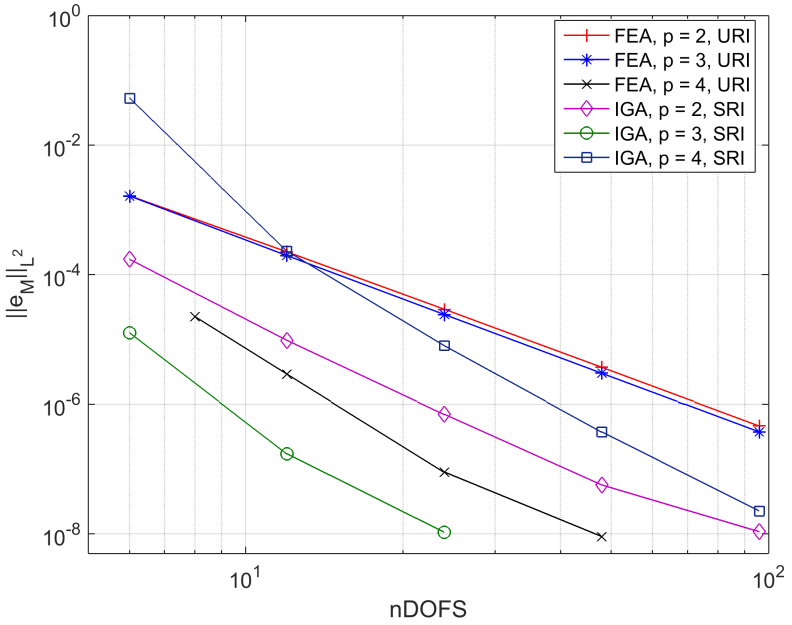

Figure 7.5: Comparison of IGA with SRI and FEA for the bending moment relative error in the L^2-norm for the non-linear analysis.

Also in the non-linear regime, SRI yields improved accuracy for all polynomial orders, and the behavior is very similar as in the linear regime. For the displacements, SRI shows precise results, but the convergence is slower than with conventional URI. Compared to FEA, only the cubic NURBS with SRI show significantly better performance.

For the bending moments, SRI does not only show improved accuracy but the convergence rates are also contained, and for $p \leq 3$ NURBS with SRI outperforms Lagrange.

Chapter 8

Summary and Conclusions

This thesis is concerned with locking-free methods for isogeometric analysis of the geometrically exact shear-flexible 3D beam model, and a family of locking-free NURBS-based elements has been developed.

In Chapter 3 the Lagrangian and the NURBS basis were used to discretize a linear Timoshenko beam. A few numerical tests prove that the implementation was successful, and that IGA performed well compared to the standard FEA. It was also proven that NURBS elements are prone to transverse shear locking, even with the conventional reduced integration rule which unlocks the Lagrangian elements.

In the next step, the geometrically exact 3D beam model, presented in Chapter 4, was discretized with Lagrangian polynomials and NURBS. With no restrictions with respect to the size of the displacements, rotations and deformations, this beam model is well accommodated for large deformation analyses. However, as the focus has been on unlocking the NURBS element by a lower order integration rule, the beam model has mostly been studied in the linear regime.

A range of numerical examples in Chapter 5 verified the implementation of the beam model. A closer study of the impact of reduced integration on IGA was also carried out, and it was found that: 1) For $p = 1$, whose basis is identical to the Lagrangian, reduced integration removes both transverse shear and membrane locking, 2) for $p = 2$, IGA with reduced integration show faster convergence and less errors than IGA with exact integration, and the impact of locking are reduced but not removed, and 3) for cubic and higher order elements, the impact of reduced

integration is negligible. Furthermore, the discretizations with only one element (i.e. $p+1$ control points and p Gauss points) showed less errors than those with two elements (i.e. $p+2$ control points and $2p$ Gauss points), and thus indicated an over-constrained equation system for $n_e \geq 2$. The standard Lagrangian elements, which were tested in parallel showed, as expected, locking free behavior with reduced integration.

In Chapter 6, a study of the constraint ratio and the minimum number of Gauss points needed for a rank sufficient stiffness matrix resulted in two patch-wise reduced integration schemes, shown in Table 6.1. These were applied to the translational part only (selective reduced integration), using $n_{GP} = p$ on the bending part, and to both the translational and the bending part (uniform reduced integration). The proposed integration rules were carefully tested through a selection of numerical tests with various geometries, loads and boundary conditions. Studies of the strain fields were emphasized, from which locking and the condition of the equation system may be seen. Convergence with respect to the number of degrees of freedom and the slenderness were also investigated.

It was proven that a lower order, patch-wise integration rule may be used to alleviate both transverse shear and membrane locking of the NURBS elements. The study also revealed that the additional Gauss points stabilize the strain amplitudes (and thus improve the condition number), which determine their optimal placement. The best support is given when the additional Gauss point(s) are added: 1) Near the center of the patch for $p = 2$, and 2) to the two boundary elements for $p \geq 3$.

Further it was seen that while selective reduced integration sample all strain fields with good accuracy, the uniform reduced integration rules leave the rotational part incorrectly, resulting in large errors and slow convergence.

The numerical study therefore points out the following integration rule:

- $\forall p$, the bending stiffness matrix should be integrated with $n_{GP} = p$ Gauss points.
- $\forall p$, the membrane stiffness matrix should be integrated with $n_{GP} = 1$ Gauss point, except for:
    1. $p = 2$: one extra Gauss point should be added near the center, and
    2. $p \geq 3$: the two boundary elements should be integrated with $n_{GP} = p-1$ Gauss points.

This complies with the scheme proposed by Bouclier *et al.* [9] for $p = 2$. However, they recommend it for both the translational and the bending part, while it is here only recommended for the translational part. The integration scheme also comply with that proposed by Adam *et al.* [1], but only for $p = 3$.

Unfortunately, the convergence rates are reduced and thickness dependent with the proposed integration rule. High proportion of membrane stiffness slows down the convergence. Furthermore, any strong form solution is also lost, even if the polynomial order is sufficient. The convergence study in Appendix C suggests that the convergence rates for the displacements are bound within a lower limit, $e = \mathcal{O}(h^1)$, and upper limit, $e = \mathcal{O}(h^{p+1})$. However, these limits are not sufficiently studied to draw any conclusions.

In Chapter 7 a non-linear, large displacement analysis with the selective reduced integration rule was carried out, and it was proven that the elements perform likewise or even better in the non-linear regime.

To conclude, the patch-wise selective reduced integration rule proposed in this thesis has proven to be a good candidate to alleviate transverse shear and membrane locking in the NURBS-based geometrically exact 3D Timoshenko beam. The technique is not only easy to implement (see Appendix E), but less integration points do also have a significant impact on the computational efficiency, which is especially beneficial for non-linear analyses.

The study of alleviating locking in NURBS-based beam elements is by no means complete. For this framework open questions remain concerning: 1) Effect of lower regularity within the patch, 2) computational efficiency compared to uniform reduced integration rules, and also the standard FEA and 3) extension to multi-dimensional formulations, such as shells.

Furthermore, selective reduced integration is only one of many promising alternatives to overcome numerical locking. Linked interpolation, proposed for FEA by e.g. Xu [46], which to the author's knowledge has not yet been proposed for IGA at the present time, and $\overline{B}$ and $\overline{F}$ projection methods proposed by Elguedj *et al.* [18] and Bouclier *et al.* [9], which has been successfully applied in linear analyses but not yet tested in the non-linear regime, may be potential competitors for a locking-free NURBS-based geometrically exact 3D beam element.

Appendix A

Relation between n_{els} and n_{nodes}

To give a fair comparison of the different element types, the number of DOFs (n_{dofs}) or number of nodes (n_{nodes}) are matched. The relation between number of nodes and number of elements (n_e) vary with the polynomial order and continuity across elements. Table A.1 shows this relation.

FEA	$p=2$	n_e	1	2	4	8	16	32	64
		n_{nodes}	2	4	8	16	32	64	128
		n_{dofs}	12	24	48	96	192	384	768
	$p=3$	n_e	1	2	3	5	10	20	40
		n_{nodes}	3	6	9	15	30	60	120
		n_{dofs}	18	36	54	90	180	360	720
	$p=4$	n_e		1	2	4	8	16	32
		n_{nodes}		4	8	16	32	64	128
		n_{dofs}		24	48	96	192	384	768
IGA	$p=2$	n_e	1	3	7	15	31	63	127
		n_{nodes}	2	4	8	16	32	64	128
		n_{dofs}	12	24	48	96	192	384	768
	$p=3$	n_e	1	2	6	14	30	62	126
		n_{nodes}	3	4	8	16	32	64	128
		n_{dofs}	18	24	48	96	192	384	768
	$p=4$	n_e		1	5	13	29	61	125
		n_{nodes}		4	8	16	32	64	128
		n_{dofs}		24	48	96	192	384	768

Table A.1: Relation between n_e and n_{nodes}.

Appendix B

Curved beam under distributed moment loading: An investigation of 4^{th} order elements with URI.

A closer investigation of the kink that appeared for $4th$ order elements in Figure 6.28 has been carried out. The aim is to find out whether there is a bug in the code, or if the elements behave like this. The kink in question is pointed out in Figure B.1.

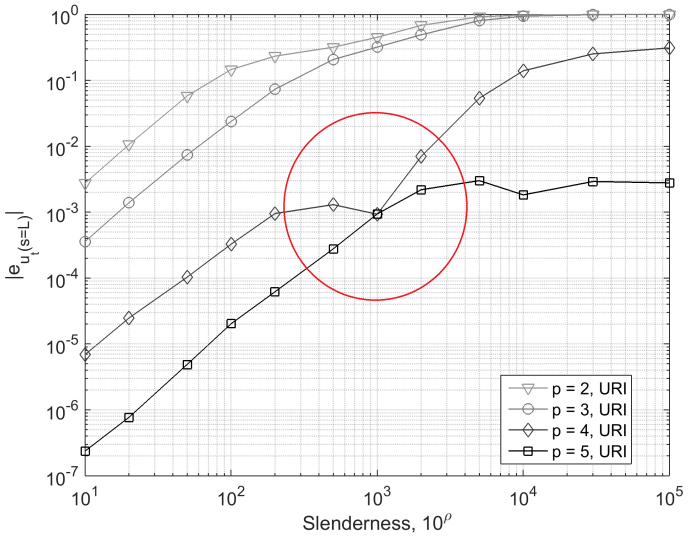

Figure B.1: Convergence of tangential tip displacement with respect to the slenderness for NURBS elements with conventional reduced integration.

The measurement for this study was the relative error in tangential tip displacement, computed from Eqs. 6.14 and 3.25. A more refined analysis has been carried out with uniform meshes of 3, 5, 7 and 9 quartic NURBS elements, and reported in Figure B.2. For the same analysis, the relative error in normal tip displacement and tip rotation is reported in Figures B.3 and B.4, respectively.

Apparently, the kink does only appear for the tangential tip displacement. The two other measurements also lock in two steps (most significantly for the rotations), but the errors do never decrease along the horizontal axis. All discretizations show the same behavior.

It is shown by Prathap [33] and pointed out by Adam *et al.* [1], that the two-step locking distinguishes between transverse shear and membrane locking, where the latter dominates for higher slendernesses.

As the rotations, which is energy conjugate with couples, replicate this behavior, and that the kink smoothen out with a refined analysis and show the same behavior for several meshes, it is most likely only some transition effect between transverse shear and membrane locking. This is supported by Figure B.5, where the L^2-norm of the magnitude in the displacement fields (Eq. B.1) is computed.

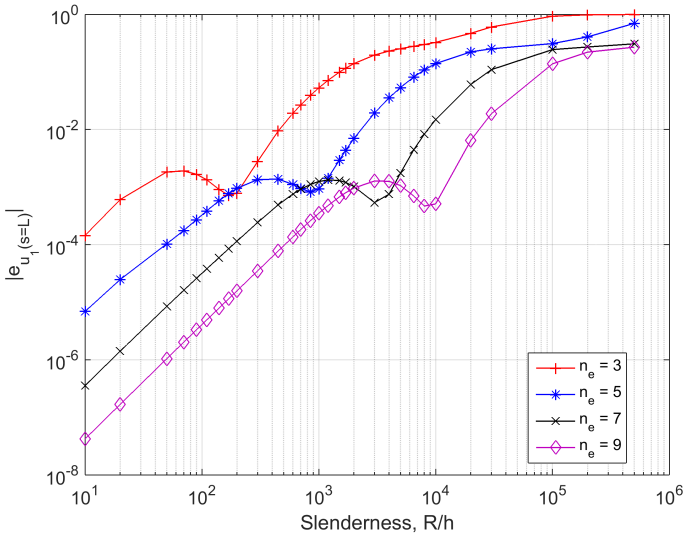

Figure B.2: Relative error in tangential tip displacements for various discretizations with quartic elements.

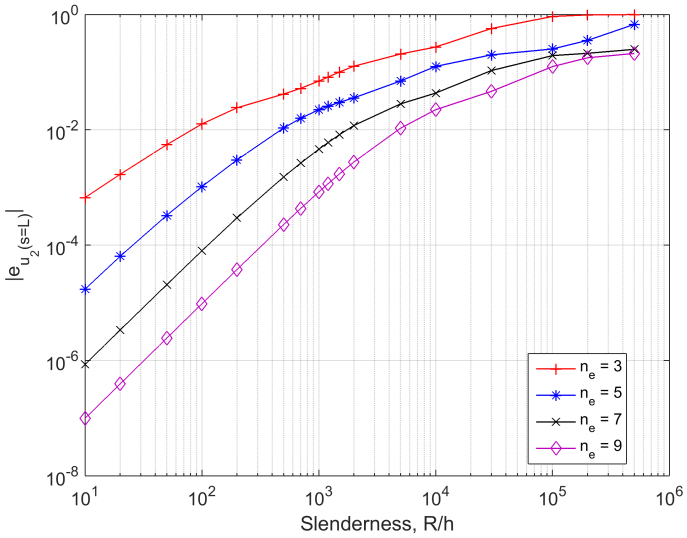

Figure B.3: Relative error in normal tip displacements for various discretizations with quartic elements.

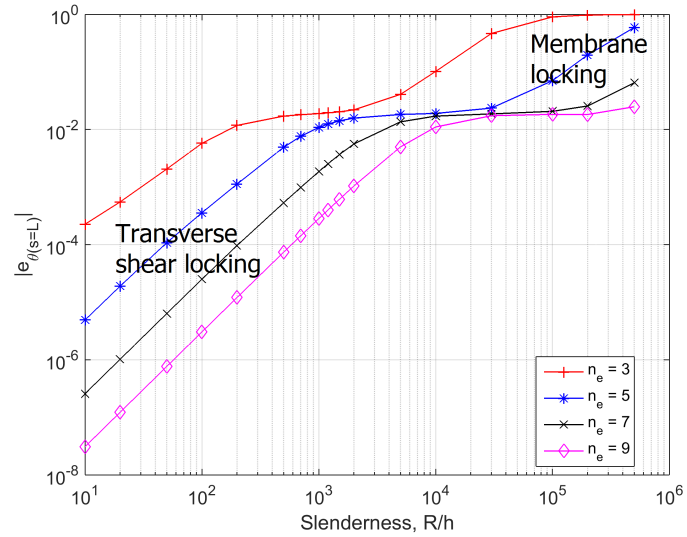

Figure B.4: Relative error in tip rotation for various discretizations with quartic elements.

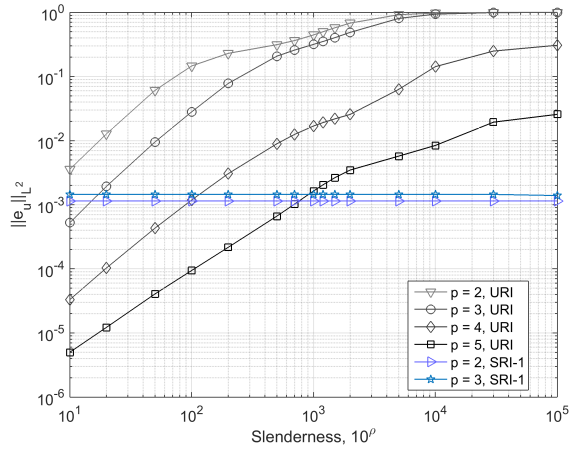

a)

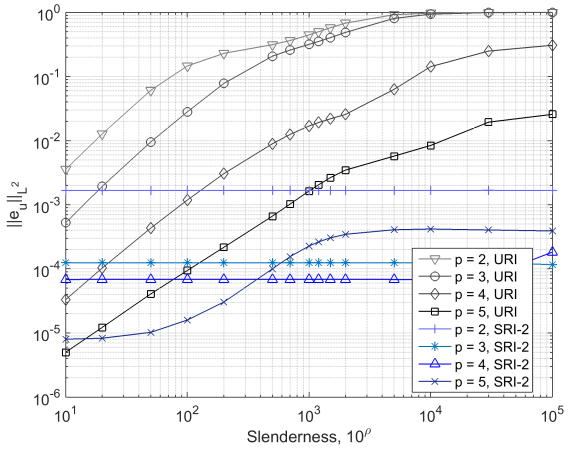

b)

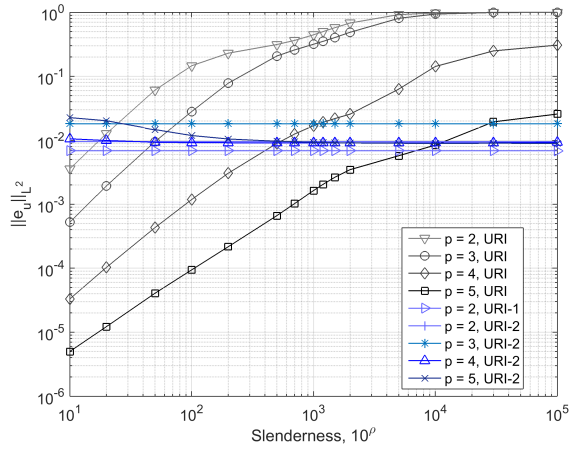

c)

Figure B.5: L^2-norm of relative error in the magnitude of the displacement field with respect to ρ for the various integration rules with quadratic to quintic elements: a) SRI-1, b) SRI-2, c) URI-1 and URI-2.

$$||e_u||_{L^2} = \sqrt{\frac{\int_L \left(\sqrt{(u_t(s))^2 + (u_n(s))^2} - \sqrt{(u_1^h(s))^2 + (u_2^h(s))^2}\right)^2 ds}{\int_L \left(\sqrt{(u_t(s))^2 + (u_n(s))^2}\right)^2 ds}} \tag{B.1}$$

Appendix C

Convergence study of elements with SRI and URI.

The curved cantilever beam subjected to a transverse tip load at the free end, analyzed in Section 6.3.4 has been subject to a closer study of the convergence rates with the proposed selective and uniform reduced integration regimes from Table 6.1.
It was proven through the numerical examples in Section 6.3 that the convergence rates for $p = 3$ or higher depend on the slenderness. The aim with this study is to investigate if there exists an upper and lower bound for the convergence rates with SRI-2, which has shown the best results for higher order elements. Furthermore, the instabilities seen with quadratic elements and coarse discretizations (see e.g. Figure 6.38) have also been investigated in this Appendix.

The convergence is studied for slendernesses from $\rho = -1$ to $\rho = 4$, and are reported in Figures C.1 to C.3 for $p = 3$ to $p = 5$, respectively. Unfortunately, the convergence of the slender beams is terminated when the floating-point accuracy in MATLAB® becomes equal to the 1-norm of the stiffness matrix [31], $||\mathbf{K}||_1$, recognized from the vibrations and increasing errors. For that reason any upper bound cannot be seen for $p = 4$ and $p = 5$. However, for $p = 3$ the initial convergence for $\rho \geq 2$ is of $4th$ order, i.e. $e_u = \mathcal{O}(h^{p+1})$. Further, it seems that the final convergence for all slendernesses is linear, i.e. $e_u = \mathcal{O}(h^1)$, which is also the lower bound. The latter observation is also valid for $p = 4$ and $p = 5$.

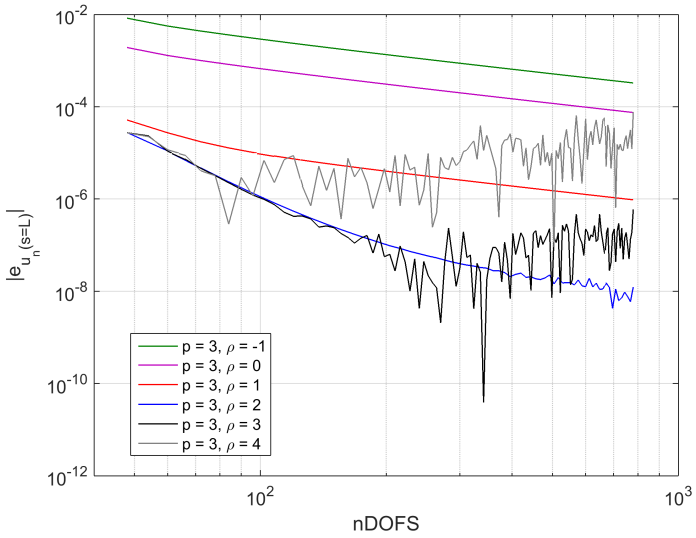

Figure C.1: Convergence of normal tip displacement for $p = 3$ and SRI-2 for various slendernesses.

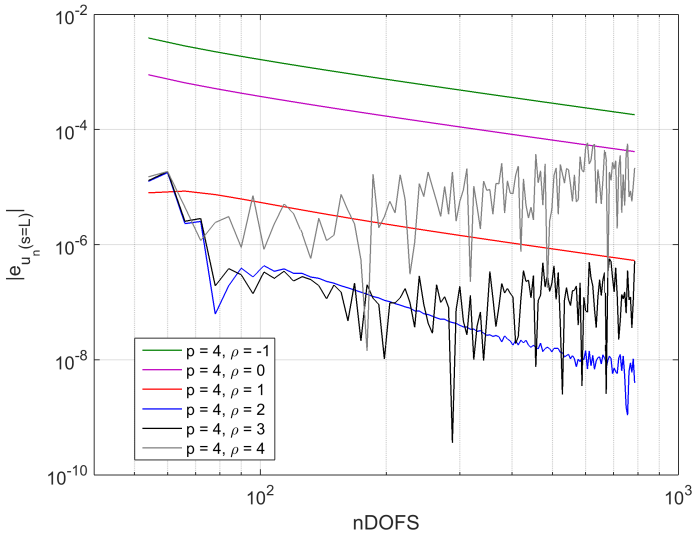

Figure C.2: Convergence of normal tip displacement for $p = 4$ and SRI-2 for various slendernesses.

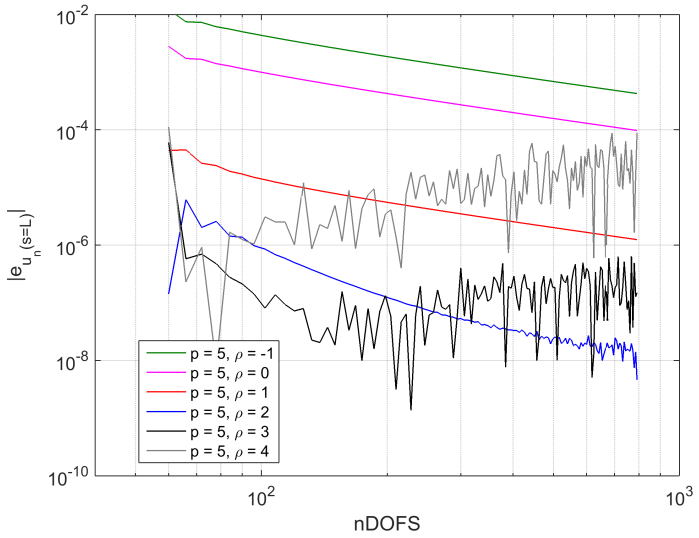

Figure C.3: Convergence of normal tip displacement for $p = 5$ and SRI-2 for various slendernesses.

Furthermore, a refined analysis of the quadratic elements with the different integration models has been carried out in order to investigate the zig-zag pattern that turns up especially for URI-1 and URI-2. Figure C.4 shows convergence plots for all integration models with $\rho = 1$. Together with Figure C.5, showing the sampling points for transverse shear strains for $n_e = 5,6,7,8,9$, it is seen that some discretizations give a more accurate representation of the strains in the element with $n_{GP} = 2$ than others, which causes the oscillating convergence. Nevertheless, all integration models show quadratic convergence in average, independent of the slenderness.

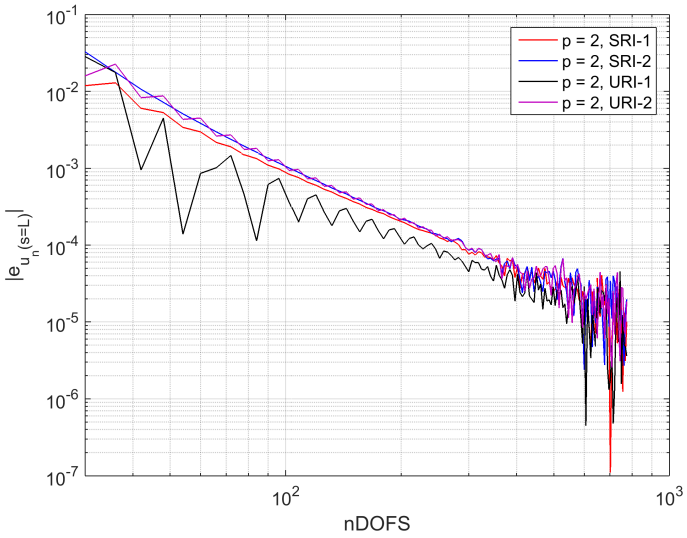

Figure C.4: Convergence of normal tip displacement $p = 2$ for the different integration models.

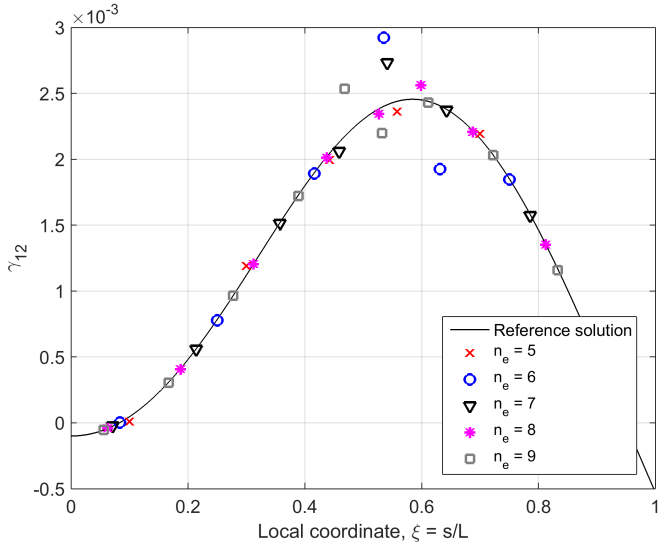

Figure C.5: Transverse shear strain Gauss points for a various number of quadratic NURBS elements with URI-1.

Appendix D

k-refinement of circular arc

This code perform k-refinement of a 90° arc up to a desired number of elements and polynomial order. The code may be used to any NUBRS-geometry by changing the initial geometry.

```
% Purpose: Generate knot vector and Control Points for a given polynomial
% order and number of NURBS elements for a 90 deg. circular arc from
% (0,0,0) to (1,1,0).
%
% Input:    p       = pol. order
%           nELS    = number of spline elements
% Output:   C0      = Control points and weights
%           Xi      = Knot vector
%
% Nested functions:
%   DegreeElevateCurve.m
%           Algorithm A5.9, s207, Piegl: the NURBS-book
%
%   knot_insertion.m
%           Algorithm A5.1, s151, Piegl: the NURBS-book
%
% Coding:
%   Tore Helgedagsrud, 2/2-15
```

```
function [C0,Xi]=NURBS_knots_CP_QCircle(p,nELS)
% Initial geometry
c45=cos(pi()/4);
C0=[0 0 1;0 1 1;0 0 0;1 c45 1];
Xi=[0 0 0 1 1 1];
% Create weighted control points for p=2
C0w=C0;
for i=1:3
    C0w(1:3,i)=C0w(1:3,i).*C0w(4,i);
end
% ORDER ELEVATION
if p>=3
for i=1:p-2
    [~,C0w,Xi] = DegreeElevateCurve(i+1,C0w,Xi,1);
    if i==1 % adjust points and weights for p=3
        C0w(4,2:3)=C0w(2,end-1);
        C0=C0w;
        [~,l]=size(C0);
        for j=1:l
            C0(1:3,j)=C0(1:3,j)./C0(4,j);
        end
        nweight=C0(4,2);
    elseif i==2 % adjust points and weights for p=4
        C0w(4,2:4)=C0w(2,end-1);
        C0w(4,3)=nweight;
        C0=C0w;
        [~,l]=size(C0);
        for j=1:l
            C0(1:3,j)=C0(1:3,j)./C0(4,j);
        end
```

```
        nweight=C0(4,3);
    else% adjust points and weights for p>=5
        C0=C0w;
        [~,l]=size(C0);
        for j=1:l
            C0(1:3,j)=C0(1:3,j)./C0(4,j);
        end
    end
    if i<p-1
    % Weigh points at end of loop
        C0w=C0;
        [~,l]=size(C0w);
    for j=1:l
        C0w(1:3,j)=C0(1:3,j).*C0(4,j);
    end
    end
end
end
% KNOT INSERTION
% weigh control points
C0w=C0;
[~,l]=size(C0w);
for j=1:l
    C0w(1:3,j)=C0w(1:3,j).*C0w(4,j);
end
%Parametric knot values:
if nELS>=2
kv=linspace(0,1,nELS+1);
for i=nELS:-1:2
   [~, Xi, C0w]=knot_insertion(p,Xi,C0w,kv(i),p+1,0,1);
```

```
end
% Back to control points and weights
C0=C0w;
[~,l]=size(C0);
for j=1:l
    C0(1:3,j)=C0(1:3,j)./C0(4,j);
end
end % function
```

Appendix E

Implementation of patch-wise selective reduced integration

The patch-wise integration rule proposed in this thesis may be implemented by adding the following `if`-statements when the element loop is entered (`i_el` $= \mathbb{Z} \in [1, n_e]$):

```
% BEGIN SELECTIVE INTEGRATION SCHEME
% nGP  = number of Gauss points for bending part
% nGPm = number of Gauss points for translational part
    if p==1
        nGP=1; % Conventional reduced integration
        nGPm=1;
    elseif p==2
        nGP=2;
        if i_el==ceil((1+nELS)/2);
            nGPm=2;
        else
            nGPm=1;
        end
```

```
    else
        nGP=p;
        if i_el==nELS;
            nGPm=p-1;
        elseif i_el==1
            nGPm=p-1;;
        else
            nGPm=1;
        end
    end
% END SELECTIVE INTEGRATION SCHEME
```

Appendix F

Report for MekIT'15

The following report, "On Locking-free Methods for Isogeometric Large Deformation Analysis of Geometrically Exact 3D Beams", was written with Siv Bente Raknes and Kjell Magne Mathisen for the MekIT'15 Eight National Conference on Computational Mechanics in Trondheim May 18th-19th, 2015.

8. National Conference on Computational Mechanics
MekIT'15
B. Skallerud and H I Andersson (Eds)

ON LOCKING-FREE METHODS FOR ISOGEOMETRIC LARGE DEFORMATION ANALYSIS OF GEOMETRICALLY EXACT THREE-DIMENSIONAL BEAMS

TORE A. HELGEDAGSRUD, SIV B. RAKNES AND KJELL M. MATHISEN

Department of Structural Engineering
Norwegian University of Science and Technology
Richard Birkelands v 1a, NO-7491 Trondheim, Norway
e-mail: kjell.mathisen@ntnu.no,

Key words: Isogeometric analysis, NURBS, Large deformation analysis, Beam structures, Timoshenko beams, Locking-free elements, Geometrically exact beam theory

Abstract. In this work the geometrically exact three-dimensional beam theory has been used as basis for development of a family of isogeometric large deformation curved beam elements. Geometrically exact three-dimensional beam theory has no restrictions with respect to size of displacements, rotations and deformations. While reduced integration may be used to alleviate transverse shear and membrane locking in standard C^0-continuous Lagrange elements, this does not automatically extend to isogeometric elements. In this study we investigate how uniform and selective reduced patch-wise numerical quadrature rules may be used to obtain locking-free isogeometric large deformation geometrically exact curved beam elements. A carefully selected numerical example serves to illustrate and assess the performance of the various quadrature regimes.

1 INTRODUCTION

The finite element (FE) method has been widely used in nonlinear analysis of three-dimensional (3D) curved beam-like structural systems subjected to large displacements and large strains for several decades. Numerous approaches have been proposed, but the vast majority of them have been limited to considering the beam element reference geometry being a straight line. In this work we aim to extend the *geometrically exact beam model* (GEBM) (see Simo [33] and Simo and Vu-Quoc [34, 35]) based on Reissner's 3D beam theory [31], to model arbitrary shaped curved beam geometry. Several authors, e.g., Stolarski and Belytschko [36] and Ibrahimbegović [22], have observed that increasing the accuracy of the approximated curved beam geometry entails a significant increase in accuracy. The curved 3D geometrically exact beam formulation presented herein is

able to accommodate large displacements, finite rotations and finite strains. In contrast to the corotational-type of beam elements (see, e.g., Crisfield [15] and Mathisen and Bergan [24]), it can be easily extended to higher-order beam elements. Saje [32] extended the GEBM to higher-order two-dimensional (2D) curved beams and Ibrahimbegović [22] to 3D curved beams. However, the latter work was restricted to quadratic hierarchical displacement interpolation. To our knowledge the current work represent the first attempt to extend the GEBM to an arbitrary order formulation. Also our extension of the linearly interpolated straight beam formulation proposed by Simo and Vu-Quoc [34] follows more closely the corotational approach since we derive the energy-conjugate strains from a polar decomposition of the deformation tensor rather than defining stress resultants and couples *a priori* and achieving energy-conjugate strain measures through the variational formulation which was employed in the original work.

With the introduction of isogeometric analysis (IGA) [14, 20], the exact geometry of the structure may be represented by the same approximation functions used to discretize the solution space. Thus, Lagrange polynomials are replaced by *non-uniform rational B-splines* (NURBS) functions, which today constitute the most commonly used technology in computer-aided design (CAD). An inherent property of NURBS functions of order p is that they have higher continuity, C^{p-1} at interior knots, compared to C^0 at nodal points for Lagrange. Patch-wise discretizations with NURBS in combination with the use of the well-known k-refinement and smooth order elevation (see, e.g., [14, 28]), result in improved accuracy and robustness compared to conventional C^0-continuous Lagrange polynomials. Since its conception, IGA has penetrated many areas of computational mechanics, engineering and sciences, in many cases showing improved performance over the standard FE method (FEA). In the area of structural and solid mechanics IGA has been successfully employed in the computation of cable structures [29], 2D and 3D solids, including large deformation, incompressibility, near-incompressibility and plasticity [18, 25], contact [26, 27], fracture [8] and fluid–structure interaction [7].

Unfortunately, as shown by, e.g., Echter and Bishoff [16] and Bouclier *et al.* [9], NURBS-based IGA suffer from the same locking pathologies as FEA. For curved beams this imply that both transverse shear and membrane locking [36] may appear as well with NURBS-based discretizations. Both transverse shear and membrane locking have been attributed to the inability of the interpolation functions to reproduce bending properly in the Kirchhoff limit, i.e., when the thickness becomes very small compared to the length of the beam (or radius of curvature for curved members). The proposed remedies to overcome locking in FEA has recently been applied successfully to eliminate (or at least alleviate) the occurrence of the various locking phenomena also for IGA: 1) Reduced and selective reduced integration [1, 2, 9], 2) NURBS-based discrete shear gap (NURBS-DSG) methods [16, 17], 3) $\overline{\mathrm{B}}$ and $\overline{\mathrm{F}}$ projection techniques [9, 10, 11, 18], 4) assumed natural strain methods [13], 5) hybrid-mixed methods [17], and 6) collocation methods [5, 6]. Apart from the $\overline{\mathrm{B}}$ and $\overline{\mathrm{F}}$ projection methods proposed by Elguedj *et al.* [18] and Bouclier *et al.* [11], these works were limited to linear elastic analysis.

In this context, our aim is to develop a family of NURBS-based geometrically exact 3D beam elements free of locking for the analysis of geometrically nonlinear finite deformation curved beam-like structural systems. In order to do that, we propose an extension of the GEBM presented in [33, 34, 35], to IGA with higher-order NURBS-based discretization of both the geometry, displacement, and the rotational fields. To alleviate locking, we have proposed and validated various quadrature rules based on either uniform or selective reduced integration of the translational and rotational part of the beam model.

This paper is outlined as follows. In Section 2, an interpretation of the GEBM due to Simo [33] and Simo and Vu-Quoc [34, 35] is presented at the continuous level. Section 3 gives an overview of the discretization with B-splines and NURBS. In Section 4, the discrete form of the isogeometric beam element is presented. Section 5 highlight locking effects in curved beams together with a presentation of the various reduced quadrature regimes proposed to alleviate locking. In Section 6, the various proposed integration schemes are tested and compared on a carefully selected curved beam problem. Finally, in Section 7 we draw conclusions.

2 A GEOMETRICALLY EXACT BEAM MODEL

In this section we consider the continuum basis for a geometrically exact beam theory that is optimally suited for computational solution by the finite element method. Geometrically exact beam theory is sometimes referred to as the Reissner's beam theory [31], but strictly speaking, the latter is only exact for a planar beam [30]. The theory presented herein is based on the pioneering work of Simo [33] and Simo and Vu-Quoc [34, 35], that in [35] introduced the still-used terminology GEBM to indicate that Reissner's theory was recasted in a form which is valid for finite rotations. The GEBM has later been revisited and further developed by numerous authors over more than two decades, e.g., Cardona and Géradin [12] and Ibrahimbegović [22], in which the latter extended the theory to handle curved reference geometry.

2.1 Beam geometry in 3D space

The beam is viewed as a 3D body, whose material placement can be described by the line of centroids $\mathcal{B}_0 \subset \mathbb{R}^3$, that has attached at each point a planar non-deformable cross section A_0 in the reference configuration. A local curvilinear coordinate system is chosen to parameterize this line through an arc-length coordinate S along $\mathcal{B}_0$ in the reference configuration. Let $\{\boldsymbol{i}_i(S,t)\}_{i=1,2,3}$ represent a local Cartesian moving frame whose origin is fixed at the centroid at all times, $\boldsymbol{i}_1(S,t)$ remains perpendicular to A and $\{\boldsymbol{i}_\alpha(S,t)\}_{\alpha=2,3}$ span the cross section of the beam in the current configuration. Henceforth, we use the summation convention with Latin indices ranging from 1 to 3 and with Greek indices ranging from 2 to 3. In the reference configuration the orthonormal basis vectors are denoted $\boldsymbol{i}_i^0(S) = \boldsymbol{i}_i(S,0)$ and the associated set of cross section coordinates x_α^0 (see Fig. 1). Let $\boldsymbol{X}(S)$ and $\boldsymbol{x}(S,t)$ define the position of $\mathcal{B}_0$ and $\mathcal{B}$ in the 3D space in the reference

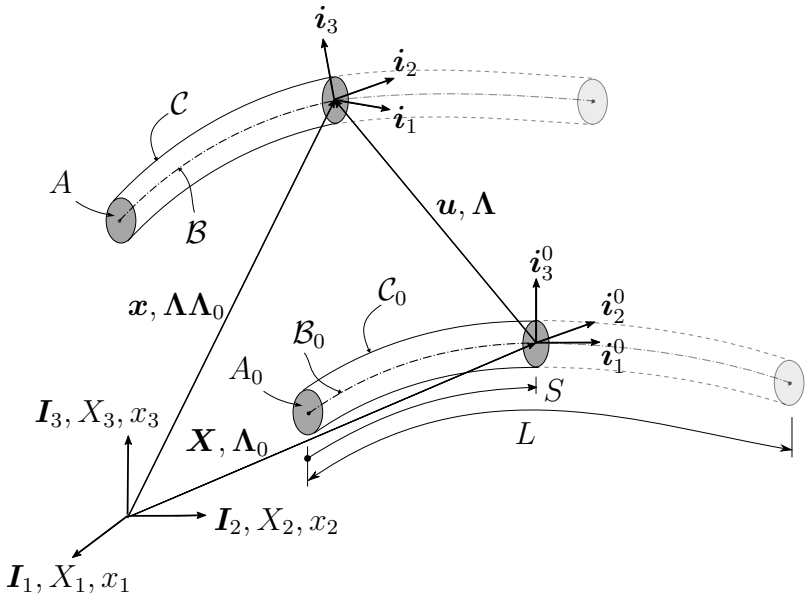

Figure 1: Definition of the various frames and configurations for the geometrically exact beam model.

and current configuration, respectively:

$$\boldsymbol{x}(S,t) = \boldsymbol{X}(S) + \boldsymbol{u}(S,t), \tag{1}$$

where $\boldsymbol{u}(S,t)$ denote the displacement of $\mathcal{B}_0$ at any time t. We assume that the length of the line of centroids $\mathcal{B}_0$ and $\mathcal{B}$ is L_0 and L, respectively.

Without loss of generality, we assume that; (1) the beam has uniform cross sections, i.e., cross-sectional properties remain constant along the entire length of the beam, (2) the beam is unstrained and unstressed in the reference configuration, and (3) the cross sections are initially normal to $\mathcal{B}_0$, hence:

$$\boldsymbol{i}_1^0(S) = \frac{d\boldsymbol{X}(S)}{dS} = \boldsymbol{X}'(S), \tag{2}$$

where prime denotes the derivative with respect to the arc-length coordinate S.

In accordance with standard hypothesis for beams, we further assume that:

(i) The cross sections remain plane and undeformed in the current configuration, i.e., warping effects are not accounted for.

(ii) The cross sections that initially are normal to $\mathcal{B}_0$ do not necessarily remain normal to the deformed line of centroids $\mathcal{B}$ in the current configuration, i.e., transverse shear deformations are accounted for; hence $\boldsymbol{i}_1(S,t)$ remain normal to A but not necessarily tangent to $\mathcal{B}$.

The orientation of the moving local Cartesian frame $\boldsymbol{i}_i(S,t)$ along $S \in [0,L]$, and through time $t \in [0,T]$ is governed by the orthogonal two-point tensor $\boldsymbol{\Lambda}(S,t)$ such that

$$\boldsymbol{i}_i(S,t) = \boldsymbol{\Lambda}(S,t)\boldsymbol{i}_i^0(S) \Rightarrow \boldsymbol{\Lambda}(S,t) = \boldsymbol{i}_i \otimes \boldsymbol{i}_i^0; \| \boldsymbol{i}_i \| = \| \boldsymbol{i}_i^0 \| = 1 \Rightarrow \boldsymbol{\Lambda}^T\boldsymbol{\Lambda} = \boldsymbol{\Lambda}\boldsymbol{\Lambda}^T = \boldsymbol{I}, \quad (3)$$

where $\boldsymbol{I}$ denote the identity tensor. Defining the reference and current configurations with respect to a global Cartesian frame $\boldsymbol{I}_i$, the above transformation reads:

$$\boldsymbol{i}_i(S,t) = \boldsymbol{\Lambda}(S,t)\boldsymbol{\Lambda}_0(S)\boldsymbol{I}_i \Rightarrow \boldsymbol{\Lambda}_0(S) = \boldsymbol{i}_i^0 \otimes \boldsymbol{I}_i, \quad (4)$$

where $\boldsymbol{\Lambda}_0(S)$ defines the orientation of the local Cartesian frame $\boldsymbol{i}_i^0(S)$ in the reference configuration. The current configuration $\mathcal{C}$ of the 3D beam at any time t will then be uniquely determined by the current position and the rotation of the centroid of the cross section, i.e., the origin of the moving frame:

$$\mathcal{C} = \{\boldsymbol{\varphi} = (\boldsymbol{x}, \boldsymbol{\Lambda}) : [0,L] \times [0,T] \longrightarrow \mathbb{R}^3 \times SO(3)\}, \quad (5)$$

where $SO(3)$ represents the special orthogonal (Lie) group, i.e., the group of all rotations about the origin of $\mathbb{R}^3$ under the operation of composition. As a consequence, the 3D kinematic description of the beam is reduced to a 1D kinematic description with the arc-length coordinate S as the only parameter. With these definitions, the 3D beam geometry in the current configuration may be defined as

$$\boldsymbol{x}^{3\mathrm{D}}(S, x_\alpha^0, t) = \boldsymbol{x}(S,t) + \boldsymbol{p}(S, x_\alpha^0, t), \quad (6)$$

where

$$\boldsymbol{p}(S, x_\alpha^0, t) = \boldsymbol{\Lambda}(S,t)\boldsymbol{p}_0(S, x_\alpha^0) = \boldsymbol{\Lambda}(S,t)x_\alpha^0\boldsymbol{i}_\alpha^0(S). \quad (7)$$

$\boldsymbol{p}$ and $\boldsymbol{p}_0$ denotes the cross section position vector along $\mathcal{B}$, i.e., the position of a point P relative to the centroid within a cross section, in the current and reference configuration, respectively. Herein, we only consider quasi-static analysis of beam problems, however, the kinematic description presented in this section is identical for static and dynamic problems. For that reason, "time" and "pseudo-time" as well as "time step", "incremental step" and "load step" are used as equivalents throughout this work.

2.2 Parameterization of finite 3D rotations

The principal difficulty by representing 3D finite rotations by an orthogonal tensor $\boldsymbol{\Lambda}$ is due to the fact that $SO(3)$ is not a linear (vector) space, but rather a manifold, hence consistent linearization and update procedures are no longer straightforward. In the context of time-independent (static) analysis Ibrahimbegović [23] overcame this problem by reparameterizing the configuration space of the beam by making use of the so-called rotation vector $\boldsymbol{\theta}$, defined by

$$\boldsymbol{\theta} = \theta\boldsymbol{n}, \quad (8)$$

where $\boldsymbol{n}$ is a unit vector defining the axis of rotation and $\theta = \sqrt{\theta_1^2 + \theta_2^2 + \theta_3^2}$ is the magnitude of the rotation vector. The relation between $\boldsymbol{\Lambda}$ and $\boldsymbol{\theta}$ is governed by the Rodriguez formula which represents a closed form solution of the exponential mapping

$$\boldsymbol{\Lambda} = \exp[\widetilde{\boldsymbol{\theta}}] = \boldsymbol{I} + \frac{\sin\theta}{\theta}\widetilde{\boldsymbol{\theta}} + \frac{1-\cos\theta}{\theta^2}\widetilde{\boldsymbol{\theta}}\widetilde{\boldsymbol{\theta}}, \tag{9}$$

where $\widetilde{\boldsymbol{\theta}}$ denote the skew-symmetric tensor for which $\boldsymbol{\theta}$ is the axial vector, i.e.:

$$\boldsymbol{\theta} = [\theta_1, \theta_2, \theta_3] \Rightarrow \widetilde{\boldsymbol{\theta}} = \text{skew}[\boldsymbol{\theta}] = \begin{bmatrix} 0 & -\theta_3 & \theta_2 \\ \theta_3 & 0 & -\theta_1 \\ -\theta_2 & \theta_1 & 0 \end{bmatrix}. \tag{10}$$

With such a parameterization, the configuration space $\mathcal{C}$ becomes a linear space:

$$\mathcal{C} = \{\boldsymbol{\varphi} = (\boldsymbol{x}, \boldsymbol{\Lambda}) : [0, L] \times [0, T] \longrightarrow \mathbb{R}^3 \times \mathbb{R}^3\}. \tag{11}$$

The admissible variation $\delta\boldsymbol{\Lambda}$ of the orthogonal tensor of finite rotations can be constructed by making use of the exponential mapping

$$\delta\boldsymbol{\Lambda} = \widetilde{\delta\boldsymbol{w}}\boldsymbol{\Lambda} = \boldsymbol{\Lambda}\widetilde{\delta\boldsymbol{\psi}}. \tag{12}$$

Physically, $\widetilde{\delta\boldsymbol{w}}$ and $\widetilde{\delta\boldsymbol{\psi}}$ represent infinitesimal spatial and material rotations superposed onto the existing rotation $\boldsymbol{\Lambda}$. The spatial spin variables, $\delta\boldsymbol{w}$, are also related to the variation of the rotational vector through [23]

$$\delta\boldsymbol{w} = \boldsymbol{T}_s(\boldsymbol{\theta})\,\delta\boldsymbol{\theta}, \tag{13}$$

where

$$\boldsymbol{T}_s(\boldsymbol{\theta}) = \boldsymbol{I} + \frac{1-\cos\theta}{\theta^2}\widetilde{\boldsymbol{\theta}} + \frac{\theta-\sin\theta}{\theta^3}\widetilde{\boldsymbol{\theta}}\widetilde{\boldsymbol{\theta}}. \tag{14}$$

If the rotational vector is used as parameterization, the rotations become additive and are updated at each iteration. However, the relation in Eq. (13) cease to be bijection respectively for $\theta = 2n\pi$. Consequently, with the parameterization using the rotational vector the angle of rotation is limited to 2π. In large deformation analysis, and especially in dynamic large deformation analysis, angles of rotation can become much larger than 2π. In order to overcome this limitation, Cardona and Géradin [12] and Ibrahimbegović *et al.* [23] proposed to apply Eq. (13) only within an increment and introduced the concept of incremental rotation vector, based on the following update procedure:

(i) At the beginning at the time step $(n+1)$, i.e., for iteration $i = 0$, the incremental rotation vector is set to zero:

$$\boldsymbol{\theta}_{n+1}^0 = \boldsymbol{0}. \tag{15}$$

(ii) At the i^{th} iteration the incremental rotation vector is updated additively

$$\boldsymbol{\theta}_{n+1}^{i} = \boldsymbol{\theta}_{n+1}^{i-1} + \Delta\boldsymbol{\theta}, \tag{16}$$

where $\Delta\boldsymbol{\theta}$ represents the iterative change of the incremental rotation vector.

(iii) The corresponding orthogonal tensor $\boldsymbol{\Lambda}$ is updated using exponential mapping

$$\boldsymbol{\Lambda}_{n+1}^{i} = \exp[\widetilde{\boldsymbol{\theta}_{n+1}^{i}}]\boldsymbol{\Lambda}_{n}. \tag{17}$$

Hence, additive updates still apply within each time step and the amplitude of the rotations are thus just limited within each time step. Alternatively, if the spatial spin variables are used to parameterize the finite rotations, the update is performed according to

$$\boldsymbol{\Lambda}_{n+1}^{i} = \exp[\widetilde{\Delta\boldsymbol{w}}]\boldsymbol{\Lambda}_{n+1}^{i-1}, \tag{18}$$

where $\Delta\boldsymbol{w}$ denote the corresponding iterative change of the spatial spin variables.

2.3 Strain measures

In contrast to previous works [12, 22, 23, 30, 31, 33, 34, 35], where energy-conjugate strain measures were based on stress resultants defined *a priori*, Auricchio *et al.* [3] derived a GEBM in which proper strain measures at any point of the beam in $\mathcal{C}$ were obtained by a polar decomposition of the deformation gradient $\boldsymbol{F}$. With the definition of the 3D geometry in $\mathcal{C}$, see Eq. (6), the deformation gradient may be expressed as

$$\boldsymbol{F} = \frac{\partial \boldsymbol{x}^{\text{3D}}}{\partial x_i^0} \otimes \boldsymbol{i}_i^0 = \left(\boldsymbol{x}' + \boldsymbol{\Lambda}' x_\alpha^0 \boldsymbol{i}_\alpha^0\right) \otimes \boldsymbol{i}_1^0 + \boldsymbol{i}_\alpha \otimes \boldsymbol{i}_\alpha^0. \tag{19}$$

Utilizing Eq. (12), the derivative of the rotation tensor $\boldsymbol{\Lambda}$ with respect to S may be expressed as

$$\boldsymbol{\Lambda}' = \widetilde{\boldsymbol{\kappa}}\boldsymbol{\Lambda} \Leftrightarrow \widetilde{\boldsymbol{\kappa}} = \boldsymbol{\Lambda}'\boldsymbol{\Lambda}^T, \tag{20}$$

where $\widetilde{\boldsymbol{\kappa}} = \widetilde{\boldsymbol{\kappa}}(S)$ is a skew-symmetric tensor represented by the axial vector $\boldsymbol{\kappa}$ denoting the spatial rotational (torsional and bending) strains, i.e., the spatial curvature. Furthermore, adding and subtracting the tensor $\boldsymbol{i}_1 \otimes \boldsymbol{i}_1^0$ to the right-hand-side and recognizing that $\boldsymbol{i}_i \otimes \boldsymbol{i}_i^0 = \boldsymbol{\Lambda}$, we may rewrite Eq. (19) and make a material polar decomposition of $\boldsymbol{F}$

$$\boldsymbol{F} = \boldsymbol{\Lambda}\left\{\boldsymbol{I} + \left[\boldsymbol{\Lambda}^T\left(\boldsymbol{x}' - \boldsymbol{i}_1\right) + \boldsymbol{\Lambda}^T\widetilde{\boldsymbol{\kappa}} x_\alpha^0 \boldsymbol{i}_\alpha^0\right] \otimes \boldsymbol{i}_1^0\right\} = \boldsymbol{\Lambda}\boldsymbol{U}. \tag{21}$$

In Eq. (21) $\boldsymbol{U}$ defines the right (current local) stretch tensor from which we may derive the Biot strain measure $\boldsymbol{B}$ (often referred to as the Jaumann strains), that are objective corotated engineering strains independent of rigid body displacements

$$\boldsymbol{B} = \boldsymbol{\Lambda}^T\boldsymbol{F} - \boldsymbol{I} = \boldsymbol{U} - \boldsymbol{I} = \boldsymbol{\varepsilon} \otimes \boldsymbol{i}_1 \quad \text{with} \quad \boldsymbol{\varepsilon} = \boldsymbol{\Lambda}^T\left(\boldsymbol{\gamma} + \widetilde{\boldsymbol{\kappa}}\boldsymbol{p}\right) = \boldsymbol{\Gamma} + \widetilde{\boldsymbol{K}}\boldsymbol{p}_0, \tag{22}$$

where $\boldsymbol{\varepsilon}$ represents a generalized convected strain measure, $\boldsymbol{\gamma}$ the translational (axial and transverse shear) spatial strains and $\boldsymbol{\kappa}$ the rotational (torsional and bending) spatial curvature strain vector. The corresponding convected material strains are represented by upper case letters $\boldsymbol{\Gamma}$ and $\boldsymbol{K}$. The relationship between the material and spatial form may then be expressed as

$$\begin{aligned} \boldsymbol{\Gamma} &= \boldsymbol{\Lambda}^T\boldsymbol{\gamma} \quad \text{with} \quad \boldsymbol{\gamma} = \boldsymbol{x}' - \boldsymbol{i}_1, \\ \boldsymbol{K} &= \boldsymbol{\Lambda}^T\boldsymbol{\kappa} \quad \text{with} \quad \boldsymbol{\kappa} = \boldsymbol{T}_s(\boldsymbol{\theta})\boldsymbol{\theta}'. \end{aligned} \tag{23}$$

A physical interpretation of the spatial strain measures is that the components of $\boldsymbol{\gamma}$ represent the true axial and transverse shear strain measures with respect to the current moving frame $\boldsymbol{i}_i(S,t)$, e.g., γ_1 represents the elongation of an infinitesimal fiber in the direction normal to the cross section while γ_2 and γ_3 are the corresponding transverse shear strains. Similarly, the three components of $\boldsymbol{\kappa}$, represents the true torsional (κ_1) and bending strain measures (κ_2 and κ_3) with respect to the moving frame.

In order to establish an expression for the internal virtual work, we have to establish the (virtual) variation of the strain measures established above. To do so, we introduce the corotational or Lie variation for the current spatial strain measure, defined as

$$\delta_{\mathcal{L}}(\cdot) = \boldsymbol{\Lambda}\delta[\boldsymbol{\Lambda}^T(\cdot)], \tag{24}$$

in which the quantity first goes trough a pull-back rotation from the current to the reference configuration, followed by the virtual variation and finally by a push-forward rotation to the current configuration, for more details see, e.g., Cardona and Géradin [12]. The Lie derivative of the translational part of the current strain measure is obtained as

$$\delta_{\mathcal{L}}(\boldsymbol{\gamma}) = \boldsymbol{\Lambda}\delta(\boldsymbol{\Lambda}^T\boldsymbol{\gamma}) = \boldsymbol{\Lambda}\delta\boldsymbol{\Gamma}, \tag{25}$$

where

$$\delta\boldsymbol{\Gamma} = \delta(\boldsymbol{\Lambda}^T\boldsymbol{\gamma}) = \delta\boldsymbol{\Lambda}^T\boldsymbol{\gamma} + \boldsymbol{\Lambda}^T\delta\boldsymbol{\gamma} = \boldsymbol{\Lambda}^T(\delta\boldsymbol{x}' - \widetilde{\delta\boldsymbol{w}}\boldsymbol{x}') = \boldsymbol{\Lambda}^T(\delta\boldsymbol{x}' + \boldsymbol{x}' \times \delta\boldsymbol{w}). \tag{26}$$

After a push-forward rotation to the current configuration we obtain the Lie variation of the translational spatial strain measure

$$\delta_{\mathcal{L}}(\boldsymbol{\gamma}) = \boldsymbol{\Lambda}\delta(\boldsymbol{\Lambda}^T\boldsymbol{\gamma}) = \boldsymbol{\Lambda}\boldsymbol{\Lambda}^T(\delta\boldsymbol{x}' + \boldsymbol{x}' \times \delta\boldsymbol{w}) = \delta\boldsymbol{x}' + \boldsymbol{x}' \times \delta\boldsymbol{w}. \tag{27}$$

The variation of the rotational strain parameter can be obtained similarly by utilizing once again the variation of a rotation tensor (see Eq. (12)), and applying the chain rule for partial derivatives. Recall the definition of the skew-symmetric of the curvature tensor from Eq. (20), its variation may now be obtained as

$$\begin{aligned} \delta\widetilde{\boldsymbol{\kappa}} &= \delta(\boldsymbol{\Lambda}'\boldsymbol{\Lambda}^T) = \delta\boldsymbol{\Lambda}'\boldsymbol{\Lambda}^T + \boldsymbol{\Lambda}'\delta\boldsymbol{\Lambda}^T = (\widetilde{\delta\boldsymbol{w}}\boldsymbol{\Lambda})'\boldsymbol{\Lambda}^T - \boldsymbol{\Lambda}'(\boldsymbol{\Lambda}^T\widetilde{\delta\boldsymbol{w}}) \\ &= \widetilde{\delta\boldsymbol{w}}'\boldsymbol{\Lambda}\boldsymbol{\Lambda}^T + \widetilde{\delta\boldsymbol{w}}\boldsymbol{\Lambda}'\boldsymbol{\Lambda}^T - \boldsymbol{\Lambda}'\boldsymbol{\Lambda}^T\widetilde{\delta\boldsymbol{w}} = \widetilde{\delta\boldsymbol{w}}' + \widetilde{\delta\boldsymbol{w}}\widetilde{\boldsymbol{\kappa}} - \widetilde{\boldsymbol{\kappa}}\widetilde{\delta\boldsymbol{w}}. \end{aligned} \tag{28}$$

Utilizing Lie algebra, $\widetilde{\boldsymbol{a}}\widetilde{\boldsymbol{c}} - \widetilde{\boldsymbol{c}}\widetilde{\boldsymbol{a}} = (\widetilde{\boldsymbol{a}\boldsymbol{c}})$, the expression for the variation of the axial (curvature) vector may be written

$$\delta\boldsymbol{\kappa} = \delta\boldsymbol{w}' + \widetilde{\delta\boldsymbol{w}}\boldsymbol{\kappa}. \tag{29}$$

With this result in hand we obtain the following expression for the variation of the curvature $\boldsymbol{K}$

$$\delta\boldsymbol{K} = \delta(\boldsymbol{\Lambda}^T\boldsymbol{\kappa}) = \delta\boldsymbol{\Lambda}^T\boldsymbol{\kappa} + \boldsymbol{\Lambda}^T\delta\boldsymbol{\kappa} = (\widetilde{\delta\boldsymbol{w}}\boldsymbol{\Lambda})^T\boldsymbol{\kappa} + \boldsymbol{\Lambda}^T(\delta\boldsymbol{w}' + \widetilde{\delta\boldsymbol{w}}\boldsymbol{\kappa}) = \boldsymbol{\Lambda}^T\delta\boldsymbol{w}'. \tag{30}$$

Using the expression for the Lie derivative the variation of the rotational spatial strain now take the form

$$\delta_{\mathcal{L}}(\boldsymbol{\kappa}) = \boldsymbol{\Lambda}\delta(\boldsymbol{\Lambda}^T\boldsymbol{\kappa}) = \boldsymbol{\Lambda}\delta(\boldsymbol{K}) = \delta\boldsymbol{w}'. \tag{31}$$

2.4 Stress resultants, constitutive equations and balance laws

Work conjugate with the strain measures in Eq. (23), we define material and spatial stress resultants and couples, $\boldsymbol{N}, \boldsymbol{M}$ and $\boldsymbol{n}, \boldsymbol{m}$, where the latter are obtained by a push-forward of the convected resultants and couples:

$$\boldsymbol{n} = \boldsymbol{\Lambda}\boldsymbol{N} \quad \text{and} \quad \boldsymbol{m} = \boldsymbol{\Lambda}\boldsymbol{M}. \tag{32}$$

The first component of the force resultants $\boldsymbol{n}, \boldsymbol{N}$ denotes the axial force in the direction of $\boldsymbol{i}_1, \boldsymbol{i}_1^0$, while component 2 and 3 denote the transverse shear forces in the directions of $\boldsymbol{i}_\alpha, \boldsymbol{i}_\alpha^0$, respectively. Similarly, the first component of the stress couples $\boldsymbol{m}, \boldsymbol{M}$ denotes the torsional moment in the direction of $\boldsymbol{i}_1, \boldsymbol{i}_1^0$, while component 2 and 3 denote the bending moments in the directions of $\boldsymbol{i}_\alpha, \boldsymbol{i}_\alpha^0$, respectively. The stress resultants and couples may be obtained by integrating the first Piola–Kirchhoff stress tensor $\boldsymbol{P}$ and the Biot stress tensor $\boldsymbol{T}_{\mathrm{B}}$ over the reference cross section A_0, respectively.

For a hyperelastic material the convected resultants may be obtained from a strain energy function $\Psi(\boldsymbol{\Gamma}, K)$ through the relations

$$\boldsymbol{N} = \frac{\Psi(\boldsymbol{\Gamma}, K)}{\boldsymbol{\Gamma}} \quad \text{and} \quad \boldsymbol{M} = \frac{\Psi(\boldsymbol{\Gamma}, K)}{\boldsymbol{K}}. \tag{33}$$

In our study we assume that we have a linear isotropic relation between stresses and strains. This results in a St. Venant–Kirchhoff-type constitutive relation that may be expressed in terms of E and G, denoting the Young's and the shear modulus, respectively. The corresponding resultant constitutive laws reads

$$\boldsymbol{N} = \begin{bmatrix} N^1 \\ N^2 \\ N^3 \end{bmatrix} = \begin{bmatrix} EA_0 & 0 & 0 \\ 0 & G\bar{A}_{02} & 0 \\ 0 & 0 & G\bar{A}_{03} \end{bmatrix} \begin{bmatrix} \Gamma_1 \\ \Gamma_2 \\ \Gamma_3 \end{bmatrix} = \boldsymbol{C}_N\boldsymbol{\Gamma} \text{ with } \begin{matrix} N^i = \boldsymbol{N}\cdot\boldsymbol{i}_i^0 \\ \Gamma_i = \boldsymbol{\Gamma}\cdot\boldsymbol{i}_i^0 \end{matrix}, \tag{34}$$

and

$$\boldsymbol{M} = \begin{bmatrix} M^1 \\ M^2 \\ M^3 \end{bmatrix} = \begin{bmatrix} GI_T & 0 & 0 \\ 0 & EI_{33} & -EI_{32} \\ 0 & -EI_{23} & EI_{22} \end{bmatrix} \begin{bmatrix} K_1 \\ K_2 \\ K_3 \end{bmatrix} = \boldsymbol{C}_M\boldsymbol{\Gamma} \text{ with } \begin{matrix} M^i = \boldsymbol{M}\cdot\boldsymbol{i}_i^0 \\ K_i = \boldsymbol{K}\cdot\boldsymbol{i}_i^0 \end{matrix}, \tag{35}$$

where $G\bar{A}_{0\alpha}$ denotes the reduced cross section shear area in the direction of $\boldsymbol{i}^0_\alpha$, I_T the torsional stiffness and $I_{\alpha\beta} = \int_{A_0} x^0_\alpha x^0_\beta dA$ the cross section second moment of area.

The corresponding relation between the spatial stress resultants and couples energy conjugate to $\boldsymbol{\gamma}$ and $\boldsymbol{\kappa}$ may be obtained by combining Eqs. (23), (32), (34) and (35)

$$\boldsymbol{n} = \boldsymbol{\Lambda} \boldsymbol{C}_N \boldsymbol{\Lambda}^T \boldsymbol{\gamma} \quad \text{and} \quad \boldsymbol{m} = \boldsymbol{\Lambda} \boldsymbol{C}_M \boldsymbol{\Lambda}^T \boldsymbol{\kappa}. \tag{36}$$

As shown by Reissner [30, 31], Simo [33] and Simo and Vu-Quoc [34, 35] , the beam balance equations can be obtained without any simplifying hypothesis regarding geometry, and size of displacements and rotations, hence, this theory is referred to as geometrically exact. If we consider $\bar{\boldsymbol{n}}$ and $\bar{\boldsymbol{m}}$ to be the externally applied force and moment per unit length the time-independent linear and angular momentum balance (strong form) equations for the GEBM reads:

$$\boldsymbol{n}' + \bar{\boldsymbol{n}} = \boldsymbol{0} \quad \text{and} \quad \boldsymbol{m}' + \boldsymbol{x}' \times \boldsymbol{n} + \bar{\boldsymbol{m}} = \boldsymbol{0}. \tag{37}$$

A unique strong form solution must satisfy the balance equations stated in Eq. (37) supplemented with the boundary conditions:

$$\begin{aligned} &\boldsymbol{x} = \bar{\boldsymbol{x}} \ \text{ on } \ \mathcal{B}^\varphi_x \quad \text{and} \quad \boldsymbol{\Lambda} = \bar{\boldsymbol{\Lambda}} \ \text{ on } \ \mathcal{B}^\varphi_\Lambda, \\ &\boldsymbol{n} = \bar{\boldsymbol{n}} \ \text{ on } \ \mathcal{B}^\sigma_n \quad \text{and} \quad \boldsymbol{m} = \bar{\boldsymbol{m}} \ \text{ on } \ \mathcal{B}^\sigma_m, \end{aligned} \tag{38}$$

where $\mathcal{B}^\varphi_x$, $\mathcal{B}^\varphi_\Lambda$, $\mathcal{B}^\sigma_n$ and $\mathcal{B}^\sigma_m$ denote the part of the beam where displacements, rotations, stress resultants and couples are prescribed, respectively.

2.5 Variational equations

The variational or weak form of the static equilibrium equations states that the solution to the beam problem (37) with the associated boundary conditions (38) is the motion $\boldsymbol{\varphi} = (\boldsymbol{x}, \boldsymbol{\Lambda}) \in \mathcal{V}$ that satisfies the principle of virtual work, which states that

$$\delta W = \delta W^{\text{int}} + \delta W^{\text{ext}}, \tag{39}$$

for all admissible virtual variations $\delta\boldsymbol{\varphi} = (\delta\boldsymbol{x}, \delta\boldsymbol{w})$. The internal virtual work carried out by the spatial stress resultants and couples over the associated admissible variations in the current configuration is given by:

$$\delta W^{\text{int}} = \delta W^{\text{int}}(\boldsymbol{\varphi}, \delta\boldsymbol{\varphi}) = \int_L \{\delta_{\mathcal{L}}\boldsymbol{\gamma}\cdot\boldsymbol{n} + \delta_{\mathcal{L}}\boldsymbol{\kappa}\cdot\boldsymbol{m}\} d\ell = \int_L \{(\delta\boldsymbol{x}' + \boldsymbol{x}'\times\delta\boldsymbol{w})\cdot\boldsymbol{n} + \delta\boldsymbol{w}'\cdot\boldsymbol{m}\} d\ell. \tag{40}$$

The external virtual work due to the distributed externally applied force and moment per unit length may be expressed as:

$$\delta W^{\text{ext}} = \delta W^{\text{ext}}(\delta\boldsymbol{\varphi}) = -\int_L \{\delta\boldsymbol{x}\cdot\bar{\boldsymbol{n}} + \delta\boldsymbol{w}\cdot\bar{\boldsymbol{m}}\} d\ell. \tag{41}$$

Combining the internal and external virtual work terms, we obtain the following spatial form of the variational formulation of the GEBM: Find $\boldsymbol{\varphi} = (\boldsymbol{x}, \boldsymbol{\Lambda}) \in \mathcal{S}$, such that $\forall \delta\boldsymbol{\varphi} = (\delta\boldsymbol{x}, \delta\boldsymbol{w}) \in \mathcal{V}$:

$$\int_L \{(\delta\boldsymbol{x}' + \boldsymbol{x}' \times \delta\boldsymbol{w}) \cdot \boldsymbol{n} + \delta\boldsymbol{w}' \cdot \boldsymbol{m}\} d\ell = \int_L \{\delta\boldsymbol{x} \cdot \bar{\boldsymbol{n}} + \delta\boldsymbol{w} \cdot \bar{\boldsymbol{m}}\} d\ell. \tag{42}$$

In the formulation, $\mathcal{S}$ and $\mathcal{V}$ are suitable defined trial and test function sets for the geometrically exact beam problem. Strictly speaking, the space of kinematically admissible variations for the GEBM is the tangent space at $\boldsymbol{\varphi}$ to the abstract configuration manifold $\mathcal{C}$, which is denoted $\mathcal{T}_\varphi\mathcal{C}$. Hence, in general $\delta\boldsymbol{\varphi}$ must be a member of the tangent space $\mathcal{T}_\varphi\mathcal{C}$. However, as pointed out in Section 2.2, when $\delta\boldsymbol{w}$ is an infinitesimal rotation superposed on the finite rotation $\boldsymbol{\Lambda}$ and the update is performed as an exponential map, the space of admissible variations is defined as:

$$\mathcal{V} = \{\delta\boldsymbol{\varphi} = (\delta\boldsymbol{x}, \delta\boldsymbol{w}) : [0, L] \times [0, T] \in \mathbb{R}^3 \times \mathbb{R}^3 | \delta\boldsymbol{x} = \boldsymbol{0} \text{ on } \mathcal{B}_x^\varphi \text{ and } \delta\boldsymbol{w} = \boldsymbol{0} \text{ on } \mathcal{B}_\Lambda^\varphi\}. \tag{43}$$

2.6 Linearized variational equations

The virtual work equations for the finite deformation GEBM are in general highly nonlinear. For this reason the problem is reduced to a set of nonlinear algebraic equations, whose solution is obtained utilizing an incremental-iterative Newton–Raphson approach. In order to obtain the consistent tangent of Newton's method, i.e., the tangent granting quadratic convergence rate, a consistent linearization of the associated variational equations must be performed. Denoting $\mathcal{L}[\delta W(\boldsymbol{\varphi}, \delta\boldsymbol{\varphi}, \Delta\boldsymbol{\varphi})]$ the linear part of the virtual work $\delta W(\boldsymbol{\varphi}, \delta\boldsymbol{\varphi})$ at the current configuration $\boldsymbol{\varphi} = (\boldsymbol{x}, \boldsymbol{\Lambda})$, by definition we have

$$\mathcal{L}[\delta W(\boldsymbol{\varphi}, \delta\boldsymbol{\varphi}, \Delta\boldsymbol{\varphi})] = \delta W(\boldsymbol{\varphi}, \delta\boldsymbol{\varphi}) + \Delta[\delta W(\boldsymbol{\varphi}, \delta\boldsymbol{\varphi}, \Delta\boldsymbol{\varphi})], \tag{44}$$

where $\delta W(\boldsymbol{\varphi}, \delta\boldsymbol{\varphi})$ evaluated at $\boldsymbol{\varphi} = (\boldsymbol{x}, \boldsymbol{\Lambda})$ gives rise to the internal and external forces, whose difference yield the so-called unbalanced or residual forces, whereas $\Delta[\delta W(\boldsymbol{\varphi}, \delta\boldsymbol{\varphi}, \Delta\boldsymbol{\varphi})]$ is the incremental virtual work depending linearly on the configuration increments $\Delta\boldsymbol{\varphi} = (\Delta\boldsymbol{x}, \Delta\boldsymbol{w})$, yield the so-called consistent tangent stiffness.

When performing the consistent linearization of the variational equations, it is important to recall that the space of finite rotations is not linear, but a manifold, $\mathcal{T}_\varphi\mathcal{C}$. However, as pointed out in the previous section, when applying appropriate parameterization of the finite rotations the consistent linearized weak form is calculated with the directional rather than the covariant derivative of the variational equations. Hence the admissible space for the incremental displacements is defined as:

$$\mathcal{V} = \{\Delta\boldsymbol{\varphi} = (\Delta\boldsymbol{x}, \Delta\boldsymbol{w}) : [0, L] \times [0, T] \in \mathbb{R}^3 \times \mathbb{R}^3 | \Delta\boldsymbol{x} = \boldsymbol{0} \text{ on } \mathcal{B}_x^\varphi \text{ and } \Delta\boldsymbol{w} = \boldsymbol{0} \text{ on } \mathcal{B}_\Lambda^\varphi\}. \tag{45}$$

The incremental spatial strain measures are obtained similarly to the variational spatial strain measures defined in Eqs.(27) and (31)

$$\Delta_{\mathcal{L}}(\boldsymbol{\gamma}) = \Delta\boldsymbol{x}' + \boldsymbol{x}' \times \Delta\boldsymbol{w} \quad \text{and} \quad \Delta_{\mathcal{L}}(\boldsymbol{\kappa}) = \Delta\boldsymbol{w}'. \tag{46}$$

The linearized virtual spatial strain measures may now be obtained by taking the direction derivative of the variational spatial strain measures defined in Eqs.(27) and (31)

$$\Delta_{\mathcal{L}}\delta_{\mathcal{L}}(\boldsymbol{\gamma}) = (\delta\boldsymbol{x}' + \boldsymbol{x}' \times \delta\boldsymbol{w}) \times \Delta\boldsymbol{w} - \delta\boldsymbol{w} \times \Delta\boldsymbol{x}' \quad \text{and} \quad \Delta_{\mathcal{L}}\delta_{\mathcal{L}}(\boldsymbol{\kappa}) = \delta\boldsymbol{w}' \times \Delta\boldsymbol{w}. \tag{47}$$

The incremental virtual work results in two contributions to the tangent stiffness, the material and geometrical part. With the expressions for the incremental and linearized virtual spatial strain measures at hand the material part is obtained by keeping the geometry constant varying the material resultants

$$\int_L \{(\delta\boldsymbol{x}' + \boldsymbol{x}' \times \delta\boldsymbol{w}) \cdot \boldsymbol{\Lambda}\boldsymbol{C}_N\boldsymbol{\Lambda}^T(\Delta\boldsymbol{x}' + \boldsymbol{x}' \times \Delta\boldsymbol{w}) + (\delta\boldsymbol{w}') \cdot \boldsymbol{\Lambda}\boldsymbol{C}_M\boldsymbol{\Lambda}^T\Delta\boldsymbol{w}'\}d\ell, \tag{48}$$

whereas the geometric part is obtained keeping the material properties constant while varying the geometry

$$\int_L \{[(\delta\boldsymbol{x}' + \boldsymbol{x}' \times \delta\boldsymbol{w}) \times \Delta\boldsymbol{w} - \delta\boldsymbol{w} \times \Delta\boldsymbol{x}'] \cdot \boldsymbol{n} + (\delta\boldsymbol{w}' \times \Delta\boldsymbol{w}) \cdot \boldsymbol{m}\}d\ell. \tag{49}$$

3 DISCRETIZATION WITH B-SPLINES AND NURBS

The continuous formulation presented in the previous section is discretized using either B-splines or NURBS. For B-splines or NURBS basis functions of order $p \geq 2$ this provides among others, the advantage of higher inter-element continuity within patches which ensures smooth representation without kinks between the elements. In what follows, some basic concepts for B-spline and NURBS curves are briefly reviewed, the reader is referred to [14, 20, 28] for further details.

Geometrical objects are in general defined by explicit, implicit or parametric equations. NURBS curves, surfaces and volumes belong to the latter category, as they depend on a set of continuous parameters. NURBS are a generalization of B-splines and are constructed by projective transformation of B-spline basis functions. Contrary to the Lagrange basis functions that are local to elements, the B-spline parametric space is local to "patches". Patches are subdomains within which polynomial order of the basis functions and material parameters are assumed to be kept constant.

Univariate B-spline basis functions are defined by a *knot vector* Ξ, which is a set of non-decreasing parametric coordinates. The parameter space is the space where the basis functions are defined, and is partitioned into knot spans between the knots. The knot vector is written as:

$$\Xi = \{\xi_1, \xi_2, \ldots, \xi_{n+p+1}\}, \tag{50}$$

where ξ_i is the ith knot value, i is the knot index, $i = 1, 2, \ldots, n+p+1$, p is the polynomial order, and n is the number of basis functions. If a knot ξ_i is placed m_i times at the same location in the parametric space, the *multiplicity* of knot ξ_i is m_i, and the functions are C^{p-m_i} continuous at that location. If the knot vector has no repeated interior knots

ξ_i, it defines $n-p$ non-zero knot spans (elements). If the knots are equally spaced; $\xi_{i+1} - \xi_i = \text{const.}, \forall i \in [1, n+p]$, the knot vector is said to be *uniform*, otherwise it is denoted as *non-uniform*. Furthermore Ξ is termed an *open* knot vector if the first and last entries have multiplicity $p+1$. In what follows we assume that Ξ is an open non-uniform knot vector.

B-spline basis functions for a given order are defined recursively by the Cox-de Boor recursion formula:

$$N_i^0(\xi) = \begin{cases} 1, & \text{if } \xi_i \leq \xi < \xi_{i+1}, \\ 0, & \text{otherwise,} \end{cases} \tag{51}$$

and

$$N_i^p(\xi) = \frac{\xi - \xi_i}{\xi_{i+p} - \xi_i} N_i^{p-1}(\xi) + \frac{\xi_{i+p+1} - \xi}{\xi_{i+p+1} - \xi_{i+1}} N_{i+1}^{p-1}(\xi), \ \ \forall p \geq 1. \tag{52}$$

The order of the basis functions is equal to its polynomial degree, i.e., $p = 0, 1, 2, 3,$ etc., describes constant, linear, quadratic, cubic, etc., piecewise polynomials, respectively. The B-spline basis functions satisfy the following important properties:

1. Partition of unity: $\sum_{i=1}^{n} N_i^p(\xi) = 1, \ \ \forall \xi \in [\xi_1, \xi_{n+p+1}]$.
2. Local support: $\forall i$ the support of N_i^p is compact and contained in the interval $[\xi_i, \xi_{i+p+1}]$.
3. Non-negativeness: $N_i^p(\xi) \geq 0, \ \ \forall \xi \in [\xi_i, \xi_{i+p+1}]$.
4. Continuity: $\forall i$ each N_i^p is C^{p-m_i} continuous in the interval $[\xi_i, \xi_{i+p+1}]$.
5. Non-interpolatory: Except for the end knots or knots where the multiplicity $m_i = p-1$, $N_i^p(\xi_j) \neq \delta_{ij}$.
6. For $p = 0$ and $p = 1$, B-spline and Lagrange basis functions coincide.

A B-spline curve in $\mathbb{R}^{n_{sd}}$ can be expressed as a linear combination of the basis functions N_i^p with the spatial coordinates $\mathbf{P}_i$ of the *control points*:

$$\mathbf{C}(\xi) = \sum_{i=1}^{n} N_i^p(\xi) \mathbf{P}_i, \tag{53}$$

where n_{sd} denotes the number of spatial dimensions and $\mathbf{P}_i \in \mathbb{R}^{n_{sd}}$. What separates B-spline curves from curves constructed from a linear combination of the Lagrange basis functions with the nodal point coordinates, is that B-spline curves are related to a set of control point coordinates. These control points are the equivalent to the nodes, but B-spline curves will generally not pass through the control points.

NURBS curves can be constructed analogously to B-spline curves by replacing N_i^p with rational basis functions R_i^p:

$$\mathbf{C}(\xi) = \sum_{i=1}^{n} R_i^p(\xi)\mathbf{P}_i, \tag{54}$$

where the rational basis functions are obtained from a weighted linear combination of the B-spline functions by

$$R_i^p(\xi) = \frac{N_i^p w_i}{\sum_{j=1}^{n} N_j^p(\xi) w_j} = \frac{N_i^p w_i}{W(\xi)}. \tag{55}$$

where w_i is the weight associated with the ith control point $\mathbf{P}_i$. The weights normally have to fulfil the condition

$$w_i > 0 \ \ \forall i \in [1, n]\,. \tag{56}$$

As a NURBS curve does not necessarily interpolate control points, the weights can be used to influence the shape of the curve independently from the position of the control points. If the weights are increased, the curve approaches the shape of the control polygon, containing all the control points. While B-spline curves in general are not able to represent conic sections, by selecting appropriate values for the weights NURBS curves may represent conic sections, like circles, exactly. Provided that all of the weight functions are unity, NURBS basis functions are identical to B-spline functions. Thus, NURBS inherits the fundamental properties of the B-spline basis functions.

4 ISOGEOMETRIC GEOMETRICAL EXACT BEAM FORMULATION

Following the concept of isogeometric analysis [20], the continuous formulation presented in Section 2 is discretized using NURBS basis functions. We assume that NURBS of order p and continuity C^{p-1} are used to discretize both the geometry in the reference and the current configuration, $\boldsymbol{X}$ and $\boldsymbol{x}$, and the virtual and incremental displacement and rotational fields, $\delta\boldsymbol{\varphi} = (\delta\boldsymbol{x}, \delta\boldsymbol{w})$ and $\Delta\boldsymbol{\varphi} = (\Delta\boldsymbol{x}, \Delta\boldsymbol{w})$, of the centroidal line $\boldsymbol{\mathcal{B}}$:

$$\begin{aligned}
&\boldsymbol{X}^h = \sum_{A=1}^{n_{cp}} R_A \boldsymbol{X}_A, \quad \boldsymbol{x}^h = \sum_{A=1}^{n_{cp}} R_A \boldsymbol{x}_A, \quad \delta\boldsymbol{x}^h = \sum_{A=1}^{n_{cp}} R_A \delta\boldsymbol{x}_A, \\
&\delta\boldsymbol{w}^h = \sum_{A=1}^{n_{cp}} R_A \delta\boldsymbol{w}_A, \quad \Delta\boldsymbol{x}^h = \sum_{A=1}^{n_{cp}} R_A \Delta\boldsymbol{x}_A \ \text{ and } \ \Delta\boldsymbol{w}^h = \sum_{A=1}^{n_{cp}} R_A \Delta\boldsymbol{w}_A,
\end{aligned} \tag{57}$$

where n_{cp} is the number of control points associated with $\boldsymbol{\mathcal{B}}_0$, R_A is the NURBS basis function accompanying control point A, whereas $\boldsymbol{X}_A$, $\boldsymbol{x}_A$, $\delta\boldsymbol{x}_A$, $\delta\boldsymbol{w}_A$, $\Delta\boldsymbol{x}_A$ and $\Delta\boldsymbol{w}_A$ are the corresponding reference and current coordinate, virtual and incremental displacement and rotation parameter, respectively.

The above parameterization also applies to each individual knot span element of $\mathcal{B}_0$:

$$\begin{aligned} \boldsymbol{X}_e^h &= \sum_{a=1}^{n_e} R_a \boldsymbol{X}_a, \quad \boldsymbol{x}_e^h = \sum_{a=1}^{n_e} R_a \boldsymbol{x}_a, \quad \delta\boldsymbol{x}_e^h = \sum_{a=1}^{n_e} R_a \delta\boldsymbol{x}_a, \\ \delta\boldsymbol{w}_e^h &= \sum_{a=1}^{n_e} R_a \delta\boldsymbol{w}_a, \quad \Delta\boldsymbol{x}_e^h = \sum_{a=1}^{n_e} R_a \Delta\boldsymbol{x}_a \quad \text{and} \quad \Delta\boldsymbol{w}_e^h = \sum_{a=1}^{n_e} R_a \Delta\boldsymbol{w}_a, \end{aligned} \tag{58}$$

where n_e is the number of control points whose basis functions have support on a single knot span element of $\mathcal{B}_0$.

Analogous interpolations are used for the Lagrange polynomial discretization, where standard Lagrangian basis functions and nodal points are used in place of NURBS basis functions and control points, respectively.

4.1 Discrete formulation

The Galerkin formulation of Eq. (42) is obtained by restricting the trial and test function sets to their finite dimensional counterpart comprised of NURBS or Lagrange suitable basis functions as: Find $\boldsymbol{\varphi}^h = (\boldsymbol{x}^h, \boldsymbol{\Lambda}^h) \in \mathcal{S}^h$, such that $\forall \delta\boldsymbol{\varphi}^h = (\delta\boldsymbol{x}^h, \delta\boldsymbol{w}^h) \in \mathcal{V}^h$:

$$\int_L \{[\delta(\boldsymbol{x}^h)' + (\boldsymbol{x}^h)' \times \delta\boldsymbol{w}^h] \cdot \boldsymbol{n}^h + \delta(\boldsymbol{w}^h)' \cdot \boldsymbol{m}^h\} d\ell = \int_L \{\delta\boldsymbol{x}^h \cdot \bar{\boldsymbol{n}} + \delta\boldsymbol{w}^h \cdot \bar{\boldsymbol{m}}\} d\ell, \tag{59}$$

where $\boldsymbol{n}^h$ and $\boldsymbol{m}^h$, are the current spatial stress resultants and couples derived from the discretized solution $\boldsymbol{\varphi}^h = (\boldsymbol{x}^h, \boldsymbol{\Lambda}^h)$. The matrix counterpart of the discrete form of the variational equations may be written on compact form as:

$$\sum_{A=1}^{n_{cp}} \delta\mathbf{d}_A (\mathbf{F}_A^{\text{int}} - \mathbf{F}_A^{\text{ext}}) = \mathbf{0}, \tag{60}$$

where $\mathbf{d}_A = [\boldsymbol{x}_A, \boldsymbol{w}_A]^T$ denotes the vectors of NURBS control-point displacement and rotation unknowns, and $\mathbf{F}_A^{\text{int}}$ and $\mathbf{F}_A^{\text{ext}}$ the vectors of internal and external control-point forces related to control point A, respectively:

$$\mathbf{F}_A^{\text{int}} = \int_L \mathbf{B}_A^T \mathbf{r} d\ell \quad \text{with} \quad \mathbf{B}_A = \begin{bmatrix} R_A' \mathbf{I}_3 & \mathbf{0} \\ R_A \widetilde{\boldsymbol{x}}' & R_A' \mathbf{I}_3 \end{bmatrix} \quad \text{and} \quad \mathbf{r} = \begin{Bmatrix} \boldsymbol{n}^h \\ \boldsymbol{m}^h \end{Bmatrix}, \tag{61}$$

and

$$\mathbf{F}_A^{\text{ext}} = \int_L R_A \mathbf{I}_6 \bar{\mathbf{r}} d\ell \quad \text{with} \quad \bar{\mathbf{r}} = \begin{Bmatrix} \bar{\boldsymbol{n}} \\ \bar{\boldsymbol{m}} \end{Bmatrix}, \tag{62}$$

where R_A is the NURBS basis function accompanying control point A, $\mathbf{I}_k = \lceil 1, 1, \ldots, 1 \rfloor$ is a diagonal unit matrix of dimension k, and $\widetilde{\boldsymbol{x}}'$ is a skew-symmetric matrix whose axial vector is $\boldsymbol{x}'$.

Similarly, the incremental solution, $\Delta\boldsymbol{\varphi}^h = (\Delta\boldsymbol{x}^h, \Delta\boldsymbol{w}^h) \in \mathcal{V}^h$, of the Galerkin formulation associated with the linearized form (44) is found from its associated discrete approximation that on matrix form can be written:

$$\sum_{A=1}^{n_{cp}} \sum_{B=1}^{n_{cp}} \delta\mathbf{d}_A \{(\mathbf{F}_A^{\text{int}} - \mathbf{F}_A^{\text{ext}}) + (\mathbf{K}_{AB}^{\text{m}} - \mathbf{K}_{AB}^{\text{g}})\Delta\mathbf{d}_B\} = \mathbf{0}. \tag{63}$$

The material and geometric stiffness matrices, $\mathbf{K}_{AB}^{\text{m}}$ and $\mathbf{K}_{AB}^{\text{g}}$, are obtained by substituting the discrete approximation counterparts of the virtual and incremental displacements from Eq.(57) into Eqs. (48) and (49):

$$\mathbf{K}_{AB}^{\text{m}} = \int_L \mathbf{B}_A^T \mathbf{C} \mathbf{B}_B d\ell \quad \text{with} \quad \mathbf{C} = \begin{bmatrix} \boldsymbol{C}_N & \mathbf{0} \\ \mathbf{0} & \boldsymbol{C}_M \end{bmatrix}, \tag{64}$$

and with some manipulations (see, e.g., Simo and Vu-Quoc [34, 35])

$$\begin{aligned} \mathbf{K}_{AB}^{\text{g}} = \textstyle\int_L \mathbf{G}_A^T \mathbf{H} \mathbf{G}_B d\ell \quad \text{with} \quad \mathbf{G}_A = \begin{bmatrix} R_A' \mathbf{I}_3 & \mathbf{0} \\ \mathbf{0} & R_A' \mathbf{I}_3 \\ \mathbf{0} & R_A \mathbf{I}_3 \end{bmatrix} \\ \text{and} \quad \mathbf{H} = \begin{bmatrix} \mathbf{0} & \mathbf{0} & -\widetilde{\boldsymbol{n}}^h \\ \mathbf{0} & \mathbf{0} & -\widetilde{\boldsymbol{m}}^h \\ \widetilde{\boldsymbol{n}}^h & \mathbf{0} & (\boldsymbol{n}^h \otimes \boldsymbol{x}' - \boldsymbol{x}' \boldsymbol{n}^h \mathbf{I}_3) \end{bmatrix}. \end{aligned} \tag{65}$$

We recall again that in the expression for $\mathbf{H}$, $\widetilde{\boldsymbol{n}}^h$ and $\widetilde{\boldsymbol{m}}^h$ are the skew-symmetric matrices whose axial vectors are $\boldsymbol{n}^h$ and $\boldsymbol{m}^h$, respectively.

It is noted that the final form of the tangent stiffness $\mathbf{K}^{\text{t}} = \mathbf{K}^{\text{m}} + \mathbf{K}^{\text{g}}$, in general, is nonsymmetric. Since symmetry of the material part follows from the symmetry of the constitutive matrix $\mathbf{C}$, the lack of symmetry stems from the geometric part. As pointed out by Simo and Vu-Quoc [34, 35], for conservative loading at an equilibrium state:

$$\mathcal{L}[\delta W(\boldsymbol{\varphi}, \delta\boldsymbol{\varphi}, \Delta\boldsymbol{\varphi})] = \delta W(\boldsymbol{\varphi}, \delta\boldsymbol{\varphi}) + \Delta[\delta W(\boldsymbol{\varphi}, \delta\boldsymbol{\varphi}, \Delta\boldsymbol{\varphi})] = 0, \tag{66}$$

the tangent stiffness is symmetric. However, in general, at nonequilibrated configurations, the tangent stiffness is nonsymmetric. The reason for that is that the configuration space, $\mathcal{T}_\varphi\mathcal{C}$, is a manifold. Numerical studies has revealed that replacing the nonsymmetric geometric stiffness by its symmetric counterpart will not jeopardize the quadratic convergence rate expected in the Newton iterations.

Parameterizing the finite rotations with the incremental rotation vector, $\boldsymbol{\theta}$ (see Section 2.2), rather than the spatial spin tensor, $\boldsymbol{w}$, yields similar expressions for the tangent stiffness matrices and the out of balance force vector, and may be found in Ibrahimbegović *et al.* [23].

5 LOCKING EFFECTS IN CURVED BEAMS

It is well-known that purely displacement-based isoparametric, especially low-order, elements are often affected by spurious strains and stresses which lead to an overestimation of the stiffness. As a consequence, the primary variables like displacements will be underestimated. In the context of curved beam elements, this implies that both spurious transverse shear and axial (membrane) strains may develop in bending dominated problems, consequently the element will have no ability to capture the state of (transverse) shear-free or inextensional bending. The corresponding locking phenomena denoted transverse shear and membrane locking, in general reduces the accuracy and slow down the convergence as the ratio between thickness to length (for straight members) or thickness to radius of curvature (for curved beams) approaches zero. From the definition of the translational spatial strains (23) we observe that $\boldsymbol{\gamma}^h$ is obtained by subtracting the normal to the cross section $\boldsymbol{i}_1^h$ from the arc-length derivative of the discrete line of centroids $\mathcal{B}^h$ in the current configuration. In the following, we investigate whether $\boldsymbol{\gamma}^h$, i.e., the axial and the transverse shear strains may vanish when the element is subjected to a state of pure bending. Without loss of generality we consider an initially 2D straight beam of length L with a rectangular cross section ($A = bh$, with $b = 1$ and $h = 10^{-\rho}$) clamped at one end and subjected to a concentrated moment M at the free end (see Fig. 2). We assume that $L = 1$, $\rho = 3$, $E = 24 \times 10^9$ and $M = \pi EI/2L = \pi$, for which the closed form solution is represented by a quarter of a circle. For simplicity all discrete unknowns are prescribed to the corresponding analytical solution of the problem. Fig. 3 shows the resulting distribution of axial and transverse shear strains obtained when the beam is discretized with a uniform mesh of one and two quadratic C^0 Lagrange and C^1 NURBS-elements, respectively. We observe that, while Lagrange discretizations sample the exact solution ($\boldsymbol{\gamma} = \mathbf{0}$) at the two Gauss points ($n_g = p = 2$) corresponding to uniform reduced integration (URI), the NURBS-based solutions do not vanish at the sampling points corresponding to $n_g = p$ within each knot-span element. The ability of the curved Lagrange

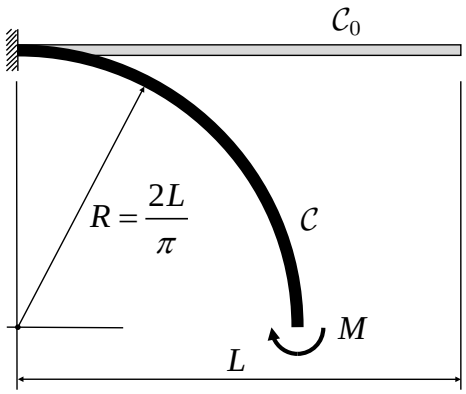

Figure 2: Initial and deformed configuration of a cantilever subjected to a concentrated end moment.

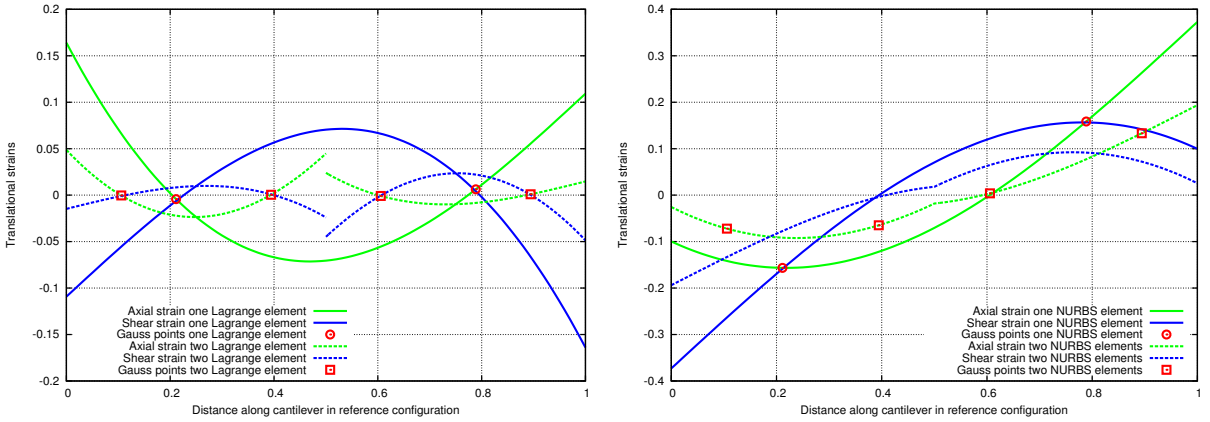

a) b)

Figure 3: Discrete translational strain fields obtained with quadratic basis functions in a cantilever beam subjected to a concentrated end moment with one and two elements, respectively: a) Lagrange C^0 solutions, and b) NURBS-based C^1 solutions.

C^0 isoparametric beam elements to alleviate spurious transverse shear and axial strains with URI was first explored and reported by Stolarski and Belytschko [36] for quadratic and cubic interpolated elements.

In order to evaluate an elements propensity of locking, Hughes [19] introduced an heuristic approach, the so-called *constraint count* method. This method relies on the constraint ratio, r, which is defined as the ratio of the total number of equilibrium equations (n_{eq}) to the total number of constraint equations (n_c):

$$r = \frac{n_{eq}}{n_c}. \tag{67}$$

In order to investigate whether an element is prone to locking, the constraint ratio, r, of the continuous problem is compared with the constraint ratio, r^h, of the discretized problem in the limit of infinite number of elements, $n_e \to \infty$:

$$r^h = \lim_{n_e \to \infty} \frac{n_u^e}{n_c^e}. \tag{68}$$

Here n_u^e denotes the number of unknowns added to the system by adding one more element to a uniform mesh of an infinite number of elements, while n_c^e is the corresponding number of constraints added by this element. Thus, n_c^e is related to the number of quadrature points, n_g, where the constraints are to be evaluated.

For an element with $r^h < r$, and especially with $r^h < 1$ (which implies that there are more constraints added than unknowns), the propensity of locking is high. In contrast when $r^h > r$, this indicate that there are too few constraints to approximate the constraint accurately. Consequently, the optimal element satisfy the criterion $r^h = r$.

As pointed out in [36], when investigating the locking behavior of curved C^0 beams for higher-order elements there exists an interrelationship between transverse shear and membrane locking. Thus, transverse shear and membrane locking must be considered simultaneously. Again, for simplicity, we consider a 2D GEBM, for which we have three unknowns per control point (node) and two new constraints per Gauss point. The optimal constraint ratio for the 2D continuous problem is

$$r_{\text{2D}} = \frac{3}{2} = 1.5. \tag{69}$$

For the discrete problem we distinguish between C^0 Lagrange and C^{p-1} NURBS-based discretization. Let us first consider the discrete constraint ratio for the C^0 Lagrange discretization:

$$r^h_{\text{2D},L} = \frac{3p}{2n_g}. \tag{70}$$

Thus, applying URI with $n_g = p$ yields an optimal constraint ratio for the Lagrange 2D beam. The corresponding discrete constraint ratio for NURBS reads:

$$r^h_{\text{2D},N} = \frac{3}{2n_g}. \tag{71}$$

In order to obtain the optimal constraint ratio for NURBS, we should apply one single Gauss point per added new element.

While applying URI to the Lagrange elements implies that the rank of the global tangent stiffness is equal to the total number of unknowns, the above optimal quadrature rule for NURBS is not sufficient to guarantee rank-sufficiency and thus produce zero-energy modes which need to be stabilized. Adam *et al.* [1, 2] have studied the use of reduced and selective reduced integration rules for higher-continuity NURBS-based analysis. Rather than evaluating the integrals element-by-element, the authors suggest using patch-wise optimal integration schemes, which accounts for the smoothness of the approximation space $\mathcal{V}^h$. However, the optimal quadrature points and weights may only be obtained by solving non-linear equation systems, thus, may compromise the overall computational efficiency.

The above investigation has resulting in two proposed integration schemes which will be referred to as URI-1 and SRI-1, and URI-2 and SRI-2, respectively. In URI-1 and URI-2, both the translational and the rotational part is integrated with the proposed rule, while for SRI-1 and SRI-2, only the translational parts are integrated with the rules in Tab. 1, while the rotational part is integrated with $n_g = p$ per NURBS element.

6 NUMERICAL RESULTS

The purpose of the numerical tests is to study the performance of isogeometric elements with the selective and uniform reduced integration regimes proposed in Tab. 1, and compare them for Lagrange and NURBS-based elements integrated with conventional reduced integration.

p	SRI-1/URI-1	SRI-2/URI-2
1	$n_g = 1$	$n_g = 1$
2	$n_g = 1 \setminus e = (1 + n_e)/2 : n_g = 2$	$n_g = 1 \setminus e = n_e : n_g = 2$
3	$n_g = 1 \setminus e = 2, n_e - 1 : n_g = 2$	$n_g = 1 \setminus e = 1, n_e : n_g = 2$
4	$n_g = 1 \setminus e = 2, (1 + n_e)/2, n_e - 1 : n_g = 2$	$n_g = 1 \setminus e = 1, n_e : n_g = 3$
5	$n_g = 1 \setminus e = 2, n_e - 1 : n_g = 2 \wedge e = (1 + n_e)/2 : n_g = 3$	$n_g = 1 \setminus e = 1, n_e : n_g = 4$

Table 1: Selective reduced integration schemes.

6.1 Curved beam subjected to distributed moment

Fig. 4 shows geometry and material properties for a planar 90° circular arch subjected to a sinusoidally distributed moment $m(s) = h^3 \sin(\pi s/2L)$. This load imposes a state of pure bending with no membrane and transverse shear energy and is therefore a severe test for membrane and transverse shear locking. Also note that by choosing a sinusoidally distributed moment, the closed form solution is obviously not contained in the approximation space $\mathcal{V}^h$. The load is proportional with the bending stiffness such that the displacements and rotations are independent of the thickness. Introducing the thickness parameter ρ, the slenderness is defined as: $R/h = 10^\rho$. We also observe that the geometry of the circular arch cannot be represented exactly by Lagrange polynomials, while with NURBS, one single quadratic element can exactly represent the initial geometry. This problem has also been studied by Adam *et al.* [1] and Bouclier *et al.* [9], however they both applied a small strain curved linear Timoshenko beam formulation.

Denoting the displacements parallel to the local Cartesian bases, $\boldsymbol{i}_1^0$ and $\boldsymbol{i}_2^0$, $u_t(s)$ and $u_n(s)$, respectively, the analytical solution for the corresponding linear problem may be

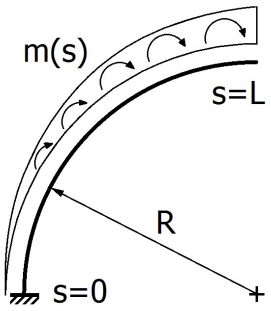

Young's modulus:	$E = 1000$
Poisson's ratio:	$\nu = 0$
Radius:	$R = 1$
Width:	$b = 0.2$
Thickness:	$h = R/10^\rho$

Figure 4: Geometry and material data for a curved beam under sinusoidally moment loading.

obtained by solving the strong form governed by Eq. (37), and is given by [1, 9]:

$$\begin{aligned} u_n(s) &= \frac{3\pi R^3}{Eb}\sin\left(\frac{s}{R}\right) \\ u_t(s) &= \frac{6R^3}{Eb}\left[\sin\left(\frac{s}{R}\right) - \frac{s}{R}\cos\left(\frac{s}{R}\right)\right] \\ \theta(s) &= \frac{12R^2}{Eb}\sin\left(\frac{s}{R}\right) \end{aligned} \tag{72}$$

The three nonzero strain fields, $\varepsilon_1 = \gamma_1$ (axial strain), $\gamma_{12} = \gamma_2$ (transverse shear strain), and κ_3 (bending strain), for the different reduced integration models are studied for the slenderness ratios $\rho = 1$ and $\rho = 3$, using a mesh of $n_e = 5$ equally sized knot-span elements with the maximum continuity available. Note that for the GEBM the strains are computed in the current configuration and will consequently not coincide with the linear solution that may be derived from Eq. (72). For this reason the analytical solution is approximated with a reference solution, obtained with 32 quintic isogeometric elements each integrated with p Gauss points ($n_g = p$). The sinusoidally varying moment is taken into consideration with a consistent load vector, integrated numerically with $n_g = 5p$.

For comparison, the beam is also analyzed with quadratic C^0-continuous Lagrangian elements applying uniform reduced integration (URI). In order to keep the number of approximation functions n equal for Lagrange ($n \propto n_e p$) and NURBS ($n \propto n_e + p - 1$) based solutions, a uniform mesh of three quadratic Lagrange elements is used. The strain fields for ε_1, γ_{12} and κ_3, reported in Fig. 5, confirm that the strains sampled at the Gauss points for the Lagrangian elements coincide with the reference solution for both $\rho = 1$ and $\rho = 3$ for all strain fields, and thus appear to be locking-free. However, for the isogeometric elements of equal order and with the same quadrature rule, i.e., URI with $n_g = p$ within each knot-span element, we observe that all of the three strain fields when sampled at the Gauss points deviate from the reference solution. We also observe that the deviation increases with increased slenderness, and thus, the elements reveal both membrane and transverse shear locking.

With a fixed slenderness of $\rho = 3$, the beam is now analyzed with the two different selective reduced integration regimes proposed above, denoted SRI-1 and SRI-2, respectively, on the translation part of the residual and tangent stiffness only, while the rotational part is integrated with $n_g = p$. The strain fields obtained with quadratic and cubic NURBS elements with the various SRI rules are depicted in Figs. 6 and 7, respectively. It is observed that all three strain fields coincide with the reference solution when sampled at the Gauss points for both SRI-1 and SRI-2, and consequently yield a precise approximation of the corresponding curvature field. This observation is also valid for higher order elements (see Fig. 8). However, for SRI-1, where the additional Gauss points are not located at the boundary elements, the translational strains show oscillations when the polynomial order is increased.

The beam is analyzed once more applying SRI-1 and SRI-2 on both the translational

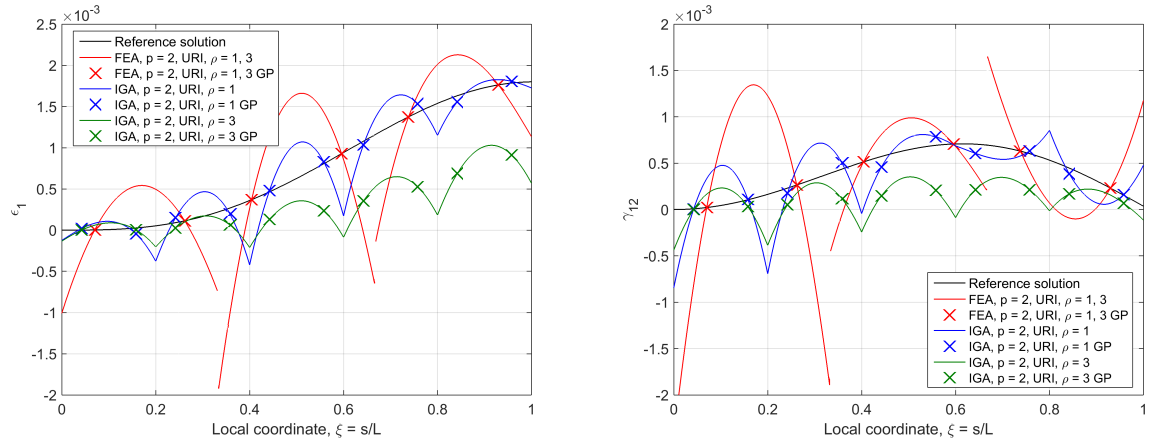

Figure 5: Comparison of Lagrange (FEA) and NURBS (IGA) based solutions applying conventional URI for $p = 2$: a) Axial strain, b) transverse shear strain, and c) bending strain.

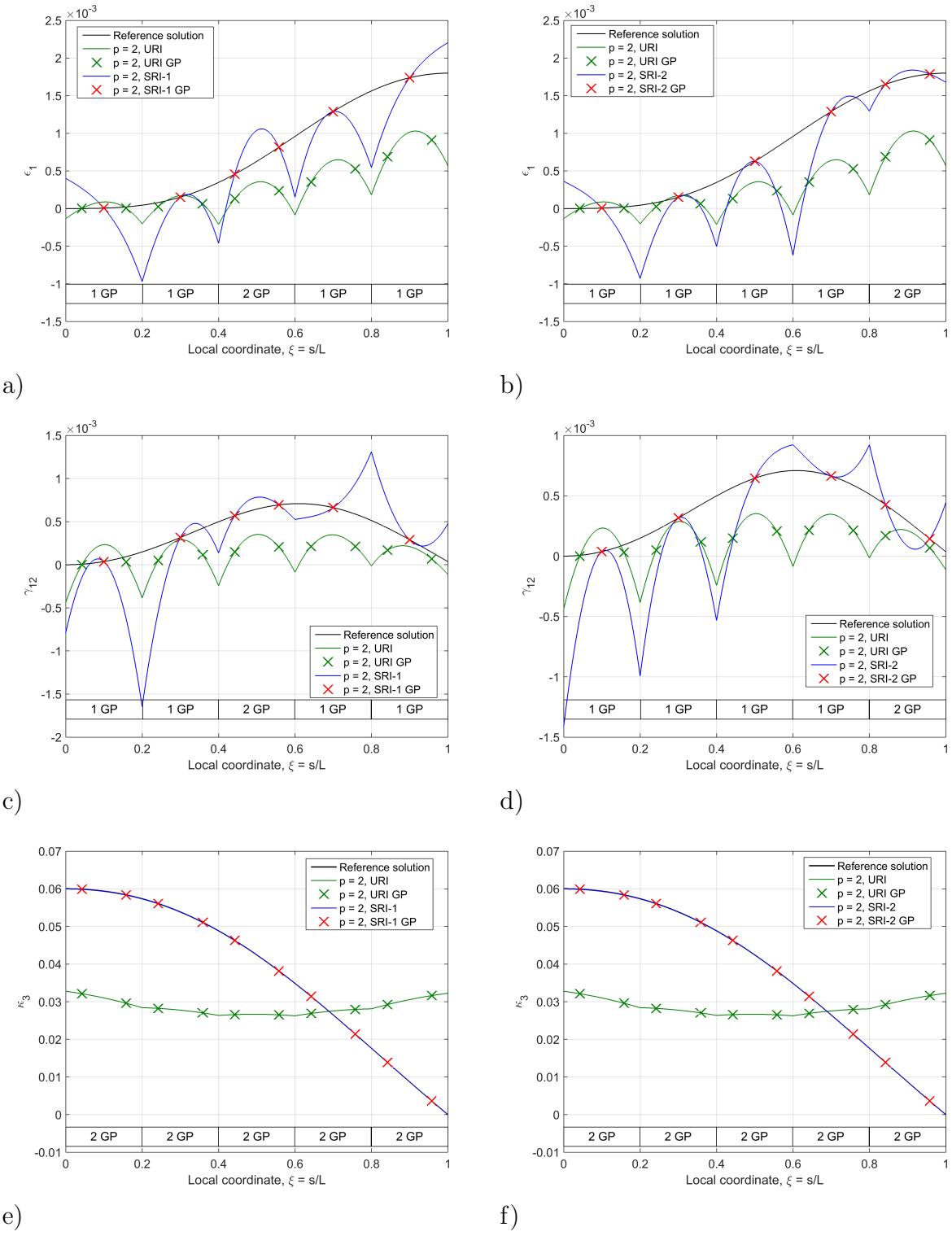

Figure 6: Comparison of the solutions obtained with the various SRI rules applied to the translational part only, for $p = 2$: a) Axial strain (SRI-1), b) axial strain (SRI-2), c) transverse shear strain (SRI-1), d) transverse shear strain (SRI-2), e) bending strain (SRI-1), and f) bending strain (SRI-2).

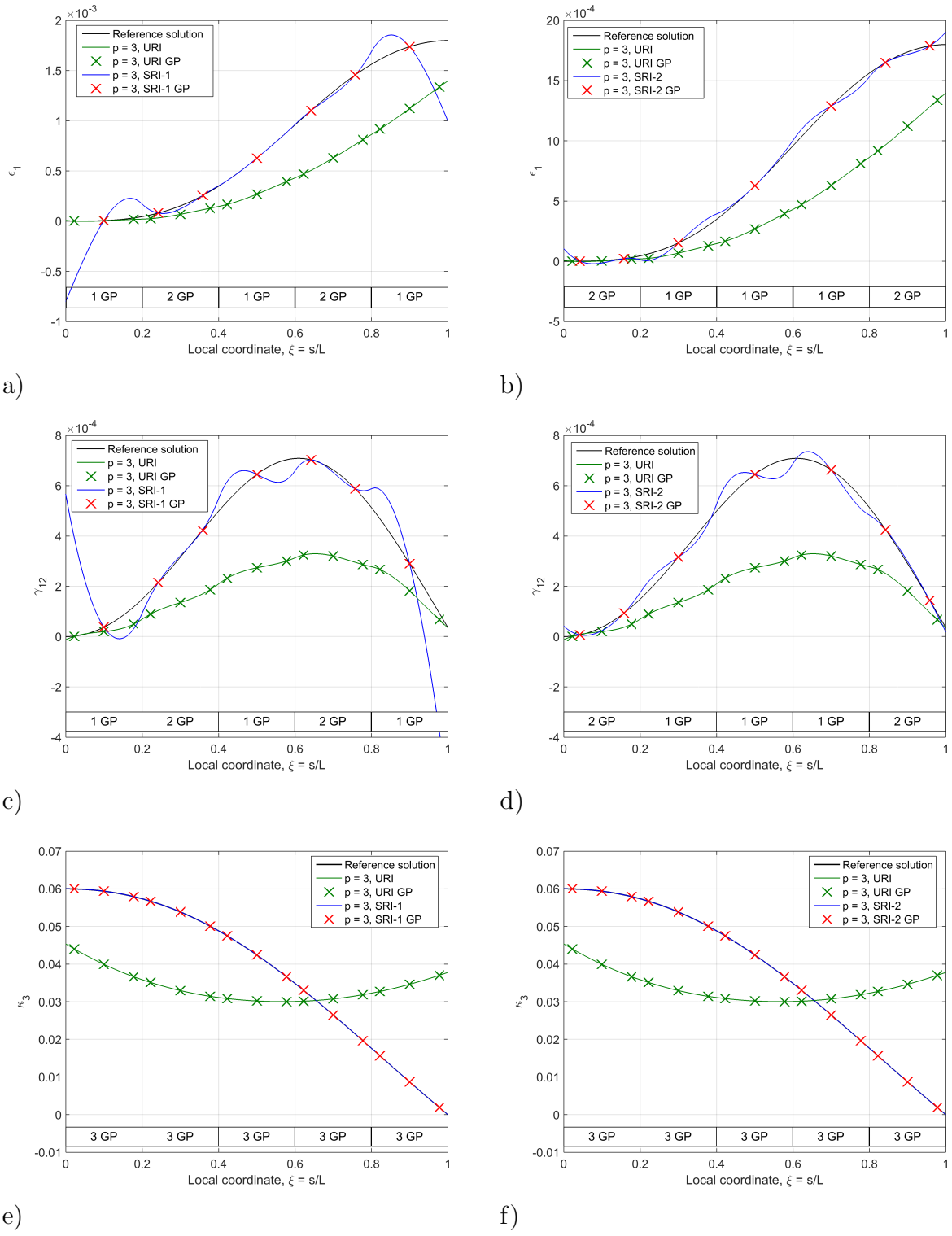

Figure 7: Comparison of the solutions obtained with the various SRI rules applied to the translational part only, for $p = 3$: a) Axial strain (SRI-1), b) axial strain (SRI-2), c) transverse shear strain (SRI-1), d) transverse shear strain (SRI-2), e) bending strain (SRI-1), and f) bending strain (SRI-2).

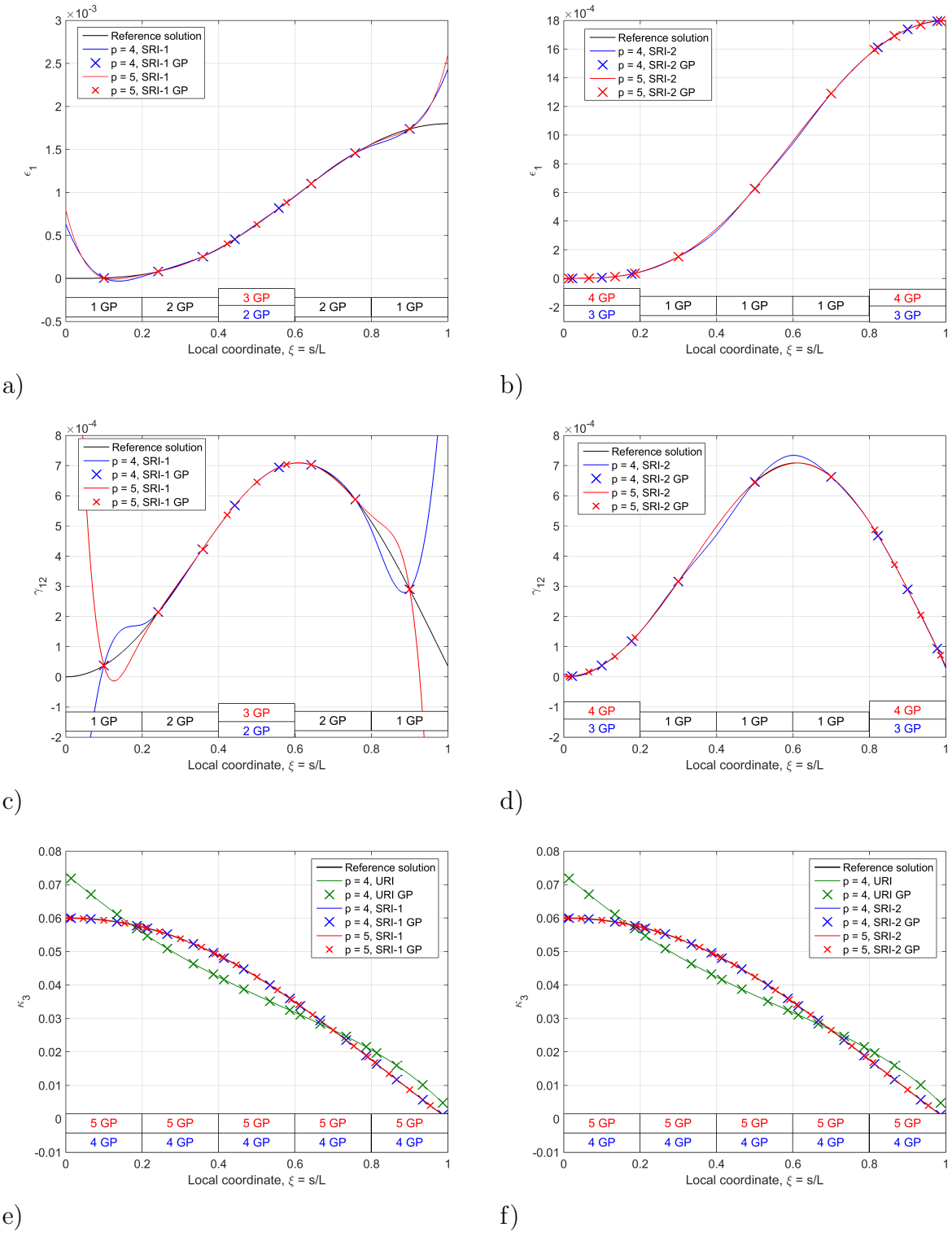

Figure 8: Comparison of the solutions obtained with the various SRI rules applied to the translational part only, for quartic and quintic order elements: a) Axial strain (SRI-1), b) axial strain (SRI-2), c) transverse shear strain (SRI-1), d) transverse shear strain (SRI-2), e) bending strain (SRI-1), and f) bending strain (SRI-2).

and rotational parts. Since we apply the same reduced rules on all strain fields, they are denoted URI-1 and URI-2, to distinguish them from the SRI quadrature rules. Applying URI-1 or URI-2, thus represent the lowest number of integration points needed to keep the correct rank of the global matrix, which is similar to applying conventional URI to the Lagrangian elements. The corresponding strain field solutions are reported in Figs. 9 and 10 for the quadratic and cubic elements, respectively. For $p = 3$ or higher, we observe that the solution is not convergent unless the additional Gauss points are added to the boundary elements (SRI-2). Results obtained for the quartic and quintic order elements are not shown here, but they behave similar to the cubic elements. Again, strains sampled at the Gauss points coincide with the reference solution for the translational strains. However, applying less than $n_g = p$ on the rotational part does not produce accurate results for the bending strains.

Furthermore, a convergence study is carried out to study the impact of the various reduced quadrature rules on accuracy. The tangential tip displacement is chosen as measurement, and the relative error is computed from Eq. (73), where u^{ex} represents $u_t(s = L)$ from Eq. (72).

$$|e_u| = \frac{|u^{ex} - u^h|}{|u^{ex}|} \tag{73}$$

Figs. 11 and 12 show convergence plots for the various reduced integration rules with NURBS, for $\rho = 1$ and $\rho = 3$, respectively. Firstly, it is seen that the absolute errors from the conventional URI elements shift with approximately 4 orders, going from $\rho = 1$ to $\rho = 3$ which strongly indicate locking. Elements with SRI provide slower convergence, but the absolute errors are small for coarse discretizations and they are not shifted with ρ. We observe that quadratic elements integrated with URI-1 or URI-2 performs similar to the associated SRI-1 and SRI-2 elements for which the reduced quadrature rules are only applied to the translational part, while the associated cubic and higher order elements has rather poor performance with slow convergence and large errors.

In Fig. 13 the thickness dependency is studied. For this analysis, ρ is varied from 1 to 5, keeping a fixed number of five NURBS elements. Fig. 13 shows logarithmic plots of the relative error and tangential tip displacements for the various reduced integration regimes. Elements with conventional reduced integration (URI) are included for comparison. Apart from $p = 5$, all elements appear to be locking-free. The slight thickness dependency of the quintic elements may be due to the fact that the proposed quadrature rule adds two more Gauss points than needed to avoid rank deficiency and thus creates an over-constrained system.

7 CONCLUDING REMARKS

The study reveals that the chosen numerical quadrature scheme significantly impacts not only the computational efficiency but also the propensity of membrane and transverse shear locking in NURBS-based geometrically exact curved Timoshenko beam elements.

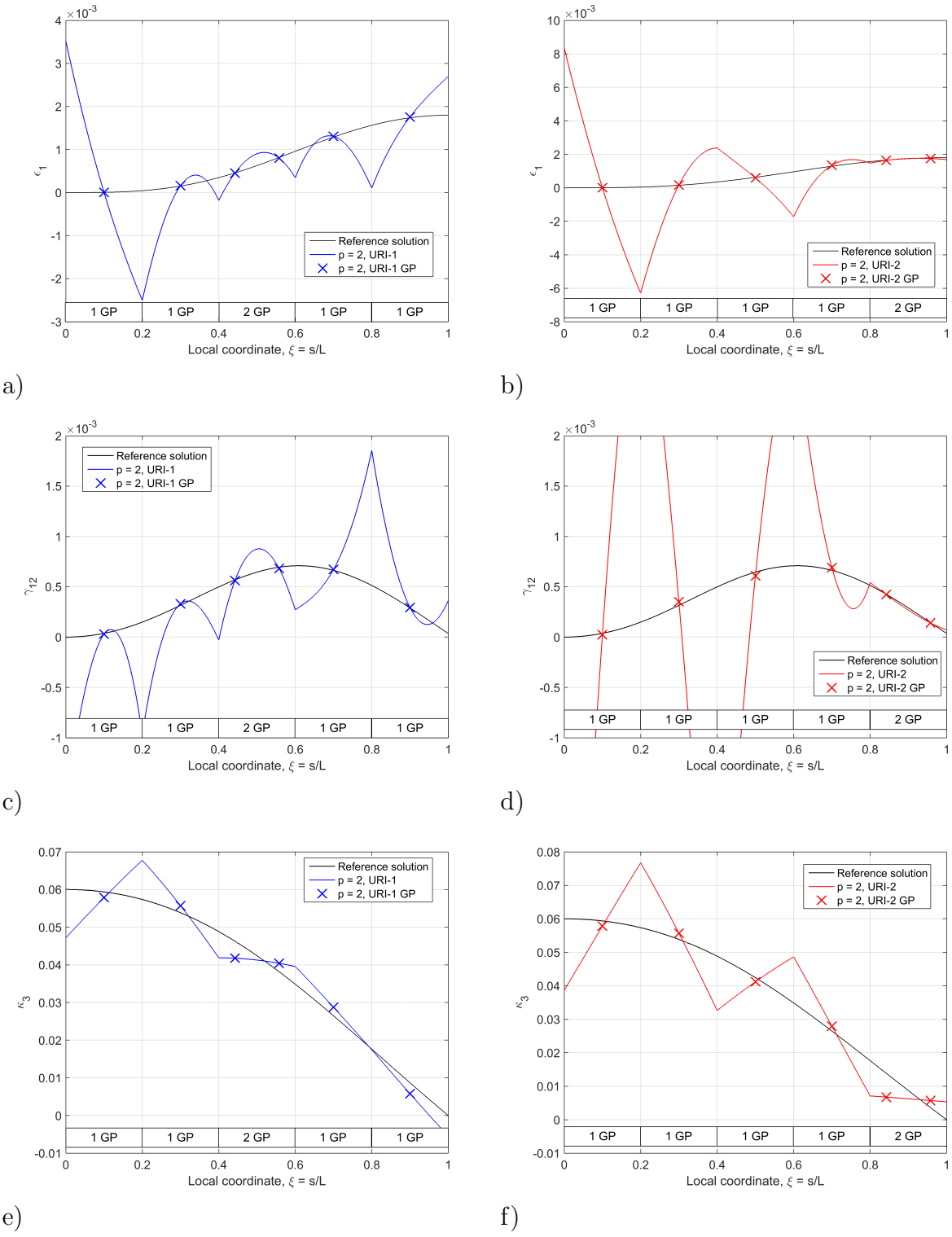

Figure 9: Comparison of solutions obtained with the various URI rules applied to both the translational and the rotational parts, for $p = 2$: a) Axial strain (URI-1), b) axial strain (URI-2), c) transverse shear strain (URI-1), d) transverse shear strain (URI-2), e) bending strain (URI-1), and f) bending strain (URI-2).

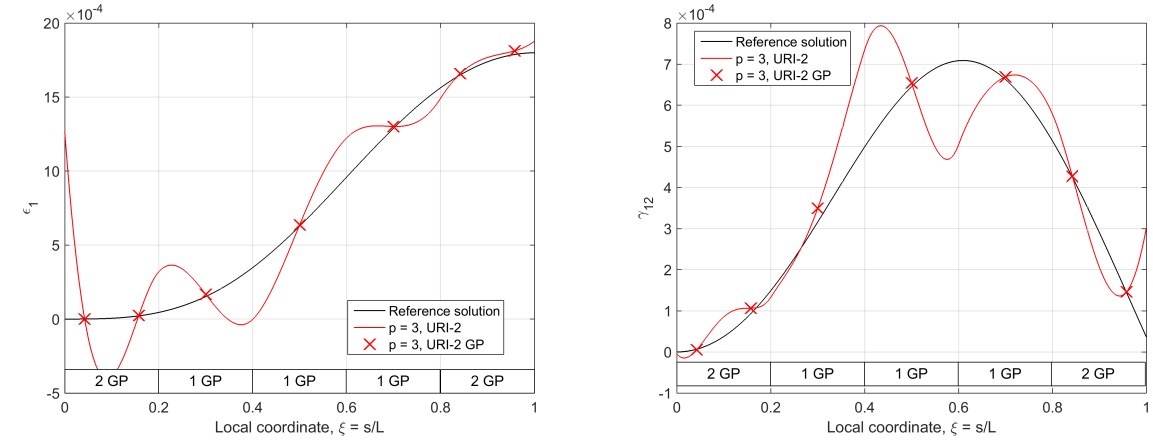

a) b)

c)

Figure 10: Comparison of solutions obtained with the URI-2 rule applied to both the translational and the rotational parts, for $p = 3$: a) Axial strain, b) transverse shear strain, and c) bending strain.

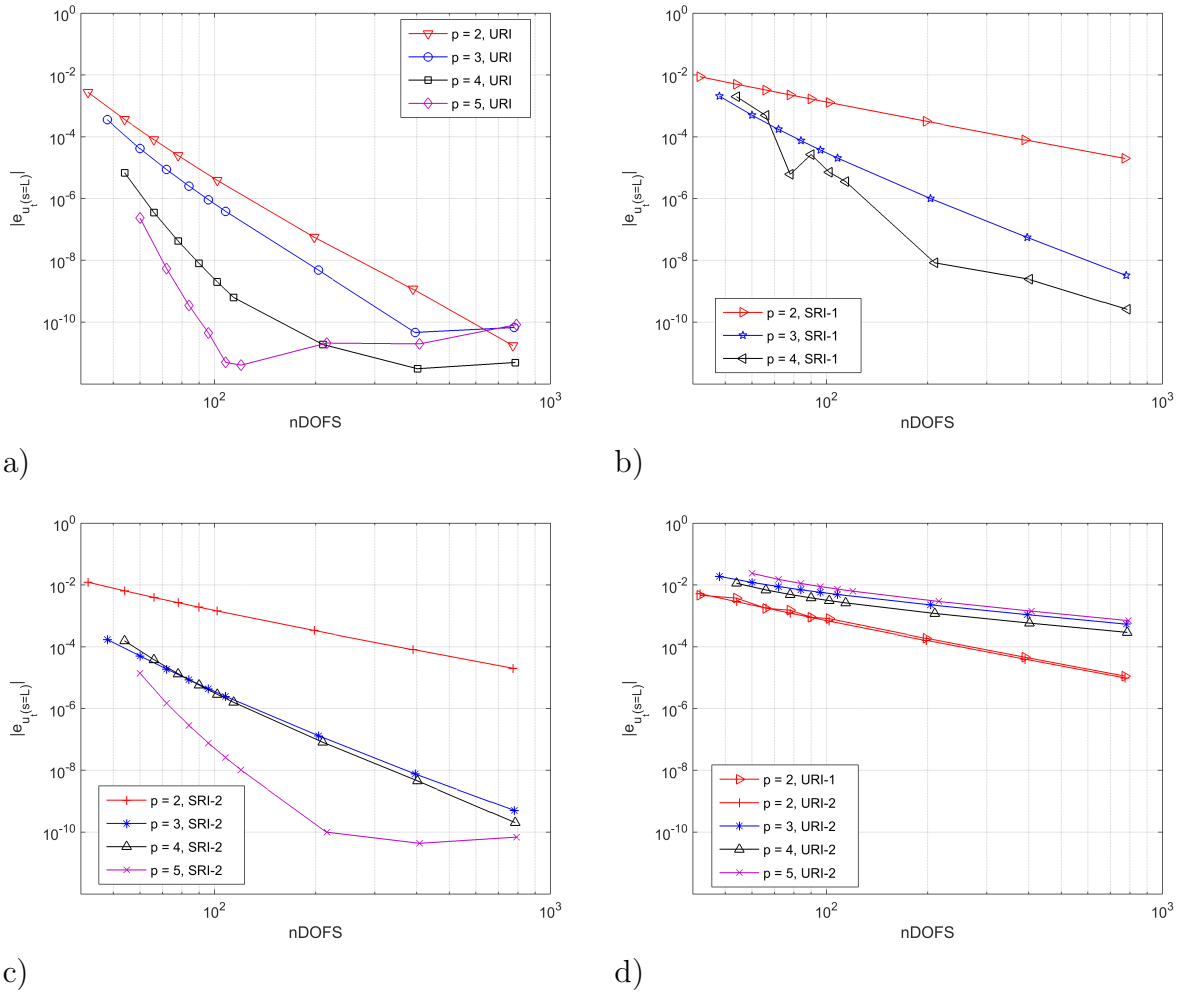

Figure 11: Relative error in tangential tip displacement for the various reduced quadrature rules with NURBS, for $\rho = 1$: a) URI, b) SRI-1, c) SRI-2, d) URI-1 and URI-2.

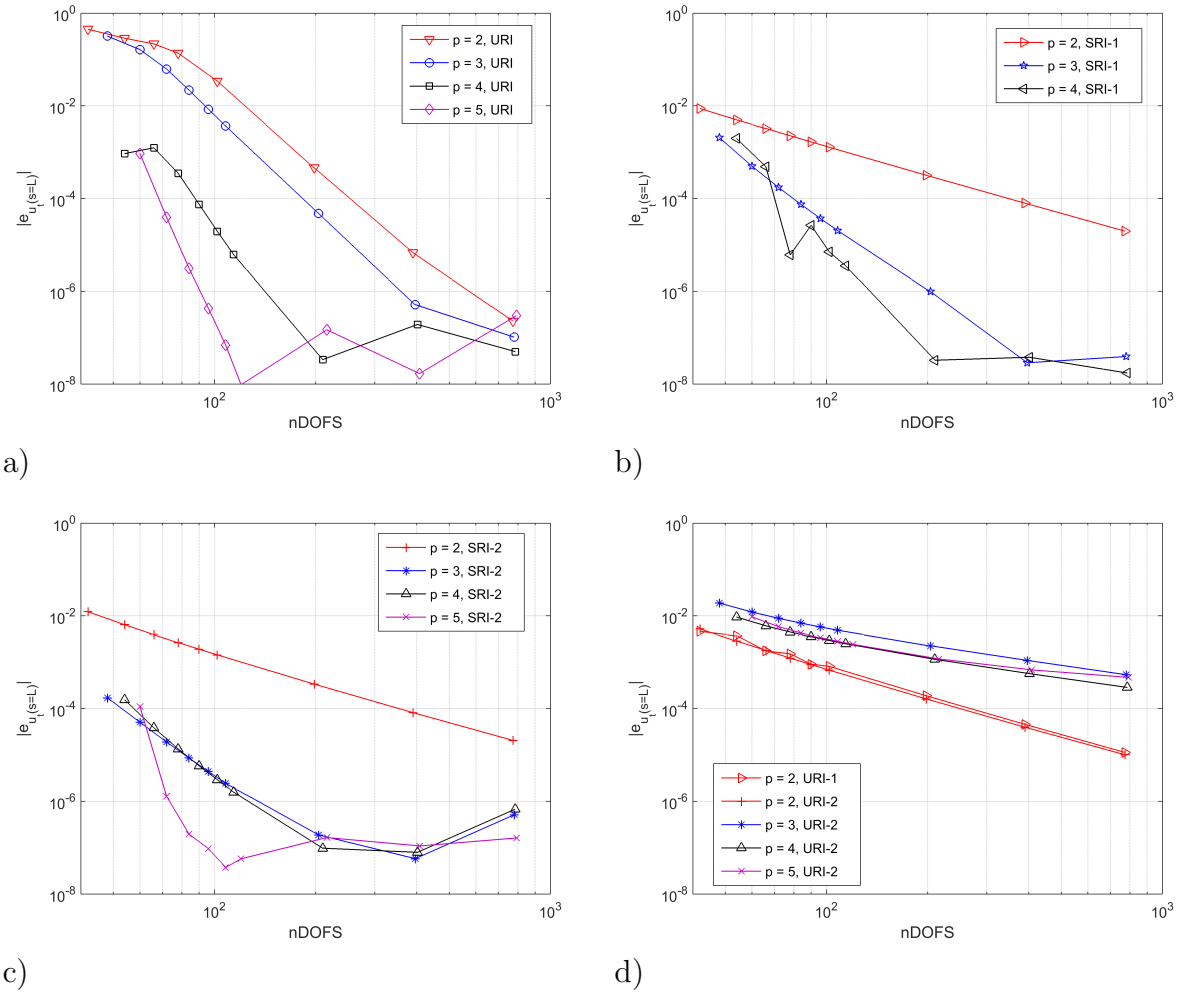

Figure 12: Relative error in tangential tip displacement for the various reduced quadrature rules with NURBS, for $\rho = 3$: a) URI, b) SRI-1, c) SRI-2, d) URI-1 and URI-2.

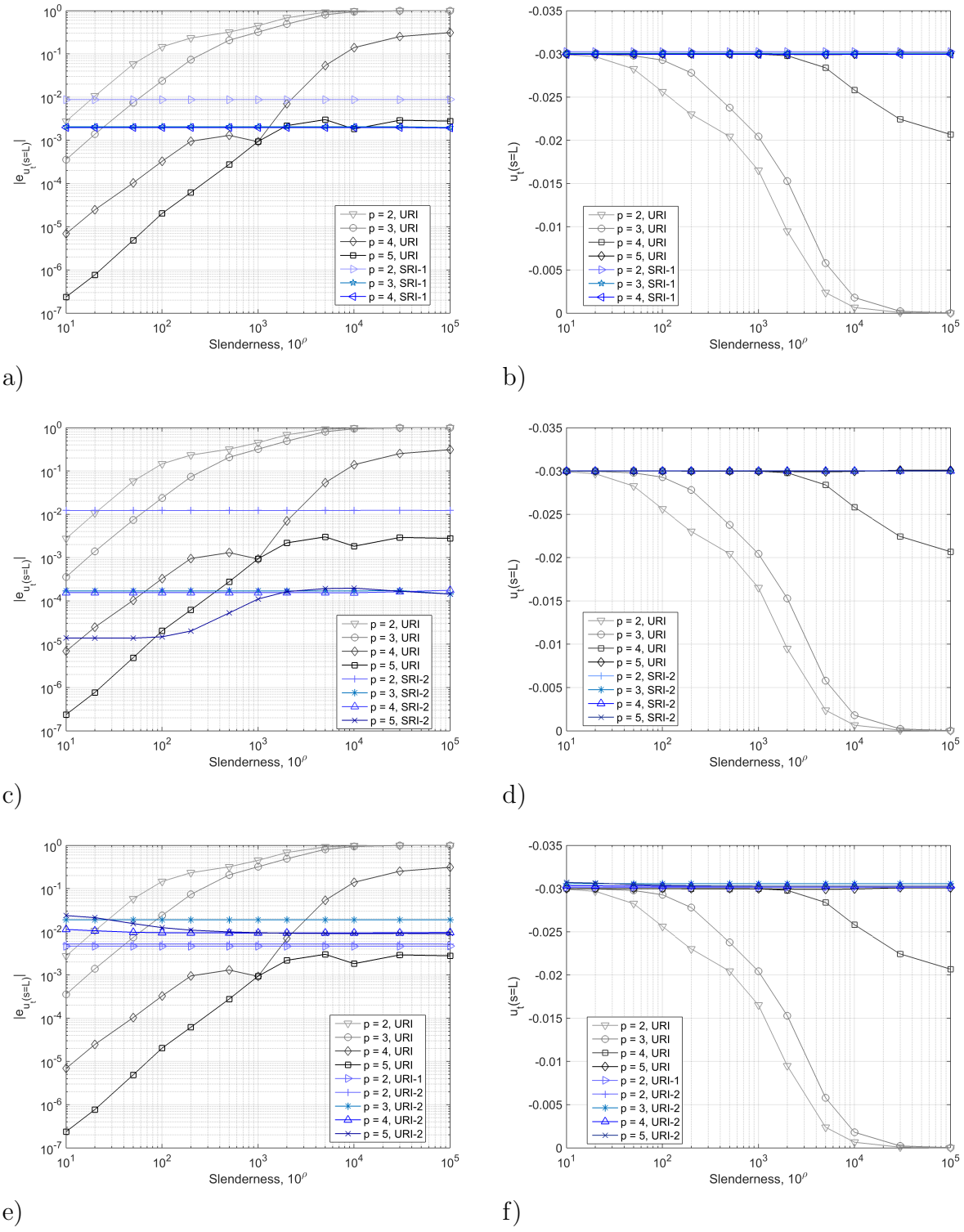

Figure 13: Convergence of the tangential tip displacement with respect to the slenderness of the beam for NURBS: a) Relative error (SRI-1), b) displacement (SRI-1), c) relative error (SRI-2), d) displacement (SRI-2), e) relative error (URI-1 and URI-2), and f) displacement (URI-1 and URI-2).

The numerical study shows that applying conventional URI with $n_g = p$ per knot-span element, locking is revealed in all strain fields. In contrast, applying conventional URI to both the translational and rotational part of the residual and the tangent stiffness are the best quadrature rules for C^0-continuous Lagrange Timoshenko beam elements based on the geometrically exact beam model.

Our study has proven that SRI of the translational part may be used to alleviate both membrane and transverse shear locking for the NURBS discretizations. The numerical results also show that: 1) For all polynomial orders p, the rotational part of the residual and tangent stiffness should be integrated with $n_g = p$, 2) for all polynomial orders p, the translational part should be integrated with a one-point quadrature rule except; a) for $p = 2$, an extra Gauss point should be added to an element near the center, and b) for $p \geq 3$, the two boundary elements that should be integrated with $n_g = p - 1$.

Note that for NURBS of cubic order and larger we recommend to add extra Gauss points to the two boundary elements to stabilize and support the strain fields within the patch. However, for quadratic NURBS the best support is obtained by adding an extra Gauss point near the center. This also complies with the scheme proposed by Bouclier *et al.* [9] for quadratic elements, but while we recommend this rule only for the translational part, they used the same rule for both the translational and the rotational part. The above recommended scheme also comply with that proposed by Adam *et al.* [1], but only for NURBS of cubic order.

We have also applied the above recommended quadrature rules for both the translational and rotational parts, which turns out to sample the translational part of the strain fields accurately, however, leaving the rotational part incorrect. Also note that for NURBS the convergence rates are reduced with SRI, and for cubic and higher order elements they are also depending on the slenderness ratio.

8 ACKNOWLEDGEMENT

The authors would like to acknowledge Dr. Ing. Knut Morten Okstad at SINTEF, Department of Applied Mathematics, for his comments and for carefully reading this manuscript.

REFERENCES

[1] Adam, C., Bouabdallah, S., Zarroug, M. and Maitournam, H. Improved numerical integration for locking treatment in isogeometric structural elements, Part I: Beams. *Comput. Meth. Appl. Mech. Engrg.* (2014) **279**:1–28.

[2] Adam, C., Hughes, T.J.R., Bouabdallah, S., Zarroug, M. and Maitournam, H. Selective and reduced numerical integrations for NURBS-based isogeometric analysis. *Comput. Meth. Appl. Mech. Engrg.* (2014) **279**:1–28.

[3] Auricchio, F., Carotenuto, P. and Reali, A. On the geometrically exact beam model: A consistent, effective and simple derivation from three-dimensional finite-elasticity. *Int. J. Solids. Struct.* (2008) **45**:4766–4781.

[4] Auricchio, F., Calabrò, F., Hughes, T.J.R., Reali, A. and Sangalli, G. A simple algorithm for obtaining nearly optimal quadrature rules for NURBS-based isogeometric analysis. *Comput. Meth. Appl. Mech. Engrg.* (2012) **249–252**:15–27.

[5] Auricchio, F., Beirão da Veiga, L, Kiendl, J., Lovadini, C. and Reali, A. Locking-free isogeometric collocation methods for spatial Timoshenko rods. *Comput. Meth. Appl. Mech. Engrg.* (2013) **263**:113–126.

[6] Beirão da Veiga, L, Lovadina, C. and Reali, A. Avoiding shear locking for the Timoshenko beam problem via isogeometric collocation methods. *Comput. Meth. Appl. Mech. Engrg.* (2012) **241–244**:38–51.

[7] Takizawa, K., Tezduyar, T.E., Hsu, M-C., Øiseth, O., Mathisen, K.M., Kostov, N. and McIntyre, S. Engineering Analysis and Design with ALE-VMS and Space-Time Methods. *Arch. Comput. Meth. Engrg.* (2014) **21**:481–508.

[8] Borden, M.J., Scott, M.A., Verhoosel, C.V., Hughes, T.J.R. and Landis, C.M. A phase-field description of dynamic brittle-fracture *Comput. Meth. Appl. Mech. Engrg.* (2012) **217–220**:77–95.

[9] Bouclier, R., Elguedj, T. and Combescure, A. Locking free isogeometric formulations of curved thick beams. *Comput. Meth. Appl. Mech. Engrg.* (2012) **245–246**:144–162.

[10] Bouclier, R., Elguedj, T. and Combescure, A. An isogeometric locking-free NURBS-based solid-shell elements for nonlinear analysis. *Int. J. Numer. Meth. Engrg.* (2014) **101**:774–808.

[11] Bouclier, R., Elguedj, T. and Combescure, A. Locking free isogeometric formulations of curved thick beams. *Comput. Meth. Appl. Mech. Engrg.* (2012) **245–246**:144–162.

[12] Cardona, A. and Géradin, M. A beam finite element non-linear theory with finite rotations. *Int. J. Numer. Meth. Engrg.* (1988) **26**:2403–2438.

[13] Caseiro, J.F., Valente, R.A.F., Reali, A., Kiendl, J., Auricchio, F. and Alves de Sousa, R.J. On the assumed natural strain method to alleviate locking in solid-shell NURBS-based finite elements *Comput. Mech.* (2014) **53**:1341–1353.

[14] Cottrell, J.A., Hughes, T.J..R. and Bazilevs Y. *Isogeometric Analysis: Toward Integration of CAD and FEA*. John Wiley & Sons, Chichester, England, (2009).

[15] Crisfield, M. A consistent corotational formulation for non-linear, three-dimensional beam elements. *Comput. Meth. Appl. Mech. Engrg.* (1990) **81**:131–150.

[16] Echter, R. and Bischoff, M. Numerical efficiency, locking and unlocking of NURBS finite elements. *Comput. Meth. Appl. Mech. Engrg.* (2005) **199**:374–382.

[17] Echter, R., Oesterle, B. and Bischoff, M. A hierarchic family of isogeometric shell finite elements. *Comput. Meth. Appl. Mech. Engrg.* (2005) **199**:374–382.

[18] Elguedj, T, Bazilevs, Y., Calo, V.M. and Hughes, T.J.R. $\overline{\mathrm{B}}$ and $\overline{\mathrm{F}}$ projection methods for nearly incompressible linear and non-linear elasticity and plasticity using higher-order NURBS elements. *Comput. Meth. Appl. Mech. Engrg.* (2008) **197**:2732–2762.

[19] Hughes, T.J.R. *The Finite Element Method*. Prentice–Hall, Englewood Cliffs, NJ, USA, (1987).

[20] Hughes, T.J.R., Cottrell, J.A. and Bazilevs, Y. Isogeometric Analysis: CAD, Finite Elements, NURBS, Exact Geometry and Mesh Refinement. *Comput. Meth. Appl. Mech. Engrg.* (2005) **194**:4135–4195.

[21] Ibrahimbegović, A. and Frey, F. Finite element analysis of linear and nonlinear planar deformations of elastic initially curved elements. *Int. J. Numer. Meth. Engrg.* (1992) **36**:3239–3258.

[22] Ibrahimbegović, A. On finite element implementation of geometrically nonlinear Reissner's beam theory: Three-dimensional curved beam elements. *Comput. Meth. Appl. Mech. Engrg.* (1995) **122**:11–26.

[23] Ibrahimbegović, A., Frey, F. and Kožar, I. Computational aspects of vector-like parameterization of three-dimensional finite rotations. *Int. J. Numer. Meth. Engrg.* (1995) **38**:3653–3673.

[24] Mathisen, K.M. and Bergan, P.G. Large displacement analysis of submerged multibody systems. *Engrg. Comput.* (1992) **9**:609–634.

[25] Mathisen, K.M., Okstad, K.M., Kvamsdal, T. and Raknes, S.B. Isogeometric analysis of finite deformation nearly incompressible solids. *J. Struct. Mech.* (2011) **44**:260–278.

[26] Mathisen, K.M., Okstad, K.M., Kvamsdal, T. and Raknes, S.B. Isogeometric analysis applied to frictionless large deformation elastoplastic contact. *Proc. XII Int. Conf. Comput. Plast. (COMPLAS 2013)*, Oñate, E., Owen, D.R.J., Peric, D. and Suárez, B. (Eds.), CIMNE, Barcelona, Spain (2013) pp. 969–986.

[27] Mathisen, K.M., Okstad, K.M., Kvamsdal, T. and Raknes, S.B. Simulation of contact between subsea pipeline and trawl gear using mortar-based isogeometric analysis. *Proc. VI Int. Conf. Comput. Meth. Marine Engrg. (MARINE 2015)*, Salvatore, F., Broglia, R. and Muscari, R. (Eds.), CIMNE, Barcelona, Spain (2015).

[28] Piegl, L. and Tiller, W. *The NURBS Book*. Springer, Berlin, Germany, 2nd edition, (1996).

[29] Raknes, S.B., Deng, X., Bazilevs, Y., Benson, D.J., Mathisen, K.M. and Kvamsdal, T. Isogeometric rotation-free bending-stabilized cables: Statics, dynamics, bending strips and coupling with shells. *Comput. Meth. Appl. Mech. Engrg.* (2013) **263**:127–143.

[30] Reissner, E. On one-dimensional finite-strain beam theory: The plane problem. *J. Appl. Math. Phys.* (1972) **32**:795–804.

[31] Reissner, E. On finite deformations of space curved beams. *J. Appl. Math. Phys.* (1981) **32**:734–744.

[32] Saje, M. Finite element formulation of finite planar deformation of curved elastic beams. *Comput. Struct.* (1991) **39**:327–337.

[33] Simo, J.C. A finite strain beam formulation. The three-dimensional dynamic problem. Part I. *Comput. Meth. Appl. Mech. Engrg.* (1985) **49**:55–70.

[34] Simo, J.C. and Vu-Quoc, L. A three-dimensional finite strain rod model. Part II: Computational aspects. *Comput. Meth. Appl. Mech. Engrg.* (1986) **58**:79–116.

[35] Simo, J.C. Vu-Quoc, L. A geometrically-exact rod model incorporating shear and torsion-warping deformation. *Int. J. Solids. Struct.* (1991) **27**:371–393.

[36] Stolarski, H. and Belytschko, T. Shear and membrane locking in curved C^0 elements. *Comput. Meth. Appl. Mech. Engrg.* (1983) **41**:279–296.

Appendix G

Presentation for MekIT'15 and IGA2015

The following presentation, "On Locking-free Methods for Isogeometric Large Deformation Analysis of Geometrically Exact 3D Beams", was held on the MekIT'15 Eight National Conference on Computational Mechanics in Trondheim May 18th-19th 2015, and on the IGA2015 III International Conference on Isogeometric Analysis in Trondheim June 1st-3rd, 2015.

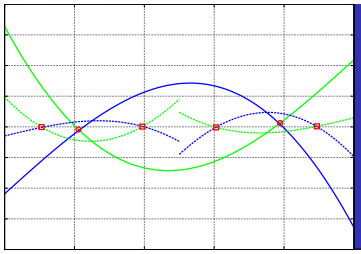

IGA 2015

III International Conference on Isogeometric Analysis

Trondheim, 1–3 June, 2015

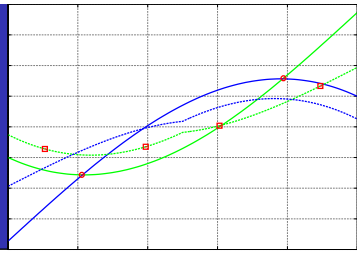

On Locking-free Methods for Isogeometric Large Deformation Analysis of Geometrically Exact 3D Beams

Tore A. Helgedagsrud and Kjell M. Mathisen

Department of Structural Engineering
Norwegian University of Science and Technology
Trondheim, Norway
kjell.mathisen@ntnu.no

Motivation

- Geometrically exact 3D curved Timoshenko elements considering large displacements/finite rotations have been proposed earlier:
  - Linearly interpolated C^0-element: Simo & Vu-Quoc (CMAME 86), and Cardona and Géradin (IJNME 88).
  - Hierarchical quadratic C^0-element: Ibrahimbegovic (CMAME 95).
- Previous proposed formulations are utilizing Lagrange polynomials:
  - Curved geometry cannot be represented exactly.
  - C^0-continuity between elements.
- Utilizing NURBS basis functions:
  - Curved geometry can be exactly represented.
  - C^{p-k}-continuity between elements.
- Challenge: Numerical transverse shear and membrane locking !!!

Geometrically exact beam model – Kinematics

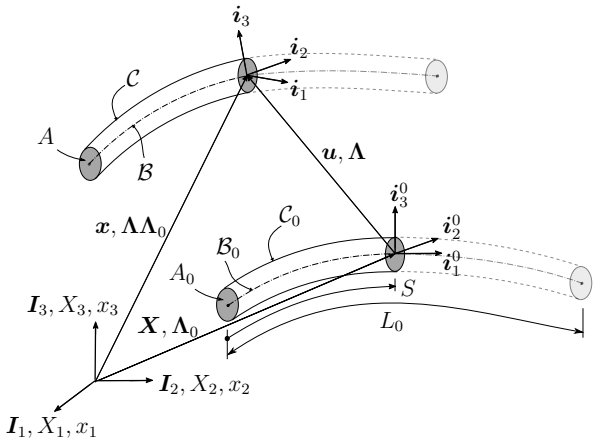

- 3D beam geom.: $\mathbf{x}^{\mathrm{3D}}(S, x_\alpha^0, t) = \mathbf{x}(S, t) + \mathbf{\Lambda}(S, t) x_\alpha^0 \mathbf{i}_\alpha^0(S)$.
- Position of $\mathcal{B}$: $\mathbf{x}(S, t) = \mathbf{X}(S) + \mathbf{u}(S, t)$.
- Reference frame: $\mathbf{i}_i^0(S, t) = \mathbf{\Lambda}_0(S)\mathbf{I}_i$ with $\mathbf{i}_1^0(S) = \frac{d\mathbf{X}(S)}{dS} = \mathbf{X}'(S)$.
- Moving frame: $\mathbf{i}_i(S, t) = \mathbf{\Lambda}(S, t)\mathbf{i}_i^0(S)$ with $\mathbf{i}_1(S, t) \perp A \wedge \nparallel \mathbf{x}'(S)$.

Geometrically exact beam model – Strain measures

- Deform. gradient: $\mathbf{F} = \frac{\partial \mathbf{x}^{\mathrm{3D}}}{\partial x_i^0} \otimes \mathbf{i}_i^0$.
- Biot strains: $\mathbf{B} = \mathbf{\Lambda}^T \mathbf{F} - \mathbf{I} = \boldsymbol{\varepsilon} \otimes \mathbf{i}_1$.
- Convected strain: $\boldsymbol{\varepsilon} = \mathbf{\Lambda}^T (\boldsymbol{\gamma} + \widetilde{\boldsymbol{\kappa}}\mathbf{p})$.
- Cross-section pos.: $\mathbf{p}(S, x_\alpha^0, t) = \mathbf{\Lambda}(S, t)\mathbf{p}_0(S, x_\alpha^0) = \mathbf{\Lambda}(S, t) x_\alpha^0 \mathbf{i}_\alpha^0(S)$.
- Spatial true strain measures:

$$\boldsymbol{\gamma} = \mathbf{x}' - \mathbf{i}_1 \quad : \text{Translational strains.}$$
$$\widetilde{\boldsymbol{\kappa}} = \mathbf{\Lambda}' \mathbf{\Lambda}^T \rightarrow \boldsymbol{\kappa} \quad : \text{Curvature.}$$

Locking in curved Timoshenko beams

- Numerical locking: Spurious strains and stresses:

  $\Rightarrow$ Stiffness overestimated.

  $\Rightarrow$ Displacements underestimated.

- Transverse shear and membrane locking in Timoshenko beams:
  - Element cannot capture the state of shear-free and inextensional bending due to spurious transverse shear and axial (membrane) strains developing in bending dominated problems.
  - Reduces accuracy and slow down convergence as:

    $h/L \to 0$ for straight beams, or

    $h/R \to 0$ for curved beams.

- In curved Timoshenko beams, transverse shear and membrane locking must be considered simultaneously (Stolarski and Belytschko, 1983).

Cantilever subjected to a concentrated end moment

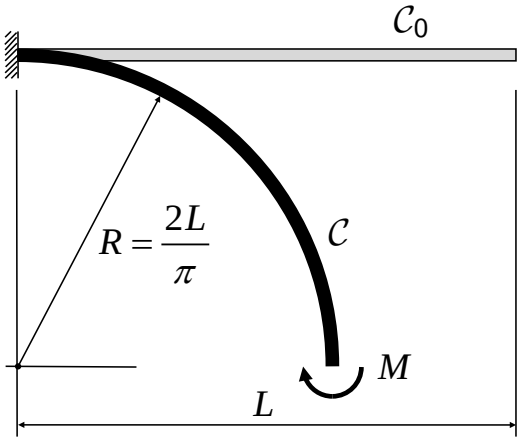

Width:	$b = 0.2$
Thickness:	$h = 0.001$
Length:	$L = 1$
Young's mod.:	$E = 24 \times 10^9$
Moment:	$M = \pi EI/2L = \pi$
Radius:	$R = 2/\pi$

- Investigate whether Lagrange and NURBS discretization of the Timoshenko beam capture the state of shear-free and inextensional bending, i.e. do transverse shear and axial strains vanish for a quadrature rule corresponding to Gauss points $n_g = p = 2$ (URI):

$$\gamma^h = (\mathbf{x}^h)' - \mathbf{i}_1^h \stackrel{!}{=} \mathbf{0}.$$

Cantilever subjected to a concentrated end moment

Lagrange

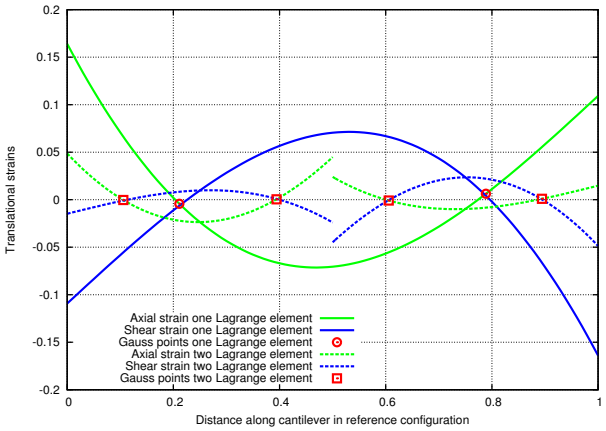

NURBS

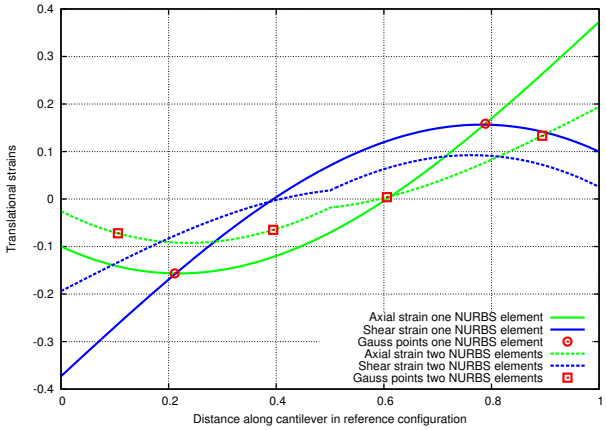

- C^0 Lagrange sample the exact solution at URI points $\Rightarrow \gamma_L^h = \mathbf{0}$.
- C^1 NURBS do not vanish at sampling points corresponding to $n_g = p$ within each NURBS element $\Rightarrow \gamma_N^h \neq \mathbf{0}$.

Constraint count method

- *Constraint count* method (heuristic approach):
  Evaluate an elements propensity of locking (Hughes 1987).
- 2D curved Timoshenko beam:
  - Optimal constraint ratio $r_{\mathrm{2D}} = \frac{3}{2}$.
  - C^0 Lagrange: $r_{\mathrm{2D},L}^h = \frac{3p}{2n_g} \Rightarrow n_g = p$.
  - C^1 NURBS: $r_{\mathrm{2D},N}^h = \frac{3}{2n_g} \Rightarrow n_g = 1$.
- URI ($n_g = p$) for Lagrange $\Rightarrow \mathrm{rank}(\mathbf{K}_T) = n_u$.
- Optimal rule: $n_g = 1$ for NURBS $\Rightarrow \mathrm{rank}(\mathbf{K}_T) < n_u$
  $\Rightarrow$ zero-energy-modes need to be stabilized.

Proposed integration schemes for NURBS

p	SRI-1/URI-1
1	$n_g = 1$
2	$n_g = 1 \setminus e = (1+n_e)/2 : n_g = 2$
3	$n_g = 1 \setminus e = 2, n_e - 1 : n_g = 2$
4	$n_g = 1 \setminus e = 2, (1+n_e)/2, n_e - 1 : n_g = 2$
5	$n_g = 1 \setminus e = 2, n_e - 1 : n_g = 2 \wedge e = (1+n_e)/2 : n_g = 3$

p	SRI-2/URI-2
1	$n_g = 1$
2	$n_g = 1 \setminus e = n_e : n_g = 2$
3	$n_g = 1 \setminus e = 1, n_e : n_g = 2$
4	$n_g = 1 \setminus e = 1, n_e : n_g = 3$
5	$n_g = 1 \setminus e = 1, n_e : n_g = 4$

- URI-1/URI-2: Translational and rotational part same rule.
- SRI-1/SRI-2: Only translational part with proposed rule.

Numerical example: Curved beam under moment loading

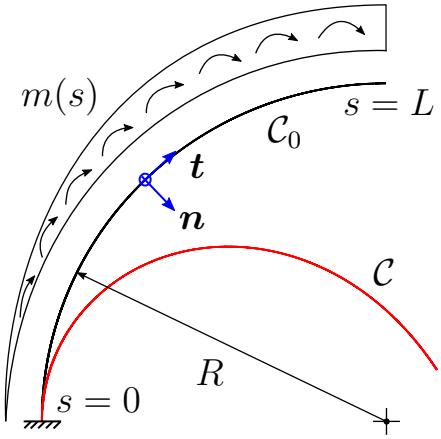

Young's modulus:	$E = 1.2 \times 10^4$ (LFEA)
	$E = 1.2 \times 10^1$ (NFEA)
Poisson's ratio:	$\nu = 0$
Radius:	$R = 1$
Width:	$b = 1$
Thickness:	$h = R/10^\rho$
Moment loading:	$m(s) = h^3 \sin\left(\frac{\pi s}{2L}\right)$

- Inextensional bending with no membrane and transverse shear strains.
- Analytical solution: $\varphi = (\mathbf{x}, \mathbf{\Lambda}) \notin \mathcal{S}^h$.
- Strong form solution for LFEA (Adam *et al.*, Comp. Mech., 2014).
- NFEA reference solution obtained with 48 octic elements (Q8L).

URI: FEA/IGA, $p = 2$ – Transverse shear strain: γ_{12}

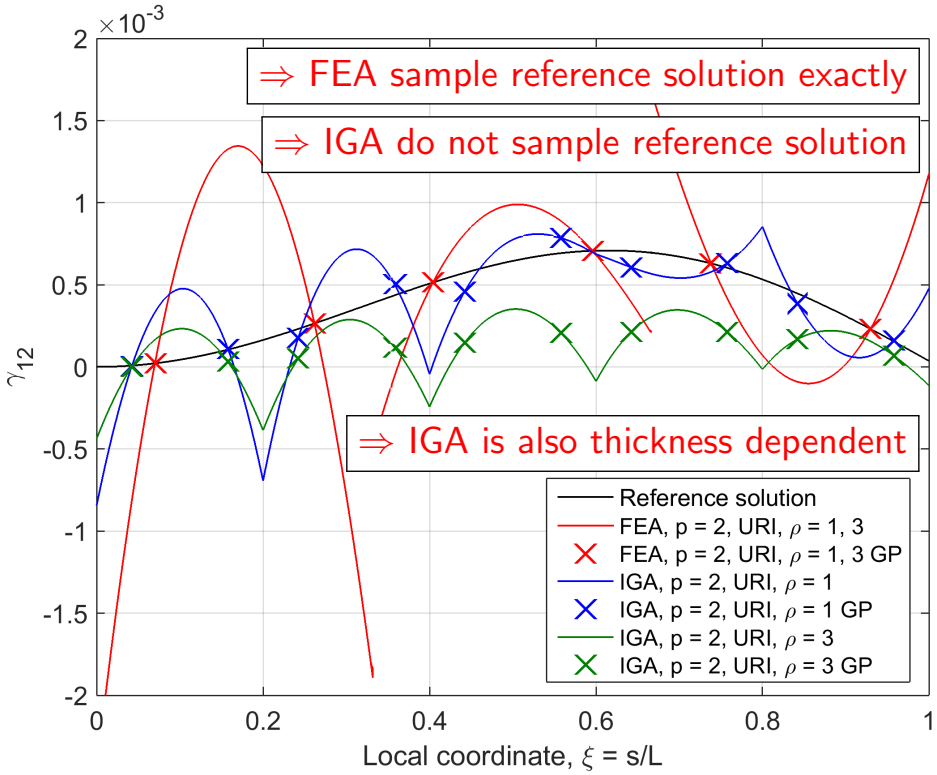

URI: FEA/IGA, $p = 2$ – Bending strain: κ_3

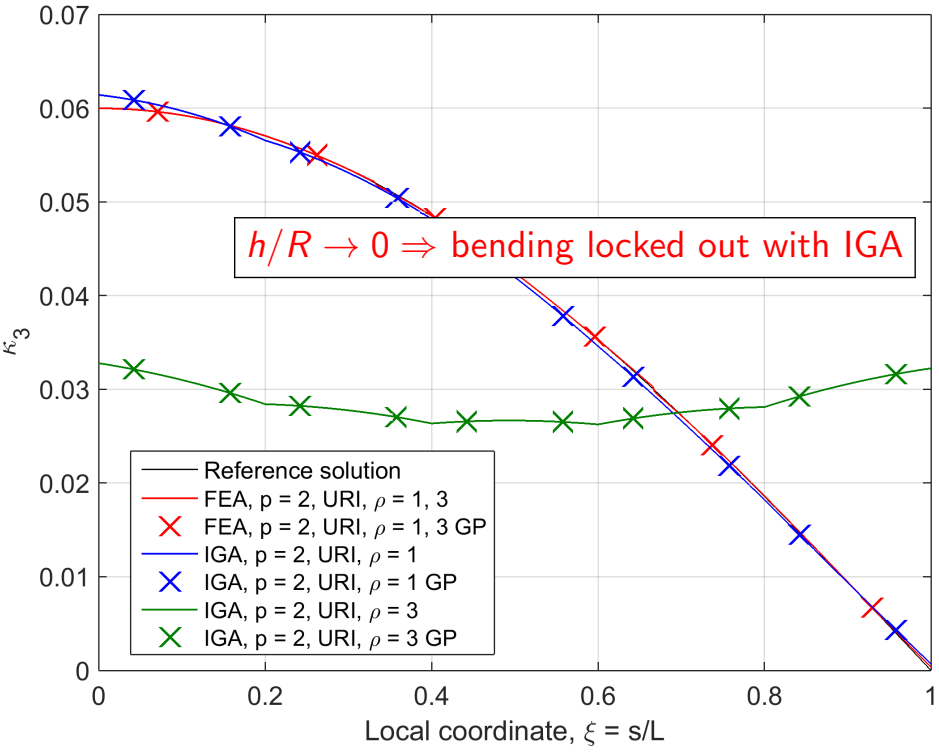

SRI-1 vs URI: IGA, $p = 2$, $\rho = 3$ – Axial strain: ε_1

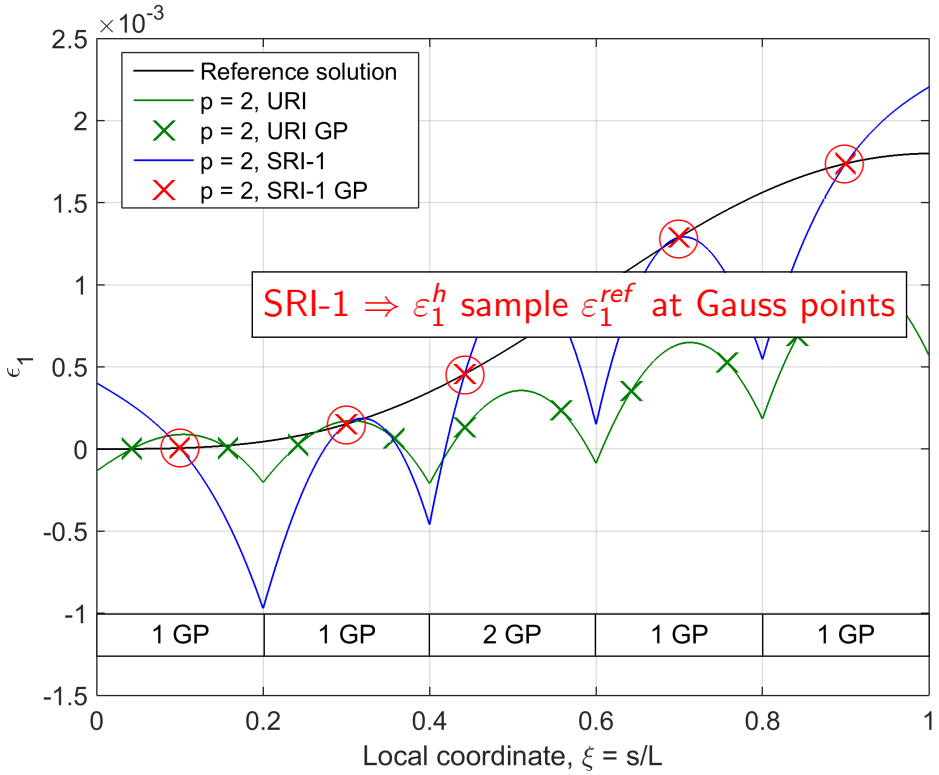

SRI-1 vs URI: IGA, $p = 2$, $\rho = 3$ – Trans. shear strain: γ_{12}

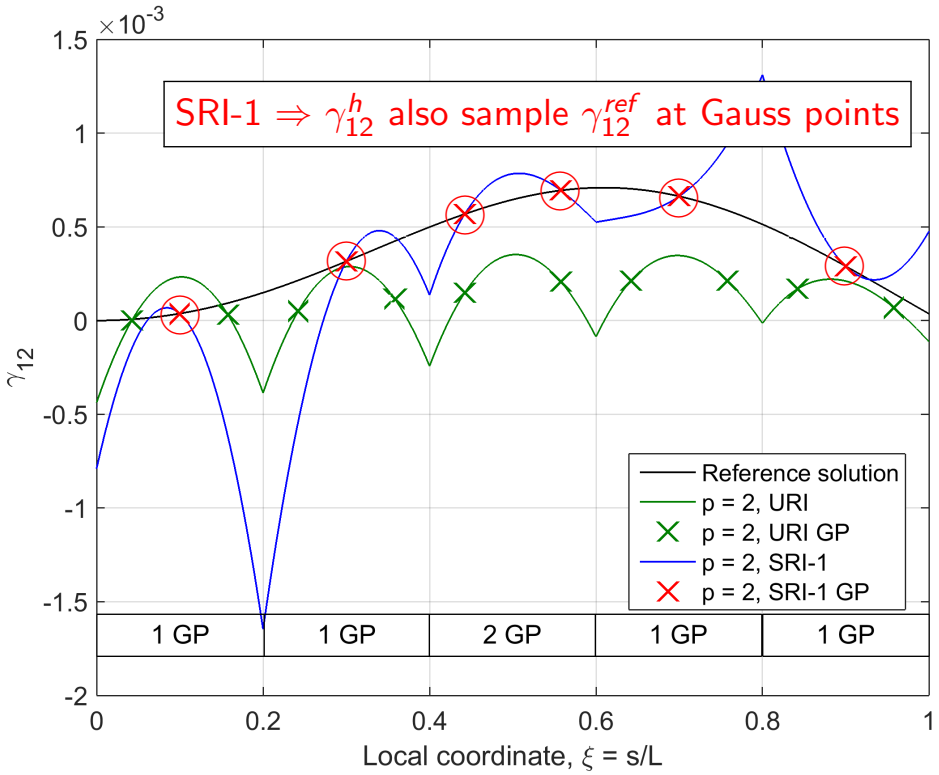

SRI-1 vs URI: IGA, $p = 2$, $\rho = 3$ – Bending strain: κ_3

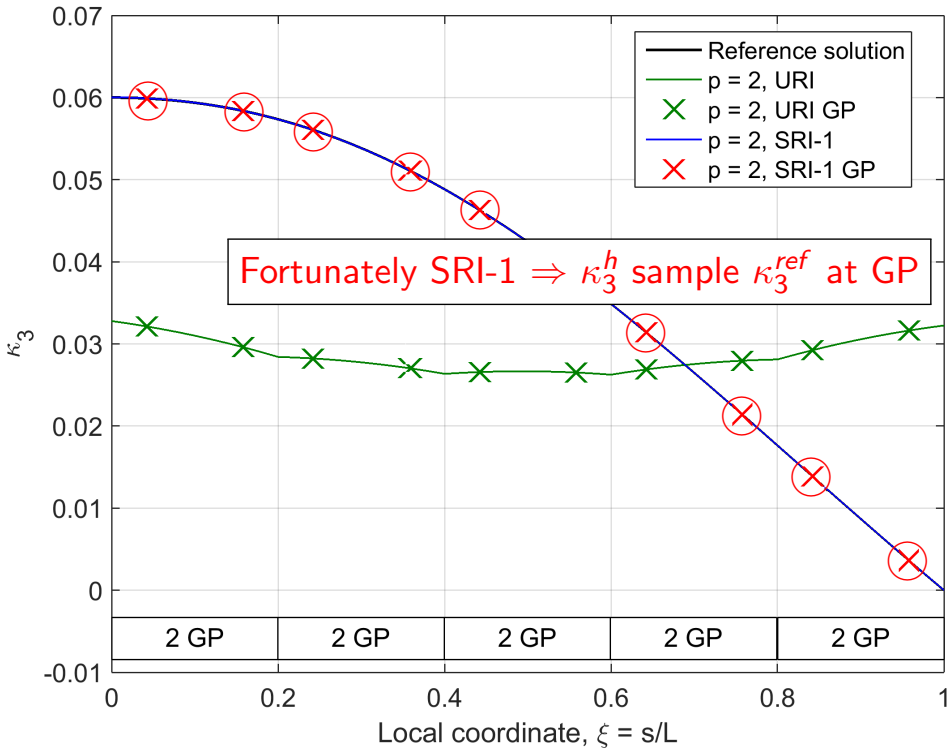

URI-1: IGA, $p = 2$, $\rho = 3$ – Axial strain: ε_1

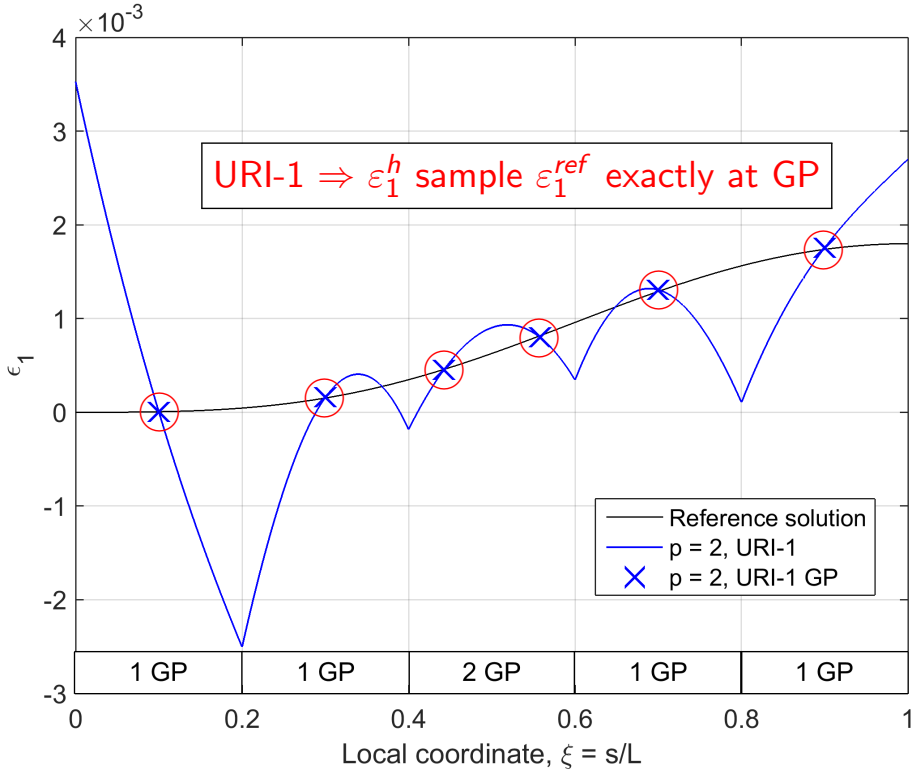

URI-1: IGA, $p = 2$, $\rho = 3$ – Transverse shear strain: γ_{12}

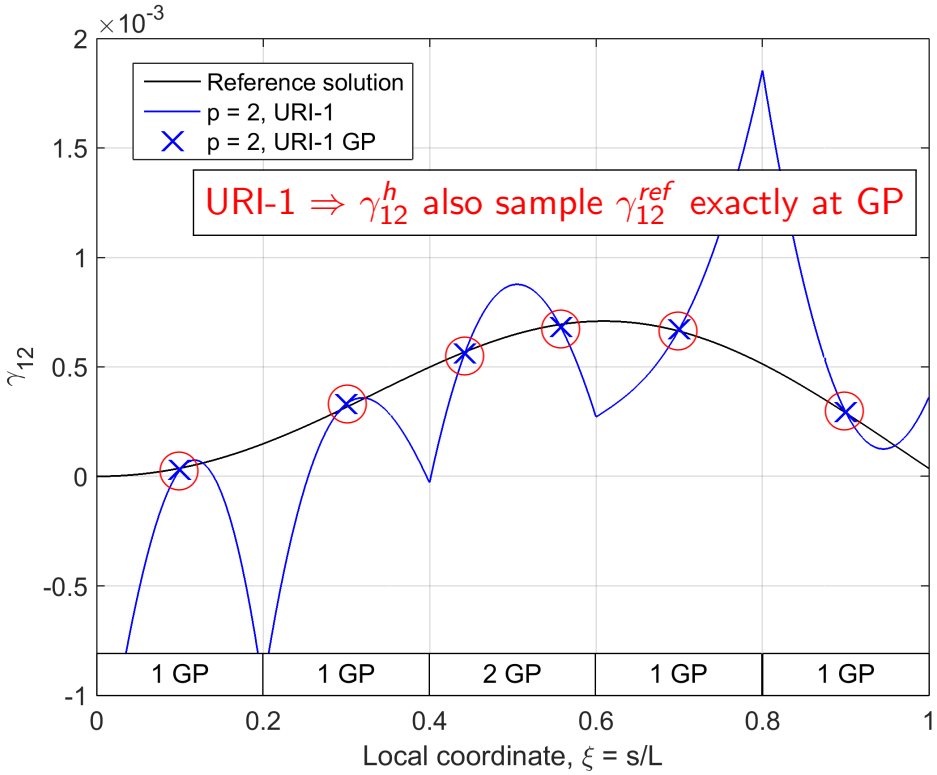

URI-1: IGA, $p = 2$, $\rho = 3$ – Bending strain: κ_3

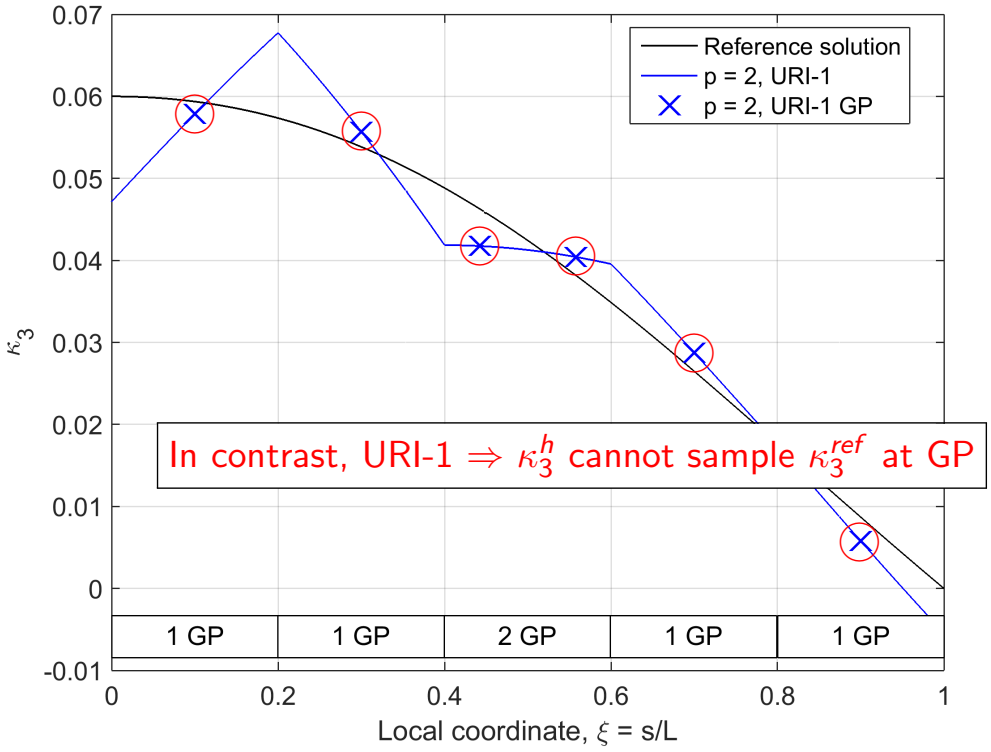

SRI: IGA, $p = 4, 5$, $\rho = 3$ – Trans. shear strain: γ_{12}

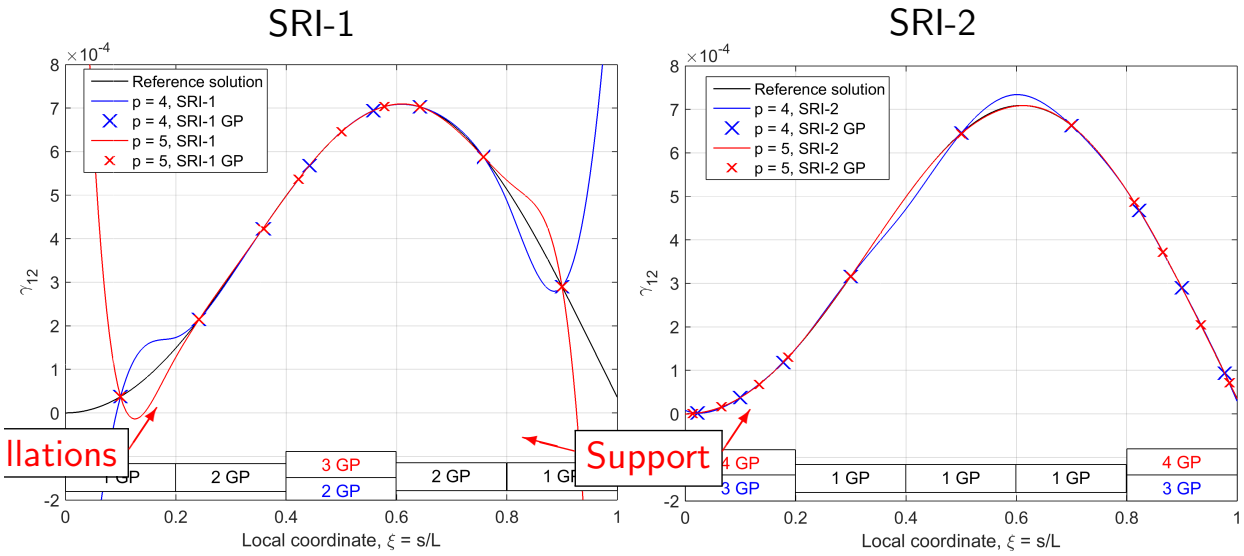

- Add gauss points adjacent to C^0-continuities to support the strain fields.

Thickness dependency – L^2-norm of error in displacements

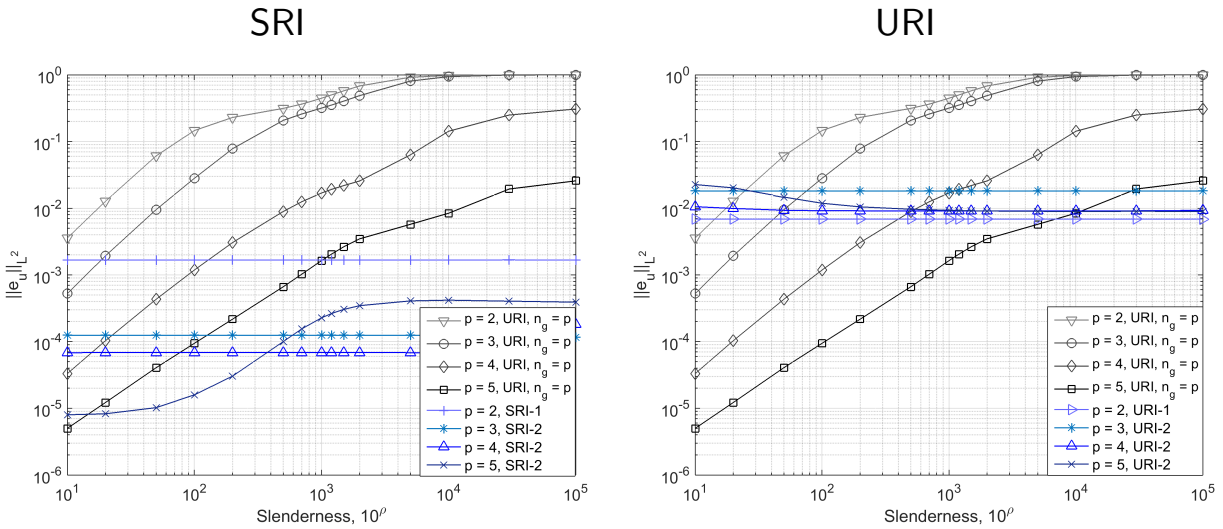

- Locking-free up to 4^{th} order.
- URI cannot sample bending accurately $\Rightarrow$ shift in absolute errors.
- Equation system slightly over-constrained with quintic elements.

Displacement relative error in L^2-norm (LFEA)

NURBS – URI vs SRI

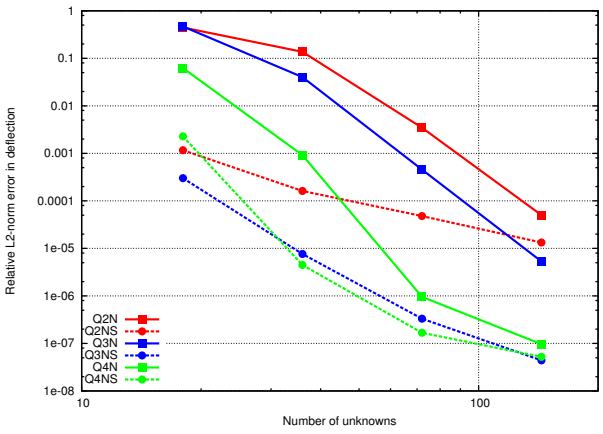

NURBS vs Lagrange

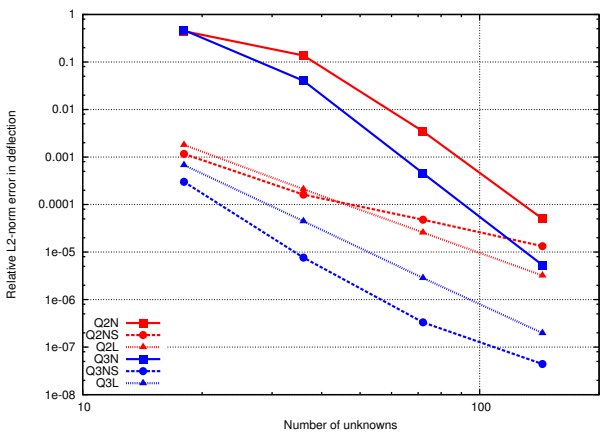

- NURBS: The low accuracy obtained with conventional URI reduced several orders with SRI.
- Conventional URI: Lagrange outperforms NURBS.
- Cubic NURBS-SRI exhibit superb performance and outperforms Lagrange.

Bending moment relative error in L^2-norm (LFEA)

NURBS – URI vs SRI

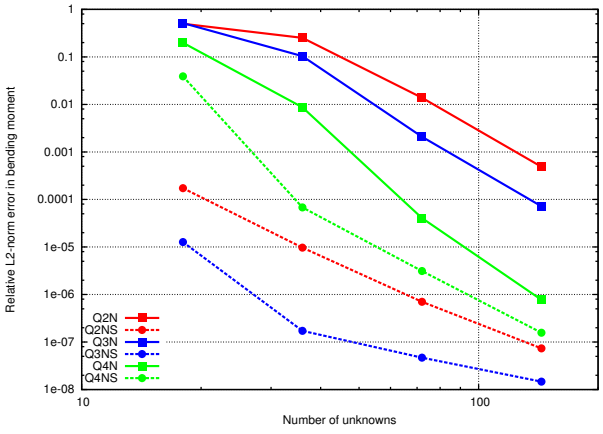

NURBS vs Lagrange

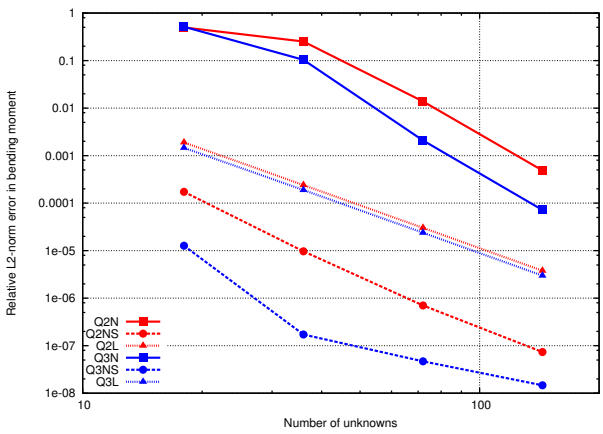

- The low accuracy obtained with conventional NURBS-URI reduced several orders with SRI.
- Lagrange outperforms NURBS with conventional URI.
- NURBS-SRI exhibit superb performance and outperforms Lagrange.

Displacement relative error in L^2-norm (NFEA)

NURBS – URI vs SRI

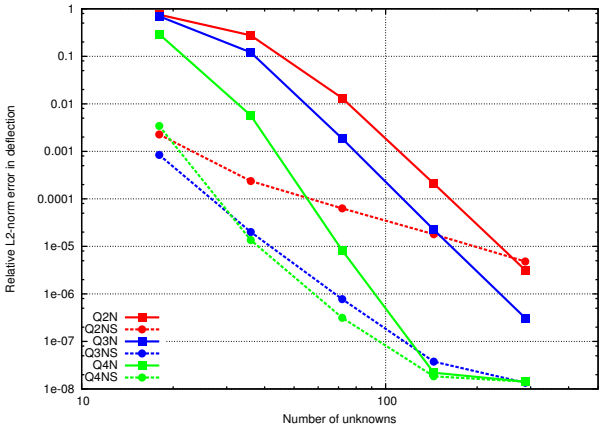

NURBS vs Lagrange

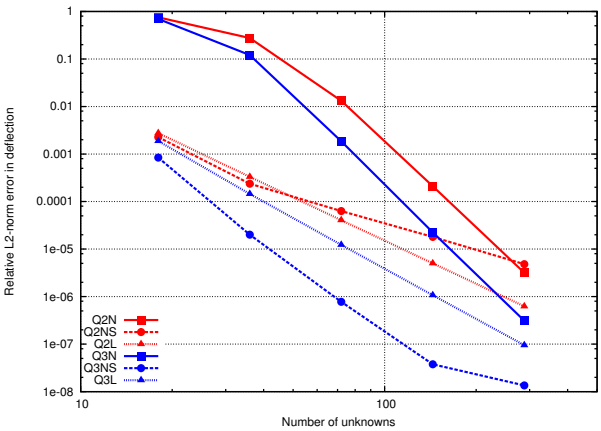

- NURBS: The low accuracy obtained with conventional URI reduced several orders with SRI also for NFEA.
- Conventional URI: Lagrange outperforms NURBS.
- Cubic NURBS-SRI exhibit superb performance and outperforms Lagrange.

Bending moment relative error in L^2-norm (NFEA)

NURBS – URI vs SRI

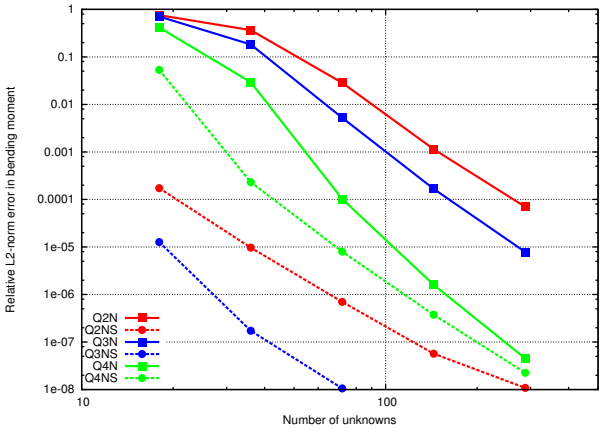

NURBS vs Lagrange

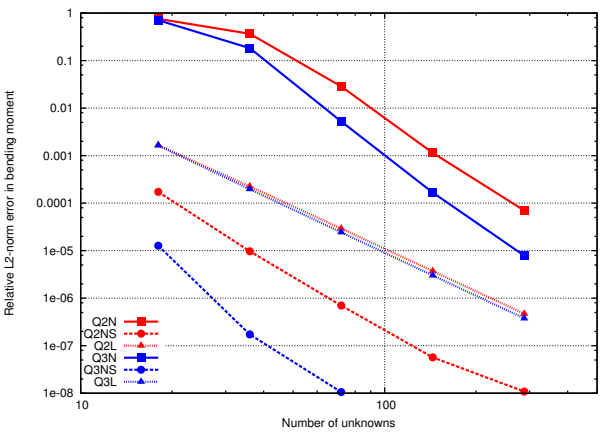

- The low accuracy obtained with conventional NURBS-URI reduced several orders with SRI.
- Lagrange outperforms NURBS with conventional URI.
- NURBS-SRI exhibit superb performance and outperforms Lagrange.

Concluding remarks

- Quadrature rule significantly impacts not only the computational efficiency but also propensity of locking in NURBS-based curved Timoshenko elements.
- Applying conventional URI with $n_g = p$ per NURBS element, locking is revealed in all strain fields for NURBS.
- Our study has revealed that SRI of the translational part may be used to alleviate both membrane and transverse shear locking for NURBS.
- The numerical results also show that:
  1) $\forall p$, the rotational part should be integrated with $n_g = p$,
  2) $\forall p$, the translational part should be integrated with $n_g = 1$, except;
     a) $p = 2$, an extra GP should be added to an element near the center.
     b) $p \geq 3$, the two boundary elements that should be integrated with $n_g = p - 1$.
- Applying recommended quadrature rules for all parts, sample the translational part of the strain fields accurately, however, leaving the rotational part incorrect.
- The recommended SRI quadrature rules for NURBS yields improved accuracy for all polynomial orders for both LFEA and NFEA.
- Recommended quadrature rules for cubic interpolated NURBS yields superb accuracy in both displacements and stress resultants and outperform Lagrange for both LFEA and NFEA.

Thank you for your attention!

Bibliography

[1] Adam, C., Bouabdallah, S., Zarroug, M., and Maitournam, H. (2014a). Improved numerical integration for locking treatment in isogeometric structural elements, part I: Beams. *Comput. Methods Appl. Mech. Engrg.*, **279**:1–28.

[2] Adam, C., Hughes, T., Bouabdallah, S., Zarroug, M., and Maitournam, H. (2014b). Selective and reduced numerical integrations for NURBS-based isogeometric analysis. *Comput. Methods Appl. Mech. Engrg.*, **279**:1–28.

[3] Antmann, S. (1995). *Nonlinear Problems of Elasticity*. Springer.

[4] Auricchio, F., Beirão da Veiga, L., Kiendl, J., Lovadini, C., and Reali, A. (2013). Locking-free isogeometric collocation methods for spatial Timoshenko rods. *Comput. Meth. Appl. Mech. Engrg.*, **263**: 113–126.

[5] Bathe, K. and Bolourchi, S. (1979). Large displacement analysis of three-dimensional beam structures. *Int. journal for numerical methods in engineering.*, **14:** 961–986.

[6] Beirão da Veiga, L., Lovadina, C., and Reali, A. (2012). Avoiding shear locking for the Timoshenko beam problem via isogeometric collocation methods. *Comput. Meth. Appl. Mech. Engrg.*, **241–244**: 38–51.

[7] Bell, K. (2013). *An engineering approach to finite element analysis of linear structural mechanics*. Akademika Publ., Trondheim, 1st edition.

[8] Borden, M., Scott, M., Verhoosel, C., Hughes, T., and Landis, C. (2012). A phase-field description of dynamic brittle-fracture. *Comput. Meth. Appl. Mech. Engrg.*, **217–220**: 77–95.

[9] Bouclier, R., Elguedj, T., and Combescure, A. (2012a). Locking free isogeometric formulations of curved thick beams. *Comput. Methods Appl. Mech. Engrg.*, **245–246:** 144–162.

[10] Bouclier, R., Elguedj, T., and Combescure, A. (2012b). Locking free isogeometric formulations of curved thick beams. *Comput. Meth. Appl. Mech. Engrg.*, **245–246**: 144–162.

[11] Bouclier, R., Elguedj, T., and Combescure, A. (2014). An isogeometric locking-free nurbs-based solid-shell elements for nonlinear analysis. *Comput. Methods Appl. Mech. Engrg.*, **101**: 774–808.

[12] Caseiro, J., Valente, R., Reali, A., Kiendl, J., Auricchio, F., and Alves de Sousa, R. (2014). On the assumed natural strain method to alleviate locking in solid-shell NURBS-based finite elements. *Comput. Meth. Appl. Mech. Engrg.*, **53**: 1341–1353.

[13] Cazzani, A., Magalù, M., and Turco, E. (2014). Isogeometric analysis of plane-curved beams. *Mathematics and Mechanics of Solids*, 1–16.

[14] Cook, R., Malkus, D., and Plesha, M. (1989). *Concepts and Applications of Finite Element Analysis*. John Wiley and Sons Inc., New York, 3rd edition.

[15] Echter, R. (2013). *Isogeometric Analysis of Shells*. PhD thesis, Baustatik und Baudynamik, Univerität Stuttgart.

[16] Echter, R. and Bischoff, M. (2010). Numerical efficiency, locking and unlocking of nurbs finite elements. *Comput. Meth. Appl. Mech. Engrg.*, **199**: 374–382.

[17] Echter, R., Oesterle, B., and Bischoff, M. (2013). A hierarchic family of isogeometric shell finite elements. *Comput. Meth. Appl. Mech. Engrg.*, **199**: 374–382.

[18] Elguedj, T., Bazilevs, Y., Calo, V. M., and Hughes, T. (2008). $\overline{\mathrm{B}}$ and $\overline{\mathrm{F}}$ projection methods for nearly incompressible linear and non-linear elasticity and plasticity using higher-order nurbs elements. *Comput. Meth. Appl. Mech. Engrg.*, **197**: 2732–2762.

[19] Farin, G. (2002). *Curves and surfaces for CAGD: A practical guide*. Academic press, San Diego.

[20] Helgedagsrud, T., Raknes, S., and Mathisen, K. (2015). On locking-free methods for isogeometric large deformation analysis of geometrically exact three-dimensional beams. *8. National Conference on Computational Mechanics.*

[21] Hughes, T. (1987). *The Finite Element Method.* Prentice-Hall, Englewood Cliffs, NJ, USA.

[22] Hughes, T., Cottrell, J., and Bazilevs, Y. (2005). Isogeometric analysis: CAD, finite elements, NURBS, exact geometry and mesh refinement. *Comput. Methods Appl. Mech. Engrg.*, **194**:4135–4195.

[23] Ibrahimbegović, A. (1995). Finite element analysis of linear and nonlinear planar deformations of elastic initially curved elements. *Int. J. Numer. Meth. Engrg.*, **122**: 11–26.

[24] Ibrahimbegović, A., Frey, F., and Kožar, I. (1995). Computational aspects of vector-like parameterization of three-dimensional finite rotations. *Int. J. Numer. Meth. Engrg.*, **38**: 3653–3673.

[25] J. Austin Cottrell, Thomas J.R. Hughes, Y. B. (2009). *Isogeometric analysis : toward integration of CAD and FEA.* Wiley, Chichester, 1st edition.

[26] Kiendl, J. (2010). *Isogeometric analysis and shape optimal design of shell design of shell structures.* PhD thesis, Fakultät für Bauingenieur- und Vermessungswesen, Technische Universität München.

[27] Lee, P. and Sin, H. (1994). Locking-free curved beam element based on curvature. *Int. J. for Num. Meth. in Engrg.*, **37**: 989–1007.

[28] Mathisen, K., Okstad, K., Kvamsdal, T., and Raknes, S. (2011). Isogeometric analysis of finite deformation nearly incompressible solids. *J. Struct. Mech.*, **44**: 260–278.

[29] Mathisen, K., Okstad, K., Kvamsdal, T., and Raknes, S. (2013). Isogeometric analysis applied to frictionless large deformation elastoplastic contact. *Proc. XII Int. Conf. Comput. Plast. (COMPLAS 2013)*, Oñate, E., Owen, D.R.J., Peric, D. and Suárez, B. (Eds.), CIMNE, Barcelona, Spain pp. 969–986.

[30] Mathisen, K., Okstad, K., Kvamsdal, T., and Raknes, S. (2015). Simulation of contact between subsea pipeline and trawl gear using mortar-based isogeometric analysis. *Proc. XII Int. Conf. Comput. Plast. (COMPLAS 2013)*, Proc. VI Int. Conf. Comput. Meth. Marine Engrg. (MARINE 2015), Salvatore, F., Broglia, R. and Muscari, R. (Eds.), CIMNE, Barcelona, Spain.

[31] MathWorks (2015). MATLAB®documentation.

[32] Piegl, L. and Tiller, W. (1997). *The NURBS Book*. Springer, Berlin, 2nd edition.

[33] Prathap, G. (1993). *The Finite Element Method in Structural Mechanics*. Kluwer Academic Press, Dordrecht.

[34] Raknes, S., Deng, X., Bazilevs, Y., Benson, D., Mathisen, K., and Kvamsdal, T. (2012). Isogeometric rotation-free bending-stabilized cables: Statics, dynamics, bending strips and coupling with shells. *Comput. Meth. Appl. Mech. Engrg.*, **263**: 127–143.

[35] Reissner, E. (1981). On finite deformations of space curved beams. *Int. J. Solids. Struct.*, **32**: 734–744.

[36] Riesenfield, R. (1973). *Approximation of B-spline Approximation to Geometric Problems of Computer-Aided Design*. PhD thesis, Department of Systems and Information Science, Syracuse University, NY.

[37] Roark, R., Young, W., and Budynas, R. (2002). *Roark's formulas for stress and strain*. McGraw-Hill, New York, 7th edition.

[38] Simo, J. (1985). A finite strain beam formulation. the three-dimensional dynamic problem. part I. *Comput. Meth. Appl. Mech. Engrg.*, **49**: 55–70.

[39] Simo, J. and Vu-Quoc, L. (1986). A three-dimensional finite strain rod model. part II: Computational aspects. *Comput. Meth. Appl. Mech. Engrg.*, **58**: 79–116.

[40] Simo, J. and Vu-Quoc, L. (1991). A geometrically-exact rod model incorporating shear and torsion-warping deformation. *Int. J. Solids. Struct.*, **27**: 371–393.

[41] Stolarski, H. and Belytschko, T. (1983). Shear and membrane locking in curved C^0 elements. *Comput. Methods Appl. Mech. Engrg.*, **41**: 279–296.

[42] Takizawa, K., Tezduyar, T., Hsu, M.-C., Øiseth, O., Mathisen, K., Kostov, N., and McIntyre, S. (2014). Engineering analysis and design with ALE-VMS and space-time methods. *Arch. Comput. Meth. Engrg.*, **21**: 481–508.

[43] Timoshenko, S. P. (1921). On the correction for shear of the differential equation for transverse vibrations of prismatic bars. *Philosophical Magazine*, **41**: 744–746.

[44] Timoshenko, S. P. (1922). On the transverse vibrations of bars of uniform cross-section. *Philosophical Magazine*, **43**: 125–131.

[45] Versprille, K. J. (1975). *Computer-Aided design applications of the rational B-spline approximation form.* PhD thesis, Syracuse University, NY.

[46] Xu, Z. (1986). A simplc and efficient triangular finite element for plate bending. *Am Mechanicu Sinica*, **2**: 185–192.